THE UNIVERSITY OF CHICAGO

STUDIES OF ADSORBENTS FOR ACTINIDE SEPARATIONS RELEVANT TO THE NUCLEAR FUEL CYCLE

A DISSERTATION SUBMITTED TO

THE FACULTY OF THE DIVISION OF THE PHYSICAL SCIENCES

IN CANDIDACY FOR THE DEGREE OF

DOCTOR OF PHILOSOPHY

DEPARTMENT OF CHEMISTRY

BY

MAREK PIECHOWICZ

CHICAGO, ILLINOIS

DECEMBER 2019

DEDICATION

to my family

TABLE OF CONTENTS

LIST OF TABLES

LIST OF FIGURES

LIST OF EQUATIONS

LIST OF SCHEMES

LIST OF SYMBOLS AND ABBREVIATIONS

ºC	Degrees Celsius
Å	Angstrom
α	Selectivity Ratio
α particle	Alpha (i.e. helium nucleus) Particle
β particle	Beta (i.e. electron) Particle
γ particle	Gamma (i.e. photon) Particle
η	Eta
θ	Theta
μ	Micro (prefix)
ΔG	Difference in Gibbs Free Energy
4CS	4-cyanostyrene
An	Actinide
AN	Acrylonitrile
ANL	Argonne National Laboratory
AO	Amidoxime
APS	Advanced Photon Source
BAP	Bis-Amidoxime Polymer
B3LYP	Hybrid Functional from Becke, Lee, Yang, Parr
bis-AO	Bis-Amidoxime
CCS	Carbon Capture and Storage
CN	Carbon Nitrogen Triple Bond (nitrile group)
CPCM	Polarizable Conductor Calculation Model
CPM	Counts per Minute

DFT	Density Functional Theory
DPM	Disintegrations per Minute
D_W	Distribution Ratio
EtOH	Ethanol
EXAFS	Extended X-Ray Absorption Fine Structure
FTIR	Fourier Transfer Infrared Spectroscopy
GCMS	Gas Chromatography Mass Spectrometry
H_2A	Glutarimidedioxime
HEXS	High-Energy X-ray Scattering
HIPE	High Internal Phase Emulsion
HOMO	Highest Occupied Molecular Orbital
ICP-MS	Inductively Coupled Plasma Mass Spectrometry
IPCC	Intergovernmental Panel on Climate Change
IX	Ion-Exchange
LC-MS	Liquid Chromatography-Gass Spectrometry
LUMO	Lowest Unoccupied Molecular Orbital
MeOH	Methanol
mg	Milligram
mg g^{-1}	Milligrams per Gram
mM	MilliMolar (molar^{-3})
mmol	Millimoles
M	Molar (mol L^{-1})
m^2 g^{-1}	Square Meters per Gram
MS	Mass Spectrometry
N_2	Nitrogen Gas

NaOAc	Sodium Acetate
NBO	Natural Bond Orbital
NE	Nuclear Energy
NH_2OH	Hydroxylamine
NMR	Nuclear Magnetic Resonance
NNBIS	N,N′-methylenebis(acrylamide)
OLEX	Crystallography Software
poly(HIPE)	Poly(High Internal Phase Emulsion)
pH	Acidity (-log[H^+])
PPB	Parts Per Billion
PPM	Parts Per Million
QTAIM	Quantum Theory of Atoms in Molecules
RCP	Representative Concentration Pathway
RIGP	Radiation Induced Graft Polymerization
SEM	Scanning Electron Microscopy
SS	Seawater Simulant
St	Styrene
SX	Solvent Extraction
SXRD	Single-Crystal X-ray Diffraction
TGA	Thermogravimetric Analysis
Uranyl	Uranium Dioxide (+2) Cation
WBI	Wiberg Bond Index
XAFS	X-ray Absorption Fine Structure
XRD	X-ray Diffraction
ZPE	Zero-Point Energy

ABSTRACT

Our planet is experiencing unprecedented warming due to levels of anthropogenic CO_2 in the atmosphere never before attained.

Global climate change can only be addressed through a combination of policy, education, and technological effort. Central to this is the rapid adoption of energy sources which emit much less carbon dioxide than conventional sources such as coal and natural gas. Nuclear energy remains the only mature, low carbon technology capable of baseload power generation and represents our best chance at decreasing emissions without drastically lowering living standards.

Chapter 1 introduces the very basics of the nuclear fuel cycle while emphasizing the need for a robust uranium supply in the front end. A brief survey of previous work sets the basis for a discussion on the design, synthesis, and testing of advanced materials for actinide separations found in later chapters. Chapter 2 introduces the bifunctional chelator, a ditopic amidoxime/carboxylic acid functionalized diaryl ether molecule identified by computational work to exhibit ultrahigh uranium affinity.[1] Uranium isotherms indicate an equilibrium capacity of 553 mg U g^{-1} ligand, one of the highest reported to date. The next chapter further develops the ideas presented in Chapter 2. Chapter 3 discusses the synthesis of bis-amidoxime functionalized ligands[2] as well as their incorporation into robust polymer materials. These polymers show high selectivity for U over V achieving a 1:1 molar uptake of U:V after 37 days in seawater simulant. Raman spectroscopy used to gauge the extent of ligand-UO_2^{2+} binding finds a dramatic redshift of the ν_1 U═O stretching frequency suggestive of strong amidoxime binding in the equatorial sphere.[3] The following chapter provides details for *in silico* work[4] investigating the origins of selectivity within the functionalized polymer materials. Density functional theory is used to ascertain the geometrically optimized structures of functionalized ligands with the nuclear energy relevant isotopes ^{90}Sr, ^{137}Cs, and ^{233}U. Radionuclide uptake

studies confirm the trend born from calculations—U can associate with bis-amidoxime ligands under a broad range of pH. Uptake of Sr is negligible and Cs is less than 30% under all conditions.

Chapter 5 introduces the poly(HIPE), a new adsorbent platform with potential to dramatically increase efficiencies in industrial-scale actinide separations. Several amidoxime-functionalized, crosslinked poly(styrene) based poly(HIPEs) are described and characterized via FTIR, N_2 uptake, and SEM. Separation experiments show a reversal in conventional trends for amidoxime-based materials—the poly(HIPEs) display remarkable selectivity for Th over U over a pH range relevant to groundwater decontamination. High energy X-ray scattering (HEXS) data provide insight into the speciation of the bound metal providing evidence for the presence of Th oligomers bound to the polymers. This observation is used to inform upon the experiments presented in the concluding chapter. The last chapter describes work on a series of benzamidoxime functionalized poly(HIPE) materials for Th, U, and Pu separations. A summary and outlook into proposed work in this field is provided towards the end of this chapter.

ACKNOWLEDGEMENTS

Successful completion of a graduate program is an impossible task without the support and encouragement of family, friends, colleagues, and mentors. To all who have helped me on this journey, I am forever grateful.

I thank Professor Stuart Rowan, first and foremost, for recognizing my worth when I switched labs in my 3rd year. Leaving the program was a very real possibility at that point but Prof. Rowan provided me another chance. I am deeply grateful for his mentorship and am very glad that I have been able to contribute to his successful research program. It has been an absolute privilege learning polymer chemistry from the best. I also thank Dr. Soderholm for inviting me to Argonne when I was in between groups. Her mentorship was invaluable in those early days and I continue to seek her helpful guidance and support. I am proud of the work I've been able to accomplish in her group thus far and look forward to tackling emerging separations challenges in the future.

I am particularly grateful to my dissertation committee including Prof. Bozhi Tian and Prof. John Anderson for reviewing my thesis and providing valuable advice throughout graduate school. Both professors were sympathetic during the lab move—Prof. Tian taking time to talk to me, provide advice, and even suggest groups I should consider and Prof. Anderson letting me sit in on group meetings when I was considering his lab. Genuine interest in student wellbeing is often hard to find (at UChicago or elsewhere), but both Profs. Tian and Anderson *really care* about students. I wish them continued success at UChicago and am confident that through their commitment to student success, they'll lead the Chemistry Department in the right direction.

I am grateful for starting off in the lab of Professor Wenbin Lin as he taught me a supremely valuable skill—resilience. Switching labs in my 3rd year was the best decision of my graduate career and I thank Prof. Lin for precipitating that decision.

I recall fondly time spent with grad students and post-docs in the Lin Lab. Carter Abney remains an ideal that all young scientists should aspire to emulate. His rigorous adherence to the scientific method, skeptical inquiry, and unrelenting effort have greatly influenced my own conduct during graduate school. I am honored to have worked with him and to call him a friend. Sharing an office with Dan Micheroni made time spent in the Lin Lab not seem so bad. I am thankful for the long discussions we had on foreign affairs, politics, and—at times—chemistry. His friendship and comic relief made the satellite lab a little brighter. Late night beamtime with Carter and Dan account for some of the best memories of my time in that group.

I also thank Chris Poon, Zekai Lin, Xin Zhou, Nathan Thacker, Connor Gilhula, and Sam Veroneau for their support and helpful discussions on a wide range of topics including synthesis difficulties (which were numerous), uranium uptake, and the graduate school experience. Waxing philosophical, I could always find someone to talk to among these friends.

I thank members of my cohort including Maggie Hudson and Erik Reinhart for their friendship and support along the way. I always look forward to our dinners together and enjoy commiserating about grad school, talking politics, and catching up. Both have greatly enriched my time in Chicago.

More recently, I am grateful for newly formed friendships with members of the Rowan group including Katie Herbert, née Greenman, Debbie Schneiderman, Nan Pon, Yefei Zhang, and Adarsh Suresh. Katie and Debbie helped put graduate school in perspective and offered useful advice on what to do (and what not to do!) upon graduation. By working late most weekdays (and overlapping with my Argonne/UChicago work schedule), I've spent a good deal of time interacting with Yefei and Nan. I thank them for helpful discussions on chemistry. I am confident that the poly(HIPE) project will live on in the trusty hands of Adarsh Suresh, a hardworking, ambitious first-year with whom I've had many engaging discussions.

I also like to thank current and former members of Bldg. 200, M-wing Heavy Elements and Separation Science Group including Mark Antonio, Gengbang Jin, Shanna Estes, Matthieu Autillo, Kaitlin Lovering, and Will Rock. Mark Antonio remains a wealth of knowledge on all things X-ray, E-chem, and 3rd phase. I hope to continue exchanging cheese Danishes for access to his encyclopedic separations knowledge in the future. Shanna Estes taught me the unwritten tips and tricks in handling rad materials crucial to my development as a separations scientist. I am also grateful for Matthieu Autillo for teaching me the proper ways to handle bulk amounts of Pu and Np. I'm also glad to have met Gengbang Jin, a former M-Wing resident, for taking an interest in my life—often asking how I'm doing, and really caring about the answer. I also thank my former officemates, Kaitlin Lovering and Will Rock, for commiserating when things went poorly and for celebrating with me when things went well.

I think about those who have influenced me during my studies but are no longer here to see me finish. I recall Alan Swartz's friendship during that first summer in Chicago and am very glad to have known him. Eating expensive food truck food in the sweltering July heat as young 0th years seems like it happened only yesterday. I also remember Dr. Renato Chiarizia, the prototypical **mentor**, *my* mentor, and friend. He taught me most of what I know about separation science and did so in an unassuming, patient manner uncharacteristic of many these days. It is not often that one learns directly from one of the giants in a field. I am privileged to have worked in the lab with Renato and to have thought about separations challenges with one of the field's most experienced scientists—for that I am truly grateful.

I thank collaborators at the Advanced Photon Source (APS) including Yu-Sheng Chen (15-ID), John Katsoudas (10-BM), and Joshua Wright (10-BM) for their patience and helpful advice throughout the hundreds of hours I've spent at the beamline. I thank John Strain from Agilent in his assistance in troubleshooting the ICP-MS system when the lines were clogged, the autosampler was stuck, and the turbomolecular pump exploded.

I’m also grateful for all those who have supported me in one capacity or another why at the University of Chicago and Argonne including James Marsicek for helping with radioactive sample transport to and from the APS and Bradford Stacy and Gordon Johnson, two topnotch HP techs for their kind support as I worked in the hot labs.

I am grateful for my family—my mother and father, grandmother, and sisters—who dealt with my ups and downs and never once doubted me. I attribute my success to the values of perseverance, resourcefulness, and optimism instilled in me from a young age. This degree is a testament to their unwavering belief in me.

I’d also like to thank the DOE Office of Science, Basic Energy Sciences, the Nuclear Energy University Program, and the Physical Sciences Division at the University of Chicago for funding my research over the years.

Finally, I thank all those who offered words of encouragement, a hug, a handshake, or a piece of advice throughout my time in grad school. Those little things help more than you know. Thank you.

Chapter 1: Motivation and Introduction to Actinide Separations

1.1 The Role of CO_2

It has been known since Arrhenius' work[5] in 1896 that carbon dioxide (along with methane, water vapor, and certain other gases) greatly contribute to the warming of the atmosphere due to their absorption of infrared radiation. Carbon dioxide (CO_2) levels in the atmosphere, in particular, are at their highest point since the beginning of measured records (i.e. ~800,000 years ago).[6] Records from the Mauna Loa Observatory in Hawaii[7] show a near exponential growth of this greenhouse gas (GHG) since the 1960s (**Figure 1.1**). Levels above 415 ppm were observed for the first time on record in 2019.[8]

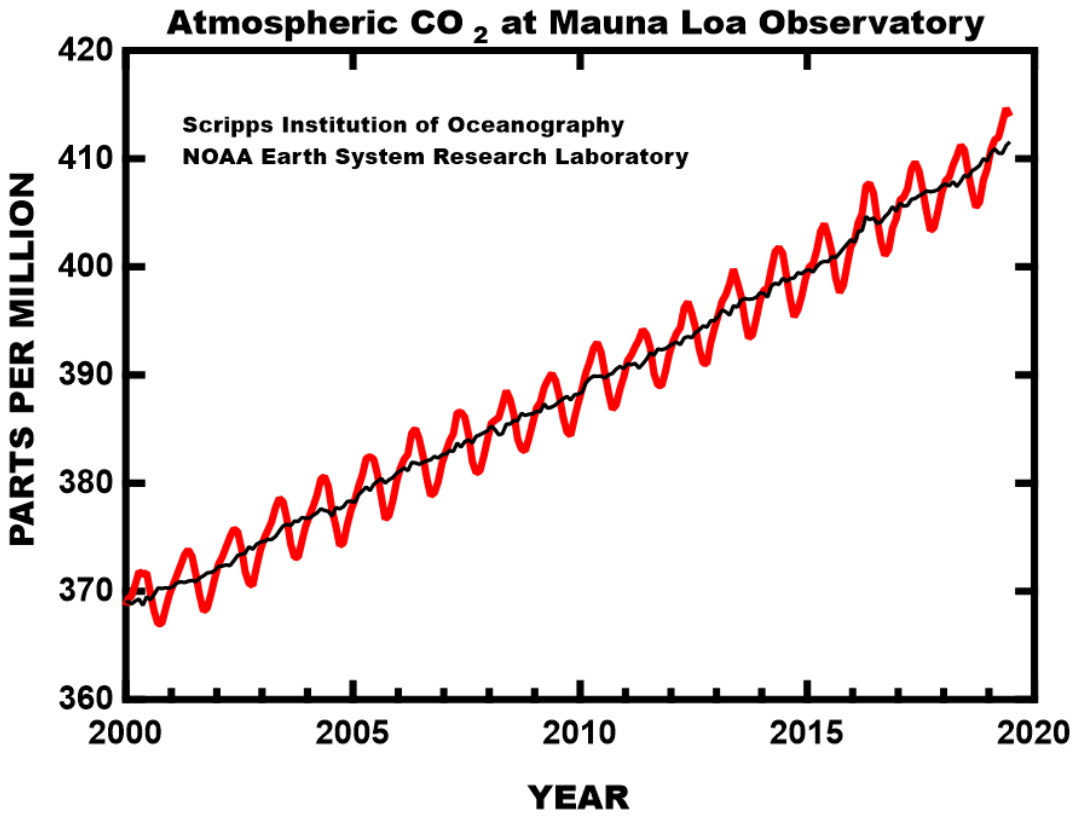

Figure 1.1 Red curve is average, monthly carbon dioxide levels measured at Mauna Loa Observatory, Hawaii. Black line is moving average of seven adjacent values. Data adapted from Keeling et al.

While the genesis of CO_2 in the atmosphere is varied, the vast majority is due to the burning of fossil fuels for electricity production, heat generation, and transportation.[9] Correlations between these anthropogenic sources of carbon dioxide and global average temperature have been identified by dozens of organizations worldwide.[10] Despite these clear trends, there remains a national reluctance to adopt clean energy technology. Public disapproval of certain clean energy policies (e.g. carbon taxes) has hindered efforts at addressing the problem.

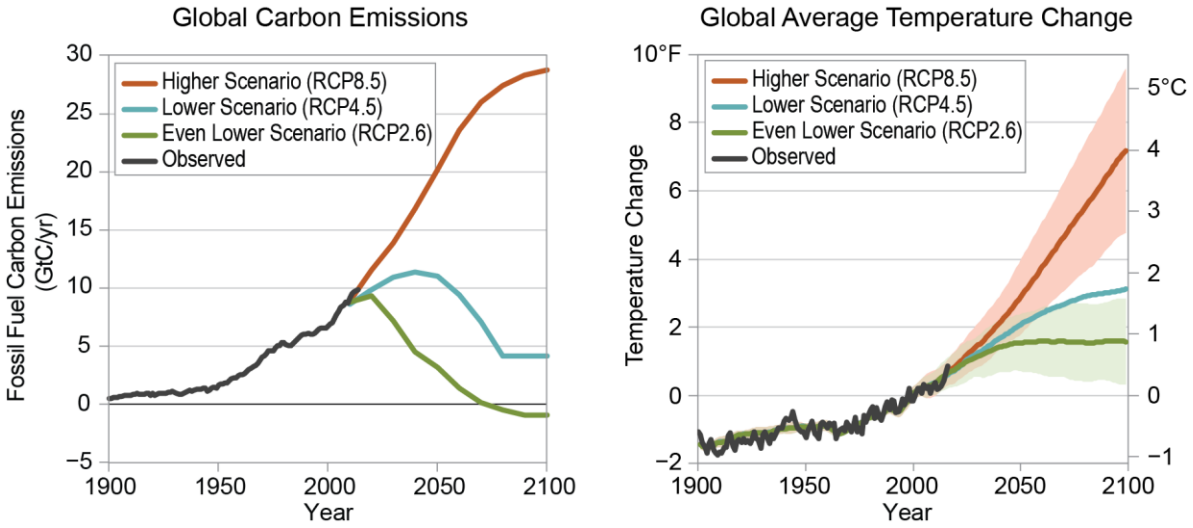

Figure 1.2 Observed and projected global fossil fuel emissions under each IPCC scenario in gigatonnes carbon year^{-1} (left) and observed and projected changes in global average temperature (right). Reprinted from Ch. 2: Our Globally Changing Climate. Climate Science Special Report: Fourth National Climate Assessment, Volume I.

Three of the most common climate modeling scenarios used by the IPCC are RCP2.6, RCP4.5, and RCP8.5. Each representative concentration pathway (RCP) is an expected GHG trajectory based on a set of inputs determined by the IPCC, labeled as the amount of expected radiative forcing in W m^{-2} in year 2100.[11] The RCP2.6 model is the most optimistic, suggesting a peak in GHG generation around 2040 with CO_2 levels averaging <425 ppm by 2100. The RCP4.5

trajectory describes a scenario where CO_2 mitigation is slower but sustainable with CO_2 concentrations leveling off around 560 ppm by century's end. Without any mitigation to CO_2 emissions in the near term, the RCP8.5 scenario predicts an atmospheric CO_2 concentration above 1150 ppm by 2100.

Under the most optimistic emissions scenario, the earth is expected to warm at least 1 ºC by 2100 (**Figure 1.2**).[12] Under a scenario where the current status quo is maintained, we are likely to see between 3– 5 ºC of warming by century's end. As the effects of climate change stated earlier are only those that can be predicted and the externalities of global warming are not yet understood, there exists an acute need to decarbonize to avoid potentially cataclysmic effects.

1.2 An Inhospitable Planet: The Existential Threat We Face

Global climate change remains one of the largest threats to the continued survival of the human species on earth.[13]

Although we may not experience the full effects of the warming already locked into our climate system until the middle to end of this century,[14] certain effects are already being felt.[15] Principal among these are increased occurrence of temperature extremes,[16] increases in record-breaking precipitation,[17] rising sea levels,[18] increased frequency and severity of severe weather events including droughts,[19] hurricanes,[20–22] floods,[23] and fires,[24] and loss of biodiversity.[25,26]The present and future impact of these effects in the United States will be briefly discussed in turn.

Around the world, high temperature records are being broken faster than low temperature records are being set. Research suggests that the ratio of temperature maxima (T_{max}) to temperature minima (T_{min}) on average, over time should approach 1:1 for a stable climate.[27] Recent analysis of an ensemble of T_{max} and T_{min} data from 66 cities in the United States found this ratio to average

4.89 since 2010 with Chicago's ratio being 3.14.[28] Statistical analysis and modeling of data procured from close to 2000 weather stations in the USA by McDaniel and co-workers[27] finds this ratio increasing to ~20 by the year 2050 and close to 50 by the end of the century (**Figure 1.3**).

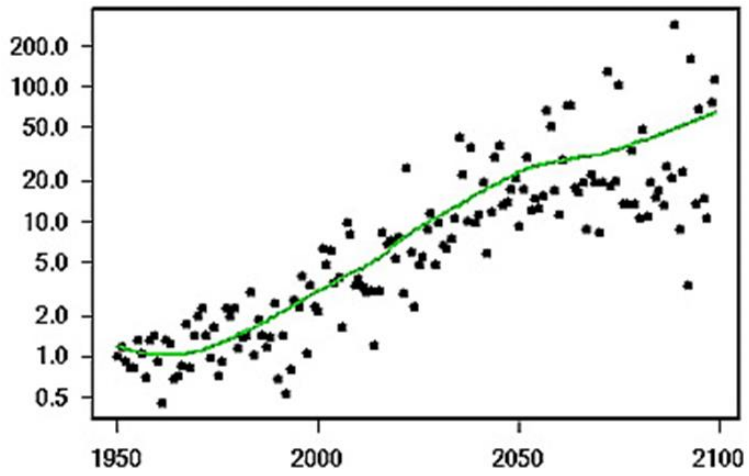

Figure 1.3 Dots are historic and model data of T_{max}/T_{min} ratio. Green line indicates smooth curve fit. Reprinted from Meehl, G. A.; Tebaldi, C.; Walton, G.; Easterling, D.; McDaniel, L. *Geophys. Res. Lett.* **2009**, *36* (23), 1–5.

Under current rates of greenhouse gas emissions, it is estimated that monthly T_{max} records will be set in >50% of the world every year, the percentage rising to ~65% in the least developed countries.[16] By most accounts, our future climate will be dominated by an increased frequency of record high temperature events.

Dramatic shifts in precipitation amount and location are expected to occur as the planet warms. Parts of the West and Midwest are expected to receive greater than average precipitation while areas that have historically suffered prolonged periods of drought are expected to receive even less precipitation (**Figure 1.4**).[29] It is likely that winter and spring seasons in the West and Midwest will experience between a 10 and 20% increase in total precipitation. Areas in Alaska,

historically home to vulnerable ecosystems, are expected to see precipitation increases between 20 and 30%—dramatically influencing habitability, lifestyles, and economics in our largest state.

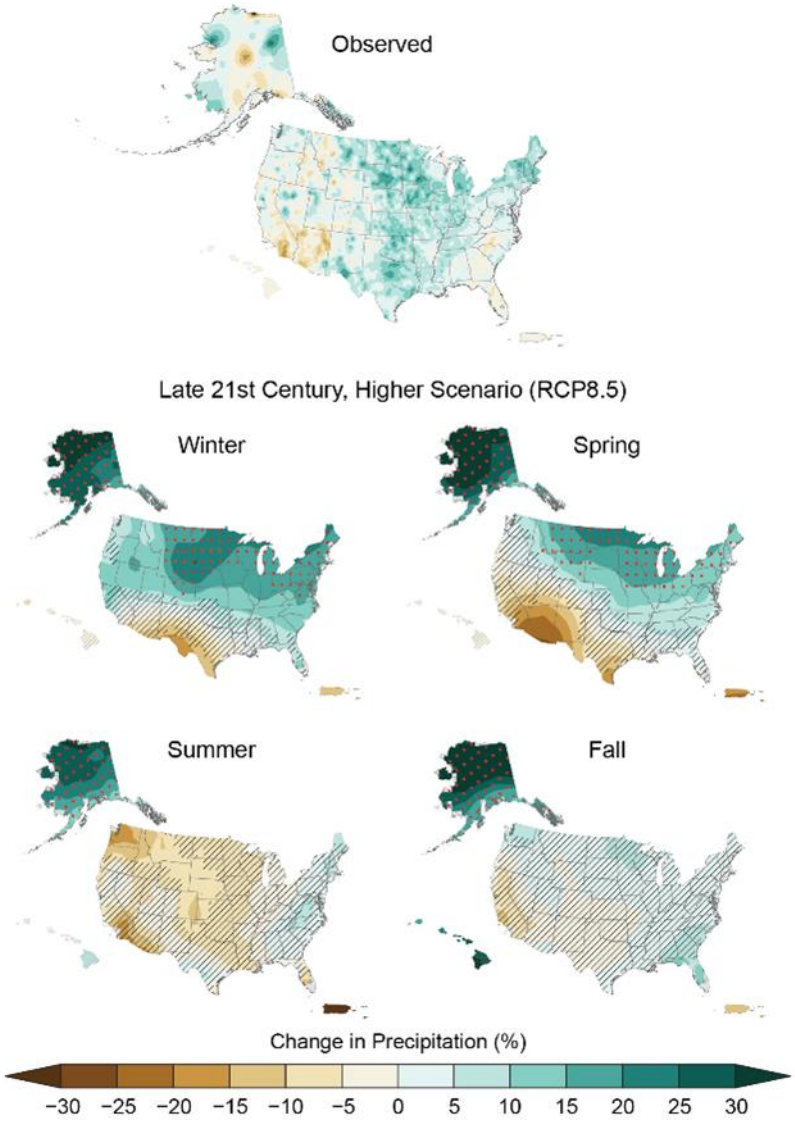

Figure 1.4 Observed and seasonally projected precipitation changes for the USA. Green indicates net positive percent change in precipitation, orange indicates net negative change in precipitation. Red dots show large projected changes; hatches show insignificant projected changes. RCP8.5 is a scenario where GHG concentrations continue to increase without abatement. Reprinted from Ch. 7: Precipitation Change in the United States. Climate Science Special Report: Fourth National Climate Assessment, Volume I.

The height of the sea level is of paramount importance for the more than 120 million people who currently live in coastal communities in the United States.[30] Under scenarios where the earth continues to warm due to unrestrained greenhouse gas emissions (i.e. RCP8.5), many coastal areas of the USA will experience a sea level rise of 2-6 feet (**Figure 1.5**), potentially displacing ~40% of the nation's population by 2100.[31] Even under an optimistic scenario where GHG emissions dramatically decrease by 2040 (i.e. RCP4.5), areas in the Gulf of Mexico and east coast are likely to see 1-4 feet of sea level rise.

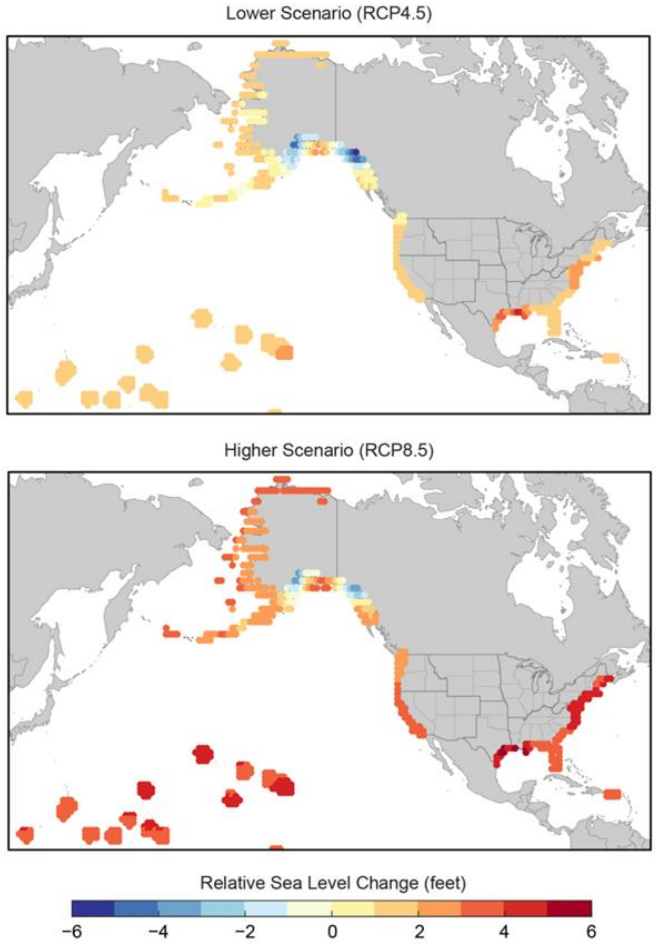

Figure 1.5 Map of projected changes in relative sea level from 2000 to 2100 under the RCP4.5 scenario (i.e. GHG emissions peak by 2040 and decline; top) and RCP8.5 scenario (i.e. current levels of GHG emissions, unmitigated; bottom). Reprinted from Chapter 1 : Overview. Impacts, Risks, and Adaptation in the United States: The Fourth National Climate Assessment, Volume II.

With increases in global temperature, research suggests dramatic increases in lightning strikes,[32] forest fires,[33] category 4 and 6 hurricanes,[34] and great floods.[35] The interested (or perhaps discouraged[36]) reader is encouraged to read the latest reports from the Intergovernmental Panel on Climate Change (IPCC),[11] the U.S. Global Change Research Program,[37] and the American Meteorological Society[38] for more detailed information on the current and future effects of climate change. Along with strong national policy and technological advancements, an educated citizenry is absolutely critical to addressing this climate crisis.

1.3 Proposed Solutions

Proposed solutions to mitigate the CO_2 in the atmosphere broadly fall into two categories: policy and technology. The most effective strategy would draw from *both* policy and technology realms incorporating strong climate policy as well as carbon capture and alternative energy technology.

Most policy solutions include some sort of tax on carbon or subsidy for a specific energy generating technology. A carbon tax scheme is usually levied on consumers (e.g. similar to a sales tax) or corporations which buy and sell carbon credits (i.e. permissions to pollute) among themselves in a regulated marketplace. Economically viable and endorsed by thought leaders[39] in the green economy space, such market mechanisms are often unpopular and have failed to garner support of general populations in the United States. Industry driven initiatives such as carbon offsets for air travel[40] or "climate bonds" (i.e. bonds sold to consumers to purchase clean energy generating equipment thereby introducing efficiencies into the market resulting in lower general prices)[13] represent new measures which potentially high impact on climate change.

Carbon capture and storage (CCS) is a broad term used to describe a suite of technologies that capture, transport, and store atmospheric carbon dioxide or CO_2 that is produced by conventional means.[41–43] Unfeasible to use as the sole means of addressing the climate change challenge,[44] CCS nevertheless represents a part of the solution along with investment in alternative energy sources.

Globally, energy demand is projected to increase by 28% by year 2040 using current growth trends as a predictor (**Figure 1.6**).[45] Much of this change is attributed to continued growth in China, India, and other countries in South East Asia. Proposals calling for a global curb in energy consumption are untenable as global population increases and quality of life rises. Energy technologies with low CO_2 emissions characteristics, therefore, are particularly desirable and serve as key components of climate change mitigation strategies.

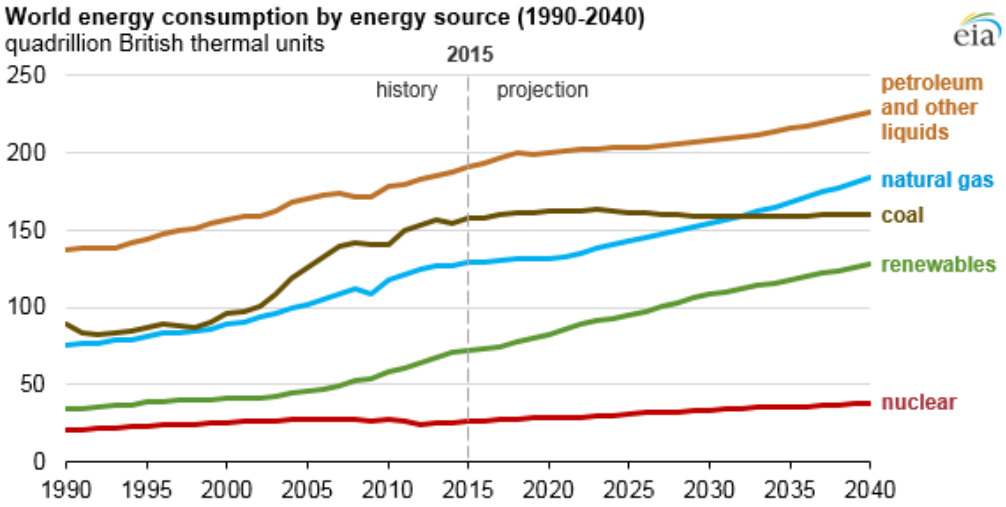

Figure 1.6 Historical and projected world energy consumption by energy source from 1990 to 2040 based on current growth rates and future population energy demands. Source: U.S. Energy Information Administration.

Solar, wind, hydrothermal, and nuclear represent the most heavily researched and invested sources of energy alternatives to fossil fuels. All four technologies have low CO_2 emissions

profiles per gigawatt-hour energy generated and all have been utilized in the United States to achieve CO_2 output goals. Meta-analysis and screening of 2100 published CO_2 emission life cycle assessment (LCA) studies by the National Renewable Energy Laboratory[46] resulted in the 1400 data points plotted in **Figure 1.7** by the author.

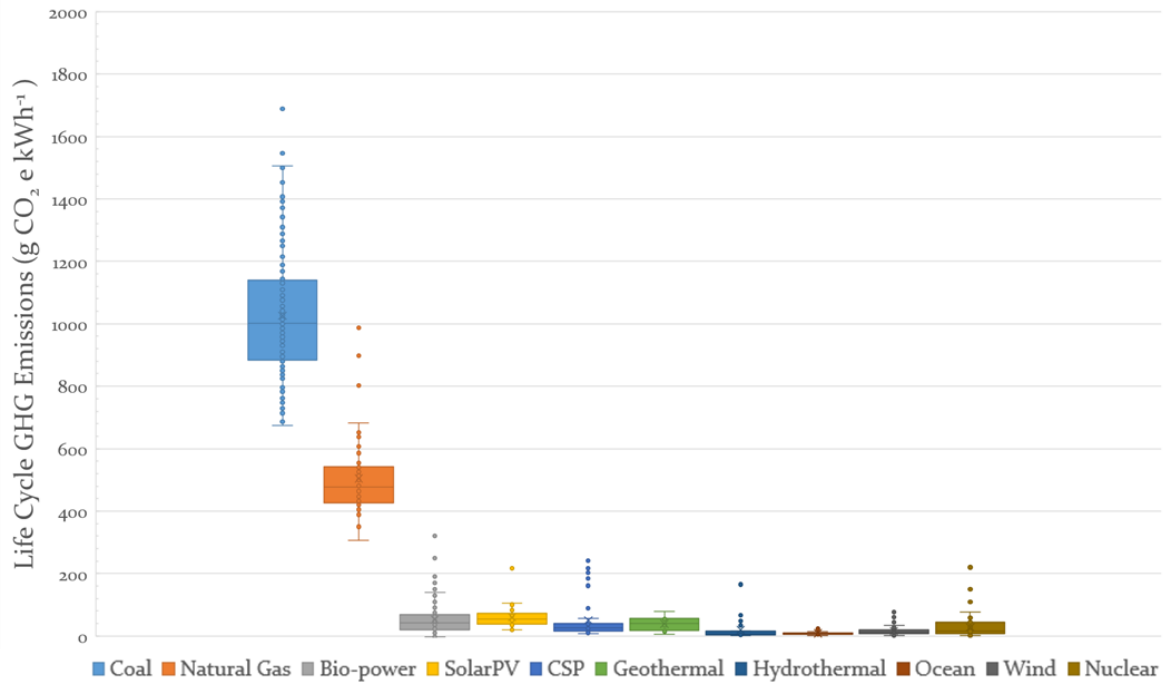

Figure 1.7 CO_2 emissions profiles for selected energy sources in grams of CO_2 equivalent per kilowatt-hour based on life cycle assessment studies. Data adapted from the National Renewable Energy Laboratory.

Coal energy production emits the highest amount of CO_2 throughout its lifecycle followed by natural gas. The bulk of these GHG emissions is from combustion of the fuel source. Conventional alternative energy technologies including solar photovoltaics, hydrothermal, wind, and nuclear all exhibit ultralow CO_2 emissions profiles. However, nuclear energy (NE) is the only technology that is capable of baseload power generation—not suffering from the intermittency problems inherent in solar and wind technologies. Capacity factors, typically used as measures of

intermittency, are defined as the ratio of actual energy output to the maximum possible energy output over a period of time. Capacity factors of 100% indicate actual energy production is at maximum rated production. Data obtained from the U.S. Energy Information Administration[47] on monthly capacity factors for major fossil fuel alternative energies used in the USA are plotted in **Figure 1.8**. Seasonal variability in capacity factor is readily apparent in solar photovoltaic (SolarPV) and concentrated solar power (CSP) energy sources with periods of higher efficiency evident during the cloudless summer months and lower efficiency during winter periods. Nuclear energy enjoys an average capacity factor of 92% compared to 37%, 25%, and 22% for wind, SolarPV, and CSP respectively. The reliability of nuclear power coupled with its low CO_2 emissions profile is a major driver of its attractiveness as a proposed solution to the climate crisis. It remains the only realistic alternative energy option to sustain growing global populations and their energy demand. Unfortunately, nuclear energy supply is expected to remain static over the near term (**Figure 1.6**) due to public rejection, regulatory challenges, lack of investment, and government preference for solar, wind, and natural gas. Technological advances in the nuclear fuel cycle on resource acquisition, waste handling, and dealing with environmental degradation will result in lower barriers to adoption of nuclear energy.

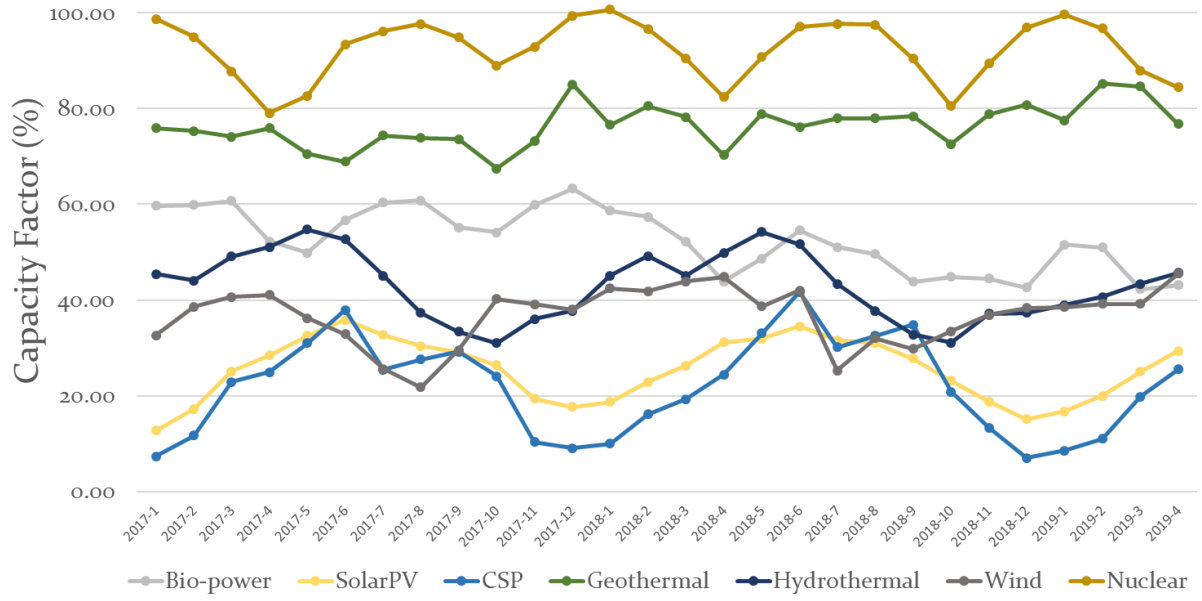

Figure 1.8 Monthly capacity factors for several fossil fuel-alternative energies in the USA since January 2017. Data adapted from U.S. Energy Information Administration.

1.4 Uranium Extraction for the Nuclear Fuel Cycle

Broadly speaking, a nuclear reactor takes advantage of the inherent instability in certain metals to heat water which produces enough steam to run a turbine generating electricity. The majority of domestic reactors are based on pressurized light water technology which utilizes uranium as a fuel source and produces large volumes of radioactive waste. As the United States is the world's largest producer of nuclear energy, particular emphasis is placed on U supply—the front end of the NE fuel cycle.[48] The front end of the nuclear fuel cycle is primarily concerned with the acquisition and enrichment of uranium as feedstock.

Uranium is traditionally extracted from ores where its concentration is on the order of 3 ppm.[49] The typical process from ore to yellowcake involves crushing and grinding, leaching, solvent extraction, precipitation, and roasting. Upon grinding and before uranium dissolution, Fe^{3+} is added as oxidant to produce the uranyl +6 cation.

$$UO_2 + 2Fe^{3+} \longrightarrow UO_2^{2+} + 2Fe^{2+}$$

The iron can be oxidized back to its +3 state with sodium chlorate. The hexavalent uranium can then easily dissolve in sulfuric acid producing the trissulfato complex

$$UO_2^{2+} + 3\ SO_4^{2-} \longrightarrow [UO_2(SO_4)_3]^{4-}$$

Tetraalkylammonium salts in appropriate organic diluents (e.g. kerosene) are then used to separate the anionic uranium complex via solvent extraction (SX):

$$4(R_4N^+) + [UO_2(SO_4)_3]^{4-} \longrightarrow (R_4N)_4[UO_2(SO_4)_3]$$

While the quaternary ammonium salts used in SX display selectivity for anionic U complexes, competition with molybdenum and vanadium as well as issues with chloride and nitrate interference require intense monitoring and modification of SX conditions. Alkylphosphoric extractants are sometimes used as an alternative. Ammonium sulfate is commonly used as a stripping agent to recover the metal from the extractant.

$$(R_4N)_4[UO_2(SO_4)_3] + 2(NH_4)_2SO_4 \longrightarrow 4(R_4N^+) + (NH_4)_4[UO_2(SO_4)_3] + 2SO_4^{2-}$$

Precipitation of the resulting U complex is typically achieved using ammonia

$$2NH_3 + 2UO_2(SO_4)_3^{4-} \longrightarrow (NH_4)_2U_2O_7 + 4SO_4^{2-}$$

The ammonium diuranate product is then filtered, recovered, dried, and heated to obtain U_3O_8 which continues the refining process via multiple SX stages to yield the required purity for a nuclear reactor.[50]

The drawbacks of conventional uranium acquisition are readily apparent. The complex process requires large volumes of concentrated mineral acid (on the order of 20 kg / ore),[51] produces large volumes of organic waste, and often leads to severely degraded environments and

ecosystems.[52,53] Moreover, each chemical step requires optimization before the protocol as a whole can be tested.

The oceans, on the other hand, contain nearly 1000 times the uranium found in terrestrial ores and represent an unconventional but potentially revolutionary source of the metal[54]. Two major technical challenges prevent widespread adoption of technology for pelagic uranium mining: U concentration and competing ions. Uranium is present at a uniform concentration of 3.3 ppb[55] throughout the world's oceans. Owing to this low concentration, ions including Na^+, Cl^-, Mg^{2+}, and Ca^{2+} are present in vast excess, on the order of >10,000 ppm[56–58]. Despite these complementary challenges, the extraction of uranium from seawater remains an important separations opportunity and the subject of intense research effort over the last 60 years.

1.4.1 Uranium from Seawater Project

While the practical inception of the uranium from seawater (UFS) initiative is often cited as work done by Davies and co-workers[59] as part of the British "Project Oyster" in the early 1960s, the practicability of UFS separations surely must have been considered when serious attention was paid to the determination of the amount of U in seawater at least a decade earlier.[60]

In fact, researchers at Argonne National Laboratory[60] were among the first to describe a practical way to determine the concentration of uranium in seawater which required small sample sizes (~25 mL) and made use of the quicker and easier solvent extraction method rather than the tedious and time consuming co-precipitation methods theretofore considered state-of-the-art.

Spurred by tremendous post-war demands for energy, UFS projects were initiated around the world with strong programs in the U.K. and Japan. The OPEC oil embargo of the 1970s only served to strengthen the UFS effort and dozens of studies were published in Japan,[61] the U.K.,[62]

and the USA[63]. The vast majority of studies focused on hydrous titanium oxide as the adsorbent of choice with little attention paid to other adsorbent materials until the 1980s.

As the global leader in UFS at the time, the Japanese were among the first to propose using a purely organic system for uranium sequestration. Two seminal papers by Nishiya and co-workers[64,65] outlined the design and synthesis of a new macrocyclic hexaketone as a specific host for uranium. While the selectivity over other common cations in seawater including Mg was significant, the uptake capacity (0.11 mg U g^{-1}) left much room for improvement. Nevertheless, the proof of concept U uptake demonstrated by Nishiya and co-workers was significant as it signaled a shift in the community from inorganic mineral adsorbents to the development of polymeric materials with pre-conceived uranium binding environments. This focus on structure-by-design functionalized polymers for uranium from seawater would come to dominate the field over the next 40 years.

Along with the emphasis on polymers came the exploration of functional groups with high affinity for uranium over the myriad other elements in seawater. The amidoxime group was chosen among a variety of ligands as the one with the optimal combination of synthetic ease, uranium affinity, and stability in seawater. A remarkable amount of emphasis has been placed on this functional group by the UFS community since the early 1980s despite phosphate-based ligands[66] remaining the most commonly used uranium extractants for most other uranium sequestration applications. Recent requirements for CHON based adsorbents, especially by the French, has renewed interest in amidoxime-functionalized sorbents and broadened the scope of their application.

The early 2000s saw a renaissance of UFS thinking with the design and synthesis of advanced, porous materials for uranium uptake. It was closer to the end of the decade when the

US began to seriously fund university-based research efforts with the Nuclear Energy University Program (NEUP). A grant for the "Development of Novel Sorbents for Uranium Extraction from Seawater" awarded to Prof. Wenbin Lin (University of North Carolina at Chapel Hill) in collaboration with Kathryn Taylor Pashow (Savannah River National Laboratory) began the current effort to develop U-selective porous, polymeric adsorbents. The field was recently surveyed in a review by Abney and coworkers.[54]

1.5 Ideal Adsorbents

Ideal solid adsorbents are those which fulfill all criteria presented in **Figure 1.9** for a specific separation application. The goal of separations is to preferentially select one or more species for removal from an often complex medium. Lack of selectivity is often correlated with low capacity for the analyte of interest and difficulties in recycling.

High capacity is another necessary criterion for an ideal adsorbent. Adsorbent design is often concerned with maximizing functional group loading (i.e. binding sites) to maximize concomitant adsorbate loading. Recent insight also indicates that macro characteristics such as site accessibility and polymer morphology can have dramatic effects on uptake capacity. Fast binding is also desirable in a separation system as cost usually scales with separation time. Uranium from seawater campaigns, for example, usually last 30+ days. While these long periods are necessary due to the low concentration of U in the oceans (and the need for mass transport of U containing water around the polymer fibers), another reason includes the slow binding of U within the polymer on account of non-specific ion binding at the surface. Regardless of time spent in solution, ideal adsorbents must be robust enough to withstand the specific environments of their deployment. This is especially important in nuclear waste separation applications where high radiation fields,

high acidity, and high ionic strength pose particular challenges to adsorbent longevity. Finally, the ability to recycle the adsorbent by stripping adsorbate and subjecting the material to further rounds of separation is a critical factor for a separations agent and the one that commonly vitiates its commercial development. Recycling state of the art polymer fibers for UFS applications ten times has been shown to have an equivalent cost-savings as increasing the capacity of a single-use adsorbent fivefold.[67]

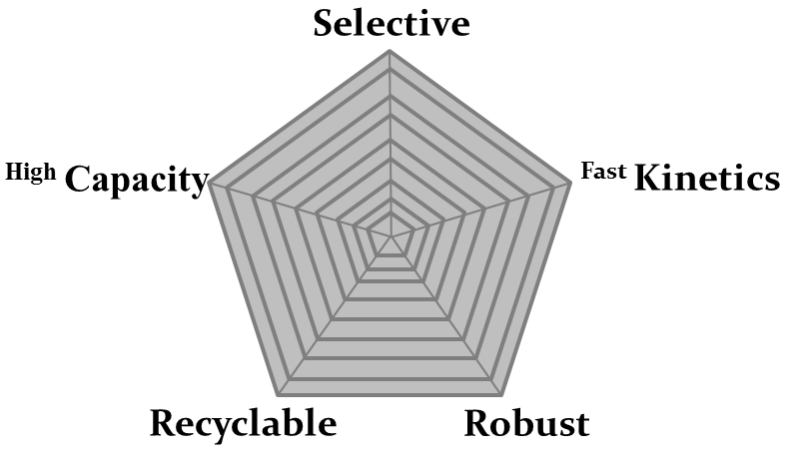

Figure 1.9 A view of the interconnectedness between the necessary characteristics of an ideal adsorbent material.

1.6 Survey of Recent Effort

Although there have been thousands of reports published on solid adsorbent design in general and uranium from seawater applications specifically, the studies which follow have been particularly instructive in determining the scope of this dissertation work.

Work performed by He and co-workers,[68] dramatically showcases the benefits of designing a binding pocket for a metal ion of interest. They first computationally screened a library of protein scaffolds with various potential uranium binding sites before sorting and scoring the top models.

Their resulting protein (i.e. super uranyl-binding protein) contained a binding site comprised of glutamine, aspartic acid, and arginine residues which bound the UO_2^{2+} via oxygens in the equatorial sphere and by the arginine nitrogen to the axial oxygen. The resulting pentacoordinate UO_2^{2+} was bound with an association constant on the order of 10^{14} and marked selectivity over competing ions in seawater—alkali metals (10^6), alkali earths (10^6), and divalent first row transition metals (10^5). This work serves as a reminder that the geometric arrangement of functionalities around a metal has a profound effect on selectivity. Moreover, the study suggests that protein architecture in addition to incorporating groups that interact with uranyl's axial oxygen are also factors that should be considered when designing new adsorbent materials.

The concept of cooperative binding (i.e. necessity of multiple functionalities together to bind a metal ion) has been used by Lin and co-workers as a guide to design materials for enhanced selectivity for uranyl. One such line of inquiry involved the development of a series of phosphoryl-functionalized UiO-68 type metal-organic frameworks (MOFs).[69] These MOFs which were comprised of Zr_6 metal clusters and phosphoryl functionalized terphenyl bridging ligands showed a uranium sorption capacity among the highest reported in laboratory conditions—217 mg g^{-1} in water and 188 mg g^{-1} in seawater simulant, both at pH 2.5

Increasing pore dimensions by lengthening the organic bridging ligand by an additional phenyl group decreased the sorption capacity to 42 mg g^{-1} under the same experimental conditions as multiple phosphorylurea groups were unable to cooperatively bind UO_2^{2+}. While this study cleared showed the utility of having multiple groups bind metal ions of interest, the inherent instability of the metal-organic framework precludes that material from consideration for operative conditions.

Focus in the Lin lab shifted to studying polymer materials tailor made for uranium from seawater applications. The first line of inquiry utilized extended X-ray absorption fine structure (EXAFS) analysis in order to investigate the uranyl coordination environment as bound by polyamidoxime fibers.[70] Six samples were prepared in total—four state-of-the-art polymer fibers and two small molecule standards. Of the amidoxime functionalized polymer fibers, one was contacted with seawater for 56 days at Pacific Northwest National Laboratory and used as received; one was contacted with seawater for 56 days and eluted of all metals except uranium and vanadium; one was contacted with seawater simulant containing uranyl nitrate for 24 hours; and one was contacted with seawater simulant containing uranyl nitrate and sodium orthovanadate for 24 hours. The small molecular standards—uranyl glutarimidedioxime and uranyl benzamidoxime exhibited the tridentate motif and η^2 amidoxime binding motifs respectively. EXAFS data were collected at beamline 10BM-B[71] of the Advanced Photon Source (APS) at Argonne National Laboratory (ANL).

The best fit model to the X-ray absorption spectra for the seawater-simulant contacted fibers was found to consist of 5 or 6 equatorially-coordinating atoms with two chelating amidoxime moieties (**Figure 1.10**). This coordination environment is consistent with that generally seen for uranyl binding. A model representative of tridentate cyclic imidioxime binding did not fit the data well—as made evident by the significant differences in bond lengths from the crystalline standard. The best fit model for the seawater-contacted fibers also consisted of 6 equatorially-coordinating atoms with two chelating amidoxime moieties. These findings are significant because they challenge conventional assumptions[72] that the tridentate amidoxime binding motif was responsible for the bulk of U uptake. In order to obtain the coordination environment revealed by the EXAFS fits, several amidoxime functionalities must bind one uranium center.

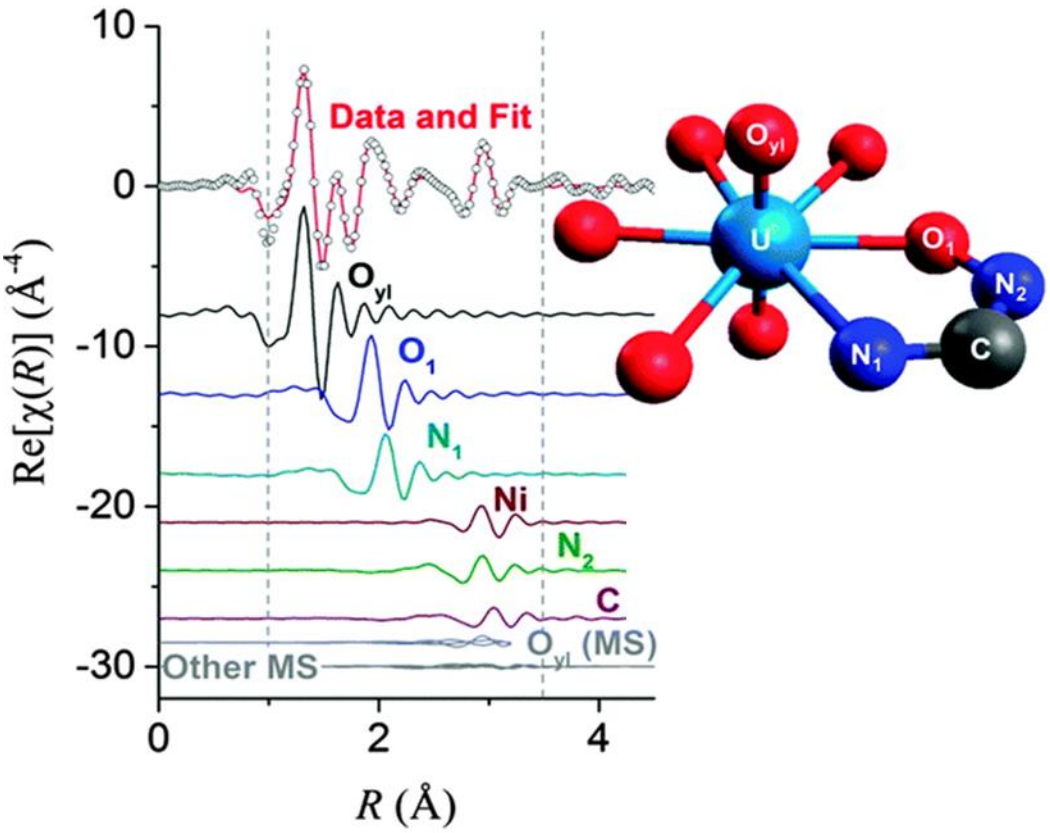

Figure 1.10 Representative EXAFS data (circles) and fit (red line) of seawater contacted amidoxime-functionalized polymer fibers displayed in *k*-space. Direct scattering paths (lines) from the structure model with labeled scatterers, offset below. Data fit over the range from 1 to 3.5 Å. Abney, C W, Mayes, R.T., Piechowicz, M., Lin, Z., Bryantsev, V.S., Veith, G.M., Dai, S., Lin, W. *Energy Environ. Sci.* **2015**. Reproduced by permission of The Royal Society of Chemistry.

Follow up work[73] focused on confirming the chelating amidoxime binding motif identified in previous work as well as identifying the origin of the broad feature at 3 Å. State of the art polymer fibers composed of poly(amidoxime-*co*-vinylphosphonic acid) were contacted with seawater simulant or filtered seawater and characterized via EXAFS. Data were fit to uranium containing small molecule standards possessing a cyclic imide dioxime or η^2 bound amidoxime measured concurrently. It was found that the best fit model comprised of 5.1 ± 1.2 light scatterers in the inner sphere. Fits to the tridentate amidoxime (i.e. cyclic imide dioxime) and η^2 bound amidoxime (i.e. $UO_2(benzamidoxime)_2(MeOH)_2$) resulted in physically unreasonable values and

were rejected. The best fit model, therefore, was proposed to consist of 1.5 chelating amidoximes, 0.5 carbonates, and one aqua ligand. Attempts to fit the feature at 3 Å with U-Fe, U-Ni, and U-Zn were inconclusive yielding similar results in each case. While uranyl-oxo Cu, Fe, Zn, and V structures are all known in the literature,[73] the significant concentration of Fe and V on the polymer fibers suggests the origin of the 3 Å peak lies with one of these metals. Regardless of the exact identity of the metal, the persistent presence of another non-uranyl metal in the 2nd coordination sphere of seawater contacted polymer fibers holds tremendous implication for the design of selective adsorbents. The discovery of cooperative binding wherein multiple amidoximes bind one uranyl served as a guiding principle for achieving high selectivity and capacity in future systems.

Intrigued by the potential to leverage cooperative binding in new porous polymer materials, attention turned to a relatively unexplored platform for separations—poly(HIPEs). Polymerized high internal phase emulsions (poly(HIPEs)) are monolithic, porous polymer materials synthesized through the careful addition of an aqueous solution (internal phase) into a well-stirred organic phase (external phase) containing monomers.[74–82]

A typical poly(HIPE) synthetic scheme is depicted in **Scheme 1.1**

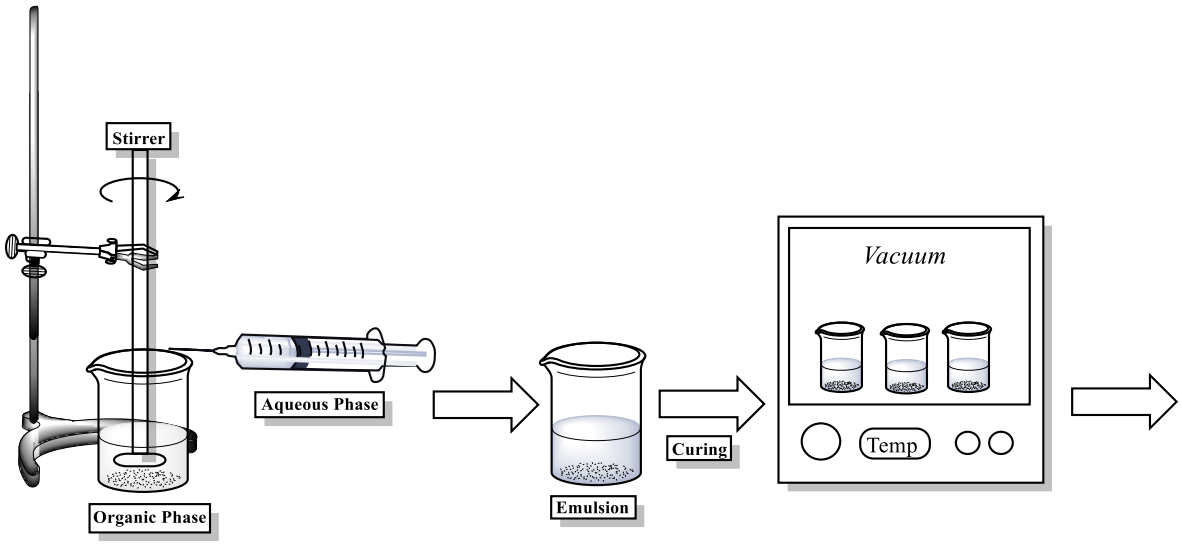

Scheme 1.1 Cartoon depiction of typical poly(HIPE) processing

The first step, as depicted in **Scheme 1.1**, consists of the dropwise addition of an aqueous phase containing water, salt, and radical initiator into a stirred solution containing monomers, crosslinker, and emulsifier. After complete incorporation, the mixture is allowed to mix for several minutes to ensure homogeneity before being placed into a vial or other suitable vessel. The samples are then sealed and placed in a vacuum oven for curing (24 hours) followed by vacuum removal of incorporated water (48 hours). The resulting polystyrene-based poly(HIPE) material, in this case in the form of a cylindrical plug, is shown in **Figure 1.11**.

Figure 1.11 Representative image of a poly(HIPE) cylindrical plug (right) next to a glass vial (left).

Owing to their high degree of porosity and resulting open-cell structure, poly(HIPEs) have found use in water uptake[83], oil remediation[84], and heavy-metal adsorption[85–89]. Moreover, as industry scale synthesis of poly(HIPEs) is already a well-established process[90], these

functionalized materials can be produced on a large-scale providing significant cost savings over other advanced materials.

Due to the relatively recent discovery and popularity of poly(HIPE) materials, there remain great opportunities for fundamental studies of their metal binding capacity, the relationship between morphology and separations efficacy, and long-term stability under *operando* conditions. This emerging field was recently reviewed by Pribyl and co-workers.[91]

Recent work by Benicewicz and co-workers[92–94] successfully demonstrated the incorporation of vinylpyridine monomers into styrenic poly(HIPEs) resulting in Pu uptake via an anion-exchange mechanism. In one study,[93] four crosslinked polystyrene based poly(HIPE) materials were synthesized with varying amounts of poly(4-vinylpyridine) grafted brushes (3.58% N - 6.24% N). Brushes grafted from reactive benzylchloride handles on the poly(HIPE) were chosen as systems to study in an effort to maximize functional group loading and accessibility compared to more limited systems where functionality is introduced during HIPE formation. Each monolith was prepared in a column and tested for Pu uptake. Results showed that both loading and elution curves for poly(HIPE) containing columns were narrower and more well defined than the ion-exchange (IX) resin control. In other words, due to the large pores present in the poly(HIPE) system, convective mass transport rather than diffusional mass transport drove Pu uptake. These data suggest that poly(HIPE) IX materials offer an attractive alternative to conventional IX materials for actinide separations due to improved efficiencies in material uptake and elution when used in column mode.

1.7 Summary and Impact

The uranium from seawater endeavor was recently indicated as one of seven chemical separations to change the world.[95] This assessment underscores the tremendous impact that separations science can have on a variety of global industries in terms of dramatic increases in energy efficiency, quality of life, and cost savings. A broader and more forward looking report was subsequently released by the National Academies of Sciences, Engineering, and Medicine (the National Academies) outlining a transformative research agenda for separations science.[96]

The National Academies' report highlights the need for a holistic approach to emerging separations challenges noting that advances in one research direction are wholly insufficient to push the field, in its entirety, forward. The report identifies two major themes namely, the need to develop materials with high selectivity, capacity, robustness, and throughput and the need to investigate how material properties perform *operando*. Both themes rely heavily on the need for collaboration among groups with orthogonal skillsets. Specifically, this includes cooperation between synthesis, modeling, and engineering efforts. This confluence of wide-ranging expertise is expected to drive the development of advanced materials in the future, especially those that leverage traditional stimuli including temperature and pressure as well as non-traditional stimuli including magnetic and electric fields to achieve targeted separations.

The work presented herein has benefited from precisely the multidisciplinary approach advocated by the National Academies. Early work using the APS to study polymer fibers relied on beamline expertise as well as material synthesized at Oak Ridge National Lab and tested for U adsorption at Pacific Northwest National Lab. Synthetic efforts at the University of Chicago began with computational work on idealized metal-ligand interactions. This modeling directly informed the synthetic scope of new uranophiles. Moreover, the synthesis and study of the bis-amidoxime

ligand (Chapter 3) directly influenced research directed towards the discovery of molecules containing the bis-amidoxime motif in an effort to maximize uranium affinity characteristics.[97] Later chapters describing advanced functionalized polymers encompass expertise in X-ray scattering, polymer chemistry, and separations among others to provide a unique perspective on early actinide separations with polymeric materials.

1.8 Thesis Scope

This dissertation serves as a record of the progress attained by the author and collaborators in early actinide separations from complex aqueous media. Chapter 2 introduces readers to the bifunctional chelator, a bespoke molecule identified by computational work to exhibit ultrahigh uranium affinity.[1] Preliminary efforts at incorporating the chelating molecule into solid support are described towards the end of the chapter. Chapter 3 discusses next generation uranophiles and their incorporation into polymeric materials for practical uranium/vanadium separations.[2] Large scale adsorption tests prove the selectivity and affinity of these materials for uranium over vanadium in simulated seawater conditions. The following chapter provides details for *in silico* work[4] investigating the origins of selectivity within the functionalized polymer materials. Results with ^{90}Sr and ^{137}Cs are particularly relevant as both isotopes are the primary fission products responsible for the high temperature and dose of spent nuclear fuel. Chapter 5 introduces the poly(HIPE), describing the design, synthesis, and actinide uptake characteristics of a series of amidoxime-functionalized poly(HIPEs). Designed to preferentially sequester uranium over thorium and plutonium in solution, the amidoxime functionalized poly(HIPE) displays remarkable affinity for thorium over uranium over a wide pH range. High energy X-ray scattering (HEXS) data provides insight into the speciation of the bound metal suggesting the materials adsorb

thorium oligomers from solution rather than molecular species. The concluding chapter includes the most recent separations results with amidoxime-functionalized poly(HIPEs) and an outlook into future work in this field. Taken together, this thesis showcases a collaborative effort addressing major challenges in separation science through the use of a wide variety of analytic, organic, inorganic, and supramolecular chemistries.

The motivated reader is encouraged also to consult the thesis of Carter W. Abney (Ph.D., 2015) as well as a review[98] by the same author in order to develop a holistic view of the uranium from seawater effort at the University of Chicago. Additionally, interest in separations of a broader scope (including applications relevant to the back end of the nuclear fuel cycle) can be satisfied by consulting work by Chiarizia,[99]Antonio,[100] and Soderholm[101] among others. Proposals by the author for future work in actinide separations using functionalized polymeric materials are included in Chapter 6.

1.9 References

(1) Piechowicz, M.; Abney, C. W.; Zhou, X.; Thacker, N. C.; Li, Z.; Lin, W. Design, Synthesis, and Characterization of a Bifunctional Chelator with Ultrahigh Capacity for Uranium Uptake from Seawater Simulant. *Ind. Eng. Chem. Res.* **2015**, *55* (15), 4170–4178.

(2) Piechowicz, M.; Abney, C. W.; Thacker, N. C.; Gilhula, J. C.; Wang, Y.; Veroneau, S. S.; Hu, A.; Lin, W. Successful Coupling of a Bis-Amidoxime Uranophile with a Hydrophilic Backbone for Selective Uranium Sequestration. *ACS Appl. Mater. Interfaces* **2017**, *9* (33), 27894–27904.

(3) Bartlett, J. R.; Cooney, R. P. On the Determination of Uranium-Oxygen Bond Lengths in Diooxouranium(VI) Compounts by Raman Spectroscopy . *Journal of Molecular Structure.* **1989**, *193*, 295–300.

(4) Piechowicz, M.; Chiarizia, R.; Soderholm, L. Insight into Selectivity: Uptake Studies of Radionuclides $^{90}Sr^{2+}$, $^{137}Cs^{+}$, and $^{233}UO_2^{2+}$ with Bis-Amidoxime Polymers. *Dalt. Trans.* **2018**, *47* (15), 5348–5358.

(5) Arrhenius, S. On the Influence of Carbonic Acid in the Air upon the Temperature of the Ground. *London, Edinburgh, Dublin Philos. Mag. J. Sci.* **1896**, *41* (251), 237–276.

(6) Lüthi, D.; Le Floch, M.; Bereiter, B.; Blunier, T.; Barnola, J.-M.; Siegenthaler, U.; Raynaud, D.; Jouzel, J.; Fischer, H.; Kawamura, K.; et al. High-Resolution Carbon Dioxide Concentration Record 650,000–800,000 Years before Present. *Nature* **2008**, *453* (7193), 379–382.

(7) Keeling, C. D.; Bacastow, R. B.; Bainbridge, A. E.; Ekdahl Jr., C. A.; Guenther, P. R.; Waterman, L. S.; Chin, J. F. S. Atmospheric Carbon Dioxide Variations at Mauna Loa Observatory, Hawaii. *Tellus* **1976**, *28* (6), 538–551.

(8) Tans, P.; Keeling, R. *Trends in Atmospheric Carbon Dioxide*.

(9) EPA. Inventory of U.S. Greenhouse Gas Emissions and Sinks: 1990-2017. **2019**.

(10) Cook, J.; Lewandowsky, S.; Skuce, A. G.; Nuccitelli, D.; Winkler, B.; Painting, R.; Oreskes, N.; Doran, P. T.; Anderegg, W. R. L.; Verheggen, B.; et al. Consensus on Consensus: A Synthesis of Consensus Estimates on Human-Caused Global Warming. *Environ. Res. Lett.* **2016**, *11* (4).

(11) Core Writing Team. *IPCC, 2014: Climate Change 2014: Synthesis Report. Contribution of Working Groups I, II and III to the Fifth Assessment Report of the Intergovernmental Panel on Climate Change*; Pachauri, R. K., Meyer, L. A., Eds.; IPCC: Geneva, Switzerland, **2014**.

(12) Wuebbles, D. J.; Easterling, D. R.; Hayhoe, K.; Knutson, T.; Kopp, R. E.; Kossin, J. P.; Kunkel, K. E.; LeGrande, A. N.; Mears, C.; Sweet, W. V.; et al. *Ch. 1: Our Globally Changing Climate. Climate Science Special Report: Fourth National Climate Assessment, Volume I*; Wuebbles, D. J., Fahey, D. W., Hibbard, K. A., Dokken, D. J., Stewart, B. C., Maycock, T. K., Eds.; Washington, DC, **2017**.

(13) Casten, S.; Durbin, D.; Foster, B.; Skilling, T.; Sisterson, D.; Gade, M. The Climate Change Forum. In *The Climate Change Forum*; **2019**.

(14) Raftery, A. E.; Zimmer, A.; Frierson, D. M. W.; Startz, R.; Liu, P. Less than 2 °C Warming by 2100 Unlikely. *Nat. Clim. Chang.* **2017**, *7* (9), 637–641.

(15) Aleixo, I.; Norris, D.; Hemerik, L.; Barbosa, A.; Prata, E.; Costa, F.; Poorter, L. Amazonian Rainforest Tree Mortality Driven by Climate and Functional Traits. *Nat. Clim. Chang.* **2019**, *9* (5), 384–388.

(16) Power, S. B.; Delage, F. P. D. Setting and Smashing Extreme Temperature Records Over the Coming Century. *Nat. Clim. Chang.* **2019**, *9* (7), 529–534.

(17) Polade, S. D.; Gershunov, A.; Cayan, D. R.; Dettinger, M. D.; Pierce, D. W. Precipitation in a Warming World: Assessing Projected Hydro-Climate Changes in California and Other Mediterranean Climate Regions. *Sci. Rep.* **2017**, *7* (1), 1–10.

(18) Barnard, P. L.; Erikson, L. H.; Foxgrover, A. C.; Hart, J. A. F.; Limber, P.; O'Neill, A. C.; van Ormondt, M.; Vitousek, S.; Wood, N.; Hayden, M. K.; et al. Dynamic Flood Modeling Essential to Assess the Coastal Impacts of Climate Change. *Sci. Rep.* **2019**, *9* (1), 1–13.

(19) Huang, S.; Leng, G.; Huang, Q.; Xie, Y.; Liu, S.; Meng, E.; Li, P. The Asymmetric Impact of Global Warming on US Drought Types and Distributions in a Large Ensemble of 97 Hydro-Climatic Simulations. *Sci. Rep.* **2017**, *7* (1), 1–13.

(20) Lin, N.; Emanuel, K.; Oppenheimer, M.; Vanmarcke, E. Physically Based Assessment of Hurricane Surge Threat under Climate Change. *Nat. Clim. Chang.* **2012**, *2* (6), 462–467.

(21) Patricola, C. M.; Wehner, M. F. Anthropogenic Influences on Major Tropical Cyclone Events. *Nature* **2018**, *563* (7731), 339–346.

(22) Ting, M.; Kossin, J. P.; Camargo, S. J.; Li, C. Past and Future Hurricane Intensity Change along the U.S. East Coast. *Sci. Rep.* **2019**, *9* (1), 1–8.

(23) Sofia, G.; Roder, G.; Dalla Fontana, G.; Tarolli, P. Flood Dynamics in Urbanised Landscapes: 100 Years of Climate and Humans' Interaction. *Sci. Rep.* **2017**, *7*, 1–12.

(24) Dowdy, A. J.; Ye, H.; Pepler, A.; Thatcher, M.; Osbrough, S. L.; Evans, J. P.; Di Virgilio, G.; McCarthy, N. Future Changes in Extreme Weather and Pyroconvection Risk Factors for Australian Wildfires. *Sci. Rep.* **2019**, *9* (1), 10073.

(25) Beaugrand, G.; Edwards, M.; Raybaud, V.; Goberville, E.; Kirby, R. R. Future Vulnerability of Marine Biodiversity Compared with Contemporary and Past Changes. *Nat. Clim. Chang.* **2015**, *5* (7), 695–701.

(26) Scheffers, B. R.; Pecl, G. Persecuting, Protecting or Ignoring Biodiversity under Climate Change. *Nat. Clim. Chang.* **2019**, *9*, 581-586.

(27) Meehl, G. A.; Tebaldi, C.; Walton, G.; Easterling, D.; McDaniel, L. Relative Increase of Record High Maximum Temperatures Compared to Record Low Minimum Temperatures in the U.S. *Geophys. Res. Lett.* **2009**, *36* (23), 1–5.

(28) Burt, C. C. U.S. Daily Record Highs Outnumber Lows 5 to 1 since 2010 https://www.wunderground.com/cat6/us-daily-record-highs-outnumber-lows-5-1-2010 (accessed Jul 19, 2019).

(29) Easterling, D. R.; Arnold, J. R.; Knutson, T.; Kunkel, K. E.; LeGrande, A. N.; Leung, L. R.; Vose, R. S.; Waliser, D. E.; Wehner, M. F. *Ch. 7: Precipitation Change in the United States. Climate Science Special Report: Fourth National Climate Assessment, Volume I*; Washington, DC, **2017**; Vol. I.

(30) NOAA. Economics and Demographics https://coast.noaa.gov/states/fast-facts/economics-and-demographics.html (accessed July 19, 2019).

(31) Jay, A.; Reidmiller, D. R.; Avery, C. W.; Barrie, D.; DeAngelo, B. J.; Dave, A.; Dzaugis, M.; Kolian, M.; Lewis, K. L. M.; Reeves, K.; et al. *Chapter 1 : Overview. Impacts, Risks, and Adaptation in the United States: The Fourth National Climate Assessment, Volume II*; Washington, DC, **2018**.

(32) Romps, D. M.; Seeley, J. T.; Vollaro, D.; Molinari, J. Projected Increase in Lightning Strikes in the United States Due to Global Warming. *Science.* **2014**, *346* (6211), 851–854.

(33) Abatzoglou, J. T.; Williams, A. P. Impact of Anthropogenic Climate Change on Wildfire across Western US Forests. *Proc. Natl. Acad. Sci.* **2016**, *113* (42), 11770–11775.

(34) Bender, M. A.; Knutson, T. R.; Tuleya, R. E.; Sirutis, J. J.; Vecchi, G. A.; Garner, S. T.; Held, I. M. Modeled Impact of Anthropogenic Atlantic Hurricanes. *Science.* **2009**, *327* (28), 454–458.

(35) Milly, P. C. D.; Wetherald, R. T.; Dunne, K. A.; Delworth, T. L. Increasing Risk of Great Floods in a Changing Climate. *Nature.* **2002**, *415* (6871), 514–517.

(36) Cunsolo, A.; Ellis, N. R. Ecological Grief as a Mental Health Response to Climate Change-Related Loss. *Nat. Clim. Chang.* **2018**, *8* (4), 275–281.

(37) *Impacts, Risks, and Adaptation in the United States: The Fourth National Climate Assessment, Volume II*; Reidmiller, D. R., Avery, C. W., Easterling, D. R., Kunkel, K. E., Lewis, K. L. M., Maycock, T. K., Stewart, B. C., Eds.; Washington, DC, **2018**.

(38) Hartfield, G.; Blunden, J.; Arndt, D. S. State of the Climate in 2017. *Bull. Am. Meteorol. Soc.* **2018**, *99* (8), 1-310.

(39) Stern, N. *The Economics of Climate Change*; Cambridge University Press: Cambridge, **2007**.

(40) Mair, J. Exploring Air Travellers' Voluntary Carbon-Offsetting Behaviour. *J. Sustain. Tour.* **2011**, *19* (2), 215–230.

(41) Gibbins, J.; Chalmers, H. Carbon Capture and Storage. *Energy Policy.* **2008**, *36* (12), 4317–4322.

(42) Pires, J. C. M.; Martins, F. G.; Alvim-Ferraz, M. C. M.; Simões, M. Recent Developments on Carbon Capture and Storage: An Overview. *Chem. Eng. Res. Des.* **2011**, *89* (9), 1446–1460.

(43) Boot-Handford, M. E.; Abanades, J. C.; Anthony, E. J.; Blunt, M. J.; Brandani, S.; Mac Dowell, N.; Fernández, J. R.; Ferrari, M.-C.; Gross, R.; Hallett, J. P.; et al. Carbon Capture and Storage Update. *Energy Environ. Sci.* **2014**, *7* (1), 130–189.

(44) Haszeldine, R. S. Carbon Capture and Storage: How Green Can Black Be? *Science.* **2009**, *325* (5948), 1647–1652.

(45) EIA. EIA projects 28% increase in world energy use by 2040 https://www.eia.gov/todayinenergy/detail.php?id=32912 (accessed July 20, 2019).

(46) NREL. Life Cycle Greenhouse Gas Emissions from Electricity Generation. **2013**.

(47) U.S. Department of Energy. Electric Power Monthly with Data for April 2014.

(48) World Nuclear Association. Nuclear Power in the USA https://www.world-nuclear.org/information-library/country-profiles/countries-t-z/usa-nuclear-power.aspx (accessed July 21, 2019).

(49) World Nuclear Association. Uranium Mining Overview https://www.world-nuclear.org/information-library/nuclear-fuel-cycle/mining-of-uranium/uranium-mining-overview.aspx (accessed July 21, 2019).

(50) *The Chemistry of the Actinide and Transactinide Elements*, 4th ed.; Morss, L. R., Edelstein, N. M., Fuger, J., Eds.; Netherlands, **2011**.

(51) Edwards, C. R.; Oliver, A. J. Uranium Processing: A Review of Current Methods and Technology. *JOM.* **2000**, *52* (9), 12–20.

(52) Gajski, G.; Orešcanin, V.; Geric, M.; Kollar, R.; Mikelic, I. L.; Garaj-Vrhovac, V. Toxicity Assessment of the Water Used for Human Consumption from the Cameron/Tuba City Abandoned Uranium Mining Area Prior/after the Combined Electrochemical Treatment/Advanced Oxidation. *Environ. Sci. Pollut. Res.* **2015**, *22* (1), 516–526.

(53) Hoover, J.; Gonzales, M.; Shuey, C.; Barney, Y.; Lewis, J. Elevated Arsenic and Uranium Concentrations in Unregulated Water Sources on the Navajo Nation, USA. *Expo. Heal.* **2017**, *9* (2), 113–124.

(54) Abney, C. W.; Mayes, R. T.; Saito, T.; Dai, S. Materials for the Recovery of Uranium from Seawater. *Chem. Rev.* **2017**, *117* (23), 13935–14013.

(55) Ku, T. L.; Knauss, K. G.; Mathieu, G. G. Uranium in Open Ocean: Concentration and Isotopic Composition. *Deep. Res.* **1977**, *24* (11), 1005–1017.

(56) Byrne, R. H. Speciation in Seawater. In *Chemical Speciation in the Environment*; Blackwell Science Ltd: Oxford, UK, 2007; pp 322–357.

(57) Bardi, U. Extracting Minerals from Seawater: An Energy Analysis. *Sustainability* **2010**, *2* (4), 980–992.

(58) Loganathan, P.; Naidu, G.; Vigneswaran, S. Mining Valuable Minerals from Seawater: A Critical Review. *Environ. Sci. Water Res. Technol.* **2017**, *3* (1), 37–53.

(59) Davies, R. V.; Kennedy, J.; McIlroy, R. W.; Spence, R.; Hill, K. M. Extraction of Uranium from Sea Water. *Nature* **1964**, *203* (4950), 1110–1115.

(60) Stewart, D. C.; Bentley, W. C. Analysis of Uranium in Sea Water. *Science.* **1954**, *120* (3106), 50–51.

(61) Shigetomi, Y.; Kojima, T.; Kamba, H. Extraction of Uranium (VI) from Sea Water Using Hydrous Metalic Oxide Binded with Hydrophilic Polymers. *Nippon Genshiryoku Gakkai-Shi.* **1978**, *20* (11), 789–795.

(62) Kim, Y. S.; Zeitlin, H. Separation of Uranium from Seawater by Adsorbing Colloid Flotation. *Anal. Chem.* **1971**, *43* (11), 1390–1393.

(63) Kelmers, A. D. Status of Technology for the Recovery of Uranium from Seawater. *Sep. Sci. Technol.* **1981**, *16* (9), 1019–1035.

(64) Tabushi, I.; Kobuke, Y.; Nishiya, T. Macrocyclic Hexaketone as a Specific Host of Uranyl Ion. **1979**, *37*, 3515–3518.

(65) Tabushi, I.; Kobuke, Y.; Nishiya, T. Extraction of Uranium from Seawater by Polymer-Bound Macrocyclic Hexaketone. *Nature* **1979**, *280* (5724), 665–666.

(66) Burger, L. L. Uranium and Plutonium Extraction by Organophosphorus Compounds. *J. Phys. Chem.* **1958**, *62* (5), 590–593.

(67) Kim, J.; Tsouris, C.; Oyola, Y.; Janke, C. J.; Mayes, R. T.; Dai, S.; Gill, G.; Kuo, L. J.; Wood, J.; Choe, K. Y.; et al. Uptake of Uranium from Seawater by Amidoxime-Based Polymeric Adsorbent: Field Experiments, Modeling, and Updated Economic Assessment. *Ind. Eng. Chem. Res.* **2014**, *53* (14), 6076–6083.

(68) Zhou, L.; Bosscher, M.; Zhang, C.; Özçubukçu, S.; Zhang, L.; Zhang, W.; Li, C. J.; Liu, J.; Jensen, M. P.; Lai, L.; et al. A Protein Engineered to Bind Uranyl Selectively and with Femtomolar Affinity. *Nat. Chem.* **2014**, *6* (3), 236–241.

(69) Carboni, M.; Abney, C. W.; Liu, S. B.; Lin, W. B. Highly Porous and Stable Metal-Organic Frameworks for Uranium Extraction. *Chem. Sci.* **2013**, *4* (6), 2396–2402.

(70) Abney, C W, Mayes, R.T., Piechowicz, M., Lin, Z., Bryantsev, V.S., Veith, G.M., Dai, S., Lin, W. XAFS Investigation of Polyamidoxime-Bound Uranyl Contests the Paradigm from Small Molecule Studies. *Energy Environ. Sci.* **2015**, *9* (448-453).

(71) Kropf, A. J.; Katsoudas, J.; Chattopadhyay, S.; Shibata, T.; Lang, E. A.; Zyryanov, V. N.; Ravel, B.; McIvor, K.; Kemner, K. M.; Scheckel, K. G.; et al. The New MRCAT (Sector 10) Bending Magnet Beamline at the Advanced Photon Source. *AIP Conf. Proc.* **2010**, *1234*, 299–302.

(72) Kobuke, Y.; Tanaka, H.; Ogoshi, H. Imidedioxime as a Significant Component in So-Called Amidoxime Resin for Uranyl Adsorption from Seawater. *Polym. J.* **1990**, *22* (2), 179–182.

(73) Abney, C. W.; Das, S.; Mayes, R. T.; Kuo, L.-J.; Wood, J.; Gill, G.; Piechowicz, M.; Lin, Z.; Lin, W.; Dai, S. A Report on Emergent Uranyl Binding Phenomena by an Amidoxime Phosphonic Acid Co-Polymer. *Phys. Chem. Chem. Phys.* **2016**, *18* (34), 23462–23468.

(74) Foudazi, R.; Gokun, P.; Feke, D. L.; Rowan, S. J.; Manas-Zloczower, I. Chemorheology of Poly(High Internal Phase Emulsions). *Macromolecules.* **2013**, *46* (13), 5393–5396.

(75) Silverstein, M. S. PolyHIPEs: Recent Advances in Emulsion-Templated Porous Polymers. *Prog. Polym. Sci.* **2014**, *39* (1), 199–234.

(76) Silverstein, M. S. Emulsion-Templated Porous Polymers: A Retrospective Perspective. *Polymer.* **2014**, *55* (1), 304–320.

(77) Cameron, N. R. High Internal Phase Emulsion Templating as a Route to Well-Defined Porous Polymers. *Polymer.* **2005**, *46* (5), 1439–1449.

(78) Barbetta, A.; Cameron, N. R.; Cooper, S. J. High Internal Phase Emulsions (HIPEs) Containing Divinylbenzene and 4-Vinylbenzyl Chloride and the Morphology of the Resulting PolyHIPE Materials. *Chem. Commun.* **2000**, No. 3, 221–222.

(79) Kimmins, S. D.; Cameron, N. R. Functional Porous Polymers by Emulsion Templating: Recent Advances. *Adv. Funct. Mater.* **2011**, *21* (2), 211–225.

(80) Carnachan, R. J.; Bokhari, M.; Przyborski, S. A.; Cameron, N. R. Tailoring the Morphology of Emulsion-Templated Porous Polymers. *Soft Matter* **2006**, *2* (7), 608–616.

(81) Cameron, N. R.; Barbetta, A. The Influence of Porogen Type on the Porosity, Surface Area and Morphology of Poly(Divinylbenzene) PolyHIPE Foams. *J. Mater. Chem.* **2000**, *10* (11), 2466–2471.

(82) Cameron, N. R.; Sherrington, D. C. Preparation and Glass Transition Temperatures of Elastomeric PolyHIPE Materials. *J. Mater. Chem.* **1997**, *7* (11), 2209–2212.

(83) Wickenheisser, M.; Paul, T.; Janiak, C. Prospects of Monolithic MIL-MOF@poly(NIPAM)HIPE Composites as Water Sorption Materials. *Microporous Mesoporous Mater.* **2016**, *220*, 258–269.

(84) Zhang, N.; Jiang, W.; Wang, T.; Gu, J.; Zhong, S.; Zhou, S.; Xie, T.; Fu, J. Facile Preparation of Magnetic Poly(Styrene-Divinylbenzene) Foam and Its Application as an Oil Absorbent. *Ind. Eng. Chem. Res.* **2015**, *54* (44), 11033–11039.

(85) Katsoyiannis, I. A.; Zouboulis, A. I. Removal of Arsenic from Contaminated Water Sources by Sorption onto Iron-Oxide-Coated Polymeric Materials. *Water Res.* **2002**, *36* (20), 5141–5155.

(86) Mert, E. H.; Kaya, M. A.; Yildirim, H. Preparation and Characterization of Polyester-Glycidyl Methacrylate PolyHIPE Monoliths to Use in Heavy Metal Removal. *Des. Monomers Polym.* **2012**, *15* (2), 113–126.

(87) Huš, S.; Kolar, M.; Krajnc, P. Separation of Heavy Metals from Water by Functionalized Glycidyl Methacrylate Poly (High Internal Phase Emulsions). *J. Chromatogr. A* **2016**, *1437*, 168–175.

(88) Zhu, Y.; Zheng, Y.; Wang, F.; Wang, A. Monolithic Supermacroporous Hydrogel Prepared from High Internal Phase Emulsions (HIPEs) for Fast Removal of $Cu^{2+}$and Pb^{2+}. *Chem. Eng. J.* **2016**, *284*, 422–430.

(89) Moghbeli, M. R.; Khajeh, A.; Alikhani, M. Nanosilica Reinforced Ion-Exchange PolyHIPE Type Membrane for Removal of Nickel Ions: Preparation, Characterization and Adsorption Studies. *Chem. Eng. J.* **2017**, *309*, 552–562.

(90) Edwards, C.; Gregory, D.; Sharples, M. Low Density Porous Elastic Cross-Linked Polymeric Materials and Their Preparation. 4,788,225, **1988**.

(91) Taylor-Pashow, K. M. L.; Pribyl, J. G. PolyHIPEs for Separations and Chemical Transformations: A Review. *Solvent Extr. Ion Exch.* **2019**, *1*, 1–26.

(92) Benicewicz, B. C.; Jarvinen, G. D.; Kathios, D. J.; Jorgensen, B. S. Open-Celled Polymeric Foam Monoliths for Heavy Metal Separations Study. *J. Radioanal. Nucl. Chem.* **1998**, *235* (1–2), 31–35.

(93) Pribyl, J.; Fletcher, B.; Steckle, W.; Taylor-Pashow, K.; Shehee, T.; Benicewicz, B. Photoinitiated Polymerization of 4-Vinylpyridine on PolyHIPE Foam Surface toward Improved Pu Separations. *Anal. Chem.* **2017**, *89* (10), 5174–5178.

(94) Pribyl, J. G.; Taylor-Pashow, K. M. L.; Shehee, T. C.; Benicewicz, B. C. High-Capacity Poly(4-Vinylpyridine) Grafted PolyHIPE Foams for Efficient Plutonium Separation and Purification. *ACS Omega*. **2018**, *3* (7), 8181–8189.

(95) Sholl, D. S.; Lively, R. P. Seven Chemical Separations to Change the World. *Nature.* **2016**, *532* (7600), 435–437.

(96) Science, S.; Sciences, C.; Earth, D.; Studies, L.; Academies, N. *A Research Agenda for Transforming Separation Science*; National Academies Press, **2019**.

(97) Stemper, J.; Tuo, W.; Mazarío, E.; Helal, A. S.; Djurovic, A.; Lion, C.; El Hage Chahine, J.-M.; Maurel, F.; Hémadi, M.; Le Gall, T. Synthesis of Bis(Amidoxime)s and Evaluation of Their Properties as Uranyl-Complexing Agents. *Tetrahedron.* **2018**, 1–9.

(98) Abney, C. W.; Mayes, R. T.; Saito, T.; Dai, S. Materials for the Recovery of Uranium from Seawater. *Chem. Rev.* **2017**, *117* (23), 13935–14013.

(99) Nash, K. L.; Barrans, R. E.; Chiarizia, R.; Dietz, M. L.; Jensen, M. P.; Rickert, P. G.; Moyer, B. A.; Bonnesen, P. V.; Bryan, J. C.; Sachleben, R. A. Fundamental Investigations of Separations Science for Radioactive Materials. *Solvent Extr. Ion Exch.* **2000**, *18* (4), 605–631.

(100) Antonio, M. R.; Williams, C. W.; Soderholm, L. Berkelium Redox Speciation. *Radiochim. Acta.* **2002**, *90* (12), 851–856.

(101) Wilson, R. E.; Skanthakumar, S.; Soderholm, L. Separation of Plutonium Oxide Nanoparticles and Colloids. *Angew. Chemie - Int. Ed.* **2011**, *50* (47), 11234–11237.

Chapter 2: The Development of a Ditopic Amidoxime-based Ligand for Uranium Uptake

2.1 Introduction

The uranium from seawater (UFS) project belongs to a class of initiatives tasked with securing a precious resource (e.g. uranium fuel) from an unconventional source (e.g. seawater). Since its inception in the 1950s, the UFS project has spurred the development of dozens of separations systems ranging from hydrous titanium oxide,[1] to mesoporous silicas[2] and carbons,[3] to functionalized polymers[4] and metal-organic-frameworks (MOFs)[5–8]. UFS work conducted in the last forty years has particularly focused on the amidoxime (-CNH_2NOH, AO) moiety (**section 2.1.1)**. Amidoxime functionalized polymers,[4] MOFs,[9] COFs,[10] mesoporous carbon,[11,12] mesoporous silica,[13–15] and other materials have been developed and tested for uranium uptake with varying uranium capacities and selectivity factors over other species in seawater.

Recent emphasis on cooperative binding has placed enormous scrutiny on the role of functional groups adjacent to the principle AO binding site. Work by Shi and co-workers,[16] for example, suggests that carboxylic acids adjacent to amidoxime groups may facilitate carbonate dissociation—from the main U species present in seawater $Ca_2[UO_2(CO_3)_3]$—resulting in enhanced capacities and kinetics in materials with both AO/COOH functionalities.

Inspired by this observation, we endeavored to design, synthesize, and characterize a bifunctional chelating ligand containing both a carboxylic acid and an amidoxime group in close proximity in order to investigate the possibility of cooperativity between functional groups.

2.1.1 The Amidoxime Choice

There is arguably no other paper that has so fundamentally influenced the direction of uranium from seawater efforts than that by Schwochau and co-workers. In their 1982 work,[27] the authors provide an overview of UFS project progress at the Nuclear Research Center of Julich, Germany at that time. The authors first discuss the desirable characteristics of a uranium adsorbent, specifically mentioning: mechanical stability, fast kinetics, high loading, facile elution and recovery, and selectivity. The authors also introduce models to quantify adsorbent performance in a pilot study.

Schwochau and co-workers then discuss the results of their resin screening study and conclude that only poly(acrylamidoxime)s meet all criteria set forth in the paper. It is worth noting that the poly(acrylamidoxime) resin materials *did not* result in the highest amount of uranium uptake. In fact, their uptake capacity after the two-hour test batch adsorption study was among the lowest. However, the poly(acrylamidoxime) materials were selected as the systems to study due to 1. The polymer's ability to extract U at seawater pH (i.e. 8.3), and 2. their selectivity for U over other competing ions in seawater. As a result of this work, a majority of UFS research has focused on the AO moiety or its derivatives including the major efforts at Oak Ridge National Laboratory,[4] Pacific Northwest National Laboratory,[28] and Lawrence Berkeley National Laboratory.[29]

2.2 Theoretical Methods

Calculations were performed on the Plutonium or Midway computational clusters at the University of Chicago using the Gaussian 09, revision A.02, software package.[30] Density Functional Theory (DFT) at the B3LYP level of theory[31,32] was used to obtain thermodynamic values. All light atoms (i.e., carbon, nitrogen, oxygen, and hydrogen) were modeled by the 6-

311+G* basis set.[33,34] Uranium was modeled by the Stuttgart RSC 1997 relativistic effective core potential[35] replacing 60 core electrons and modeling valence electrons by a contracted [8s/7p/6d/4f] basis set. All uranium, ligand, and uranium-ligand structures were first geometrically optimized and then subject to frequency calculations with the same basis set and at the same level of theory. Solvation was modeled implicitly using the polarizable conductor calculation model (CPCM).[36] All structures were computed separately and summed in order to satisfy equations 2.1 and 2.2:

$$UO_2 \cdot 5H_2O + L \rightarrow UO_2(L)_x(H_2O)_{5-x} + xH_2O \qquad \textbf{Equation 2.1}$$

$$\Delta G_{reaction} = \Sigma(\Delta G_{products}) - \Sigma(\Delta G_{reactants}) \qquad \textbf{Equation 2.2}$$

Binding enthalpies (ΔH) and Gibbs free energy values (ΔG) were calculated using zero-point energy and thermal corrections. Spin-orbit interactions were not considered explicitly.

2.3 Experimental Methods

2.3.1 General Experimental

All chemicals of reagent-grade quality were obtained from commercial sources and used as received. Nuclear Magnetic Resonance (NMR) data were recorded on a Bruker 500 MHz NMR spectrometer. Chemical shifts were determined via reference to solvent resonance [CDCl3, 7.26 ppm; dimethyl sulfoxide (DMSO), 2.50 ppm]. Thermogravimetric analysis (TGA) was performed under air at a heating rate of 5 °C min^{-1} using a Shimadzu TGA-50H equipped with a platinum pan. Liquid chromatography−mass spectrometry (LC−MS) was performed using an Agilent 6130 LC−MS instrument. Single crystal X-ray diffraction (XRD) data were collected with a Bruker

APEX II CCD-based detector at ChemMatCARS (Sector 15), Advanced Photon Source (APS), Argonne National Laboratory (ANL). Inductively coupled plasma mass spectrometry (ICP-MS) was carried out using an Agilent 7700x instrument, and samples were diluted with a 2% HNO_3 matrix in the range from 0.1 to 500 ppb. Standard curves were produced in the same concentration range with a correlation coefficient >0.9997.

The X-ray absorption data were collected at Beamline 10BM-B at the Advanced Photon Source (APS) at Argonne National Laboratory.[37] Spectra were collected at the uranium L_{III}-edge (17166 eV) in fluorescence mode by a Hitachi Vortex-ME4 four-element silicon drift fluorescence detector. The X-ray white beam was monochromatized by a Si(111) monochromator and detuned by 50% to reduce the contribution of higher-order harmonics to below the level of noise. The K-edge of an yttrium foil (17038 eV) was used as the reference for energy calibration and measured simultaneously for all samples. The incident beam intensity (I_0), transmitted beam intensity (I_t), and reference (I_r) were all measured by 20 cm ionization chambers with gas compositions of 80% N_2 and 20% Ar, 95% Ar and 5% N_2, and 100% N_2, respectively. I_0 was used for plotting the XAFS spectra for the samples, while I_t and I_{ref} were used to obtain the XAFS spectra for the yttrium foil standard.

Samples were centered on the beam and adjusted to find the most homogeneous location in the sample for data collection. The beam was reduced to dimensions of 400 × 3100 μm for all data collection. Data were collected over six regions: -250 to -30 eV (10 eV step size, dwell time of 0.25 seconds), -30 to -5 eV (5 eV step size, dwell time of 0.5 seconds), -5 to 30 eV (1 eV step size), 3 $Å^{-1}$ to 6 $Å^{-1}$ (0.05 $Å^{-1}$ step size, dwell time of 2 seconds), 6 $Å^{-1}$ to 9 $Å^{-1}$ (0.05 $Å^{-1}$ step size, dwell time of 4 seconds), and 9 $Å^{-1}$ to 15 $Å^{-1}$ (0.05 $Å^{-1}$ step size, dwell time of 8 seconds). Three scans were collected at room temperature (~25°C) for each sample.

The data were processed and analyzed using the Athena and Artemis programs of the IFEFFIT package based on FEFF 6.[38,39] Reference foil data were aligned to the first zero-crossing of the second derivative of the normalized μ(E) data, which was subsequently calibrated to the literature E_0 for the yttrium K-edge (17038 eV). Spectra were averaged in μ(E) prior to normalization. The background was removed and the data were assigned an Rbkg value of 1.0, slightly less than one-half the value of the half-path length for the nearest scattering element, prior to normalizing to obtain a unit edge step.

2.3.2 Ligand Synthesis and Characterization

The ditopic –COOH/-AO functionalized diaryl ether ligand of interest **(2.7)** was synthesized according to **Scheme 2.1**. In general, the amine group of a commercially available amine functionalized diaryl ether was replaced by an iodine in a modified Sandmeyer reaction **(2.2)** followed by oxidation of the ortho methyl group to a carboxylic acid using potassium permanganate **(2.3)**. Esterification **(2.4)** followed by a Rosemund von-Braun cyanation yields the ester/nitrile functionalized intermediate **(2.5).** Saponification **(2.6)** then treatment with hydroxylamine yields the –COOH/-AO functionalized diaryl ether ligand of interest **(2.7)**. Synthetic details are shown below.

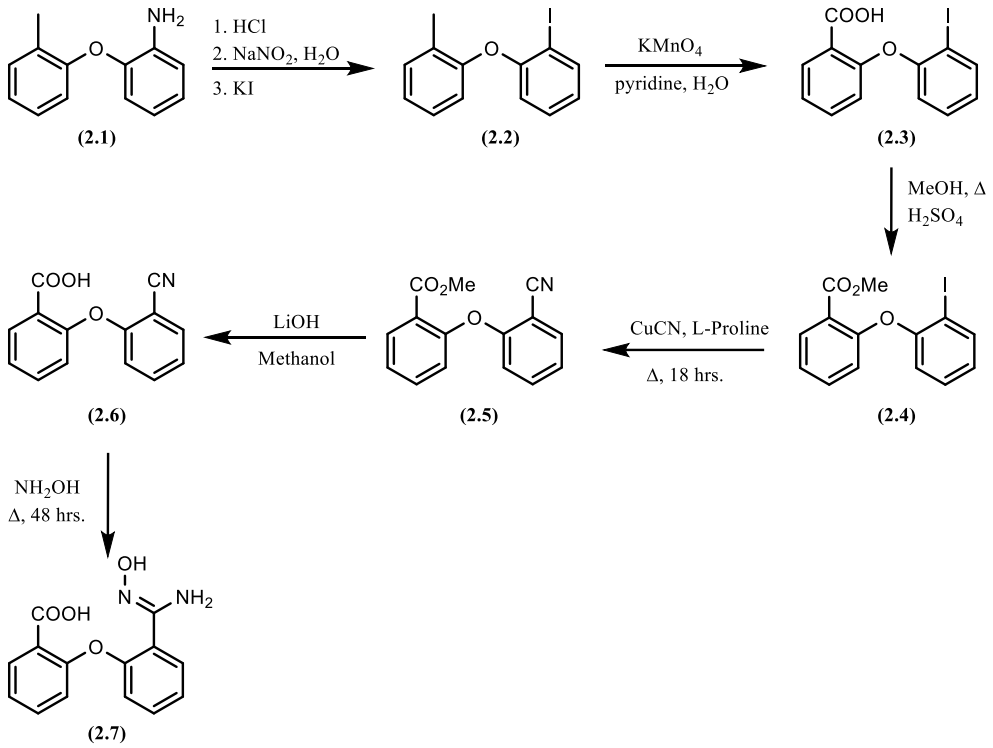

Scheme 2.1 Synthetic scheme of the ditopic –COOH/-AO U chelating ligand **(2.7)**.

2.3.2.1 Synthesis of 1-iodo-2-(2-methylphenoxy)benzene (2.2)

2-(2-methylphenoxy)aniline **(2.1)** (5.0 g, 25 mmol) was added to a solution of HCl (27.0 g, 750 mmol) in a 3:1 (v/v) solution of water and acetone (24 mL). The solution was cooled to 0 °C and an aqueous solution of $NaNO_2$ (3.45 g, 50.0 mmol) was added dropwise followed by solid KI (8.33 g, 50.0 mmol). The reaction was allowed to stir for three hours at 0 °C and then heated to 42 °C overnight. The resulting reaction mixture was cooled to room temperature, extracted with chloroform (40 mL) five times and washed with water (50 mL) twice. Organic extracts were dried with Na_2SO_4, filtered, and concentrated yielding a dark purple oil which was further purified by flash column chromatography on silica gel affording **2.2** as a red, viscous oil. Yield (6.27 g, 81%) ^{1}H NMR (500 MHz, $CDCl_3$) δ ppm: 7.86 (d, 1H, J = 9 *Hz*), 7.23 (t, 1H, J = 8.5 *Hz*), 7.17 (t, 1H, J = 7.5 *Hz*), 6.83 (q, 2H, J = 7 *Hz*), 6.68 (d, 1H, J = 7 *Hz*), 2.26 (s, 4H). ^{13}C NMR (125 MHz, $CDCl_3$)

δ ppm: 156.82, 154.26, 139.87, 131.62, 129.68, 127.24, 124.46, 119.18, 117.16, 87.59, 16.41. LRMS (EI) calculated for $C_{13}H_{11}IO$: 310.0 *m/z* expected, found: 310.0 *m/z*

2.3.2.2 Synthesis of 2-(2-iodophenoxy)benzoic acid (2.3)

Molecule **2.2** (6.0 g, 19.4 mmol) was added to a 3:1 (v/v) solution of pyridine and water (24 mL). The resulting solution was heated to 90 °C and solid $KMnO_4$ (18.4 g, 116 mmol) was added. After three hours at reflux, a second portion of solid $KMnO_4$ (18.4 g, 116 mmol) was added and the reaction was allowed to reflux for an additional three hours. The mixture was filtered through a plug of celite with lukewarm H_2O, acidified to a pH of 1 with 0.1 M HCl, extracted with ethyl acetate (25 mL) three times and washed with H_2O (25 mL) and brine (25 mL) before being dried over Na_2SO_4 and concentrated under vacuum affording **2.3** as a pale yellow solid. Yield (4.96 g, 75%).^{1}H NMR (500 MHz, $CDCl_3$) δ ppm: 8.26 (d, 1H, *J* = 6 *Hz*), 7.94 (d, 1H, *J* = 6 *Hz*), 7.42 (t, 1H, *J* = 7.5 *Hz*), 7.10 (d, 1H, *J* = 6 *Hz*), 7.05 (t, 1H, *J* = 6.5 *Hz*). ^{13}C NMR (125 MHz, $CDCl_3$) δ ppm: 156.34, 140.44, 134.86, 133.84, 130.16, 127.39, 123.88, 121.23, 116.70, 89.60. LC-MS (ES-API) calculated for $C_{13}H_9IO_3$: 340 *m/z*, found 340 *m/z*

2.3.2.3 Synthesis of methyl 2-(2-iodophenoxy)benzoate (2.4)

Molecule **2.3 (**4.85 g, 14.4 mmol) was dissolved in anhydrous methanol (22 mL). To this solution was added a catalytic amount of 18 M H_2SO_4 (80.00 μL, 1.44 mmol). The solution was heated to 65 °C for 24 hours. The solution was cooled to room temperature and concentrated under vacuum before a saturated solution of $NaHCO_3$ (20 mL) was added. The resulting mixture was extracted with ethyl acetate (25 mL) three times and brine (25 mL) before being dried over Na_2SO_4 and concentrated under vacuum to afford **2.4** as a yellow, viscous oil. Yield (4.65 g, 92%) ^{1}H NMR (500 MHz, CDCl3) δ ppm: 7.98 (d, 1H, *J* = 7 *Hz*), 7.88(d, 1H, *J* = 6.5 *Hz*), 7.50 (t, 1H, *J* = 8 *Hz*), 6.96 (d, 1H, *J* = 8 *Hz*), 6.86 (t, 1H, *J* = 4 *Hz*), 6.73 (d, 1H, *J* = 6 *Hz*), 3.83 (s, 3H). ^{13}C NMR (125

MHz, $CDCl_3$) δ ppm: 166.00, 157.01, 155.36, 139.89, 133.73, 129.74, 124.89, 124.02, 123.05, 120.66, 117.62, 87.72, 52.28. LRMS (EI) calculated for $C_{14}H_{11}IO_3$: 354.0 *m/z* expected, found: 354.0 *m/z*

2.3.2.4 Synthesis of methyl 2-(2-cyanophenoxy)benzoate (2.5)

Molecule **2.4** (4.6 g, 13 mmol) in DMF (15 mL) was added to a mixture of CuCN (2.35 g, 26 mmol) and L-proline (1.50 g, 13 mmol). The resulting solution was heated to 115 °C for 18 hours. After cooling to room temperature, 4 equivalents of NH_4Br (10.2 g, 104 mmol) in 20 mL distilled water were added and the solution was mixed well. Ethyl acetate (10 mL) was added and the reaction mixture was filtered with a Büchner funnel. Extraction with ethyl acetate (50 mL) five times and concentration under vacuum afforded the crude product as a pale brown oil. Purification by flash column chromatography on silica gel affords **2.5** as a pale yellow solid. Yield (1.38 g, 42%) ^{1}H NMR (500 MHz, CDCl3) δ ppm: 8.03 (d, 1H, *J* = 7 *Hz*), 7.66 (d, 1H, *J* = 7.5 *Hz*), 7.59 (t, 1H, *J*= 4 *Hz*), 7.42 (t, 1H, *J* = 4.5 *Hz*), 7.35 (t, 1H, *J* = 7.5 *Hz*), 7.16 (d, 1H, *J* = 9 *Hz*), 7.09 (t, 1H, *J* = 7.5 *Hz*), 6.63 (d, 1H, *J* = 8 *Hz*), 3.76 (s, 3H). ^{13}C NMR (500 MHz, $CDCl_3$) δ ppm: 160.45, 153.57, 134.17, 132.57, 125.75, 123.99, 123.05, 122.38, 118.20, 115.29, 52.32. LRMS (EI) calculated for $C_{15}H_{11}NO_3$: 253.1 *m/z* expected, found: 253.1 *m/z*

2.3.2.5 Synthesis of 2-(2-cyanophenoxy)benzoic acid (2.6)

Molecule **2.5** (1.38 g, 5.45 mmol) was added to a 1:1 v/v solution of methanol and tetrahydrofuran (14 mL). To this solution was added a 1.5 M aqueous solution of LiOH (314 mg in 5 mL water) dropwise. The solution was allowed to stir for five hours. Concentration under vacuum and acidification with 0.1 M HCl gave a white precipitate. The resulting mixture was extracted with ethyl acetate (20 mL) three times before being concentrated under vacuum to afford **2.6** as a white solid. Yield (1.25 g, 96%) ^{1}H NMR (500 MHz, CDCl3) δ ppm: 8.17 (d, 1H, *J* = 7

Hz), 7.70 (d, 1H, *J* =8 *Hz*), 7.60 (t, 1H, *J*= 10 *Hz*), 7.50 (t, 1H, *J*= 8 *Hz*), 7.36 (t, 1H, *J* =7 *Hz*), 7.19 (t, 1H, *J* = 7.5 *Hz*), 7.07 (t, 1H, *J*=7 *Hz*), 6.80 (d, 1H, *J*= 8 *Hz*). ^{13}C NMR (125 MHz, $CDCl_3$) δ ppm: 166.11, 160.42, 153.24, 135.52, 134.80, 134.39, 132.55, 126.52, 125.08, 123.40, 123.16, 115.68, 102.14

2.3.2.6 Synthesis of 2-[2-[(Z)-N'-hydroxycarbamimidoyl]phenoxy] benzoic acid (2.7)

Molecule **2.6** (992 mg, 4.1 mmol) was dissolved in a 10:1 v/v solution of ethanol:water (11 mL). To this solution was added 2 equivalents of aqueous NH_2OH (274 µL, 8.3 mmol). The solution heated to reflux at 80 °C for 24 hours. An additional equivalent of NH_2OH was added (137 µL, 4.1 mmol) and the solution was heated at 80 °C for an additional 24 hours. Concentration under vacuum and subsequent acidification with 0.1 M HCl gave a pale orange precipitate. The resulting solid was collected via centrifugation. Subsequent washing with ethanol (20 mL) three times and centrifugation afforded a white solid. White, needle-like crystals suitable for X-ray diffraction analysis were grown in methanol from a saturated solution over three days. Yield (530 mg, 44%)

^{1}H NMR (500 MHz, DMSO) δ ppm: 9.56 (s, 1H), 7.89(d, 1H, *J* = 6 *Hz*), 7.58 (m, 2H), 7.33 (t, 1H, *J* = 8 *Hz*), 7.28 (t, 1H, *J* = 7.5 *Hz*), 7.12 (t, 1H, *J* = 7.5 *Hz*), 7.01 (d, 1H, *J* = 8 *Hz*), 6.68 (d, 1H, *J* = 8 *Hz*), 5.91 (s, 2H).^{13}C NMR (125 MHz, DMSO) δ ppm: 166.96, 155.07, 154.89, 150.71, 134.34, 132.26, 130.89, 130.59, 124.63, 124.53, 123.50, 121.07, 117.54. LC-MS (ES-API) calculated for $C_{14}H_{13}N_2O_4$: 273 *m/z*, found 273 *m/z*

Successful synthesis of **(2.7)** was confirmed via ^{1}H and ^{13}C NMR, LC-MS, and SXRD. The ^{1}H spectrum displayed a sharp singlet at 5.91 ppm and a broad singlet at 9.56 ppm corresponding to the –(H)N-H and –COO-H respectively. Integration confirmed two protons for –NH_2 and one proton for –COOH (**Figure 2.1)**. ^{13}C NMR spectroscopy showed 14 peaks

corresponding to distinct carbon peaks in molecule **2.7** as expected (**Figure 2.2**). Liquid Chromatography-Mass Spectrometry (LC-MS) run in positive mode found the molecular ion corresponding to the desired product; (M+H) was found at 273.1 *m/z*. Thermal stability of **2.7** was investigated with thermogravimetric analysis (TGA). No obvious weight loss is observed until 170 °C, which suggested the chelator is stable in environments appropriate for U extraction and could withstand harsh temperature swing adsorption-desorption cycles (**Figure 2.3).** SXRD data were obtained in sector 15 at the APS and were used to render a structure of the small molecule **2.7** (**Figure 2.4**). Crystallographic data can be found in **Appendix 2.1**.

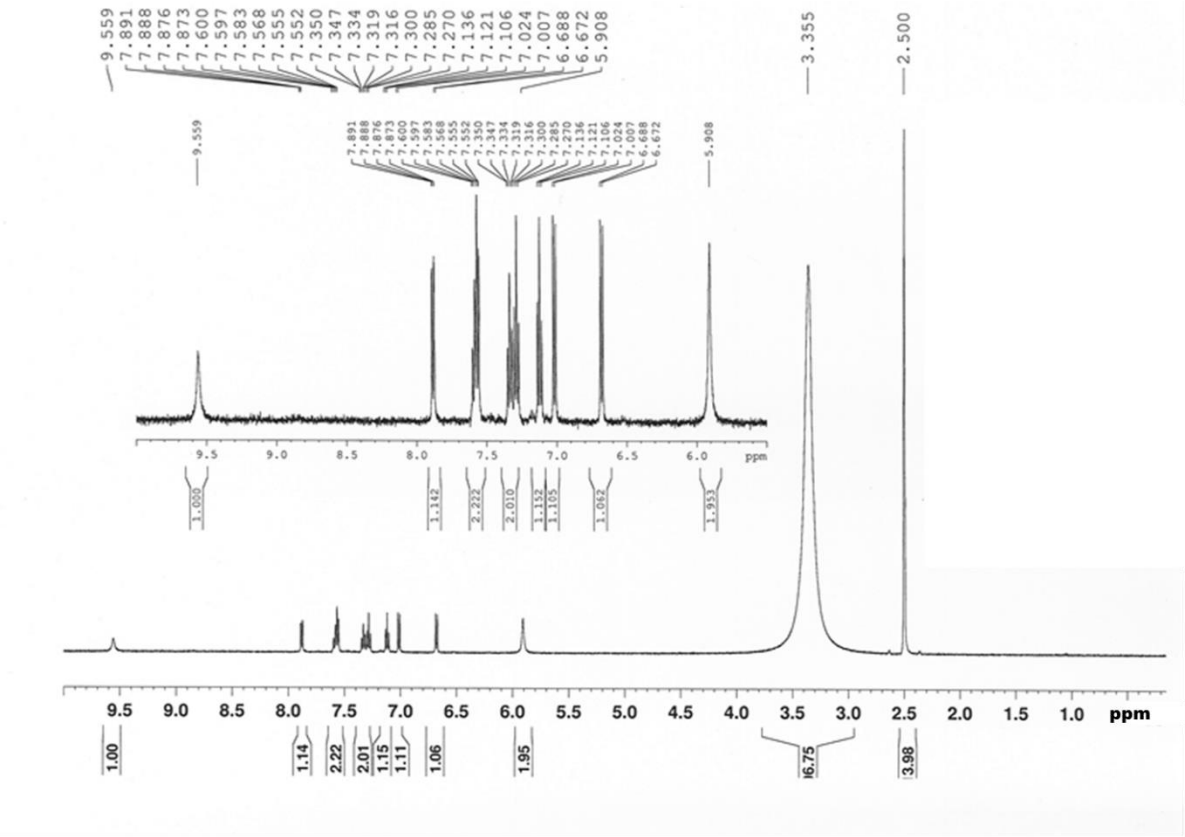

Figure 2.1 ^{1}H NMR spectrum of molecule **2.7** (inset: zoom-in of spectrum between 5.5 and 10 ppm).

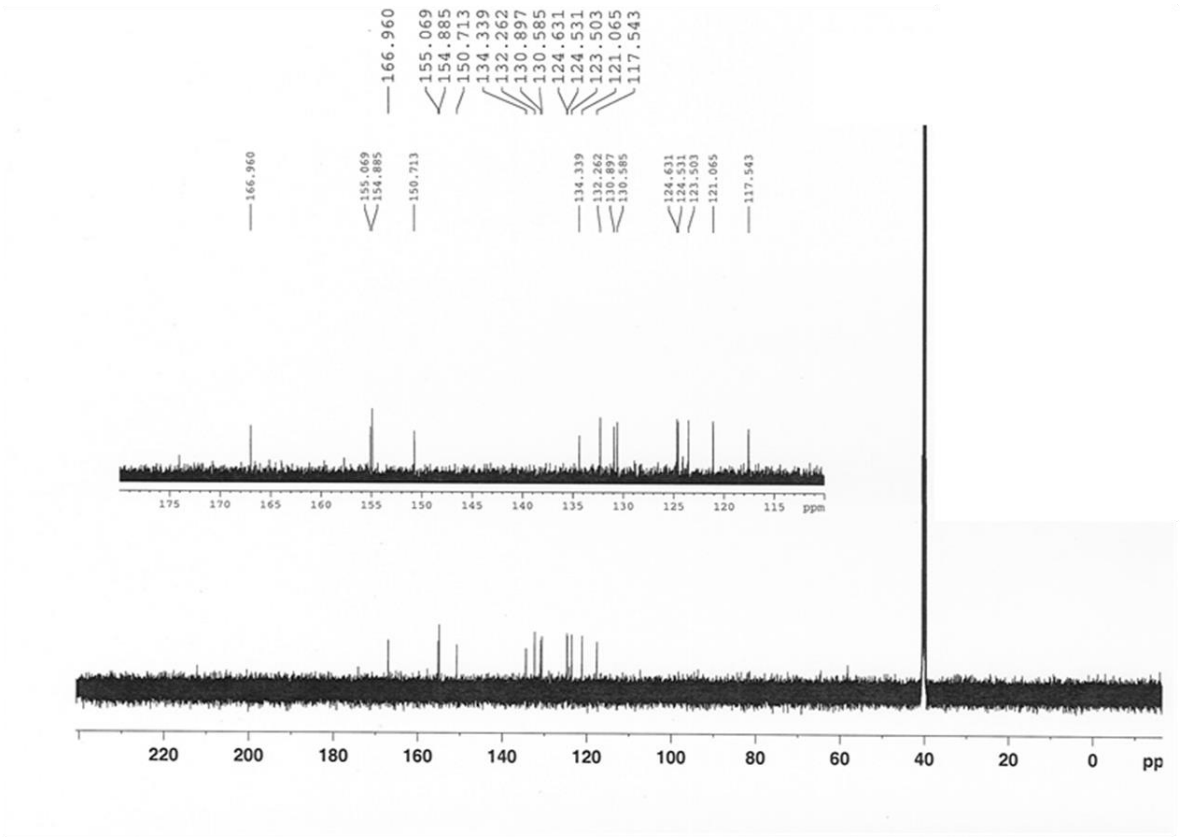

Figure 2.2 ^{13}C NMR spectrum of molecule **2.7** (inset: zoom-in of region between 115 and 170 ppm).

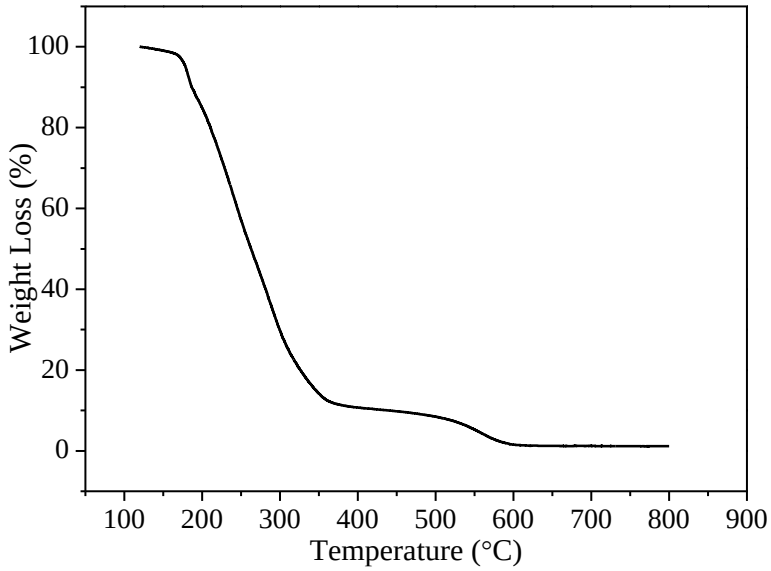

Figure 2.3 Thermogravimetric analysis of molecule **2.7**.

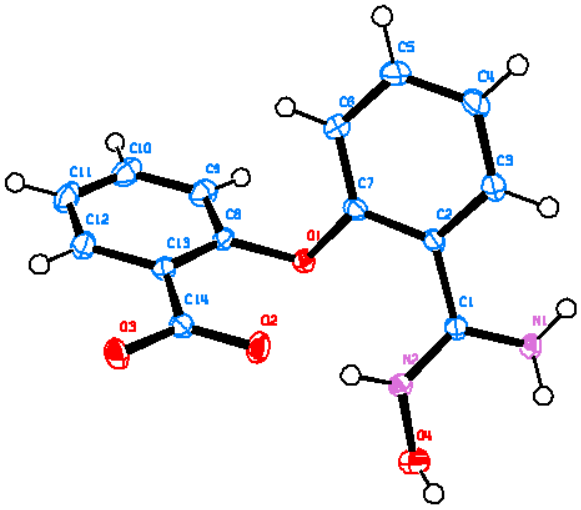

Figure 2.4 Single-crystal structure of small-molecule **2.7** (red, blue, purple, violet, and white sphere represent oxygen, carbon, nitrogen, and hydrogen respectively).

2.4 Results

2.4.1 Computational Results

The diaryl ether ($C_6H_5OC_6H_5$) was chosen as the template for further functionalization owing to its synthetic versatility[40,41] and commercial availability. Moreover, its water insolubility afforded by tethered phenyl groups as well as reactive sites in close proximity to each other made the diaryl ether an attractive choice.

Density functional theory (DFT) calculations were first used to rapidly screen several ligand derivatives for favorable uranyl binding prior to synthesis. As diaryl ethers can be functionalized either *ortho* or *meta* to the bridging heteroatom, both options were investigated computationally. Proposed structures studied are shown in **Figure 2.5** Optimized coordinates for all structures are shown in **Appendix 2.2.**

Proposed structures contain both –AO and –COOH groups either *ortho* or *meta* to the bridging atom and differ in the length of the alkyl linker between functional group and backbone. It was hypothesized that a longer linker would afford greater U binding owing to a more complete HOMO/LUMO overlap. Finally, it should be noted that geometry optimization resulted in both functional groups on the same face of the diaryl ether ligand. Efforts to modify the starting geometry so that each moiety is on opposite sides of the diaryl ether resulted in similar structures to those shown in **Figure 2.5**.

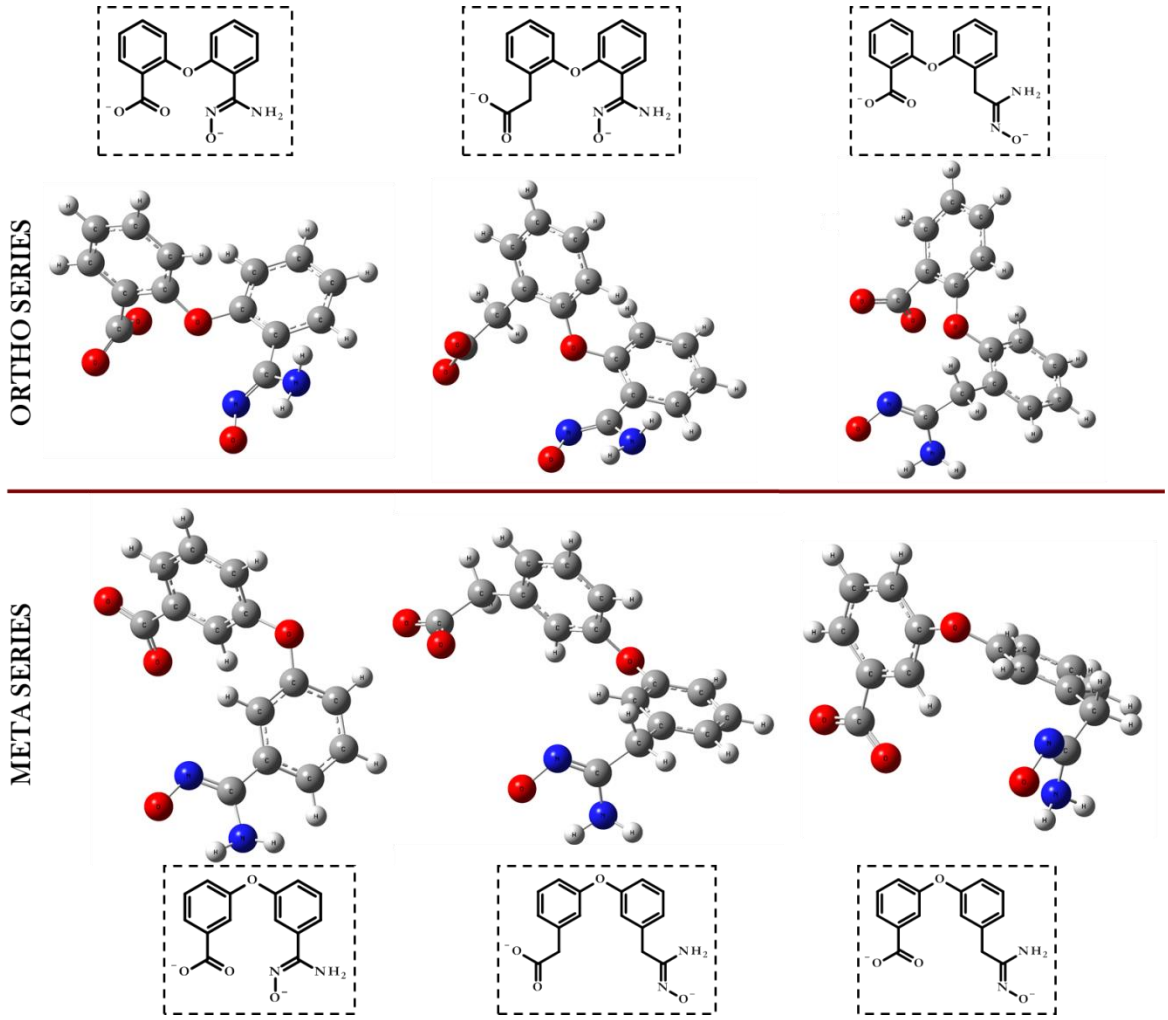

Figure 2.5 Geometrically optimized structures of ligands investigated for uranium uptake.

A comparison of selected bond lengths and angles between the crystal structure of **(2.7)** and the DFT calculated structure reveals an average error of 0.042 Å and 1.65° respectively (**Table 2.1**). Validation of the geometry optimized structure via DFT suggests that the resulting computed thermodynamic values can be expected to be reasonable.

Table 2.1 Selected Calculated and Experimental Bond Lengths and Angles of the Small Molecule **2.7**

Bond Lengths			
Bifunctional Chelator	Calc.	Exp.	|Δ|
C1-N1	1.327	1.316	0.011
C1-N2	1.314	1.307	0.007
N2-O4	1.388	1.384	0.004
C14-O3	1.246	1.268	0.022
O2-O3	2.238	2.220	0.018
O1-O2	2.879	2.702	0.177
O1-N2	2.749	2.702	0.047
N2-O2	2.661	2.713	0.052
Average Error			0.042
Angles			
Bifunctional Chelator	Calc.	Exp.	|Δ|
O3-C14-O2	125.48	122.76	2.72
C8-O1-C7	120.64	116.89	3.75
H2-N2-O4	117.67	116.84	0.83
N2-C1-N1	120.82	120.78	0.04
N2-C1-C2	118.69	118.88	0.19
O4-N2-C1	117.58	119.94	2.36
Average Error			1.65

The uranyl cation was then included in the starting calculations with the geometrically optimized ligands shown in **Figure 2.5.** The resulting optimized coordination complexes are showing in **Figure 2.6** and the resulting thermodynamic values were calculated to satisfy equations **2.1** and **2.2**. Thermodynamic values corresponding to optimized ligand/uranium coordination complexes in are shown in **Table 2.2**.

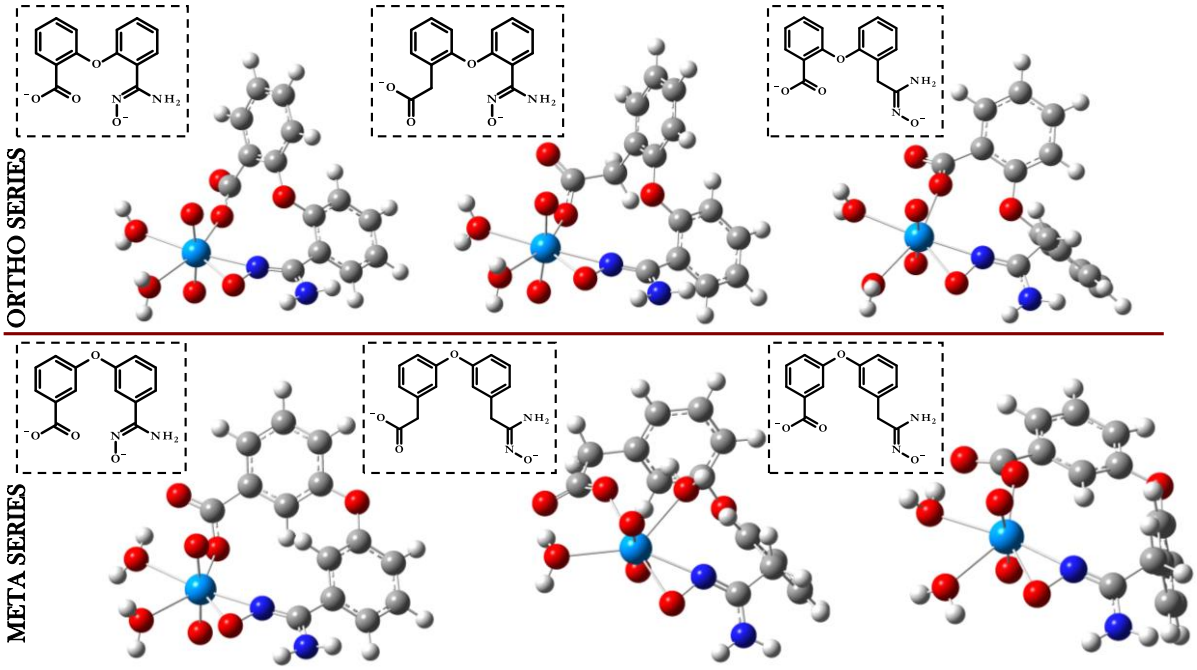

Figure 2.6 DFT optimized structures of **2.7** and UO_2^{2+}. *Ortho* functionalized ligands displayed in the top panel, *meta*-functionalized ligands displayed in the bottom panel. Red, white, gray, dark blue, and light blue spheres represent O, H, C, N, and U, respectively. Insets display structures of unbound bifunctional chelating ligands.

Table 2.2 Gibbs Free Energy Values of Functionalized Diaryl Ether/Uranium Complexes

Ligand Identity	Heteroatom	Functionalization	ΔG of complexation (kcal/mol)
COOH/AO	O	Ortho	-68.4
CH_2COOH/AO	O	Ortho	-69.6
COOH/CH_2AO	O	Ortho	-71.3
COOH/AO	O	Meta	-64.2
COOH/CH_2AO	O	Meta	-68.4
CH_2COOH/CH_2AO	O	Meta	-70.3

The UO_2^{2+} cation was made to be penta-coordinate in the equatorial sphere, a coordination number that predominates in aqueous media.[42] Each geometrically optimized structure exhibits monodentate coordination through the carboxylate moiety and η^2 bonding by the amidoxime in agreement with previous studies.[43–45] Increasing the alkyl chain length at the amidoxime and carboxylate primary positions makes the metal-ligand complex more thermodynamically favorable by allowing the binding groups to envelop the uranyl cation to a greater extent.

Optimizing the alkyl chain length at these positions can improve U-ligand bond strength by as much as 6 kcal mol^{-1}.

Diaryl amine bridged chelators were also considered as it was speculated the N-**H** may participate in hydrogen bonding with the axial uranyl oxygen. This phenomenon was not observed computationally and the calculated bond strength of uranyl binding was comparable with the diaryl ether ligands (**Table 2.3**).

Table 2.3 Gibbs Free Energy Values of Functionalized N or S Bridged Diaryl Ether/Uranium Complexes

Ligand Identity	Heteroatom	Functionalization	ΔG of complexation (kcal/mol)
COOH/AO	N	Ortho	-65.25
CH_2COOH/AO	N	Ortho	-66.38
COOH/CH_2AO	N	Ortho	-72.01
COOH/AO	N	Meta	-68.24
COOH/CH_2AO	N	Meta	-71.97
CH_2COOH/CH_2AO	N	Meta	-63.58

In addition to amine bridged diaryl ethers, we optimized the -S and –N-CH_3 analogs of **2.7** and found free energies of complexation with U to be within 4 kcal mol^{-1} (**Table 2.4**). Several aliphatic amidoxime complexes as well as other pre-organized amidoxime based ligands found in the literature were also studied to provide a comparison for **2.7 (Table 2.5)**. Uranyl triscarbonato was optimized without its corresponding calcium counterions to provide an idea of the predominant U complex's stability in seawater. It was found that the complex exhibits a free energy of complexes of -120.5 kcal mol^{-1} suggesting that any bonding interaction with **2.7** would be insufficient to displace all three coordinating carbonates. Two complexes were studied with either 2 acetamidoxime groups or 1 acetamidoxime group and 1 carboxylic acid. As expected, allowing the functional groups to arrange around UO_2^{2+} afforded the most favorable Gibbs free energy of complexation. Unexpected, however, was that two acetamidoxime groups formed compounds that

were ~20 kcal mol^{-1} more stable than the mixed –AO/COO- system. Encouraged by this result, we investigated the bis-amidoxime *ortho* functionalized diaryl ether ligand and found a free energy of complexation on the order of -280 kcal mol^{-1} (**Table 2.4**). A synthetic route for this ligand was subsequently developed and its affinity for U through uptake studies was tested. The results of this system are discussed in **Chapter 3**.

Finally, two ligands from the literature were subject to the same conditions *in silico* as the diaryl ether series as a means of comparison. The first was 1,10-phenanthroline- 2,9-dicarboxylic acid (PDA), a highly preorganized ligand identified by Dai and co-workers[46] as a promising candidate for U sequestration. Complexation of the PDA and uranyl with two water molecules in the equatorial sphere results in a free energy of -63.2 kcal mol^{-1}. Despite the rigidity of the ligand and the presence of both nitrogen and oxygen donors, the free energy of complexation is 5 kcal mol^{-1} less favorable than ligand **2.7**. On the other hand, optimized uranyl coordination complexes with the tridentate amidoxime analogue glutarimidedioxime first reported by Rao and co-workers[47] yields a free energy of complexation -221.7 kcal mol^{-1}. While the DFT calculated energies suggest favorable U binding, subsequent investigation into the stability of cyclic imide dioximes[48] as well as XAFS studies[49] on the functional groups present on industrially relevant amidoxime-functionalized polymer fibers found no evidence to support the binding of uranium by these species.

Ultimately, the AO/COOH without extension **(2.7)** was chosen as the model system to study 1.in an attempt to establish a baseline for uranium sorption, 2. due to its ease of synthesis, and 3. to test whether cooperative binding between AO and COOH in the ortho positions is evident in the solid state.

Table 2.4 Gibbs Free Energy Values of Selected Uranium/Ligand Coordination Complexes

Ligand Identity	Heteroatom	Functionalization	ΔG of complexation (kcal/mol)
COOH/AO	S	Ortho	-64.8
COOH/AO	N-Methyl	Ortho	-68.1
AO/AO	O	Ortho	-284.4

Table 2.5 Gibbs Free Energy Values of Selected Uranium Coordination Complexes

Optimized Complex or Ligand	ΔG of complexation (kcal/mol)
$UO_2(CO_3)_3$	-120.5
2 CH_3CNH_2NOH	-91.6
1 CH_3CNH_2NOH, 1 COOH	-70.5
1,10-phenanthroline- 2,9-dicarboxylic acid (PDA)	-63.2
Glutarimidedioxime	-221.7

2.4.2 Uranium Uptake Studies

2.4.2.1 Methodology

Simulated seawater (SS) solutions were spiked with ppm levels of uranium in order to facilitate comparison of **(2.7)** U uptake with other uranophiles in the literature. SS solutions were prepared by dissolving $UO_2(NO_3)_2 \cdot 6H_2O$ in 18 MΩ water containing 440 mM NaCl and 2 mM $NaHCO_3$.

The ligand **(2.7)** was added to 1 mL seawater simulant at a phase ratio of 1 mg ligand : 1 mL solution and agitated on a plate shaker at 300 rpm for 18 hours. The uranium concentration before and after agitation was determined via ICP-MS to evaluate uranium uptake efficacy by **(2.7)**. The quantity of uranium adsorbed by the –AO/-COOH chelator at equilibrium (Q_e) was calculated with Equation 2.3:

$$Q_e = \frac{(C_o - C_e) * V}{m} \qquad \textbf{Equation 2.3}$$

where Q_e is the uranium adsorbed at equilibrium, C_o is the initial uranium concentration, C_e is the uranium concentration of seawater simulant at equilibrium, V is the volume of the seawater simulant, and m is the mass of the bifunctional chelator **2.7**.

2.4.2.2 Uptake Results

Uranium adsorption data obtained at room temperature are shown in **Figure 2.7**. Due to possessing no appreciable solubility in water, the chelator can be added directly to the aqueous solution without need of any supporting structure. This separation experiment in "batch mode" results in extremely rapid sorption kinetics and facile isolation by centrifugation.

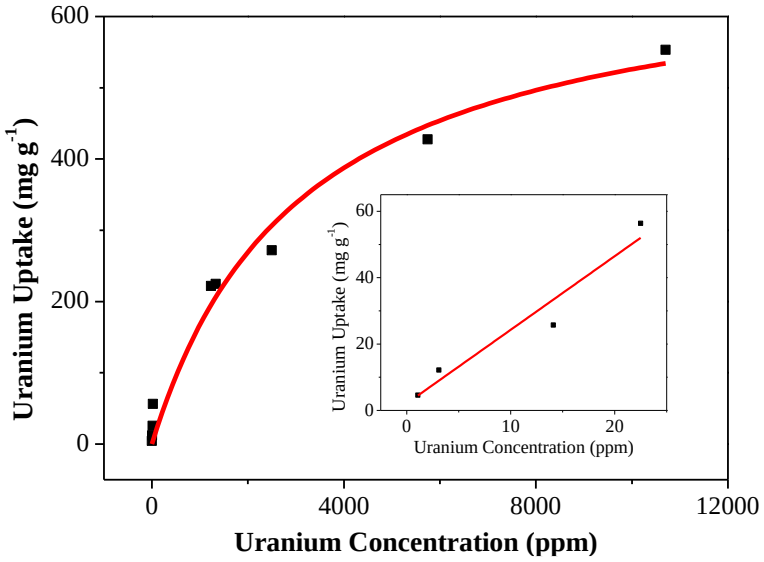

Figure 2.7 Uranium isotherm of the bifunctional chelator **(2.7)** at room temperature. Data points are black squares, with the fit obtained by the Langmuir-Freundlich model displayed as a red line, R^2 = 98.2%. Inset: the linearized data and fit at dilute uranium concentration.

The sorption data were fitted using the Langmuir-Freundlich model[50] as shown in Equation 2.4:

$$Q_e = Q_{max} \frac{bc_e^{\frac{1}{n}}}{1+bc_e^{\frac{1}{n}}} \qquad \textbf{Equation 2.4}$$

Where Q_e is the uranium uptake (mg g^{-1}) at equilibrium, Q_{max} is the uranium capacity (710 mg g^{-1}) of the accessible sorption site at saturation, c_e is the uranium concentration (ppm) in seawater simulant, b is the affinity coefficients ($7.3*10^{-4}$), n is the ideal homogeneous surface deviation.

A saturation capacity of 710 mg g^{-1} was obtained by fitting the isotherm data. A saturation capacity of 874 mg g^{-1} sorbent would be achieved if a 1:1 uranium-ligand complex is assumed to

form. These results indicate more than 80% of binding sites can be occupied under simulated seawater conditions. However, a portion of the molecule's **2.7** sorption sites are not readily accessible due to the tendency of the free ligand to agglomerate. The ditopic chelator exhibits respectable sorption capacity even at low uranium concentration—56 mg uranium g^{-1} chelator at 22 ppm—which is higher than previously reported phosphonate ligand modified mesoporous silica[2] or mesoporous carbon,[51] and is comparable with diethoxyphosphorylurea functionalized UiO-68 metal-organic frameworks.[9]

2.4.3 EXAFS Fitting of U Contacted Ligand

2.4.3.1 Methodology & Sample Preparation

Following sorption studies, the uranyl saturated adsorbent was collected by centrifugation for XAFS investigation. The resulting yellow solid was washed with water and dried *in vacuo* before being ground into a fine powder with a mortar and pestle. Samples were diluted with dextrose to prevent self-absorption phenomena and pressed into the center of a Nylon washer. The filled washer was then placed into a small, enclosed pouch made of multiple layers of Kapton film and Kapton tape to comply with radiological safety considerations.

The mass of uranium needed to achieve a 1 – 2.5 absorption length edge step was calculated for each small molecule standard based on the elemental composition and mass absorption coefficient for each element. Samples were dried under vacuum for 1 hr, ground with an agate mortar and pestle, and blended with D-(+)-Glucose to the appropriate concentration.

Approximately 20 – 25 mg of sample (after diluting) was enclosed within a nylon washer of 4.953 mm inner diameter (area of 0.193 cm^2), sealed on one side with Kapton film held in place with Kapton tape. The sample was pressed thoroughly by hand to form a firm, uniform pellet,

then sealed on the open side with a second piece of Kapton film secured with Kapton tape. The entire sample was placed into a baggie formed of Kapton tape which had been folded in half to prevent any contact with the adhesive. Small pieces of Kapton tape were used to seal the three open edges of the Kapton baggie. This method was approved in advance by the APS Radiation Safety Review Board for achieving the double containment necessary for analysis of radioactive samples.

Degeneracy from the amidoxime and carboxylic acid was varied in quadrature by scaling respective amplitude reduction factors (S_0^2) during the fitting process. The degeneracy of the axial oxygen on uranyl was not considered to vary and was fixed at 2. Parameters varied for each single scattering path include the change in scattering half-path length (ΔR) and the mean squared relative disorder of the scatterer (σ^2). A single global energy shift parameter (ΔE) was also varied. Multiple scattering paths were constructed from constituent single scattering paths.

2.4.3.2 XAFS Results

Numerous attempts to grow single crystals of uranyl chelated ligand were unsuccessful. Addition of molecule **2.7** to solvated uranyl resulted in instantaneous formation of an amorphous yellow precipitate, regardless of efforts to retard the rate of complexation. The yellow precipitate obtained during all crystal growth experiments suggests a distinct lack of strong binding. Strong ligand backbonding interactions, weakening the axial uranium-oxygen bonds, would likely result in a red-colored complex.[52] As crystallographic investigation of the uranyl-chelator structure was not feasible, we applied XAFS analysis to examine the uranium coordination environment after extraction from seawater simulant.

In addition to the coordination environment investigated by DFT, binding of two different uranyl molecules by the amidoxime and carboxylic acid functionalities would result in the formation of a coordination polymer. Models representative of both motifs were investigated through fitting of the extended XAFS (EXAFS) region.

The structure model for the uranyl coordination environment was constructed in a bottom-up fashion, including sequential shells of coordinating elements. All data were fit with multiple k-weights (k=0.5, 1, 2, 3) in R space. The best fitted coordination environment consists of 2 axial uranyl oxygen atoms (O_{yl}) tightly bound at 1.78 Å, 2.8 ± 0.3 oxygen or nitrogen atoms from amidoxime moieties (O_1) at 2.33 Å, 3.2 ± 0.3 equatorial oxygen atoms from chelating carboxylate or water (O_2) at 2.49 Å, 1.4 ± 0.4 carbon atoms from carboxylate or amidoxime moieties (C_1) at 2.87 Å, and 1.1 ± 0.6 nitrogen atoms from the amidoxime group (N_{am}) at 3.41 Å. The multiple scattering paths U→O_{yl} and U→C_1→C_2, where C_2 is the carbon atom adjacent to C1 on carboxylic acid, contributed significantly to the quadrature of the spectrum and are also included in the fitting. Final fits displayed in R-space and k-space are shown in **Figure 2.8**. **Table 2.6** lists fit parameters

Interpretation of the fit to assign the average coordination environment was made by comparing XAFS-determined bond lengths with those of representative crystal structures.[53] The best-fit model is representative of uranyl coordination by one monodentate-bound amidoxime, one or two bidentate chelating carboxylic acids, and the remainder of the equatorial plane filled with coordinating water molecules as shown in **Figure 2.7**. Uranyl species with five or six equatorially-coordinating molecules have been shown to be stable and prevalent in seawater.[54]

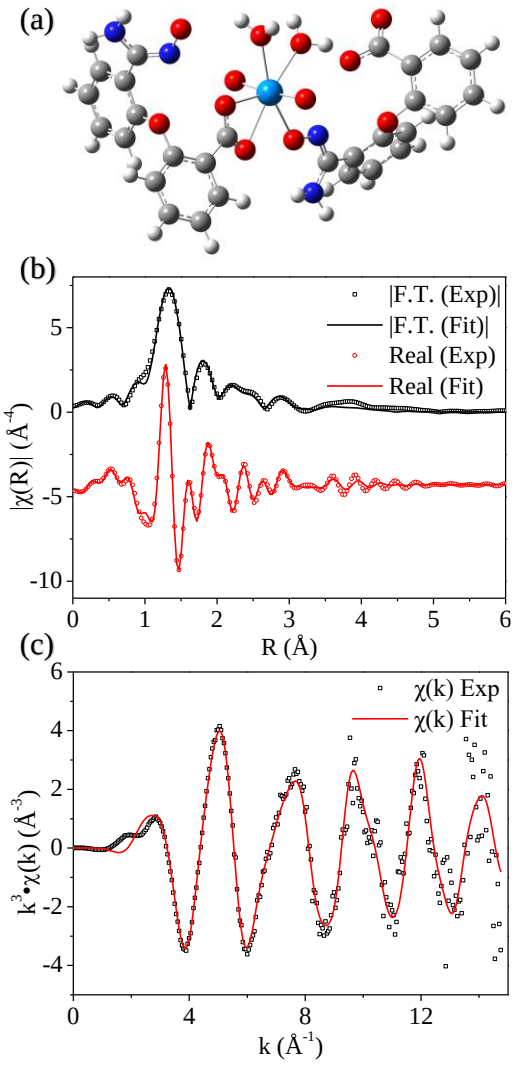

Figure 2.8 (a) The proposed uranyl coordination environment based on XAFS analysis. (b) XAFS data and fits in R space. The top plot (black) displays the magnitude of the Fourier transform. The bottom plot (red) displays the real component and is offset for the sake of clarity. Data are not phase shift corrected. (c) XAFS data and fit displayed in k space. XAFS data were fitted simultaneously with k-weighting of 1, 2, and 3. Data and fit with k-weighting of 3 are displayed.

The fit is consistent with empirical observations and suggests that strong binding via an η^2 motif is not occurring, despite previous small molecule and computational investigations. The yellow precipitate observed is likely due to weak coordination by chelating carboxylates as well as monodentate binding by amidoxime functionalities.

The rapid uranium adsorption displayed by the bifunctional chelator precludes the formation of the slower, more thermodynamically stable η^2 binding motif suggested by DFT calculations, instead favoring the formation of a coordination polymer.

Table 2.6 Scattering Paths, Path Lengths, and Mean-Square Disorder of Path Distance for the Best XAFS Fit

Scattering Path	R (Å)	Error	σ^2 (Å2)	Error	Coordination Number	Error
$U \rightarrow O_{yl}$	1.78	< 0.01	0.002	< 0.001	2	-
$U \rightarrow O_1$	2.33	0.02	0.006	0.002	2.8	0.3
$U \rightarrow O_2$	2.49	0.02	0.006	0.002	3.2	0.3
$U \rightarrow C_1$	2.87	0.02	0.002	0.002	1.4	0.4
$U \rightarrow N_{am}$	3.41	0.03	0.003	0.002	1.1	0.6
$U \rightarrow O_{yl1} \rightarrow O_{yl2}$	3.56	0.04	0.004	< 0.001	2	-
$U \rightarrow O_{yl1} \rightarrow U \rightarrow O_{yl2}$	3.56	0.04	0.004	< 0.001	2	-
$U \rightarrow O_{yl1} \rightarrow U \rightarrow O_{yl1}$	3.56	0.04	0.004	< 0.001	2	-
$U \rightarrow C_1 \rightarrow C_2$	4.35	0.02	0.003	0.002	1.4	0.4
E_0 = -0.9 ± 1.0 eV, R-factor = 0.9 %						

2.5 Conclusion

A new ligand was synthesized that shows great potential in aqueous uranium sequestration for applications to groundwater decontamination and the nuclear fuel cycle. Using density-functional theory as a high throughput tool to quickly and efficiently screen several ligand types, a bifunctional chelator based on a flexible diaryl-ether framework, was chosen as the model system to study.

Although uranyl binding did not occur through cooperative interactions by adjacent functionalities as expected, uranium sorption was nevertheless achieved. Indeed, a uranium saturation capacity of 553 mg U g^{-1} sorbent was observed in seawater simulant, which surpasses the current state of the art materials by several-fold. EXAFS analysis suggests the formation of a

coordination polymer with the carboxylate and amidoxime moieties bonding distinct uranyl groups. For practical separations, this ligand may have potential in solvent extraction schemes when used with an appropriate organic diluent. Otherwise, the ligand may be a good candidate for incorporation into hard shell enclosures for uranium uptake.[55]

As a result of this work, attention was turned to similar functionalized diaryl ethers in an attempt to determine whether stronger U binding could be achieved. Further, the use of a powder rather than a polymeric material limits the practical use of **(2.7)** as a U adsorbent. Greater attention was turned to methods of incorporating uranophiles into polymeric sorbents.

2.6 Next Steps: The Development of Ditopic Ligand Functionalized Polymeric Adsorbent

While the –COOH/-AO ligand demonstrated impressive U uptake performance, its form as a powder limits its practical use. Therefore, we proceeded to synthesize proof-of- concept polymeric systems using the appropriate vinylated **2.7** monomer with divinylbenzene or N,N′-methylenebis(acrylamide) as crosslinker. The synthetic routes to access the DVB crosslinked and NNBIS crosslinked materials are shown in **Scheme 2.2**.

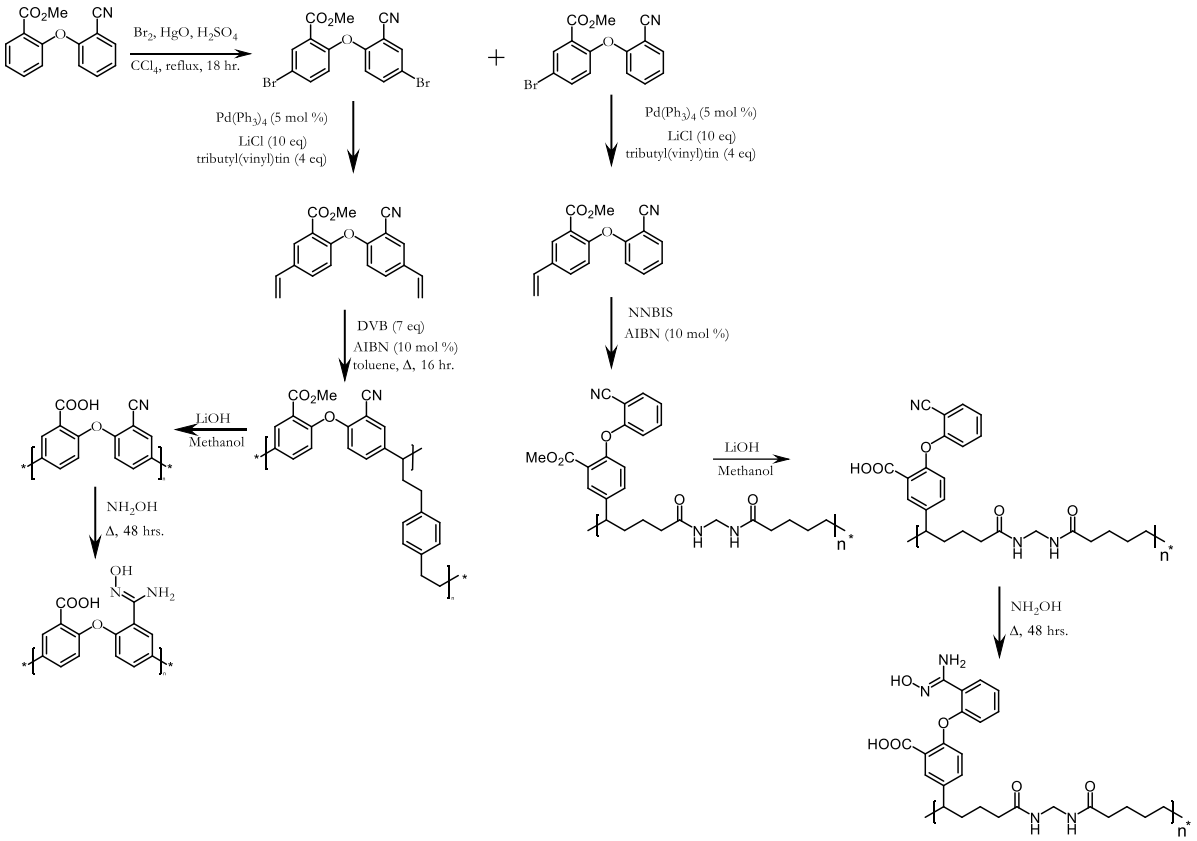

Scheme 2.2 The synthetic route to divinylbenzene or N,N′-methylenebis(acrylamide)) crosslinked ditopic polymers

Post synthesis, the two polymers were washed with excess ethanol and used for small scale, batch uranium uptake. Each polymer was contacted with 6 ppm U spiked deionized water at a phase ratio of 1 mg: 1 mL solution for 24 hours. The results are shown in **Figure 2.9**.

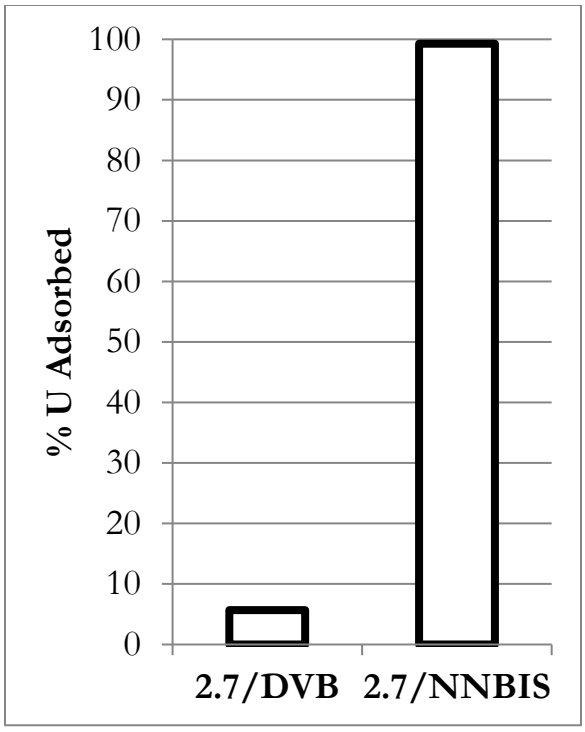

Figure 2.9 %Uranium uptake with divinylbenzene or N,N′-methylenebis(acrylamide) crosslinked bifunctional chelator functionalized polymer.

Polymer synthesized using divinylbenzene as crosslinker and divinyl functionalized **2.7** resulted in poor uranium uptake after 24 hours. The more hydrophilic polymer synthesized with monovinyl functionalized ditopic ligand resulted in nearly quantitative uranium uptake—crude evidence that polymer characteristics such as hydrophilicity, degree of crosslinking, and ligand accessibility play important roles in metal separations. This idea that favorable metal uptake results such as high capacity and selectivity can be achieved through a *holistic* approach to separations systems served as guiding principle in subsequent work.

2.7 Funding and Acknowledgements

This work was supported by the Department of Energy (DOE), Office of Nuclear Energy's Nuclear Energy University Program (Sub-Contract-20 120427 and Project 3151). MRCAT

operations are supported by the DOE and the MRCAT member institutions. This research used resources of the APS, a U.S. DOE, Office of Science User Facility, operated for the DOE, Office of Science, by ANL under Contract DE-AC02-06CH11357. We acknowledge the University of Chicago Research Computing Center, the Nuclear Magnetic Resonance Facility, and NSF instrumentation Grant CHE-1048528 in conjunction with the Mass Spectrometry Facility for support of this work.

2.8 References

(1) Kanno, M. Present Status of Study on Extraction of Uranium from Sea Water. *J. Nucl. Sci. Technol.* **1984**, *21* (1), 1–9.

(2) Vivero-Escoto, J. L.; Carboni, M.; Abney, C. W.; DeKrafft, K. E.; Lin, W. Organo-Functionalized Mesoporous Silicas for Efficient Uranium Extraction. *Microporous Mesoporous Mater.* **2013**, *180*, 22–31.

(3) Carboni, M.; Abney, C. W.; Taylor-Pashow, K. M. L.; Vivero-Escoto, J. L.; Lin, W. Uranium Sorption with Functionalized Mesoporous Carbon Materials. *Ind. Eng. Chem. Res.* **2013**, *52* (43), 15187–15197.

(4) Das, S.; Oyola, Y.; Mayes, R. T.; Janke, C. J.; Kuo, L.-J.; Gill, G.; Wood, J. R.; Dai, S. Extracting Uranium from Seawater: Promising AF Series Adsorbents. *Ind. Eng. Chem. Res.* **2016**, *55* (15), 4110–4117.

(5) Carboni, M.; Abney, C. W.; Liu, S.; Lin, W. Highly Porous and Stable Metal–organic Frameworks for Uranium Extraction. *Chem. Sci.* **2013**, *4* (6), 2396.

(6) Chen, L.; Bai, Z.; Zhu, L.; Zhang, L.; Cai, Y.; Li, Y.; Liu, W.; Wang, Y.; Chen, L.; Diwu, J.; et al. Ultrafast and Efficient Extraction of Uranium from Seawater Using an Amidoxime Appended Metal–Organic Framework. *ACS Appl. Mater. Interfaces.* **2017**, *9* (38), 32446–32451.

(7) Wang, L. L.; Luo, F.; Dang, L. L.; Li, J. Q.; Wu, X. L.; Liu, S. J.; Luo, M. B. Ultrafast High-Performance Extraction of Uranium from Seawater without Pretreatment Using an Acylamide- and Carboxyl-Functionalized Metal-Organic Framework. *J. Mater. Chem. A* **2015**, *3* (26), 13724–13730.

(8) Luo, B.-C.; Yuan, L.-Y.; Chai, Z.-F.; Shi, W.-Q.; Tang, Q. U(VI) Capture from Aqueous Solution by Highly Porous and Stable MOFs: UiO-66 and Its Amine Derivative. *J. Radioanal. Nucl. Chem.* **2016**, *307* (1), 269–276.

(9) Carboni, M.; Abney, C. W.; Liu, S.; Lin, W. Highly Porous and Stable Metal-Organic Frameworks for Uranium Extraction. *Chem. Sci.* **2013**, *4*, 2396–2402.

(10) Li, J.; Yang, X.; Bai, C.; Tian, Y.; Li, B.; Zhang, S.; Yang, X.; Ding, S.; Xia, C.; Tan, X.; et al. A Novel Benzimidazole-Functionalized 2-D COF Material: Synthesis and Application as a Selective Solid-Phase Extractant for Separation of Uranium. *J. Colloid Interface Sci.* **2015**, *437*, 211–218.

(11) Tian, G.; Geng, J.; Jin, Y.; Wang, C.; Li, S.; Chen, Z.; Wang, H.; Zhao, Y.; Li, S. Sorption of Uranium(VI) Using Oxime-Grafted Ordered Mesoporous Carbon CMK-5. *J. Hazard. Mater.* **2011**, *190* (1–3), 442–450.

(12) Górka, J.; Mayes, R. T.; Baggetto, L.; Veith, G. M.; Dai, S. Sonochemical Functionalization of Mesoporous Carbon for Uranium Extraction from Seawater. *J. Mater. Chem. A.* **2013**, *1*, 3016.

(13) Dolatyari, L.; Yaftian, M. R.; Rostamnia, S. Removal of Uranium(VI) Ions from Aqueous Solutions Using Schiff Base Functionalized SBA-15 Mesoporous Silica Materials. *J. Environ. Manage.* **2016**, *169*, 8–17.

(14) Yang, S.; Qian, J.; Kuang, L.; Hua, D. Ion-Imprinted Mesoporous Silica for Selective Removal of Uranium from Highly Acidic and Radioactive Effluent. *ACS Appl. Mater. Interfaces.* **2017**, *9* (34), 29337–29344.

(15) Huynh, J.; Palacio, R.; Safizadeh, F.; Levre, G.; Descostes, M.; Eloy, L.; Guignard, N.; Rousseau, J.; Royer, S.; Tertre, E.; et al. Adsorption of Uranium over NH 2 -Functionalized Ordered Silica in Aqueous Solutions. *ACS Appl. Mater. Interfaces* **2017**, *9* (18), 15672–15684.

(16) Wang, C. Z.; Lan, J. H.; Wu, Q. Y.; Luo, Q.; Zhao, Y. L.; Wang, X. K.; Chai, Z. F.; Shi, W. Q. Theoretical Insights on the Interaction of Uranium with Amidoxime and Carboxyl Groups. *Inorg. Chem.* **2014**, *53* (18), 9466–9476.

(17) Davies, R. V.; Kennedy, J.; McIlroy, R. W.; Spence, R.; Hill, K. M. Extraction of Uranium from Sea Water. *Nature* **1964**, *203* (4950), 1110–1115.

(18) Stewart, D. C.; Bentley, W. C. Analysis of Uranium in Sea Water. *Science.* **1954**, *120* (3106), 50–51.

(19) Shigetomi, Y.; Kojima, T.; Kamba, H. Extraction of Uranium (VI) from Sea Water Using Hydrous Metalic Oxide Binded with Hydrophilic Polymers. *Nippon Genshiryoku Gakkai-Shi* **1978**, *20* (11), 789–795.

(20) Kim, Y. S.; Zeitlin, H. Separation of Uranium from Seawater by Adsorbing Colloid Flotation. *Anal. Chem.* **1971**, *43* (11), 1390–1393.

(21) Kelmers, A. D. Status of Technology for the Recovery of Uranium from Seawater. *Sep. Sci. Technol.* **1981**, *16* (9), 1019–1035.

(22) Tabushi, I.; Kobuke, Y.; Nishiya, T. Macrocyclic Hexaketone as a Specific Host of Uranyl Ion. **1979**, *37*, 3515–3518.

(23) Tabushi, I.; Kobuke, Y.; Nishiya, T. Extraction of Uranium from Seawater by Polymer-Bound Macrocyclic Hexaketone. *Nature* **1979**, *280* (5724), 665–666.

(24) Burger, L. L. Uranium and Plutonium Extraction by Organophosphorus Compounds. *J. Phys. Chem.* **1958**, *62* (5), 590–593.

(25) Abney, C. W.; Mayes, R. T.; Saito, T.; Dai, S. Materials for the Recovery of Uranium from Seawater. *Chem. Rev.* **2017**, *117* (23), 13935–14013.

(26) Bauer, S. Seawater yields first grams of yellowcake https://www.pnnl.gov/news/release.aspx?id=4514 (accessed Jul 19, 2019).

(27) Schenk, H. J.; Astheimer, L.; Witte, E. G.; Schwochau, K. Development of Sorbers for the Recovery of Uranium from Seawater. 1. Assessment of Key Parameters and Screening Studies of Sorber Materials. *Sep. Sci. Technol.* **1982**, *17* (11), 1293–1308.

(28) Gill, G. A.; Kuo, L.-J.; Janke, C. J.; Park, J.; Jeters, R. T.; Bonheyo, G. T.; Pan, H.-B.; Wai, C.; Khangaonkar, T.; Bianucci, L.; et al. The Uranium from Seawater Program at the Pacific Northwest National Laboratory: Overview of Marine Testing, Adsorbent Characterization, Adsorbent Durability, Adsorbent Toxicity, and Deployment Studies. *Ind. Eng. Chem. Res.* **2016**, *55* (15), 4264–4277.

(29) Endrizzi, F.; Leggett, C. J.; Rao, L. Scientific Basis for Efficient Extraction of Uranium from Seawater. I: Understanding the Chemical Speciation of Uranium under Seawater Conditions. *Ind. Eng. Chem. Res.* **2016**, *55* (15), 4249–4256.

(30) Frisch, M. J.; Trucks, G. W.; Schlegel, H. B.; Scuseria, G. E.; Robb, M. a.; Cheeseman, J. R.; Montgomery, J. a.; Vreven, T.; Kudin, K. N.; Burant, J. C.; et al. Gaussian 09W Tutorial. an Introduction to Computational Chemistry Using G09W Avogadro Softwware. **2009**, 34.

(31) Lee, C.; Yang, W.; Parr, R. G. Development of the Colle-Salvetti Correlation-Energy Formula into a Functional of the Electron Density. *Phys. Rev. B* **1988**, *37* (2), 785–789.

(32) Becke, A. D. Density-functional Thermochemistry. III. The Role of Exact Exchange. *J. Chem. Phys.* **1993**, *98* (7), 5648–5652.

(33) McLean, A. D.; Chandler, G. S. Contracted Gaussian Basis Sets for Molecular Calculations. I. Second Row Atoms, *Z* =11–18. *J. Chem. Phys.* **1980**, *72* (10), 5639–5648.

(34) Krishnan, R.; Binkley, J. S.; Seeger, R.; Pople, J. a. Self-Consistent Molecular Orbital Methods. XX. A Basis Set for Correlated Wave Functions. *J. Chem. Phys.* **1980**, *72* (1), 650–654.

(35) Dolg, M.; Stoll, H.; Preuss, H.; Pitzer, R. M. Relativistic and Correlation-Effects for Element 105 (Hahnium, Ha) a Comparative-Study of M and Mo (M = Nb, Ta, Ha) Using Energy-Adjusted Abinitio Pseudopotentials. *J. Phys. Chem.* **1993**, *97* (22), 5852–5859.

(36) Cossi, M.; Rega, N.; Scalmani, G.; Barone, V. Energies, Structures, and Electronic Properties of Molecules in Solution with the C-PCM Solvation Model. *J. Comput. Chem.* **2003**, *24* (6), 669–681.

(37) Kropf, A. J.; Katsoudas, J.; Chattopadhyay, S.; Shibata, T.; Lang, E. A.; Zyryanov, V. N.; Ravel, B.; McIvor, K.; Kemner, K. M.; Scheckel, K. G.; et al. The New MRCAT (Sector 10) Bending Magnet Beamline at the Advanced Photon Source. *AIP Conf. Proc.* **2010**, *1234*, 299–302.

(38) Rehr, J. J.; Albers, R. C. Theoretical Approaches to the X-Ray Absorption Fine Structure. *Rev. Mod. Phys.* **2000**, *72*, 621.

(39) Ravel, B.; Newville, M. Athena, Artemis, Hephaestus: Data Analysis for X-Ray Absorption Spectroscopy Using IFEFFIT. *J. Synchrotron Radiat.* **2005**, *12* (4), 537–541.

(40) Theil, F. Synthesis of Diaryl Ethers: A Long-Standing Problem Has Been Solved. *Angew. Chemie Int. Ed.* **1999**, *38* (16), 2345–2347.

(41) Sergeev, A. G.; Hartwig, J. F. Selective, Nickel-Catalyzed Hydrogenolysis of Aryl Ethers. *Science.* **2011**, *332* (6028), 439–443.

(42) Buehl, M.; Diss, R.; Wipff, G.; Bühl, M.; Buhl, M. Coordination Environment of Aqueous Uranyl (VI) Ion. *J. Am. Chem. Soc* **2005**, *127* (39), 13506–13507.

(43) Vukovic, S.; Watson, L. A.; Kang, S. O.; Custelcean, R.; Hay, B. P. How Amidoximate Binds the Uranyl Cation. *Inorg. Chem.* **2012**, *51* (6), 3855–3859.

(44) Kelley, S. P.; Barber, P. S.; Mullins, P. H. K.; Rogers, R. D. Structural Clues to UO_2^{2+} /VO_2^{+} Competition in Seawater Extraction Using Amidoxime- Based Extractants. **2014**, *2*, 1–22.

(45) Barber, P. S.; Kelley, S. P.; Rogers, R. D. Highly Selective Extraction of the Uranyl Ion with Hydrophobic Amidoxime-Functionalized Ionic Liquids via H_2 Coordination. *RSC Adv.* **2012**, *2* (22), 8526.

(46) Lashley, M. A.; Ivanov, A. S.; Bryantsev, V. S.; Dai, S.; Hancock, R. D. Highly Preorganized Ligand 1,10-Phenanthroline-2,9-Dicarboxylic Acid for the Selective Recovery of Uranium from Seawater in the Presence of Competing Vanadium Species. *Inorg. Chem.* **2016**, *55* (20), 10818–10829.

(47) Tian, G.; Teat, S. J.; Zhang, Z.; Rao, L. Sequestering Uranium from Seawater: Binding Strength and Modes of Uranyl Complexes with Glutarimidedioxime. *Dalt. Trans.* **2012**, *41* (38), 11579.

(48) Kang, S. O.; Vukovic, S.; Custelcean, R.; Hay, B. P. Cyclic Imide Dioximes: Formation and Hydrolytic Stability. *Ind. Eng. Chem. Res.* **2012**, *51* (19), 6619–6624.

(49) Abney, C. W.; Mayes, R. T.; Piechowicz, M.; Lin, Z.; Bryantsev, V. S.; Veith, G. M.; Dai, S.; Lin, W. XAFS Investigation of Polyamidoxime-Bound Uranyl Contests the Paradigm from Small Molecule Studies. *Energy Environ. Sci.* **2016**, *9* (2), 448–453.

(50) Zhou, X.; Huang, W.; Miao, J.; Xia, Q.; Zhang, Z.; Wang, H.; Li, Z. Enhanced Separation Performance of a Novel Composite Material GrO@MIL-101 for CO_2/CH_4 Binary Mixture. *Chem. Eng. J.* **2015**, *266*, 339–344.

(51) Carboni, M.; Abney, C. W.; Taylor-Pashow, K. M. L.; Vivero-Escoto, J. L.; Lin, W. Uranium Sorption with Functionalized Mesoporous Carbon Materials. *Ind. Eng. Chem. Res.* **2013**, *52* (43), 15187–15197.

(52) Silver, M. A.; Dorfner, W. L.; Cary, S. K.; Cross, J. N.; Lin, J.; Schelter, E. J.; Albrecht-Schmitt, T. E. Why Is Uranyl Formohydroxamate Red? *Inorg. Chem.* **2015**, *54* (11), 5280–5284.

(53) Witte, E. G.; Schwochau, K. S.; Henkel, G.; Krebs, B. Uranyl Complexes of Acetamidoxime and Benzamidoxime. Preparation, Characterization, and Crystal Structure. *Inorganica Chim. Acta* **1984**, *94* (6), 323–331.

(54) Endrizzi, F.; Rao, L. Chemical Speciation of Uranium(VI) in Marine Environments: Complexation of Calcium and Magnesium Ions with $[(UO_2)(CO_3)_3]^{4-}$ and the Effect on the Extraction of Uranium from Seawater. *Chem. - A Eur. J.* **2014**, *20* (44), 14499–14506.

(55) Haji, Maha N., Vitry, Charles, Slocum, A. H. Decoupling the Functional Requirements of an Adsorbent for Harvesting Uranium from Seawater through the Use of Shell Enclosures. *Proc. 2015 ANS Winter Meet. Nucl. Technol. Expo Washington* (November 8-12, 2015).

2.9 Appendix 2.1: Crystal Structure Specifics for Ditopic –COOH/-AO Molecule (2.7)

(Z)-2-(2-(N'-hydroxycarbamimidoyl)phenoxy) benzoic acid

Name	Bifunctional Chelator, **(2.7)**
Formula	$C_{14}H_{12}N_2O_4$
Fw	272.26
Temperature (K)	296(2)
Wavelength (Å)	0.41328
Crystal system	orthorhombic
Space group	$Pna2_1$
a, Å	10.2721(15)
b, Å	12.9900(19)
c, Å	9.3830(14)
α, °	90
β, °	90
γ, °	90
V, Å^3	1252.0(3)
Z	4
Density (calcd. g/cm^3)	1.444
F(000)	568
θ range data collection	1.470 – 18.419
Limiting indices	$-15 \leq h \leq 15$ $-19 \leq k \leq 13$ $-14 \leq l \leq 14$
Reflection collected	4369
R(int)	0.0602
Data/restraints/parameters	4369/1/186
Goodness-of-fit on F^2	1.015
Final R indices [I>4σ(I)]	R1 = 0.0602, wR2 = 0.1437
R indices (all data)	R1 = 0.1045, wR2 = 0.1437
CCDC Identifier	No. 1421017

2.10 Appendix 2.2: Cartesian Coordinates for DFT Calculated Uranyl/Ligand Structures

C	3.778708	2.429868	1.714528
C	3.291209	1.221807	1.220262
C	2.358969	1.223385	0.180772
C	1.886676	2.420402	-0.36773
C	2.376346	3.622582	0.156132
C	3.321017	3.635915	1.181623
H	4.505278	2.425762	2.520568
H	3.629191	0.279421	1.637366
H	2.014951	4.561342	-0.25365
H	3.694017	4.580296	1.564582
O	1.790798	0.043265	-0.27575
C	2.601656	-1.05067	-0.5277
C	3.790133	-0.87024	-1.2375
C	2.193879	-2.3335	-0.09754
C	4.625056	-1.94834	-1.51709
H	4.060995	0.129153	-1.55971
C	3.073499	-3.3999	-0.38288
C	4.26478	-3.22226	-1.07781
H	5.544825	-1.79053	-2.07058
H	2.791896	-4.39357	-0.05427
H	4.903599	-4.07554	-1.28181
C	0.871893	2.429969	-1.51135
O	1.321909	2.185245	-2.65936
O	-0.31536	2.706529	-1.20289
C	0.954704	-2.62005	0.649409
N	0.979758	-3.70683	1.554026
H	1.784807	-3.71314	2.169418
H	0.106789	-3.6767	2.077871
N	-0.16507	-2.00349	0.390728
O	-1.23081	-2.42377	1.11318

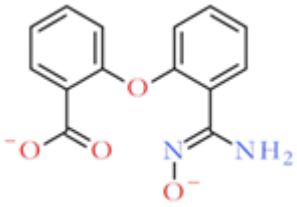

C	4.079292	-1.95124	-1.98163
C	3.523717	-0.85032	-1.33285
C	2.724503	-1.039	-0.20345
C	2.454445	-2.32295	0.296655
C	3.028897	-3.40764	-0.37609
C	3.833268	-3.23757	-1.50227
H	4.699271	-1.79968	-2.85942
H	3.708966	0.153175	-1.69902
H	2.841677	-4.40939	0.000747
H	4.265797	-4.10043	-1.99815
O	2.104944	0.025037	0.429501
C	2.774014	1.23484	0.542826
C	4.048585	1.244245	1.111307
C	2.147233	2.430334	0.128282
C	4.756207	2.433737	1.257073
H	4.486449	0.303164	1.426581
C	2.900916	3.615655	0.273791
C	4.176926	3.627424	0.825492
H	5.74609	2.424521	1.701088
H	2.450565	4.547868	-0.04684
H	4.712652	4.565896	0.926009
C	0.801617	2.516234	-0.46845
N	0.568742	3.557024	-1.39734
H	1.285222	3.643129	-2.1088
H	-0.34807	3.389627	-1.80785
N	-0.18247	1.766795	-0.05492
O	-1.37443	2.004605	-0.65046
C	1.583762	-2.52611	1.506505
H	1.765348	-1.74332	2.246421
H	1.850836	-3.47177	1.990284
C	0.041573	-2.57994	1.265051
O	-0.65717	-2.58188	2.314497
O	-0.38132	-2.64058	0.084208

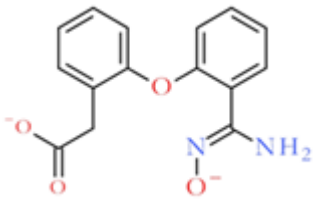

C	-4.60691	2.8766	-0.97912
C	-4.09265	1.582311	-0.96396
C	-2.82799	1.346934	-0.42361
C	-2.04786	2.386458	0.088416
C	-2.57667	3.683072	0.047314
C	-3.8465	3.931315	-0.47039
H	-5.59151	3.059814	-1.39653
H	-4.66446	0.754513	-1.3698
H	-1.9829	4.506576	0.433039
H	-4.23871	4.94307	-0.48279
O	-2.26843	0.073773	-0.47982
C	-2.92113	-0.99664	0.10163
C	-3.74118	-0.83793	1.220437
C	-2.68279	-2.26487	-0.45417
C	-4.34787	-1.94993	1.801281
H	-3.90311	0.151144	1.632596
C	-3.31233	-3.35943	0.148028
C	-4.13638	-3.21824	1.26433
H	-4.98292	-1.81895	2.671443
H	-3.15856	-4.3467	-0.27893
H	-4.61057	-4.08882	1.705088
C	-0.66126	2.133813	0.68192
O	-0.63102	1.664519	1.847233
O	0.319032	2.442968	-0.04146
C	-1.79064	-2.45402	-1.66796
H	-1.94825	-1.64685	-2.38599
H	-2.10012	-3.38584	-2.16161
C	-0.3078	-2.51239	-1.38749
N	0.153317	-3.40207	-0.40268
H	1.15517	-3.52817	-0.53411
H	-0.34471	-4.28273	-0.35675
N	0.506886	-1.75259	-2.04732
O	1.836896	-1.93904	-1.76472

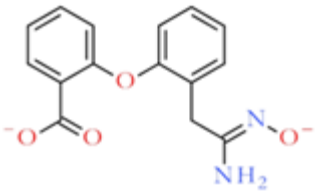

	-4.15834	0.47378	-0.09292
C	-3.63075	-0.78507	0.163284
C	-2.48943	-1.24713	-0.47641
C	-4.36115	-1.60341	1.029499
C	-2.02125	-2.55617	-0.2453
H	-1.94969	-0.60717	-1.16204
C	-3.91348	-2.90334	1.248951
H	-5.2558	-1.22034	1.507353
C	-2.75863	-3.37908	0.628418
H	-4.46634	-3.55185	1.921474
H	-2.41911	-4.38616	0.839983
C	-3.32414	1.572947	-0.23395
C	-3.67253	2.50813	-1.20713
C	-2.23588	1.793147	0.608247
C	-2.91553	3.673033	-1.33084
H	-4.52525	2.318394	-1.84997
C	-1.47298	2.958019	0.481513
H	-1.96966	1.070497	1.369173
C	-1.82197	3.897555	-0.49616
H	-3.18208	4.404305	-2.08752
H	-1.23029	4.799913	-0.59081
C	-0.27811	3.199108	1.415029
O	0.345192	4.283599	1.268286
O	-0.01887	2.293838	2.251382
C	-0.81283	-3.05216	-0.91571
N	0.007304	-2.21467	-1.49262
N	-0.50696	-4.42798	-0.8523
H	0.259342	-4.5909	-1.50347
H	-1.29077	-5.03855	-1.05198
O	1.085553	-2.76783	-2.0805

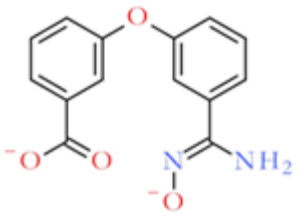

O	3.126726	-0.13359	-1.19586
C	2.896686	0.99944	-0.43279
C	2.193559	2.031857	-1.04697
C	3.407132	1.150699	0.858587
C	1.981029	3.243417	-0.38067
H	1.807911	1.883219	-2.05058
C	3.190176	2.353777	1.525456
H	3.961362	0.347847	1.330009
C	2.484485	3.39251	0.915289
H	3.581368	2.48291	2.529665
H	2.326876	4.323993	1.450454
C	3.153438	-1.39021	-0.60558
C	4.131458	-2.27688	-1.05188
C	2.198552	-1.79034	0.326535
C	4.146676	-3.57778	-0.54905
H	4.861404	-1.94516	-1.78221
C	2.21787	-3.09173	0.837501
H	1.432556	-1.10391	0.66487
C	3.201177	-3.98302	0.391651
H	4.905726	-4.27346	-0.89271
H	3.212695	-4.99096	0.788018
C	1.164123	-3.52884	1.865292
O	1.235178	-4.71601	2.279357
O	0.315647	-2.66424	2.209693
C	1.232587	4.374439	-1.07137
H	1.799939	4.706872	-1.94621
C	-0.14925	4.023112	-1.55182
N	-0.41771	4.028722	-2.81974
N	-1.10546	3.641192	-0.59581
H	-1.06969	4.166738	0.2693
H	-2.02481	3.673772	-1.03123
O	-1.70874	3.707771	-3.14482
H	1.186602	5.229374	-0.38387

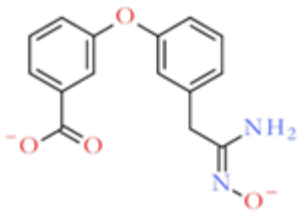

O	-3.19601	0.263979	-1.29734
C	-3.15414	1.532471	-0.74117
C	-2.12607	1.944825	0.10287
C	-4.15556	2.420373	-1.13633
C	-2.09012	3.260354	0.579743
H	-1.34456	1.24894	0.388408
C	-4.11627	3.731328	-0.67005
H	-4.94234	2.078556	-1.79964
C	-3.09482	4.149217	0.185152
H	-4.88952	4.430205	-0.9727
H	-3.07904	5.173056	0.546234
C	-2.84502	-0.85504	-0.55685
C	-3.19936	-1.00881	0.78332
C	-2.19638	-1.87736	-1.24608
C	-2.88217	-2.20673	1.422933
H	-3.7168	-0.21733	1.312365
C	-1.87973	-3.08196	-0.60895
H	-1.94535	-1.72357	-2.29111
C	-2.23314	-3.23318	0.73816
H	-3.15773	-2.34119	2.464224
H	-2.00174	-4.16084	1.253018
C	-1.1732	-4.18034	-1.35969
C	-0.97726	3.697335	1.522536
H	-1.04922	3.134197	2.458212
C	0.417079	3.497	0.994341
N	1.20957	2.640524	1.558357
N	0.800909	4.213989	-0.1516
H	0.466033	5.169415	-0.18276
H	1.81323	4.15519	-0.24094
O	2.457142	2.545998	1.002024
C	0.389735	-4.16114	-1.34258
O	0.97717	-3.2994	-0.64411
O	0.93069	-5.05184	-2.05179
H	-1.47414	-5.15647	-0.96529
H	-1.47741	-4.17633	-2.41073
H	-1.1355	4.753076	1.77898

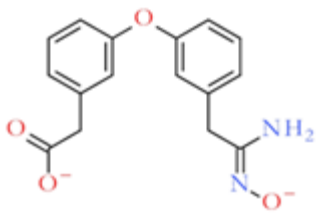

Chapter 3: Ditopic Ligand Functionalized Polymer Adsorbents for Uranium Sequestration

Adapted with permission from Piechowicz, Marek, Carter W. Abney, Nathan C. Thacker, James C. Gilhula, Youfu Wang, Samuel S. Veroneau, Aiguo Hu, and Wenbin Lin. *ACS applied materials & interfaces*, **2017**, 9, *33*, 27894-27904.

3.1 Introduction

As discussed in the previous chapter, density functional theory (DFT) was used as a screening tool to rapidly examine potential uranophiles for incorporation into robust polymer adsorbents. Bifunctional ligands were considered exclusively owing to the potential for cooperative binding between adjacent moieties. **Table 2.4** showcases the free energy of complexation between selected ditopic diaryl ethers and uranium. The bis-amidoxime functionalized ligand contained therein was found to have the most favorable interaction with uranyl—ΔG=-284.4 kcal mol^{-1}—much improved over ligand **2.7** (-68.4 kcal mol^{-1}) and the tridentate amidoxime analogue glutarimidedioxime (-221.7 kcal mol^{-1}), previously regarded as the main contributor to U binding in seawater contacted AO functionalized polymer fibers.

The bis-amidoxime ligand (**3.2, Scheme 3.1**) was chosen as next system to study owing to its *in silico* calculated favorable U binding and ease of incorporation as a comonomer into a polymeric framework.[1]

3.2 Theoretical Methods

Calculations were performed using the Gaussian 09c01 software package[2] with density functional theory (DFT) at the B3LYP level of theory.[3,4] Light atoms were modeled with the 6-311+G* basis set while U and V were modeled by the Stuttgart RSC 1997 relativistic effective core potential and 6-311+G** basis sets respectively. Solvation with water was modeled implicitly using the polarizable conductor calculation model (CPCM).[5] All structures were computed

separately and values combined in order to satisfy **Equations 2.1** and **2.2**. Structures were first geometrically optimized, and then subjected to frequency calculations and natural bond orbital (NBO) analysis with the same basis set and at the same level of theory. Gibbs free energy values (ΔG) were calculated using zero-point energy (ZPE) and thermal corrections.

3.3 Experimental Methods

3.3.1 General Experimental

2-(2-methylphenoxy)aniline was purchased from TCI and was used as received. Methanol was purchased from Fischer Scientific and dried under activated 3 Å molecular sieves for 48 hours prior to use. Acetone, sodium nitrite, potassium iodide, chloroform, pyridine, sodium bicarbonate, ammonium bromide, and tetrahydrofuran were purchased from Fischer Scientific and used as received. Potassium permanganate and L-proline were purchased from Sigma Aldrich and used as received. Aqueous hydroxylamine solution was purchased from Alfa Aesar and used as received. Uranyl nitrate and 37% w/w $KF \cdot Al_2O_3$ catalyst were prepared according to literature procedures.[6,7] All other chemicals of reagent-grade quality not listed here were obtained from commercial sources and used as received.

Raman data were collected using a Horiba LabRamHR EvolutionNMR confocal raman instrument. Raman data were collected on ground solid samples with a Horiba LabRamHR Evolution instrument using a 633 nm laser with 0.75 second capture time. Resulting spectra were background corrected prior to analysis. NMR spectra were acquired on a Bruker NMR 500 DRX spectrometer at 500 MHz. Chemical shifts were determined via reference to solvent resonance ($CDCl_3$, δ 7.26 ppm; DMSO, δ 2.50 ppm). Liquid chromatography–mass spectrometry was performed using an Agilent 6130 LC-MS instrument in positive mode. Gas chromatography–mass

spectrometry was performed using a Shimadzu GCMS-QP2010SE instrument. Single crystal X-ray diffraction data of the bis-amidoxime ligand **(3.2)** were collected with a Bruker APEX II CCD-based detector at ChemMatCARS (Sector 15), Advanced Photon Source (APS), Argonne National Laboratory (ANL). ICP-MS was carried out with an Agilent 7700x ICP-MS instrument. Samples were diluted in a 2% HNO_3 matrix and analyzed with a ^{207}Bi internal standard against a nine-point standard curve over the range from 1 ppb to 500 ppb. The correlation coefficient over all trials was >0.9997.

General crystallographic data for **3.2** are listed in **3.12 Appendix 3.1**. Diffraction maxima were consistent with the triclinic space group *P*-1, as determined via XPREP. The resulting 9911 reflections were used in the least squares refinement. The structure was solved using direct methods made accessible by the SHELXTL software package. The correct positions for the nitrogen and oxygen atoms were deduced from the electron-density map. Subsequent least-squares refinement cycles (SHELXL) revealed the positions of the remaining non-hydrogen atoms of the benzene rings. Non-hydrogen atoms were refined with independent anisotropic displacement parameters. Hydrogen atoms were placed geometrically in ideal positions and refined independently. Successful convergence was indicated by the maximum shift/error of -0.001 for the last cycle of least squares refinement. The largest peak in the residual electron density map was located 3.4 Å away from the carbon-carbon double bond in the phenyl ring.

3.3.2. Ligand Design, Synthesis, and Characterization

The domain of functionalized diaryl ligands considered in this chapter is shown in **Scheme 3.1.** During a systematic computational investigation of uranyl/oxygen donor ligand equilibrium constants, Bryantsev and co-workers[8] discovered dibenzofuran bis-amidoxime (**3.10**) to possess

one of the highest reported binding affinities for uranyl. Geometry optimization calculations showed the **3.10**/UO_2^{2+} complex to possess the most energetically favorable bis η^2 binding motif. It was suggested that the furan linkage imparted necessary rigidity to lock the amidoxime moieties in a planar configuration, binding uranyl in the equatorial plane. Relative to **3.10**, the proposed bis-amidoxime ligand **(3.2)** has an additional rotational degree of freedom along the –COC– bridge potentially allowing for a greater degree of ligand-metal orbital overlap resulting in stronger binding. Moreover, owing to the smaller ionic radius of vanadium cations, it was hypothesized that uranyl would only be able to be bound in the strong bis η^2 fashion by the bis-amidoxime functional group.

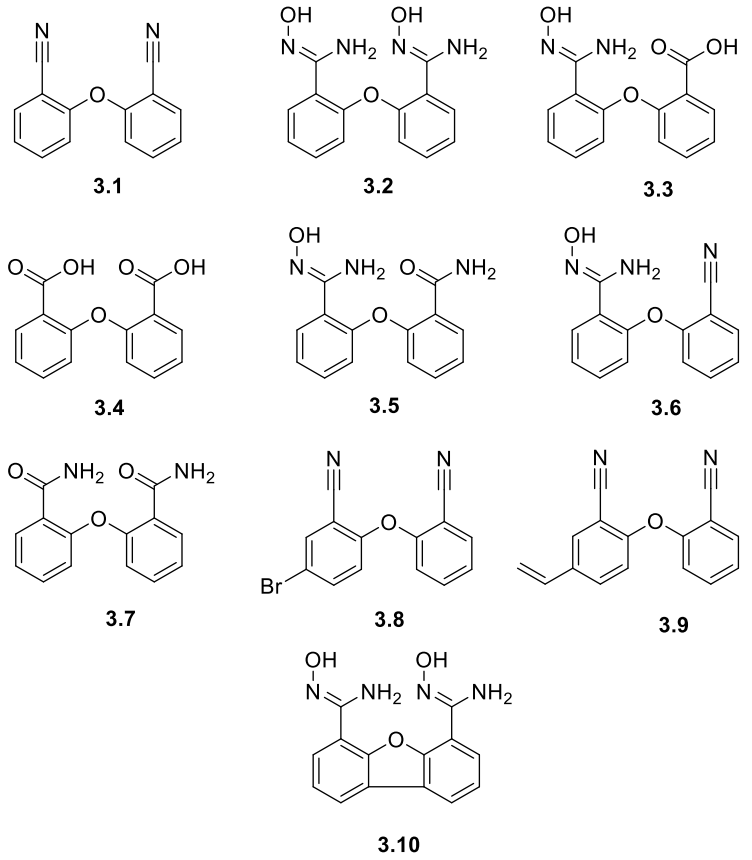

Scheme 3.1 The domain of functionalized diaryl ethers considered in this chapter

Reactions involving organic solvents were conducted using standard Schlenk line techniques under an inert atmosphere of N_2 unless otherwise specified. All glassware was kept in an oven set to 110 °C and cooled under vacuum prior to use. The bis-amidoxime (bis-AO) functionalized ligand **(3.2)** was synthesized according to **Scheme 3.2.**

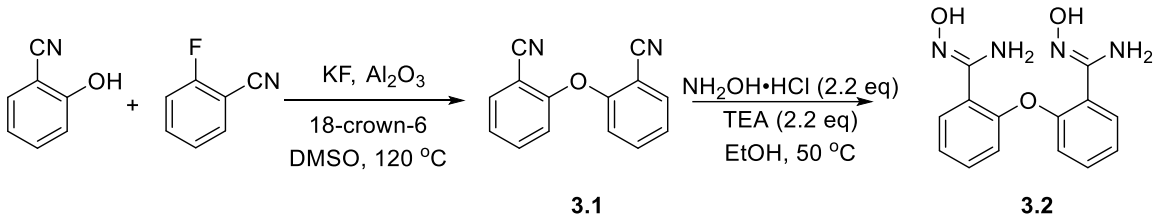

Scheme 3.2 The synthesis of bis-amidoxime functionalized diaryl ether (**3.2**)

In general, commercially available substituted aryl-nitriles were combined with KF on alumina catalyst in DMSO and heated to 120 ºC. Filtration and recrystallization from dichloromethane:hexanes resulted in the bis-cyano intermediate **(3.1)** as a white crystalline solid. Treatment with two equivalents of hydroxylamine hydrochloride under basic conditions results in the bis-AO functionalized diaryl ether ligand **(3.2)**.

3.3.2.1 Synthesis of 2-(2-cyanophenoxy)benzonitrile (3.1)

A 50 mL two-neck round bottom flask equipped with a stir bar was charged with cyanophenol (2.0 g, 18 mM) and 37% w/w $KF{\cdot}Al_2O_3$ (3.8 g, 24 mM). The apparatus was placed under vacuum and flushed with nitrogen once before the addition of 18-crown-6 (430 mg, 0.54 mM) and 2-fluorobenzonitrile (2.0 g, 16 mM). Dry DMSO (25 mL) was then added and the apparatus was quickly evacuated and backfilled with nitrogen before being placed in an oil bath at 120 °C for 36 hours. The resulting mixture was cooled to room temperature, diluted with diethyl ether, and filtered through a Buchner funnel. The filtrate was extracted with diethyl ether (3x 25

mL) and washed with brine (2x 25 mL). The resulting solution was dried over Na_2SO_4 and concentrated under vacuum to afford a tan solid. This solution was purified by flushing ethyl acetate though a silica gel plug and recrystallization from dichloromethane:hexanes (4:1) to afford a white solid. Yield (1.5 g, 41%) ^{1}H NMR (500 MHz, DMSO): δ 7.74 (d, 2H, *J* = 7.8 *Hz*), 7.59 (t, 2H, *J* = 7.7 *Hz*), 7.29(t, 2H, *J* = 7.6 *Hz*), 6.97 (d, 2H, *J* = 8.3 *Hz*) ^{13}C NMR (125 MHz, DMSO): δ 156.83, 135.75, 134.59, 125.45, 118.94, 115.30, 103.75. LR-MS (EI) calculated for $C_{14}H_8N_2O$: 220.0 *m/z*; found: 220.0 *m/z*.

3.3.2.2 Synthesis of N'-hydroxy-2-[2-[(Z)-N'-hydroxycarbamimidoyl]phenoxy]benz-amidine(3.2)

A 50 mL round bottom flask equipped with a stir bar and reflux condenser was charged with **3.1** (100 mg, 0.35 mM). Ethanol (5 mL) was added and the reaction was heated to 50 °C. Triethylamine (2.2 eq, 140 µL) was added followed by NH_2OH HCl (2.1 eq, 166.3 mg). The mixture was allowed to heat under N_2 overnight. Afterwards, the solution was cooled to room temperature before being concentrated under vacuum. Water (10 mL) and DCM (5 mL) were added and the aqueous layer was extracted 3x with DCM. The combined organics were evaporated *in vacuo* and the crude product was purified by flash column chromatography in silica gel (2% MeOH, 98% DCM to 10% MeOH 90% DCM). The resulting product was concentrated under vacuum then added benzene and concentrated again in order to azeotropically remove methanol. Yield (48 mg, 39%) ^{1}H NMR (500 MHz, DMSO): δ 9.51 (s, 2H), 7.56 (d, 2H, *J* = 7.5 *Hz*), 7.34 (t, 2H, *J* = 7.5 *Hz*), 7.15 (t, 2H, *J* = 7.5 *Hz*), 6.83 (d, 2H, *J* = 8.0 *Hz*), 5.82 (s, 4H), ^{13}C NMR (125 MHz, $CDCl_3$): δ 154.04, 150.41, 130.75, 130.55, 125.51, 123.86, 119.02. LC-MS (ES-API) calculated for $C_{14}H_{14}N_4O_3$: 286.1 *m/z*; found: 287.1 *m/z*.

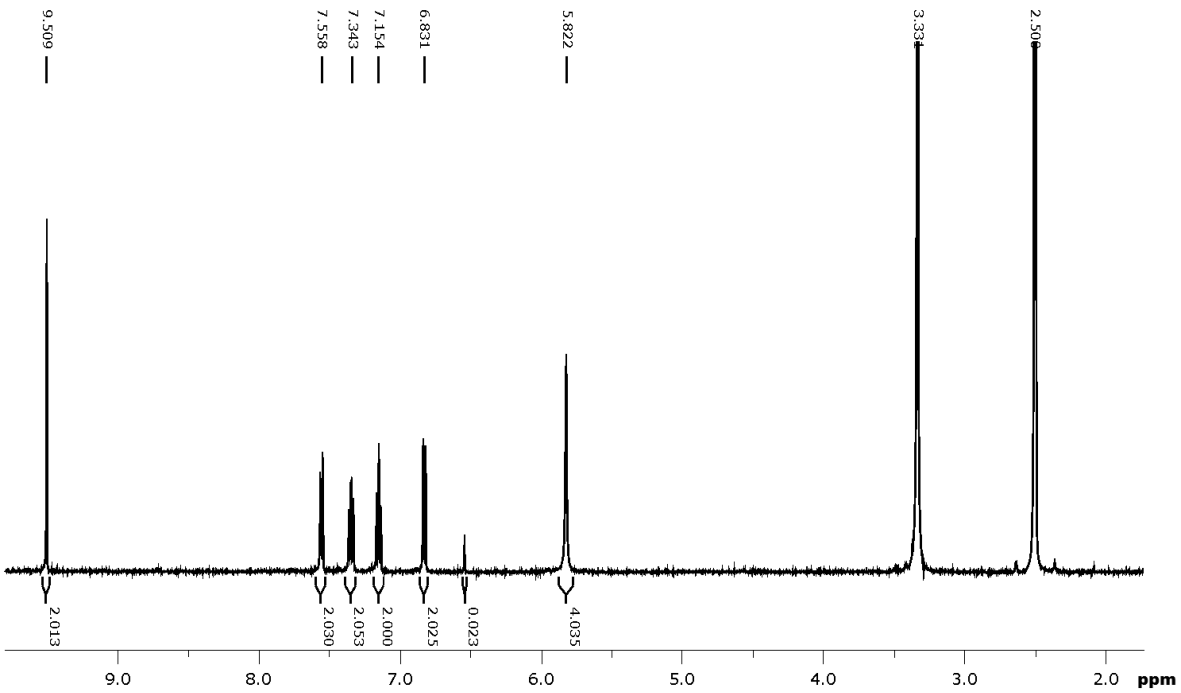

Figure 3.1 ^{1}H NMR spectrum of molecule **3.2.**

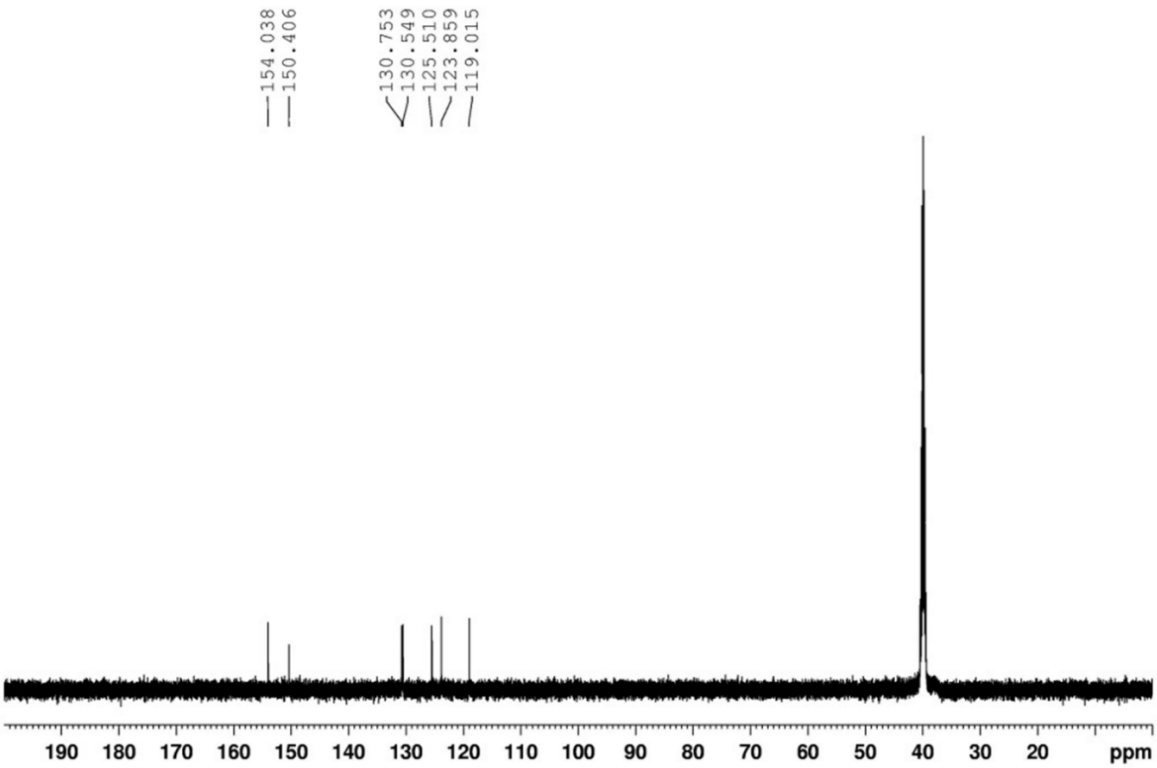

Figure 3.2 ^{13}C NMR spectrum of molecule **3.2.**

3.4 *in Silico* Studies of Small Molecule Analogs

DFT calculations were performed on several uranyl (UO_2^{2+}) and vanadyl (VO^{2+}) ligand complexes in order to explore the potential binding motifs of the most synthetically accessible ligands **3.2**, **3.3**, and **3.4**. Optimized structures of bifunctional diaryl ether uranium and vanadium complexes are shown in **Figure 3.3**. It was found that UO_2^{2+} is bound by **3.2** in a bis-η^2 fashion with average U-N and U-O bond lengths of 2.42 and 2.34 Å (**Figure 3.3A**). The bis-amidoxime functionalized ligand **3.2** cannot accommodate this same motif for VO^{2+} and VO_2^{+} (**Figures 3.3B** and **3.3C**). In both cases, the binding was calculated to be η^2 to one amidoxime and monodentate to the nitrogen or oxygen of the other. The vanadium species are therefore too small to be strongly bound despite the rotational degree of freedom inherent in the diaryl ether framework. Dihedral and –COC- angles of the DFT optimized structures are particularly illustrative and are shown in **Table 3.1**.

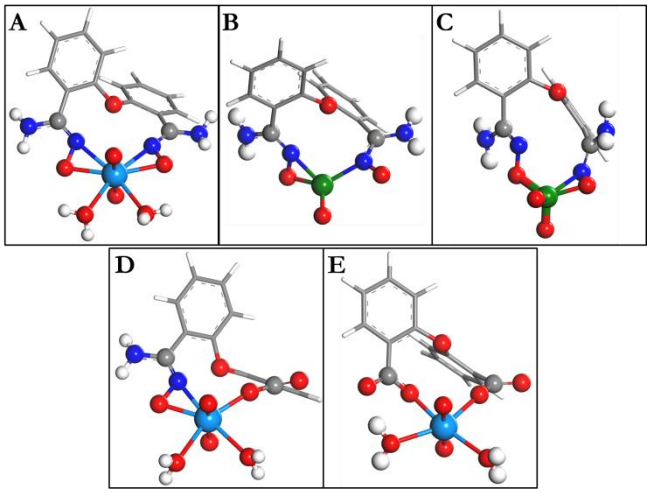

Figure 3.3 DFT optimized uranium and vanadium complexes investigated in this work. A: **3.2** + UO_2^{2+}. B: **3.2** + VO^{2+}. C: **3.2**+ VO_2^{+}. D: **3.3**+ UO_2^{2+}. E: **3.4**+ UO_2^{2+}. Red, white, gray, dark blue, light blue, and green spheres represent O, H, C, N, U, and V respectively.

Table 3.1 Dihedral and –COC– Angles of Various Functionalized Diaryl Ethers

Diaryl Ether Species	Dihedral Angle (°)	-COC- (°)
Bis-AO/UO_2^{2+} (**A**)	70.1°	121.2°
Bis-AO/VO^{2+} (**B**)	101.3°	120.8°
Bis-AO/VO_2^{+} (**C**)	77.0°	119.2°
AO/RCO_2^{-} UO_2^{2+} (**D**)	82.4°	121.0°
Bis-RCO_2^{-}/UO_2^{2+} (**E**)	77.2°	120.4°
Bis-AO crystal structure **(3.2)**	16.3°	123.8°

The bis-amidoxime small molecule **3.2** has an aryl-aryl dihedral angle of 16.3° with a –COC– angle of 123.8° as measured from its crystal structure (**Appendix 3.1**). The geometrically optimized complex with uranyl exhibits a much larger dihedral angle of 70.1° owing to the accommodation of the large uranyl cation. The diaryl ether bridge contracts to 121.2° upon U binding. The DFT optimized **3.2**/UO_2^{2+} complex exhibits the smallest dihedral angle distortion relative to the other U and V complexes studied. This smallest deviation from the crystal structure provides some insight into the mechanism of U/V selectivity.

Natural bond orbital (NBO) analysis quantitatively corroborates the observed trend in U affinity provided by thermodynamic calculations on geometrically optimized structures. Wiberg bond indices (WBIs) were calculated as part of NBO analysis on optimized uranium and vanadium complexes. The resulting indices are listed in **Table 3.2** and represent the degree to which there is a bonding interaction between two atoms. Values fall between 0.0 (nonbonding) and positive integers depending on bond order (e.g. 1.0 suggesting bond order of 1). The bis-amidoxime/U complex **A** exhibits the highest total bond index relative to the other species studied. U was found to exhibit a stronger interaction with both amidoxime oxygens as compared with the amidoxime nitrogens (0.67 vs. 0.49) likely due to both the closer proximity of the oxygen atoms and their similarity in absolute hardness with U. Both vanadium complexes showed total WBIs closer to

half that found in **A**. Interestingly, V-O bond indices were comparable to those found in the bis-AO case but the V-N WBIs were much smaller in magnitude. This is likely due to a geometric mismatch between the large ligand binding pocket and relatively small vanadium species. The AO/RCO_2^- (**D**) and Bis-RCO_2^- (**E**) systems both exhibit weaker U binding as evidenced by lower total WBIs. NBO analysis on the U chelated ligand **3.10** studied by Bryantsev and coworkers[8] yielded Wiberg bond indices comparable to but smaller than the Bis-AO/ UO_2^{2+} complex **A** discussed above (**Table 3.2**). The favorable U bonding exhibited by **A** suggests that rotational flexibility of the host makes a substantial positive contribution to guest affinity. In all cases, the U –bridging oxygen interaction is negligible with WBIs <0.01.

The HOMO of each complex and the DFT calculated NBO charge distributions are shown in Figures **3.4-3.6**. In the bis-amidoxime uranyl complex, uranium bears a small positive charge of 1.232. This result compares favorably to the value of 1.262 found for **3.10**, suggesting a large degree of electron donation from the amidoxime groups to the uranium center. The mono carboxylate/mono amidoxime **(2.7)** uranyl analog **D** reported previously[9] yields a uranium center with a charge of 1.406. The bis-carboxylate uranyl analog **E** showed even less ligand contribution, affording the most electropositive uranium value of 1.772.

These charge distributions are consistent with thermochemical bond strength calculations performed on the uranyl complexes (**Figure 3.7**). As expected, the bis-amidoxime complex **A** exhibits the most negative Gibbs free energy of -279.09 kcal mol^{-1} compared with -68.44 kcal mol^{-1} for the mono-carboxylate/amidoxime complex **D** and -51.26 kcal mol^{-1} for the bis-carboxylate species **E**. These results compare favorably with **3.10**/UO_2^{2+} which was calculated to have a Gibbs free energy of -85.08 kcal mol^{-1}. While such calculations are known to overestimate actual bond strength in uranyl complexes, a linear free energy relationship has been demonstrated in the

literature[8] and has been successfully used for the rational design and computational screening of engineered uranyl chelating ligands.[10–13]

Table 3.2. Selected Wiberg Bond Indices of U and V Complexes

Species	Moiety	Bond	WBI	Average
Bis-AO/UO_2^{2+} (**A**)	AO	U-N	0.49	0.58
		U-O	0.67	
		U-N	0.49	
		U-O	0.66	
		Total	**2.31**	
Bis-AO/VO^{2+} (**B**)	AO	V-N	0.3322	0.29
		V-O	0.48	
		V-N	0.32	
		V-O	0.037	
		Total	**1.17**	
Bis-AO/VO_2^{+} (**C**)	AO	V-N	0.26	0.42
		V-O	0.67	
		V-N	0.05	
		V-O	0.69	
		Total	**1.68**	
AO/RCO_2^{-} UO_2^{2+} (**D**)	AO	U-N	0.55	0.49
		U-O	0.72	
	COO	U-O	0.67	
		U-O	0.037	
		Total	**1.97**	
Bis-RCO_2^{-}/UO_2^{2+} (**E**)	COO	U-O	0.73	0.37
		U-O	0.04	
		U-O	0.67	
		U-O	0.03	
		Total	**1.46**	
Dibenzofuran bis-amidoxime/UO_2^{2+} (**3.10**)	AO	U-N	0.46	0.56
		U-O	0.66	
		U-N	0.46	
		U-O	0.66	
		Total	**2.24**	

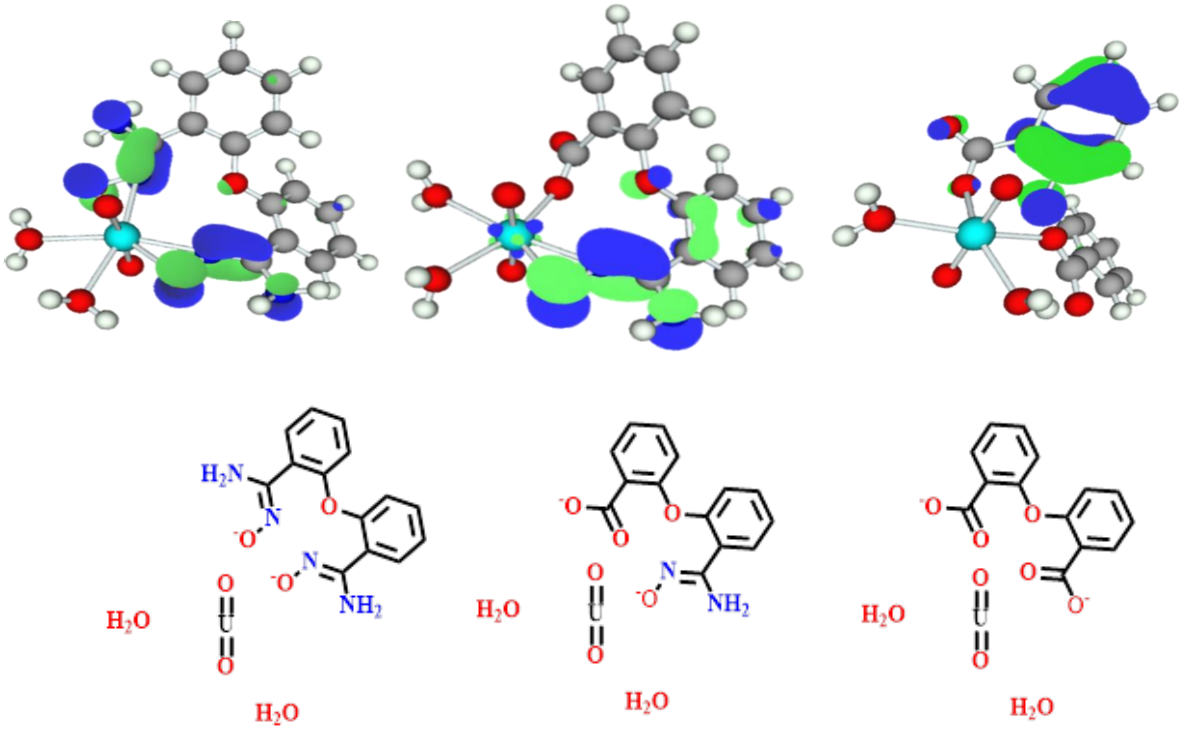

Figure 3.4 DFT-optimized structures of UO_2^{2+} with different potential diaryl ether/uranyl binding sites. Corresponding chemical diagrams are presented below. HOMOs are displayed as blue and green domains.

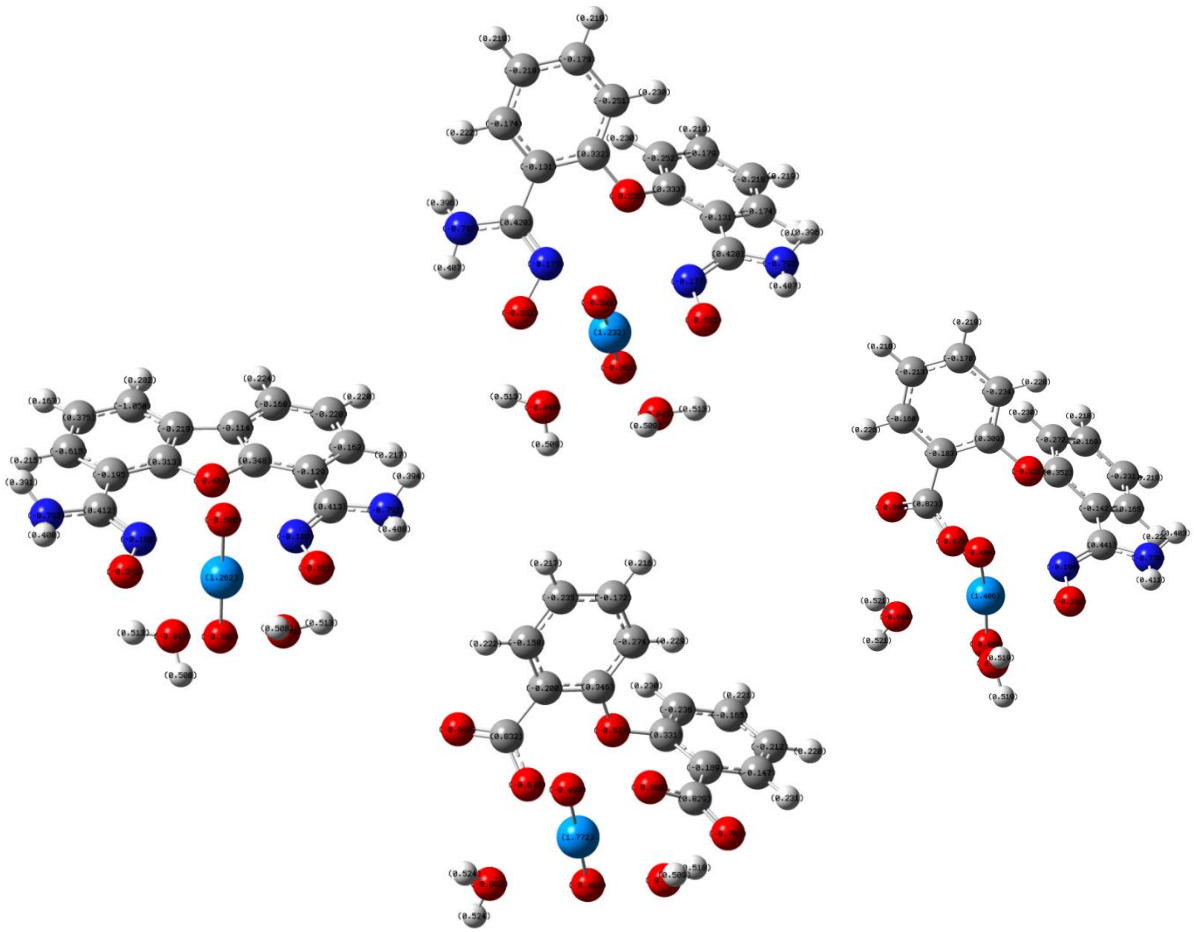

Figure 3.5 DFT-calculated NBO charge distributions structures of uranyl –bifunctional chelator species. Anticlockwise from top: (**3.2** + UO_2^{2+}), (**3.10** + UO_2^{2+}**)**, (**3.4** + UO_2^{2+}), and (**3.3** + UO_2^{2+}).

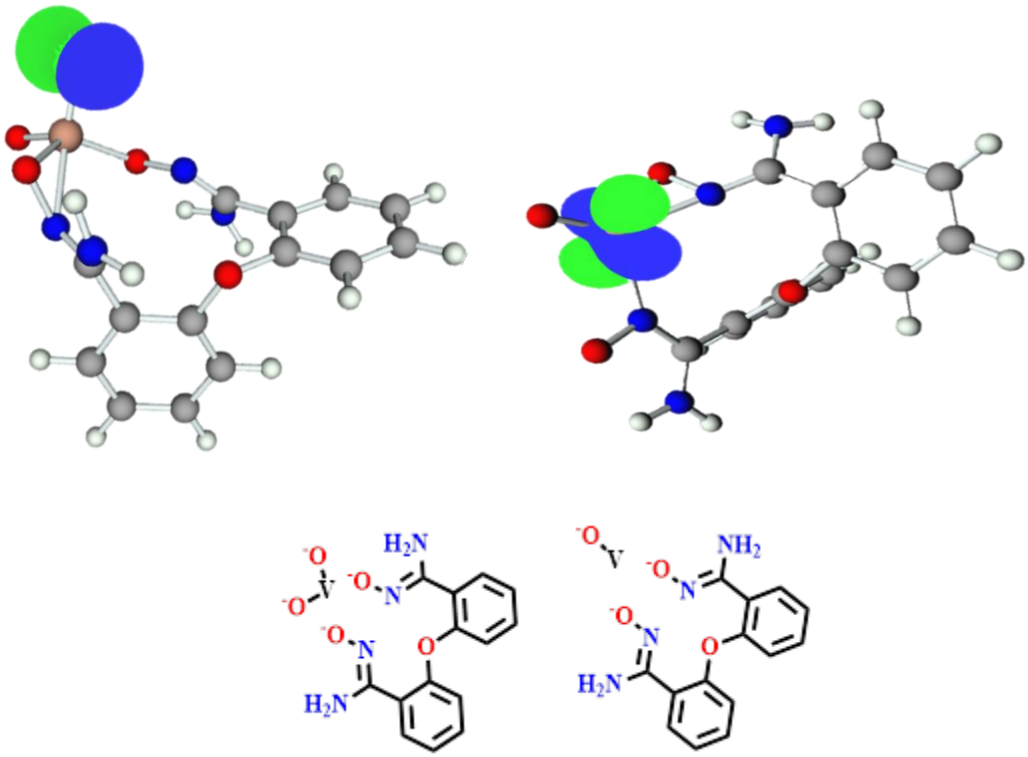

Figure 3.6 VO^{2+} and VO_2^{+} binding to ligand **3.2**. The HOMO of each complex is shown above as green/blue domains. Chemical structures are shown below.

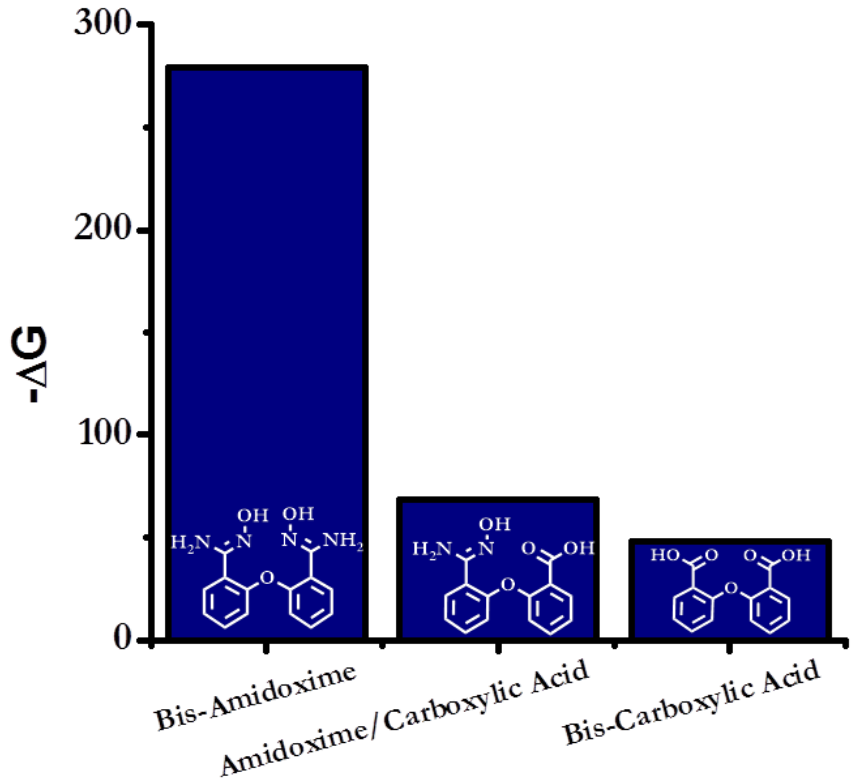

Figure 3.7 Gibbs Free energies of uranyl –bifunctional chelator species. Chemical structures of ligands used for each calculation is shown in white.

3.5 Polymer Synthesis

Encouraged by the computational results, the bis-amidoxime polymers (BAP) were synthesized according to **Scheme 3.3**. Briefly, 2-hydroxybenzonitrile was treated with 2-fluorobenzonitrile in the presence of potassium fluoride and alumina to afford the dinitrile-substituted diaryl ether in good yield **(3.1)**.[6,14] Selective mono-bromination at the meta position was achieved with slow addition of bromine, sulfuric acid, and mercuric oxide in carbon tetrachloride.[15] The vinyl group was installed after twice subjecting the brominated diaryl ether **(3.8)** to Stille coupling conditions, yielding compound **3.9**. The vinylated **3.9** was copolymerized

with *N*,*N*′-methylenebis(acrylamide) (NNBIS) in three different molar feed ratios (1:1, 2:1, and 3:1, mono-vinyl ligand : cross-linker).

To provide insight into the roles of polymer hydrophilicity as well as functional group efficacy, three control polymers were synthesized concurrently and are described in sections **3.5.5-3.5.7**.

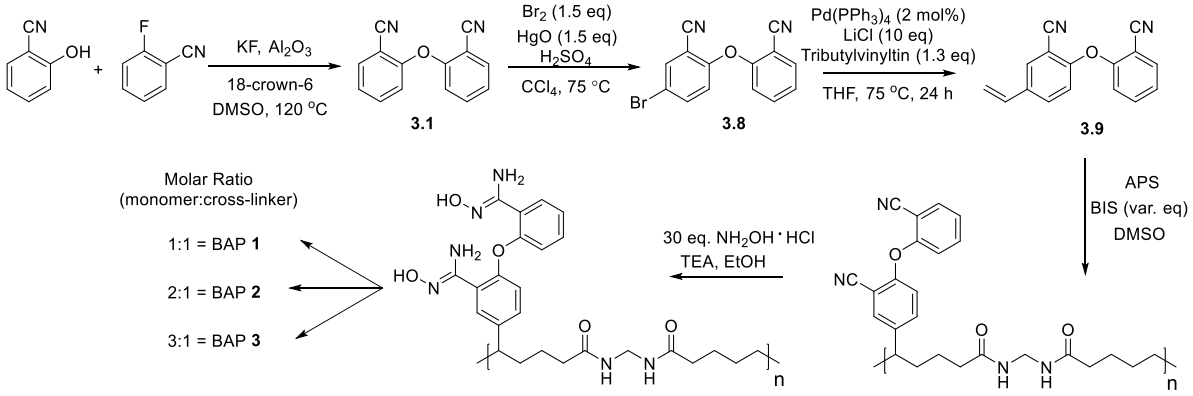

Scheme 3.3 The synthesis of bis-amidoxime functionalized polymers (BAP)

3.5.1 Synthesis of 5-bromo-2-(2-cyanophenoxy)benzonitrile (3.8)

A 50 mL round bottom flask equipped with a stir bar and reflux condenser was charged with **3.1** (50 mg, 0.23 mM). Carbon tetrachloride (1.3 mL) was added followed by H_2SO_4 (20 µL) and Br_2 (17.4 µL). The reaction mixture was heated to reflux with stirring for 2 hours. Afterwards, the solution was allowed to cool to room temperature before being filtered through a plug of celite and transferred to a separatory funnel. The filtrate was washed once with Na_2SO_3 (aq) and NaCl (aq). The resulting solution was dried over Na_2SO_4 and concentrated under vacuum. The product was purified by flash column chromatography using 20% ethyl acetate, 5% dichloromethane in hexanes as eluent system to afford the mono-brominated product. Yield (14 mg, 21%) ^{1}H NMR (500 MHz, $CDCl_3$): δ 7.82 (s, 1H), 7.73 (d, 1H, *J* = 9.0 *Hz*), 7.67 (d, 1H, *J* = 2.0 *Hz*), 7.63 (t, 1H,

J = 9.0 *Hz*), 7.34 (t, 1H, *J* = 8.0 *Hz*), 7.01 (d, 1H, *J* = 8.5 *Hz*), 6.84 (d, 1H, *J* = 9.0 *Hz*), ^{13}C NMR (125 MHz, $CDCl_3$): δ 156.83, 156.72, 137.64, 136.54, 134.79, 134.45, 125.45, 119.96, 119.14, 117.03, 114.86, 113.73, 106.87, 105.56. LR-MS (EI) calculated for $C_{14}H_7BrN_2O$: 299.0 *m/z*; found: 299.0 *m/z*.

3.5.2 Synthesis of 2-(2-cyanophenoxy)-5-vinyl-benzonitrile (3.9)

In a glove box, 5-bromo-2-(2-cyanophenoxy)benzonitrile (500 mg, 1.32 mmol) was added to a 50 mL round bottom flask charged with a stir bar along with LiCl (420 mg, 10 mmol). To this mixture was added 25 mL dry THF followed by $Pd(PPh_3)_4$ (61.1 mg, 4 mol %). Tributylvinyltin (464 µL, 1.6 mmol) was then added to the reaction mixture and the apparatus was removed from the glove box and heated to 75 °C for 12 hours. After cooling to room temperature, ethyl acetate (10 mL) was added and the lithium byproduct was removed by filtration. The filtrate was then washed with 10% NaOH (aq). (2x 15 mL) and the organics were dried over Na_2SO_4 and concentrated under vacuum. The residue was then subjected to modified reaction conditions (7 eq. LiCl, 0.5 eq. tin, 4 mol % Pd) to drive the reaction towards completion. The product was purified by flash column chromatography using 25% ethyl acetate, 5% dichloromethane in hexanes as eluent system to afford crude vinylated product. Subsequent recrystallization from dichloromethane/hexane affords 2-(2-cyanophenoxy)-5-vinyl-benzonitrile as a colorless solid. Yield (200 mg, 68%) ^{1}H NMR (500 MHz, $CDCl_3$): δ 7.71 (m, 2H), 7.59 (m, 2H), 7.29 (m, 1H), 6.98 (d, 1H, *J* = 8.5 *Hz*), 6.92 (d, 1H, *J* = 9.0 *Hz*), 6.66 (m, 1H), 5.74 (d, 1H, *J* = 17.5 *Hz*), 5.37 (d, 1H, *J* = 11 *Hz*), ^{13}C NMR (125 MHz, $CDCl_3$): δ 157.46, 156.52, 134.88, 134.65, 134.32, 133.83, 132.09, 131.68, 124.91, 119.04, 118.68, 116.40, 115.11, 115.02, 105.50, 105.21 LRMS (EI) calculated for $C_{16}H_{10}N_2O$: 246.0 *m/z*; found: 246.0 *m/z*.

3.5.3 Synthesis of 2-(2-cyanophenoxy)benzonitrile/NNBIS Copolymer

An oven dried 50 mL two-neck round bottom flask was allowed to cool under vacuum before being charged with 2-(2-cyanophenoxy)-5-vinyl-benzonitrile (90 mg) and N,N'-Methylenebisacrylamide (NNBIS) (56 mg). Dry DMSO (1 mL) and ammonium persulfate (APS) (3.0 mg) were added and the reaction mixture was allowed to warm to 80 °C for 24 hours. Two additional batches were prepared with varying amounts of crosslinker (19 or 28 mg) and radical initiator (3 or 6 mg). After the reaction cooled to room temperature, the precipitate was washed with copious amounts of MeOH (3x) and dried under vacuum.

3.5.4 Synthesis of BAP Materials

A two-neck round bottom flask was charged with the 2-(2-cyanophenoxy)benzonitrile/NNBIS copolymer and EtOH (5 mL).[1] The inhomogeneous mixture was heated with stirring to 50 °C. Afterwards, triethylamine (2.2 eq. with respect to monomer) and hydroxylamine hydrochloride (2.1 eq. with respect to monomer) were added. An additional 2.1 equivalents of NH_2OH HCl were added every 24 hours until the CN stretch determined via IR spectroscopy markedly diminished or disappeared.

3.5.5 Synthesis of Bis-AO/DVB Materials

A two-neck round bottom flask was charged with 2-(2-cyanophenoxy)-5-vinyl-benzonitrile, divinylbenzene (7 eq) and azobisisobutyronitrile (10 mol %) in toluene at 80 °C for 12 hours. After polymerization, this material was subjected to 8 equivalents of aqueous NH_2OH over 48 hours until the CN stretch determined via IR spectroscopy markedly diminished or disappeared.

3.5.6 Synthesis of PAA/DVB Materials

A two-neck round bottom flask was charged with poly(acrylic acid), divinylbenzene (7 eq) and azobisisobutyronitrile (10 mol %) in toluene at 80 °C for 12 hours. After polymerization, this material was subjected to aqueous NH_2OH until the CN stretch determined via IR spectroscopy markedly diminished or disappeared.

3.5.7 Synthesis of Poly NNBIS Homopolymer Materials

An oven dried 50 mL two-neck round bottom flask was allowed to cool under vacuum before being charged with N,N'-Methylenebis(acrylamide) (1.5 g). Degassed DMSO (7 mL) and water (3 mL) were added and the mixture was homogenized. Ammonium persulfate (APS) (230 mg) was added and the reaction mixture was allowed to warm to 40°C for 24 hours. After the reaction cooled to room temperature, the precipitate was washed with copious amounts of water and dried under vacuum.

3.6 Polymer Characterization

The degree of monomer incorporation was determined via FTIR according to protocols found in the literature[16] for monomer loading in copolymer blends. Seven pellets for IR analysis varying only in the amount of **3.1** were prepared to afford compositions varying between 0 and 50 mol%. The amount of KBr and NNBIS were kept constant for each sample. A calibration curve was constructed using molar fraction as the abscissa and the absorbance ratio of the characteristic stretching frequencies of **3.1** and NNBIS (2233.2 cm^{-1} and 1525.4 cm^{-1}, respectively) as the ordinate (**Figure 3.8**). Ordinary least squares analysis returns a line of best fit constrained to pass through the origin with an R^2 factor of 0.9916. Comparing the FTIR spectra obtained for the as-synthesized BAP materials with the constructed calibration curve and accounting for the mass of

polymer used yields monomer loadings of 1.54, 1.98, and 2.00 mmol bis-cyano diaryl ether g polymer^{-1} for BAP **1-3**, respectively.

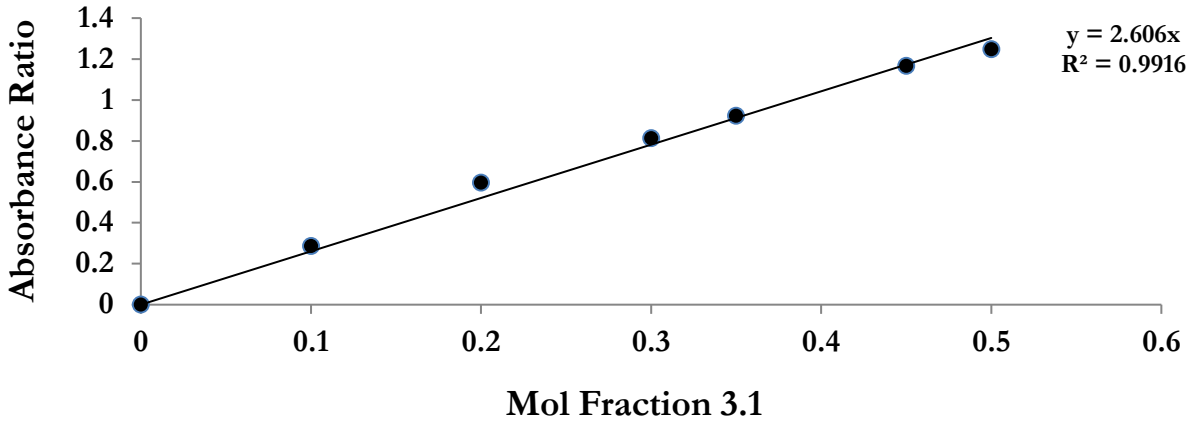

Figure 3.8 FTIR Calibration Curve for the determination of nitrile group loading.

Mol fractions were determined according to the following equation:

$$\text{Mol Fraction} = \frac{\text{mmol } \mathbf{3.1}}{(\text{mmol } \mathbf{3.1} + \text{mmol BIS})} \qquad \textbf{Equation 3.1}$$

where mmol **3.1** stands for mmols of bis-cyano monomer **3.1**, and mmol BIS stands for mmols of N,N'-Methylenebisacrylamide crosslinker used. The mass of the BIS crosslinker was kept constant for all trials while the mass of BC was allowed to vary. After grinding BC and BIS together in a mortar, 40 mg of KBr was added and the mixture was pressed into a transparent disk for FTIR studies. Each spectrum consists of 32 scans with 1 cm^{-1} resolution and was background corrected prior to analysis. The spectra obtained are shown below. For the calibration curve, the characteristic peaks at 2233.20 and 1525.44 cm^{-1} were used for **3.1** and BIS respectively.

The absorbance ratio was calculated according to the following equation:

$$\text{Absorbance Ratio} = \frac{\text{Absorbance}_{3.1}}{\text{Absorbance}_{BIS}} \qquad \textbf{Equation 3.2}$$

Absorbance values were background corrected prior to analysis.

Treatment of the polymers with several equivalents of hydroxylamine hydrochloride at 50 °C over multiple days afforded the three batches of functionalized polymer denoted as BAP **1**-**3** where the numerical suffix denotes the starting ratio of monomer to cross-linker, as discussed above.

FTIR analysis of dry material suggests complete or nearly complete conversion of the nitrile moiety due to the greatly diminished C≡N stretch at 2250 cm^{-1} (**Figure 3.9**) for each polymer formulation.

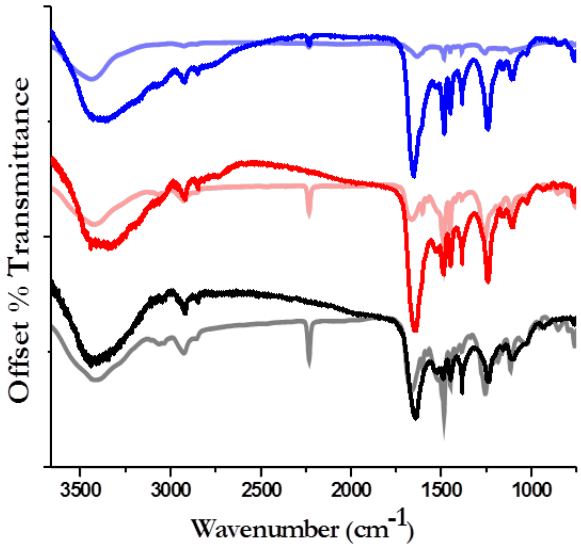

Figure 3.9 FTIR of dried BAP samples. BAP **3** is shown in blue, BAP **2** is shown in red, and BAP **1** is shown in black. Transparent traces show polymer samples before amidoximation.

In an effort to determine which species were present on the polymer, several different amidoximation reactions were conducted using the small molecule precursor **3.1** (**Scheme 3.4**).

Standard literature conditions consisting of stoichiometric amounts of aqueous hydroxylamine at 70°C for two hours resulted in a 24% isolated yield of undesirable mono-functionalized species **3.5** and **3.6**. Doubling the amount of aqueous hydroxylamine at the same temperature and time resulted in a combined 39% yield of **3.5** and **3.6**. The bis-amidoxime product (**3.2)** yield remained nearly 5% in both trials.

Switching to hydroxylamine hydrochloride and triethylamine at 70°C for 12 hours resulted in less than 10% of undesired mono-functionalized products. The yield of desirable bis-amidoxime product increased to 39%. It should be noted that the bis-amide analog **3.7** was not observed in any trial.

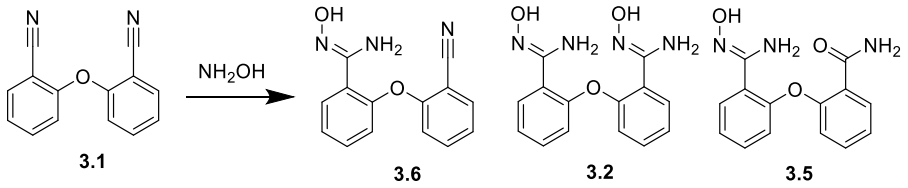

Scheme 3.4 Theoretical amidoximation products of dicyano diaryl ether (**3.1**)

When aqueous hydroxylamine was used, competing formation of the amidoxime/amide **(3.5)** lowered the desired yield of the bis-amidoxime **(3.2)**. Doubling the amount of hydroxylamine used did not result in an increased yield of bis-amidoxime **(3.2)**; instead, it doubled the amount of amidoxime/amide **(3.5)** formed. Fortunately, use of NH_2OH•HCl with trimethylamine gave reasonable yields for the desired bis-amidoxime with only trace formation of the amide likely formed during aqueous workup.

A comparison between the FTIR spectra of assorted small molecules and BAP **2**, suggests that the mono-amide hydrolysis product is only a minor component of the BAP materials (**Figure**

3.8). The broad peak at 3182 cm^{-1} attributed to the N-H stretch of the amide is not evident in the BAP **2** material. Further IR analysis of peaks at lower wavenumber is hindered by the presence of overlapping amide peaks from the NNBIS crosslinker used in the synthesis of the BAP materials (**Figure 3.9**). While the formation of mono-amide/amidoxime species **3.5** during the amidoximation step of the BAP polymer synthesis cannot be definitively ruled out by FTIR, the likelihood that this species is a major contributor to U binding is low.

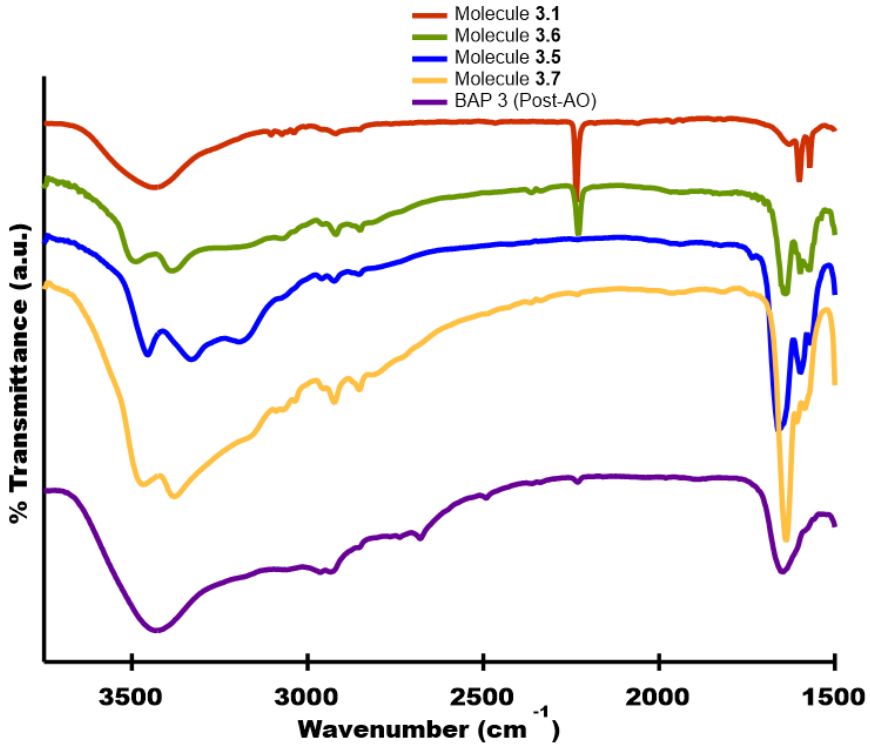

Figure 3.10 FTIR spectra of BAP **3** and several structurally related small molecules.

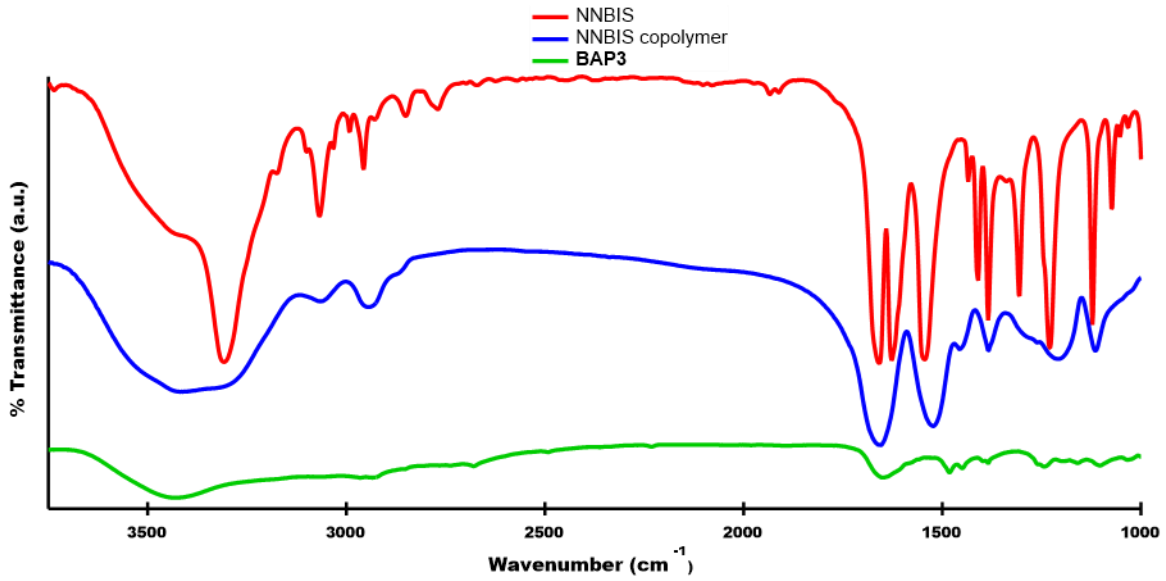

Figure 3.11 FTIR spectra of **BAP3** materials after amidoximation as well as N,N'-Methylenebisacrylamide, and poly(N,N'-Methylenebisacrylamide).

There are few examples in the literature[17] of amide binding U and it is expected that any amide formed would make a greater contribution to the hydrophilicity of the hydrogel than to uranium binding. Additionally, the separation of amidoxime groups by the ether bridge prevents formation of a cyclic imidedioxime byproduct due to requiring formation of an energetically disfavored 8-member ring.[18–20]

3.7 Uranium Uptake Experiments

3.7.1 Methodology

Two distinct procedures were used for the small-scale and large-scale U sorption experiments discussed above.

Small-scale adsorption studies were conducted in 1.5 mL polypropylene tubes with sorbent at a phase ratio of 1 mg mL solution^{-1}. Large scale experiments were conducted with ~2 mg sorbent in 500 mL LDPE Nalgene screw top bottles with 370 mL seawater simulant. Simulated seawater

solutions with various U concentrations were prepared by dissolving $UO_2(NO_3)_2 \cdot 6H_2O$ in seawater simulant (pH = 8.2, 25.6 mg L^{-1} NaCl, 194 mg L^{-1} $NaHCO_3$). In both experiments, polymer materials were re-wet with ethanol for 24 hours prior to adsorption studies. Afterwards, the apparatus was agitated on a plate shaker at 300 rpm for the allotted time. The U concentration before and after agitation was determined by ICP-MS to evaluate U uptake by the polymer systems. The quantity of uranium adsorbed at equilibrium (Q_e) was calculated with **Equation 3.3**:

$$Q_e = \frac{(C_o - C_e) * V}{m} \qquad \textbf{Equation 3.3}$$

where Q_e is the U adsorbed at equilibrium, C_o is the initial U concentration, C_e is the U concentration of seawater simulant at equilibrium, V is the volume of the seawater simulant, and m is the mass of the sorbent.

3.7.2 Uranium Uptake Results

The polymer materials were dried in order to obtain an accurate mass and re-wet with ethanol for 24 hours prior to U sorption studies. Small-scale U sorption studies were conducted with 1 mg polymer in 1 mL of seawater simulant spiked with 6 ppm U. BAP **1**, BAP **2**, and BAP **3** hydrogel materials sorbed 87.1%, 98.9%, and 99.6% U from solution after 24 hours as determined via ICP-MS analysis of initial and final U concentrations.

The preliminary U sorption results suggest these materials may find application in water purification. BAP **3** sorbed 99.6% of U from solution after 24 hours corresponding to a decrease in U concentration from 6.15 ppm to 26.5 ppb, efficiently reducing the U content below the EPA's maximum contaminant level (MCL) of 30 ppb.[21] These results compare favorably with control experiments and several other polymer formulations synthesized concurrently (**Figure 3.12**). The first material to be tested (**Bis-AO/DVB)** was a copolymer blend of mono-vinylated dicyano diaryl

ether (**3.9**) and divinyl benzene (DVB). After amidoximation, the material was found to adsorb 11% of U from 8 ppm U seawater simulant solution.

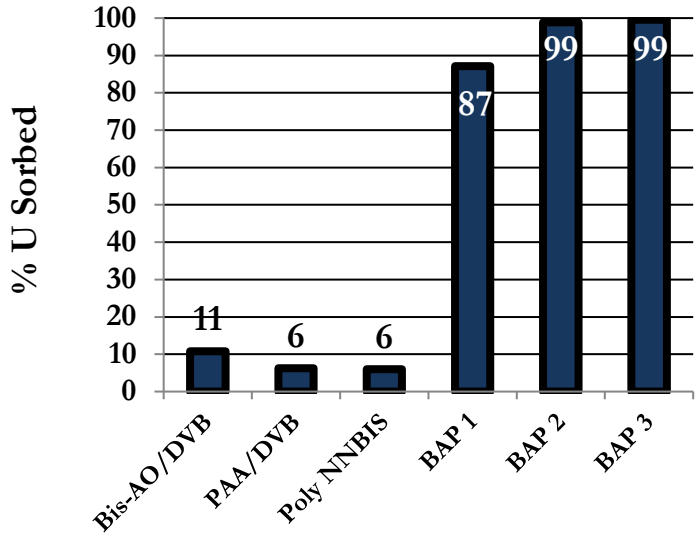

Figure 3.12 Small-scale U sorption data. Each of the trials shown above was conducted at a phase ratio of 1:1 mg : mL in 1 mL seawater simulant spiked with 6 ppm U. Each vial was shaken at 300 rpm for 24 hours prior to analysis via ICP-MS.

Low dispersibility of **Bis-AO/DVB** suggested that hydrophobic character was responsible for poor uptake. Reducing the DVB crosslinker ratio by half and copolymerizing with poly(acrylic acid) resulted in **PAA/DVB** material. Although this material was readily dispersible, it exhibited worse U adsorption capacity likely attributed to weak carboxylate binding. Finally, a homopolymer was formulated containing N,N'-methylenebis(acrylamide) in order to obtain a background adsorption capacity. This hydrophilic **Poly NNBIS Homopolymer** was able to adsorb 6% of U from the stock solution, on par with the **PAA/DVB** material, suggesting that physisorption is the primary adsorption mechanism for these materials. Successful coupling of a strong U binding moiety such as bis-amidoxime with a hydrophilic backbone, as evidenced by the BAP series of materials, results in vastly improved uptake of 87-100% in these studies.

3.7.3 Uranium and Vanadium Separation

While useful as a diagnostic tool, small scale adsorption tests often exaggerate U adsorption characteristics as the sorbent is used in vast excess. Large scale adsorption (LSA) experiments were performed in an effort to accurately depict U adsorption capacity over time by ensuring an excess of U is present at all time points. Experiments were conducted in 500 mL LDPE Nalgene screw top bottles with 2 mg of BAP material in 370 mL seawater simulant spiked with 8 ppm U and 4.6 ppm V and. A simultaneous control experiment without polymer was performed under identical conditions to confirm adsorption was attributable to binding by the hydrogel, rather than precipitation or physisorption onto the vessel walls. Aliquots were taken in triplicate at various time points and centrifuged at 13,000 rpm for 30 minutes. The supernatant was then analyzed by ICP-MS and compared to the control to determine U sorption capacity. The results are shown in **Figure 3.11**

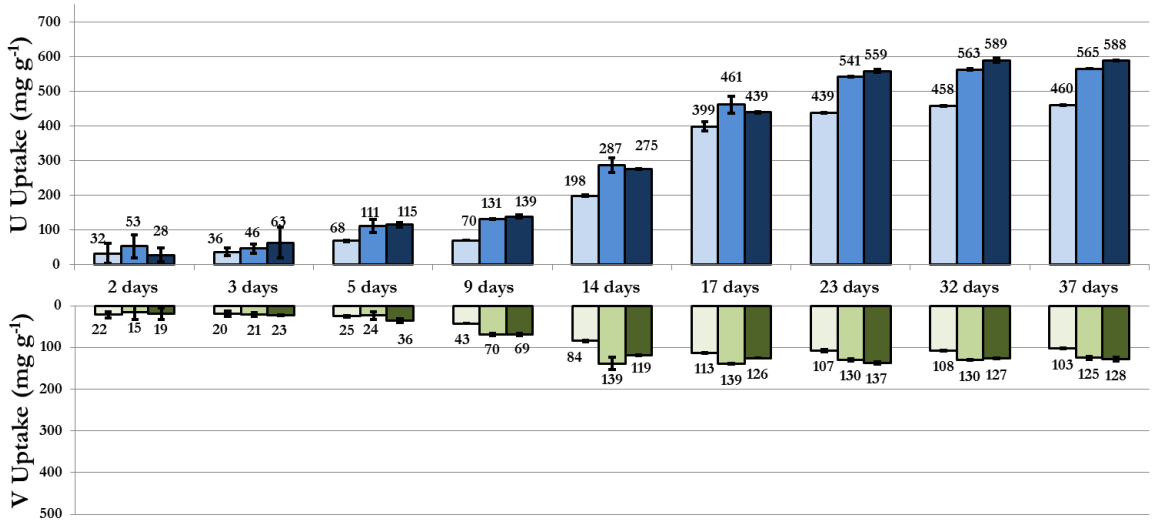

Figure 3.13 Uranium and vanadium uptake trials over time. Top: Uranium uptake of BAP materials in ~8 ppm U seawater simulant. Bottom: Vanadium uptake of hydrogel materials in 4.6 ppm V seawater simulant. Darkest bar is BAP **3**, middle bar is BAP **2**, lightest bar is BAP **1**. Data determined via ICP-MS in triplicate. Error bars representing one standard deviation are shown.

U uptake over time follows a flattened sigmoidal shape with comparatively slow U uptake within the first week, a rapid increase within 14 days, and a leveling off after 32 days. Unsurprisingly, BAP **3** achieved higher U uptake than BAP **1** and **-2**, attributable to the larger number of available bis-amidoxime binding sites. The relative rate of U saturation also appears to correlate with the extent of bis-amidoxime inclusion, with BAP **3** saturating around 23 days, while BAPs **1** and **2** requiring 32 days. Vanadium uptake follows a similar trend, with uptake leveling off after 14 days. Hydrogel materials were able to attain an impressive level of U adsorption with a maximum capacity of 588 mg U g polymer^{-1}. Satisfyingly, vanadium uptake was much lower with a maximum of 128 mg V g polymer^{-1} attained after 37 days. Previously reported sorbent materials have been challenged with high vanadium uptake, at times exceeding 3:1 w/w, supposedly due to the formation of cyclic imidedioxime binding sites that possess stronger affinity for vanadium over uranium.[22] Indeed, recent literature has demonstrated that the so-called "open-chain" amidoxime moiety contained in the state of the art polymer sorbent displays unremarkable affinity for vanadium binding.[23–25] In contrast, the BAP system is unable to form cyclic imidedioxime sites and the only binding capable of occurring is through the amidoxime functionality. As a result, selectivity for U is dramatically improved and a 1:1 molar uptake of U:V is achieved.

The raw U and V mass uptake data are shown in **Table 3.3**. At the end of the 37-day experiment, the BAP materials adsorbed ~73% U from solution and less than half of that, ~33% of V from solution. Analyzing these data in terms of the degree of monomer loading provides a useful idea of the number of metal atoms per bis-amidoxime active site.

Table 3.3 Cumulative Amount of U and V Adsorbed over the 37-Day Experiment and % of Total U Adsorbed in *Italics*

	Sample	**Day 2**	**Day 3**	**Day 9**	**Day 14**	**Day 23**	**Day 32**	**Day 37**
Cumulative U Adsorbed (μg) *(% of total)*	BAP 1	80.74 (*5%*)	90.46 (*6%*)	283.53 (*18%*)	721.11 (*46%*)	1090.03 (*69%*)	1137.90 (*72%*)	1143.94 (***73%***)
	BAP 2	106.70 (*7%*)	92.84 (*6%*)	374.54 (*24%*)	806.51 (*51%*)	1091.43 (*69%*)	1134.01 (*72%*)	1139.82 (***73%***)
	BAP 3	53.78 (*3%*)	122.15 (*8%*)	377.92 (*24%*)	758.03 (*48%*)	1137.19 (*72%*)	1137.28 (*72%*)	1134.81 (***72%***)
	Sample	**Day 2**	**Day 3**	**Day 9**	**Day 14**	**Day 23**	**Day 32**	**Day 37**
Cumulative V Adsorbed (μg) *(% of total)*	BAP 1	54.58 (*7%*)	48.65 (*7%*)	105.82 (*14%*)	209.50 (*28%*)	266.88 (*36%*)	267.24 (*36%*)	255.86 (***34%***)
	BAP 2	29.88 (*4%*)	42.10 (*6%*)	140.49 (*19%*)	280.44 (*38%*)	262.49 (*35%*)	262.67 (*35%*)	252.80 (***34%***)
	BAP 3	37.32 (*5%*)	44.25 (*6%*)	133.06 (*18%*)	229.84 (*31%*)	264.40 (*36%*)	244.94 (*33%*)	247.71 (***33%***)

Knowing the degree of monomer loading, the number of binding sites (defined as a single bis-amidoxime molecule) per weight polymer can be ascertained. Coupling this information with the amount of uranium adsorbed under equilibrium conditions yields ~1.2 uranium atoms per bis-amidoxime molecule (**Table 3.4**).

Table 3.4 Binding Site Analysis of U Loaded BAP Polymers

Material	**Degree of Bis-AO loading**	**U uptake (μg)**	**# Binding Sites**	**#UO_2^{2+} per binding site**
BAP 1	1.54 mmol g-1	1090.03	2.31E+18	1.20
BAP 2	1.98 mmol g-1	1091.43	2.41E+18	1.15
BAP 3	2.01 mmol g-1	1137.19	2.33E+18	1.23

A value of ~1 is suggestive of the desired 1:1 ligand:metal stoichiometry modeled via DFT described earlier. Values slightly higher than 1 imply a small degree of physisorption of non-specific binding to the amide-containing crosslinker used in the polymer synthesis.

3.8 Characterization of Metal Loaded Polymer

Raman spectroscopy was used to further investigate the uranyl binding and confirm the strong binding proposed. After adsorption studies were concluded, the polymer was recovered by batch centrifugation and lyophilization. The infrared inactive ν_1 U=O stretching frequency typically found between 700 and 900 cm^{-1} is easily discernable[26] in the Raman spectra (**Figure 3.14**).

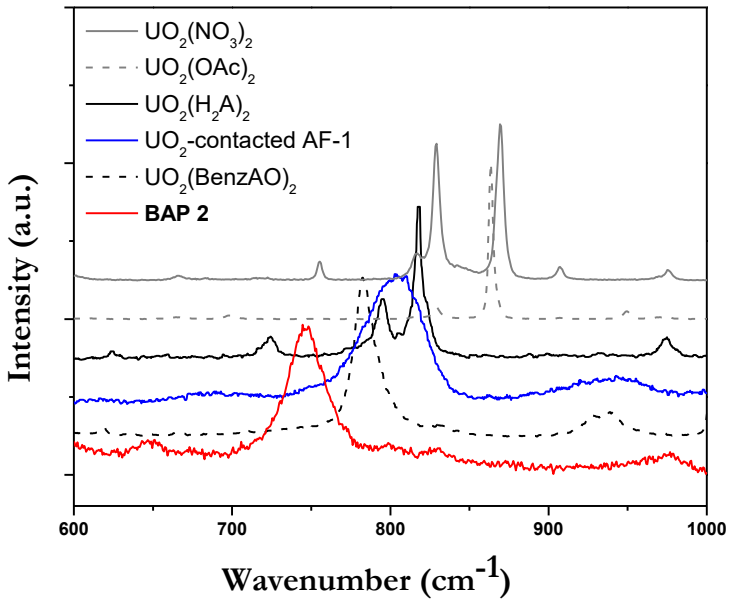

Figure 3.14 Raman spectra of various uranyl species. Excitation laser 633 nm, 0.75 second capture, 52 accumulations.

The uranyl contacted BAP hydrogel exhibits a ν_1 stretch of 744.6 cm^{-1} which is among the lowest reported in the literature. To compare, the state of the art amidoxime functionalized polymer fiber after laboratory adsorption tests exhibits a ν_1 of 802.8 cm^{-1}. Crystalline uranyl standards with

η^2 type binding have a ν_1 closer to 782 cm^{-1} while weaker binding nitrate and acetate salts have stretching frequencies in the mid-800 cm^{-1} regime. It has been previously shown by Cooney and co-workers[27] that the ν_1 stretching frequency of uranyl can be correlated with the U=O bond length according **Equation 3.4**

$$R_{U=O} = \frac{[10650\,(\nu_1)^{-\frac{2}{3}} + 57.5]}{100} \qquad \textbf{Equation 3.4}$$

where $R_{U=O}$ is the U=O bond length in angstroms and ν_1 is the symmetric U=O stretching mode. This treatment, applied to the raman data shown in **Figure 3.15**, affords the U=O bond lengths presented in **Table 3.5**.

Table 3.5 Raman, Crystal, and DFT Calculated U=O Bond Lengths

Species	**v1 (cm^{-1})**	**Raman Calc. (Å)**	**Exp. (Å)**	**DFT Calc. (Å)**
UO_2-H_2A_2	818.7	1.79	1.79	1.80
UO_2-BenzAO	782.2	1.83	1.80	1.80
U-Nitrate	869.2	1.74	1.76	1.76
U-Acetate	863.6	1.75	1.75	1.79
AF-1 Fiber	802.8	1.81	N/A	N/A
BAP 2	744.6	1.87	N/A	N/A

Weak uranyl coordination as found in uranyl nitrate, results in a short U-O bond length of 1.74 Å as determined by **Equation 3.4**. Stronger uranyl bonding, as exemplified by uranyl benzamidoxime, results in a much longer U-O bond length of 1.83 Å. Uranyl as bound by the BAP series hydrogel materials exhibits a remarkable U-O bond lengthening to 1.87 Å. These data indicate pronounced electron donation from the amidoxime functionalities to the uranyl center suggestive of strong uranyl binding in the hydrogel materials being studied. In all cases, there is good correlation between the Raman spectra-derived U=O bond lengths with those determined experimentally and via DFT (**Table 3.3**).

3.9 Conclusion and Outlook

We have successfully designed, synthesized, and screened a series of polymer materials capable of selectively adsorbing U from seawater simulant solutions. *In silico* studies were first used to compile a library of easy to synthesize ligands that would demonstrate uranium selectivity comparable to ligand **3.10** developed by Bryantsev and co-workers.[8] DFT studies conducted at the B3LYP level of theory showed that the bis-amidoxime ligand **3.1** exclusively adopts the bis-η^2 binding motif when bound to U, an indication of strong complexation. In all cases, vanadium complexes with **3.1** were found to adopt dissimilar, weaker binding motifs. Based on the flexible diaryl ether backbone found computationally, we were able to install amidoxime groups after facile polymerization to afford three hydrophilic polymer formulations with monomer loading upwards of 2 mmol g^{-1} as quantified via FTIR.

Adsorption studies conducted in seawater simulant spiked with 8 ppm U realized a uranium sorption capacity of 588 mg U per gram of polymer after 37 days contact. Vanadium uptake during that same period was nearly five times lower, at 128 mg vanadium per gram. This dramatic demonstrated selectivity for U, nearly 5:1 w/w, is among the highest reported in the literature. Raman spectroscopy confirmed the nature of strong uranyl binding in BAP materials yielding a ν_1 stretch of 744.6 cm^{-1}. Uranyl as bound by the BAP series hydrogel materials exhibits a U-O bond lengthening of 1.87 Å indicative of enhanced electron donation from the amidoxime functionalities to the uranyl center. Efforts to modify the synthesis in order to ensure the bis-amidoxime chelator is amenable to large-scale polymerization are currently underway.

3.10 Funding and Acknowledgements

This work was supported by the DOE Office of Nuclear Energy's Nuclear Energy University Program (Sub-Contract-20 No. 120427, Project No. 3151). Work at Oak Ridge National Laboratory was sponsored by the U.S. DOE, Office of Nuclear Energy. This research used resources of the Advanced Photon Source, a U.S. Department of Energy (DOE) Office of Science User Facility operated for the DOE Office of Science by Argonne National Laboratory under Contract No. DE-AC02-06CH11357. MRCAT operations are supported by the Department of Energy and the MRCAT member institutions. We acknowledge the University of Chicago Research Computing Center, the Nuclear Magnetic Resonance Facility, and NSF instrumentation grant CHE-1048528 in conjunction with the Mass Spectrometry Facility for support of this work. The United States Government retains, and by accepting the article for publication the publisher acknowledges that the United States Government retains, a non-exclusive, paid-up, irrevocable, world-wide license to publish or reproduce the published form of this manuscript, or allow others to do so, for the United States Government Purposes. The Department of Energy will provide public access to these results of federally sponsored research in accordance with the DOE Public Access Plan (http://energy.gov/downloads/doe-public-access-plan).

3.11 References

(1) Hara, K.; Fujiwara, S.; Fujii, T.; Yoshioka, S.; Hidaka, Y.; Okabe, H. Attempts to Capturing ppb-Level Elements from Sea Water with Hydrogels. *Prog. Nucl. Energy* **2016**, *92*, 228–233.

(2) Frisch, M. J.; Trucks, G. W.; Schlegel, H. B.; Scuseria, G. E.; Robb, M. a.; Cheeseman, J. R.; Montgomery, J. a.; Vreven, T.; Kudin, K. N.; Burant, J. C.; et al. Gaussian 09W Tutorial an Introduction to Computational Chemistry using G09W Avogadro Software. **2009**, 34.

(3) Lee, C.; Yang, W.; Parr, R. G. Development of the Colle-Salvetti Correlation-Energy Formula into a Functional of the Electron Density. *Phys. Rev. B* **1988**, *37* (2), 785–789.

(4) Becke, A. D. Density-Functional Thermochemistry. III. The Role of Exact Exchange. *J. Chem. Phys.* **1993**, *98* (7), 5648.

(5) Cossi, M.; Rega, N.; Scalmani, G.; Barone, V. Energies, Structures, and Electronic Properties of Molecules in Solution with the C-PCM Solvation Model. *J. Comput. Chem.* **2003**, *24* (6), 669–681.

(6) Schmittling, E. A.; Sawyer, J. S. Synthesis of Diethyl Ethers, Diaryl Thioethers, and Diarylamines Modiated by Potassium Fluoride-Alumina and 18-Crown-6. *J. Org. Chem.* **1993**, *58* (12), 3229.

(7) Kelley, S. P.; Barber, P. S.; Mullins, P. H. K.; Rogers, R. D. Structural Clues to UO_2^{2+} /VO_2^{+} Competition in Seawater Extraction Using Amidoxime-Based Extractants. *Chem. Commun.* **2014**, *50* (83), 12504–12507.

(8) Vukovic, S.; Hay, B. P.; Bryantsev, V. S. Predicting Stability Constants for Uranyl Complexes Using Density Functional Theory. *Inorg. Chem.* **2015**, *54* (8), 3995–4001.

(9) Piechowicz, M.; Abney, C. W.; Zhou, X.; Thacker, N. C.; Li, Z.; Lin, W. Design, Synthesis, and Characterization of a Bifunctional Chelator with Ultrahigh Capacity for Uranium Uptake from Seawater Simulant. *Ind. Eng. Chem. Res.* **2016**, *55* (15), 4170–4178.

(10) Vukovic, S.; Hay, B. P. De Novo Structure-Based Design of Bis-Amidoxime Uranophiles. *Inorg. Chem.* **2013**, *52* (13), 7805–7810.

(11) Grant, C. D.; Kang, S. O.; Hay, B. P. Synthesis of a Hydrophilic Naphthalimidedioxime. *J. Org. Chem.* **2013**, *78* (15), 7735–7740.

(12) Mehio, N.; Ivanov, A. S.; Williams, N. J.; Mayes, R. T.; Bryantsev, V. S.; Hancock, R. D.; Dai, S. Quantifying the Binding Strength of Salicylaldoxime–Uranyl Complexes Relative to Competing Salicylaldoxime–Transition Metal Ion Complexes in Aqueous Solution: A Combined Experimental and Computational Study. *Dalt. Trans.* **2016**, *45* (22), 9051–9064.

(13) Lashley, M. A.; Ivanov, A. S.; Bryantsev, V. S.; Dai, S.; Hancock, R. D. Highly Preorganized Ligand 1,10-Phenanthroline-2,9-Dicarboxylic Acid for the Selective Recovery of Uranium from Seawater in the Presence of Competing Vanadium Species. *Inorg. Chem.* **2016**, *55* (20), 10818–10829.

(14) Sawyer, J. S.; Schmittling, E. A.; Palkowitz, J. A.; Smith, W. J. Synthesis of Diaryl Ethers, Diaryl Thioethers, and Diarylamines Mediated by Potassium Fluoride-Alumina and 18-Crown-6: Expansion of Scope and Utility. *J. Org. Chem.* **1998**, *63* (18), 6338–6343.

(15) Khan, S. A.; Munawar, M. A.; Siddiq, M. Monobromination of Deactivated Active Rings Using Bromine, Mercuric Oxide, and Strong Acid. *J. Org. Chem.* **1988**, *53* (8), 1799–1800.

(16) Mao, R.; Huglin, M. B.; Davis, T. P. Quantitative Analysis of Copolymers by FTIR. *Eur. Polym. J.* **1993**, *29* (4), 475–481.

(17) Dalley, N. K.; Mueller, M. H.; Simonsen, S. H. Neutron Diffraction Study of Monoaquotetraureadioxouranium(VI) Nitrate. *Inorg. Chem.* **1972**, *11* (8), 1840–1845.

(18) Astheimer, L.; Schenk, H. J.; Witte, E. G.; Schwochau, K. Development of Sorbers for the Recovery of Uranium from Seawater. Part 2. The Accumulation of Uranium from Seawater by Resins Containing Amidoxime and Imidoxime Functional Groups. *Sep. Sci. Technol.* **1983**, *18*, 307–339.

(19) Tian, G.; Teat, S. J.; Zhang, Z.; Rao, L. Sequestering Uranium from Seawater: Binding Strength and Modes of Uranyl Complexes with Glutarimidedioxime. *Dalt. Trans.* **2012**, *41* (38), 11579.

(20) Kang, S. O.; Vukovic, S.; Custelcean, R.; Hay, B. P. Cyclic Imide Dioximes: Formation and Hydrolytic Stability. *Ind. Eng. Chem. Res.* **2012**, *51* (19), 6619–6624.

(21) US Environmental Protection Agency. Radionuclides Rule: A Quick Reference Guide http://nepis.epa.gov/Exe/ZyPDF.cgi?Dockey=30006644.txt (accessed August 12, 2019).

(22) Leggett, C. J.; Parker, B.; Teat, S.; Zhang, Z.; Dau, P.; Lukens, W.; Peterson, S. J.; Cardenas, A. J. P.; Warner, M. G.; Gibson, J.; et al. Structural and Spectroscopic Studies of a Rare Non-Oxido V(V) Complex Crystallized from Aqueous Solution. *Chem. Sci.* **2016**, *7*, 2775–2786.

(23) Ivanov, A. S.; Bryantsev, V. S. Assessing Ligand Selectivity for Uranium over Vanadium Ions to Aid in the Discovery of Superior Adsorbents for Extraction of UO_2^{2+} from Seawater. *Dalt. Trans.* **2016**, *45* (26), 10744–10751.

(24) Mehio, N.; Johnson, J. C.; Dai, S.; Bryantsev, V. S. Theoretical Study of the Coordination Behavior of Formate and Formamidoximate with Dioxovanadium(V) Cation: Implications for Selectivity towards Uranyl. *Phys. Chem. Chem. Phys.* **2015**, *17* (47), 31715–31726.

(25) Mehio, N.; Ivanov, A. S.; Ladshaw, A. P.; Dai, S.; Bryantsev, V. S. Theoretical Study of Oxovanadium(IV) Complexation with Formamidoximate: Implications for the Design of Uranyl-Selective Adsorbents. *Ind. Eng. Chem. Res.* **2016**, *55* (15), 4231–4240.

(26) Dembowski, M.; Bernales, V.; Qiu, J.; Hickam, S.; Gaspar, G.; Gagliardi, L.; Burns, P. C. Computationally-Guided Assignment of Unexpected Signals in the Raman Spectra of Uranyl Triperoxide Complexes. *Inorg. Chem.* **2017**, *56* (3), 1574–1580.

(27) Bartlett, J. R.; Cooney, R. P. On the Determination of Uranium-Oxygen Bond Lengths in Diooxouranium(VI) Compounts by Raman Spectroscopy . *Journal of Molecular Structure.* **1989**, *193*, 295–300.

3.12 Appendix 3.1 Bis-Amidoxime Crystal Structure Details

Name	Bisamidoxime
Formula	C73 N13 O14 Cl4
Fw	39.27
Temperature (K)	100
Wavelength (Å)	0.43128
Crystal system	Triclinic
Space group	*P*-1
a, Å	11.5039(5)
b, Å	13.4991(6)
c, Å	13.6851(6)
α, °	106.8850(10)
β, °	108.7230(10)
γ, °	94.0300(10)
V, Å^3	1894.35(14)
Z	39
Density (calcd. g/cm^3)	1.342
F(000)	810
θ range data collection	2.33 - 19.81
Limiting indices	-15≤ h ≤ 18 -22 ≤ k ≤ 22 -21 ≤ l ≤ 13
Reflection collected	19406
R(int)	0.1870
Data/restraints/parameters	19406/3/962
Goodness-of-fit on F^2	1.102
Final R indices [I>4σ(I)]	0.0598
R indices (all data)	0.0701
CCDC Identifier	1530634

3.13 Appendix 3.2 Cartesian Coordinates of Geometrically Optimized Species *in silico*

C	4.33034400	2.51808900	1.41792700
C	3.73399100	1.30957100	1.07463600
C	2.45529900	1.28612900	0.51657000
C	1.73260700	2.47951500	0.32078700
C	2.36269400	3.68587600	0.67696900
C	3.64501500	3.71408300	1.21152400
H	5.32381500	2.51990300	1.85304700
H	4.26003000	0.37657500	1.23666700
H	1.81999500	4.61563400	0.55767400
H	4.09728700	4.66218100	1.47994600
O	1.83602500	0.09486900	0.21026400
C	2.54204200	-0.95947600	-0.32398400
C	3.55700000	-0.74743800	-1.25782300
C	2.16151700	-2.26570800	0.04237500
C	4.23403400	-1.82482800	-1.81901600
H	3.81475400	0.26575400	-1.54135900
C	2.86666200	-3.33450500	-0.54038700
C	3.89363700	-3.12583100	-1.45300100
H	5.01836900	-1.64379000	-2.54592100
H	2.57943600	-4.34903000	-0.29251300
H	4.41092500	-3.97412000	-1.88692100
C	1.03679600	-2.58097800	0.95310600
N	1.04126300	-3.79947600	1.59622300
H	1.93544000	-4.15351200	1.90264200
H	0.29991500	-3.90044600	2.27661400
N	-0.00282900	-1.81019400	1.02552900
O	-1.07484900	-2.26955100	1.74409900
U	-1.86925100	-0.28447000	0.78322500
O	-1.78992900	0.50165700	2.40359000
O	-2.10349900	-1.08636500	-0.81435500
O	-3.77318300	-1.78218500	1.66445600
H	-3.41092400	-2.62602800	1.96456900
H	-4.38237600	-1.46946300	2.34426000
C	0.34229000	2.53643400	-0.18631200
N	-0.08948500	3.70616500	-0.77286800
N	-0.49684200	1.57720700	0.04938100
H	0.57973600	4.21263200	-1.33370400
H	-1.00855800	3.63433300	-1.18871600
O	-1.80444000	1.79019400	-0.30097900
O	-4.20870700	0.76582700	0.54116000
H	-4.13769400	1.65347900	0.16673300
H	-4.91511100	0.30715800	0.07061400

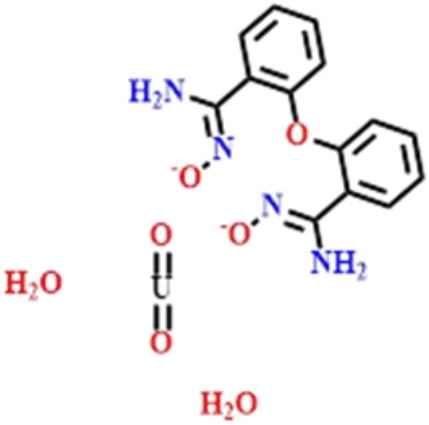

C	3.86867500	2.91065400	1.70236300
C	3.43719300	1.59102900	1.60568400
C	2.51045300	1.22990400	0.62967600
C	1.99582500	2.17365400	-0.27113300
C	2.46150200	3.49303200	-0.16452300
C	3.37845300	3.86632300	0.81181800
H	4.58396400	3.18867700	2.46887900
H	3.81027600	0.83009200	2.28226400
H	2.07830400	4.22787900	-0.86244700
H	3.70801300	4.89736800	0.87936100
O	2.05943100	-0.08164000	0.61786700
C	2.73399400	-1.05261300	-0.07385500
C	3.93784700	-0.81479100	-0.73814000
C	2.17261600	-2.34709200	-0.06470200
C	4.59849300	-1.85897800	-1.38285400
H	4.36377800	0.18057900	-0.74373400
C	2.86629500	-3.38086900	-0.70742900
C	4.07071100	-3.14765500	-1.36495400
H	5.53268900	-1.65687900	-1.89595800
H	2.43691300	-4.37647700	-0.71032200
H	4.58347600	-3.96169600	-1.86444900
C	0.96772900	1.87958700	-1.34469900
O	0.98941500	2.54007100	-2.38420200
O	0.08725200	0.96155100	-1.10138500
C	0.87706900	-2.64348300	0.58891300
N	0.72325400	-3.83023000	1.24651200
H	1.53994600	-4.26473200	1.64752000
H	-0.13257200	-3.93243900	1.77397900
N	-0.11709600	-1.82631000	0.44254200
O	-1.31778700	-2.12809300	1.03026000
U	-1.62831200	-0.07589400	0.00703600
O	-1.26393200	0.80953100	1.52337100
O	-2.18666100	-0.86092000	-1.50677400
O	-3.91429500	-0.58833800	0.94184600
H	-4.52475400	-1.22075900	0.54480200
H	-4.15450600	-0.49240100	1.87107500
O	-2.91257300	1.97053900	-0.68314500
H	-3.37575700	2.09945000	-1.51912900
H	-2.96830000	2.79223300	-0.18148800

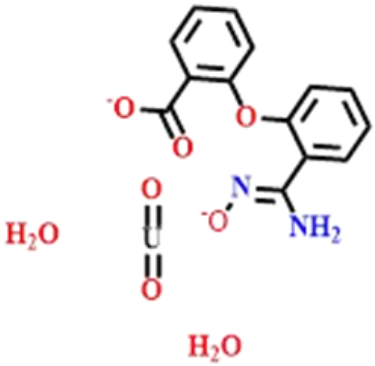

C	4.65234800	2.45655400	1.02824800
C	3.90952100	1.37387600	0.56130300
C	2.51734300	1.38485800	0.66538200
C	1.86098800	2.48264500	1.25043700
C	2.62784000	3.57133400	1.68031400
C	4.01625600	3.56468800	1.58409500
H	5.73371800	2.43088400	0.94427900
H	4.41396700	0.52917500	0.10932700
H	2.11567400	4.42319000	2.11368400
H	4.59230700	4.41140000	1.94023000
O	1.72636000	0.37823900	0.16182700
C	2.29778500	-0.79564700	-0.30416900
C	2.67605100	-0.83737000	-1.64447900
C	2.39847900	-1.94212100	0.50701000
C	3.18616900	-2.00984700	-2.19348100
H	2.56327700	0.05724000	-2.24650100
C	2.90969300	-3.11372300	-0.07291300
C	3.31015600	-3.15262100	-1.40229900
H	3.48114000	-2.02983200	-3.23703400
H	2.98064800	-3.99904300	0.54685900
H	3.70632300	-4.06983300	-1.82340700
C	1.94674700	-2.00426500	1.93585900
C	0.37214900	2.54801100	1.47217200
O	1.85198000	-3.09513400	2.52067700
O	1.66562100	-0.88215600	2.51951900
O	-0.18431300	1.48734500	1.99779300
O	-0.25557800	3.56742900	1.20767500
U	-0.13821800	-0.05975100	3.61231900
O	-2.15785700	1.10094000	4.55325200
H	-2.15009900	1.82466000	5.19111300
H	-3.07662600	0.89551600	4.34284500
O	0.91557100	0.97758000	4.60565100
O	-1.20753600	-1.09634400	2.63590400
O	0.50287100	-2.24236100	4.74071800
H	0.96230200	-2.24979300	5.58896000
H	1.05100900	-2.74127200	4.08368700

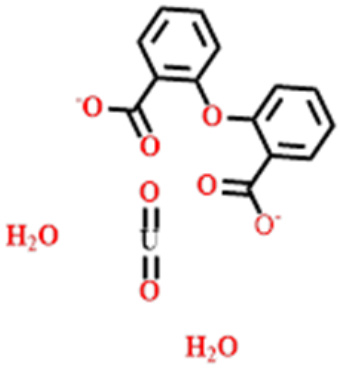

C	4.07559400	2.93298900	2.05838000
C	3.80481200	1.56854100	1.97985000
C	2.74605300	1.11182300	1.20053000
C	1.92014400	2.00869500	0.50159200
C	2.22760200	3.37435900	0.57514100
C	3.29112900	3.83804300	1.34538800
H	4.90253200	3.28281600	2.66674200
H	4.41380500	0.84478800	2.50974700
H	1.60378100	4.07893200	0.03606900
H	3.49852200	4.90128900	1.39530300
O	2.50887900	-0.25757400	1.18830100
C	2.69211500	-0.96292500	0.01450500
C	3.71668500	-0.65811700	-0.87987500
C	1.82319600	-2.03752700	-0.23300100
C	3.88427200	-1.43025800	-2.02798800
H	4.37661000	0.17759400	-0.67884200
C	2.00836000	-2.79909600	-1.39147300
C	3.03444500	-2.50454900	-2.28621300
H	4.68682800	-1.19005200	-2.71721300
H	1.33479100	-3.62594300	-1.58559400
H	3.16616700	-3.10703500	-3.17796800
C	0.67642200	-2.30998800	0.67007300
N	0.88779000	-2.64945100	1.96370400
H	1.78455700	-2.45511500	2.37942600
H	0.08208300	-2.60523600	2.57365000
N	-0.51141200	-2.25842500	0.13844400
O	-1.55657200	-2.41663500	1.07452200
C	0.74688200	1.56647300	-0.30172000
N	0.65254500	2.02135100	-1.59948300
N	-0.16434200	0.85976900	0.28177200
H	1.51851900	2.18843100	-2.09047000
H	-0.05766000	1.55168200	-2.14562100
O	-1.19455000	0.51248200	-0.60501000
V	-2.22365100	-0.87784100	0.16744500
O	-3.22379400	-1.34059400	-1.01858200
O	-3.08604800	-0.16270400	1.34844500

C	-7.71369800	-4.28006500	1.97452200
C	-7.97058200	-5.23161700	0.99071900
C	-9.08948000	-5.09475000	0.17004800
C	-9.94946200	-3.99261900	0.33133200
C	-9.65895800	-3.03423600	1.31336900
C	-8.55414300	-3.17971100	2.14305200
H	-6.84026400	-4.39848000	2.60644800
H	-7.29421300	-6.06547100	0.85144400
H	-10.32259200	-2.18522300	1.43494300
H	-8.35006100	-2.44213500	2.91015300
O	-9.37610100	-5.93919600	-0.86970300
C	-8.73041400	-7.16565400	-0.98961000
C	-7.90494300	-7.32597000	-2.09620800
C	-8.94377600	-8.21891400	-0.08128300
C	-7.26122400	-8.54176300	-2.31753900
H	-7.77121600	-6.48920300	-2.77215800
C	-8.27093800	-9.42761100	-0.31625100
C	-7.44021300	-9.59280700	-1.42054900
H	-6.62040100	-8.66090100	-3.18407500
H	-8.42617800	-10.25502900	0.36656000
H	-6.94296200	-10.54257300	-1.58242900
C	-9.83083100	-8.09548300	1.09638100
N	-9.50842900	-8.76612900	2.25019400
H	-8.52804200	-8.89479500	2.45351400
H	-10.07230200	-8.50855100	3.04950400
N	-10.92571100	-7.42060800	0.99258700
O	-11.72842200	-7.29605300	2.12329000
C	-11.10931000	-3.78749100	-0.55356200
N	-11.20374900	-2.67568900	-1.25911400
N	-12.13303500	-4.69974700	-0.60583500
H	-10.45166200	-2.00466400	-1.29541700
H	-12.03504700	-2.51895400	-1.81695400
O	-13.05729600	-4.40651200	-1.45447300
V	-12.67349800	-6.40092700	0.64176000
O	-14.19941900	-6.90824900	0.31460100

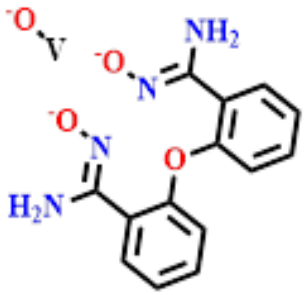

Chapter 4: Computational Investigation of Metal Selectivity by Functionalized Polymers

Adapted from Marek, Piechowicz; R. Chiarizia; and L. Soderholm. *Dalton Transactions*, **2018**, 47, *15*, 5348-5358 with permission from The Royal Society of Chemistry.

4.1 Introduction

Continuing this investigation into selective uranium binding, we describe herein the uranium uptake characteristics of a bis-amidoxime functionalized polymer, comparing its performance with uptake results of selected alkali and alkaline earth metal cations. While many studies have hitherto focused on the design and synthesis of amidoxime based materials for uranium sequestration from seawater under seawater-specific conditions, the purpose of this work is to more fully investigate the selectivity of amidoxime for uranium with particular emphasis placed on pH, buffer effects, and competing ions. Results show that >99% uranium was sorbed from an acetate buffered solution with a maximum distribution ratio of $\mathbf{1.4 \cdot 10^5}$ mL g^{-1}. Studies with ^{90}Sr and ^{137}Cs were conducted to investigate the uptake behavior of larger mono- and divalent cations which have typically caused problems in solid-phase sorbent materials by competing for available binding sites.[1] Strontium uptake is negligible throughout the pH range studied whereas cesium uptake averages less than 30% from solution under acidic or basic conditions and effectively zero under the near neutral conditions of interest. The uptake studies are in good agreement with computational work used to predict the order of selectivity.

Functionalized polymers, in the form of amidoxime-functionalized (-R=NNH_2OH) braided fibers[2] and diphosphonate-functionalized resins[3] in particular, have garnered recent interest for use in the extraction of uranium from seawater and actinide separation from mixed waste.[4] Preliminary investigations of amidoxime-metal binding in aqueous solutions[5] yielded high stability constants

for uranyl-acetamidoxime complexes, on the order of $\boldsymbol{\beta_{11} \sim 10^{10}}$, corroborating earlier studies[6] which suggested that amidoxime based polymers are among the only materials suited for uranium uptake from aqueous solutions. Moreover, follow-up work[5] demonstrated that uranium uptake by amidoxime functionalized polymers was selective over Co^{2+}, Ni^{2+}, and Zn^{2+} with empirical selectivity factors (α) on the order of ~10^3 for Co^{2+}, Ni^{2+} and ~10^4 for Zn^{+2}. Recently published studies investigating the tridentate analogue of diamidoxime—glutarimidedioxime—confirm this trend in selectivity of UO_2^{2+} over Ni^{2+}.[7] For uranium from seawater applications, where VO_2^+ is the main competitor for U binding sites,[8] recently discovered bis-amidoxime functionalized polymers enjoy an advantage with selectivity factors of U over V around 3 (corresponding to a 5:1 w/w U to V uptake ratio).[9]

4.2 Theoretical Methods

All calculations utilized the Gaussian 16RevA.03 quantum chemistry program[10] with DFT at the B3LYP[11,12] level of theory. All light atoms were modeled by the 6-311+G* basis set. Cs and Sr were modeled using the LANL2DZ effective core potential while U was modeled with the Stuttgart RSC 1997 relativistic effective core potential, known in the literature to yield reasonable geometries and thermodynamics of metal-ligand species.[13–15] The protocols used in this work are appropriate for all atoms studied including uranium and represent standard methods used by the community to investigate such coordination complexes.[16–18] Solvation with water was modeled using the conductor-like polarizable calculation model (CPCM) unless gas phase explicitly stated.[19] Generally, complexes were geometrically optimized first and then subjected to frequency calculations and natural bond orbital (NBO) analysis using the same basis set and level of theory. The quantum theory of atoms in molecules (QTAIM) approach was explored using the Multiwfn

program version 3.3.9.[20,21] Electron density, the Laplacian of electron density, the energy density at bond critical points, Wiberg, and Laplacian Bond Indices were calculated with Multiwfn 3.3.9.

4.3 Experimental Methods

4.3.1 General Experimental

Caution! Materials used herein are radioactive and as such are considered health risks. Their use requires proper facilities, correct PPE, and appropriate training.

Nitric acid was ACS reagent grade and used as received. All water used for uptake experiments was obtained from a Milli-Q2 system with a measured resistivity of at least 18 MΩ. Radiochemical experiments were performed using solutions of ^{90}Sr, ^{137}Cs, and ^{233}U obtained from ANL stock. The ^{233}U stock was 30.6 mM in 1M HNO_3. The ^{90}Sr stock was in aqueous solution. The ^{137}Cs stock was 87 μM in 0.01 M HNO_3. All other reagents including liquid scintillation counting cocktail, sodium acetate, and ammonium hydroxide were used as received.

Uptake studies were conducted in 10 mL glass vials with ~1 mg polymer at a phase ratio of 1 mg polymer per 1 mL spiked solution. Radionuclides were spiked in such a way to yield A_0 <10 000 cpm 100 μL^{-1}. Samples were shaken for 30 minutes on a plate shaker at 500 rpm prior to centrifugation and syringe filtration (Whatman, PVDF, 0.2 μm pore size). Empirically, distribution ratios were calculated according to the following equation:

$$D_{W,exp} = \frac{A_{0,corr} - A_{F,corr}}{A_{F,corr}} * \frac{V}{m} \quad \textbf{Equation 4.1}$$

Where $A_{0,corr}$ is the background corrected initial counts as determined by alpha/beta or gamma counting, $A_{F,corr}$ is the background corrected final counts post-uptake, V is the volume of the

solution in µL, and m is the mass of the polymer in mg. In all cases, approximately 1 mg of polymer was used with a phase ratio of 1 mg mL^{-1}.

Buffers were prepared according to standard procedures found in the literature. The alkaline pH region (pH 8-10) was attained with an ammonium buffer ($[NH_3] + [NH_4^+] = 0.01$ M). The near neutral pH region (pH 4-7) was attained with a sodium acetate buffer ($[CH_3COO^-] + [CH_3COOH] = 0.01$ M). Acidic conditions (pH = 2, 3) were attained with HNO_3 at the proper concentration. Conditions below pH = 2 were not investigated due to filtration difficulties encountered at higher acidities.

Complexing ion concentration was calculated for the acetate ligand used as part of the buffer media. Significant deviations in D_W values obtained with (3) have been corrected using the procedure outlined in **4.10 Appendix 4.2**. Corrected and uncorrected values are included in **Figure 4.4** below.

Owing to the challenge of accurately determining pK_a values of amidoxime groups on polymers,[22] we chose a broad pH range to study metal ion uptake. Best estimates suggest the protonated-neutral proton transfer occurs around pH ~5.5 and the neutral-anionic transition occurs around pH ~10.[23] Exploring uptake over a wide pH range allows us to investigate the performance of the amidoximated polymer over a range of potential protonation states and to make accurate comparisons with state-of-the-art materials for U uptake from water, which are typically studied at near neutral conditions.

Alpha and beta counting were performed via liquid scintillation on a Packard Model 2000 CA counter using an LSC cocktail volume of 5 mL. Gamma counting was performed using a Packard Cobra Autogamma counter. Regions of interest (ROIs) were individually selected for each isotope to include highest intensity emissions.

4.3.2 Material Design, Synthesis, and Characterization

The chemical structure and synthesis of the bis-amidoximated polymer used for uptake studies is shown in **Scheme 4.1**. Full synthetic details and characterization of the polymer material can be found **Chapter 3**. In brief, vinylated dicyano diaryl ether was copolymerized with *N,N′*-methylenebis(acrylamide) (NNBIS) to afford a hydrophilic crosslinked polymer with dicyano loading of 1.98 mmol per gram polymer. Treatment with hydroxylamine hydrochloride in ethanol afforded the bis-amidoxime species (**Scheme 4.1**).

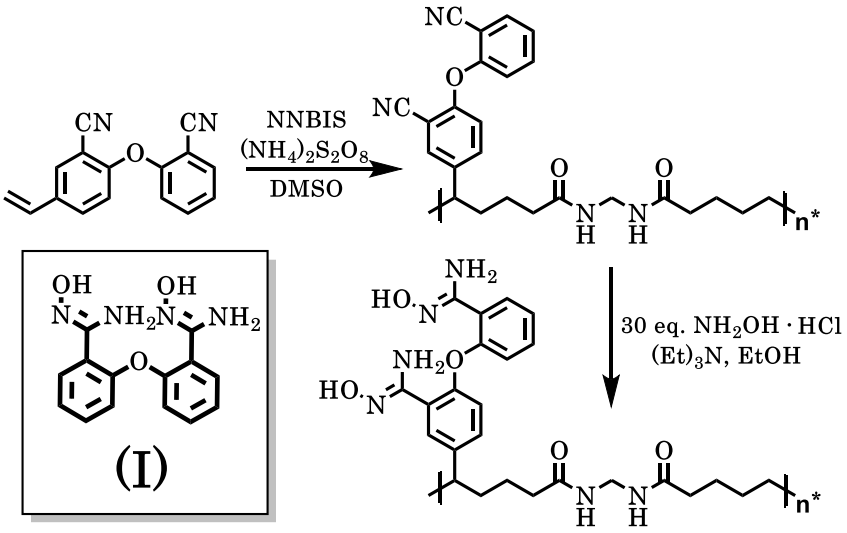

Scheme 4.1 Synthesis of bis-amidoxime functionalized polymer

4.4 *in Silico* Studies of Bis-Amidoxime Coordination Complexes

DFT calculations were performed on Sr, Cs, and U complexed bis-amidoxime species. Various starting geometries were investigated to assess optimized structures and provide a reasonable representation of the metal coordination environment on the polymer. Optimized structures obtained for Sr, Cs, and U complexes with the bis-AO ligand (I) in different protonation states are shown in Figures 1, 2, and 3. Corresponding Cartesian coordinates are provided in **4.9**

Appendix 4.1. In most cases, starting geometries consist of (A) one metal ion near one amidoxime, (B) one metal ion in a binding pocket, (C) one metal ion near each amidoxime, and (D) one metal ion near amidoxime and one in a binding pocket. In these instances, the binding pocket is taken to be the region between the amidoximes where a metal can interact with both functional groups and the central diaryl ether oxygen. It was originally hypothesized that uranium would be strongly bound by the amidoxime ligands[24] and that both cesium and strontium would be excluded from strong binding on account of their larger ionic radii. However, since methylenebisacrylamide was used as the crosslinker in the original polymer synthesis, some amount of Cs and Sr uptake was expected.

4.4.1 Calculations with Sr^{2+}

Strontium is bound by the deprotonated bis-amidoxime ligand in a monodentate fashion in plane with the amidoxime oxygen at a distance of 2.51 Å (**Table 4.2**). Upon protonation, the metal rotates below the plane of the amidoxime and the corresponding Sr-O bond length increases to 2.79 Å, similar to Sr-O distances in Sr-NO_2 published structures.[25] Further protonation maintains the bonding geometry but lengthens the Sr-O distance by 0.2 Å to 2.98 Å as expected. The complexation reaction between the bis-amidoxime ligand and strontium is exergonic for the deprotonated ligand and endergonic for both the neutral and positive states. The reaction between strontium and deprotonated bis-amidoxime is the only one that occurs spontaneously at room temperature (**Table 4.1**).

Table 4.1 Thermodynamics of Sr-bis-AO Complexes

		Sr^{2+}	
ΔG (kcal mol^{-1})	bis-AO^{-1}	bis-AO	bis-AO^{+1}
(A) 1 Sr	-6.217	6.079	9.716
(B) 1 Sr in binding pocket	5.425	8.897	7.039
(C) 2 Sr	1.881	13.668	20.175
(D) 2 Sr, only 1 in binding pocket	13.296	18.652	

The QTAIM approach was used to provide more insight into the binding character of bis-amidoxime and strontium. Specifically, the electron density (ρ), the Laplacian of the electron density ($\nabla^2\rho$), and the energy density at a bond critical point ($H(r)$) were calculated using the Multiwfn program with DFT optimized structures as discussed above. These metrics have been successfully used in the literature to evaluate metal ligand binding in solid sorbent materials.[26] The electron density (ρ) at the critical point between Sr and the amidoxime oxygen decreases from 0.032 a.u. to 0.017 a.u. to 0.010 a.u. as the bis-amidoxime ligand undergoes successive protonation (**Table 4.2**). In general, values of $\rho > 0.20$ a.u. suggest a greater degree of covalency in comparison with ρ values < 0.10 a.u. which suggest a greater degree of ionic character. Using these guides therefore, the Sr-O interaction can ostensibly be considered ionic in character although other metrics including long Sr-O distances suggest a non-bonding interaction. The Laplacian of electron density ($\nabla^2\rho$), the divergence of the gradient of electron density over *xyz* space, is positive in all three cases and decreases as expected. Negative (positive) values for $\nabla^2\rho$ would suggest covalent (ionic) character. Finally, the energy density at bond critical points ($H(r)$) serves as another check of bond character. Positive values are suggestive of ionic bond character and are observed for each Sr-O interaction in these cases.

Natural Bond Orbital (NBO) analysis was performed in order to obtain natural population analysis on the metal centers of interest. In all three Sr complexes above, the natural charge on the

Sr deviates insignificantly from the expected value of +2.0 corroborating the non-bonding interactions observed. Wiberg and Laplacian bond indices were calculated using the Multiwfn program. Wiberg bond indices (WBIs) often correlate well with formal bond order while the Laplacian bond order (LBO) correlates well with *covalent* bond order. The WBIs for the Sr-O bond steadily decrease in magnitude from 0.33 to 0.19 to 0.14 upon successive ligand protonation. Concurrently, the LBO remains a small, positive value below 0.06, further suggesting the lack of covalent character in the Sr-O interactions.

Initially placing the strontium within the binding pocket of the bis-amidoxime chelator yields optimized structures where the strontium lies above the plane of the diaryl ether oxygen, with the smallest (largest) angular deviation apparent in the deprotonated (protonated) complex (**Figure 4.1**). Long Sr-C**O**C bond distances, on the order of 3.3 to 4.1 Å, suggest limited influence of the diaryl ether oxygen. In both deprotonated and neutral cases, the amine nitrogen exhibits a binding interaction with the Sr metal ion with WBIs of 0.26 and 0.19 respectively. Thermodynamics of complexation do not improve with binding pocket geometry, with an average Gibbs free energy change of approximately +7 kcal mol^{-1} (**Table 4.1**). For comparison, the complexation of strontium cation with dicyclohexano-18-crown-6, a ligand with demonstrated affinity for Sr,[27,28] was also studied with DFT under identical conditions. The optimized structure gave a ΔG of -7.01 kcal mol^{-1}, signifying that strontium complexation is favorable at room temperature.

The addition of another strontium to form complexes wherein each amidoxime binds one strontium dication yields optimized structures geometrically similar to the mono-strontium cases discussed above. In all cases, the Sr-O bond distance increases with increasing ligand charge and Sr associates out of the amidoxime plane with charged or neutral amidoxime species. In no case is

there any amine contribution to Sr binding. WBIs suggest neither N nor O donates appreciable electron density to the Sr metal center as evidenced by an NPA on Sr close to the dication ideal of +2.0 (**Table 4.2**).

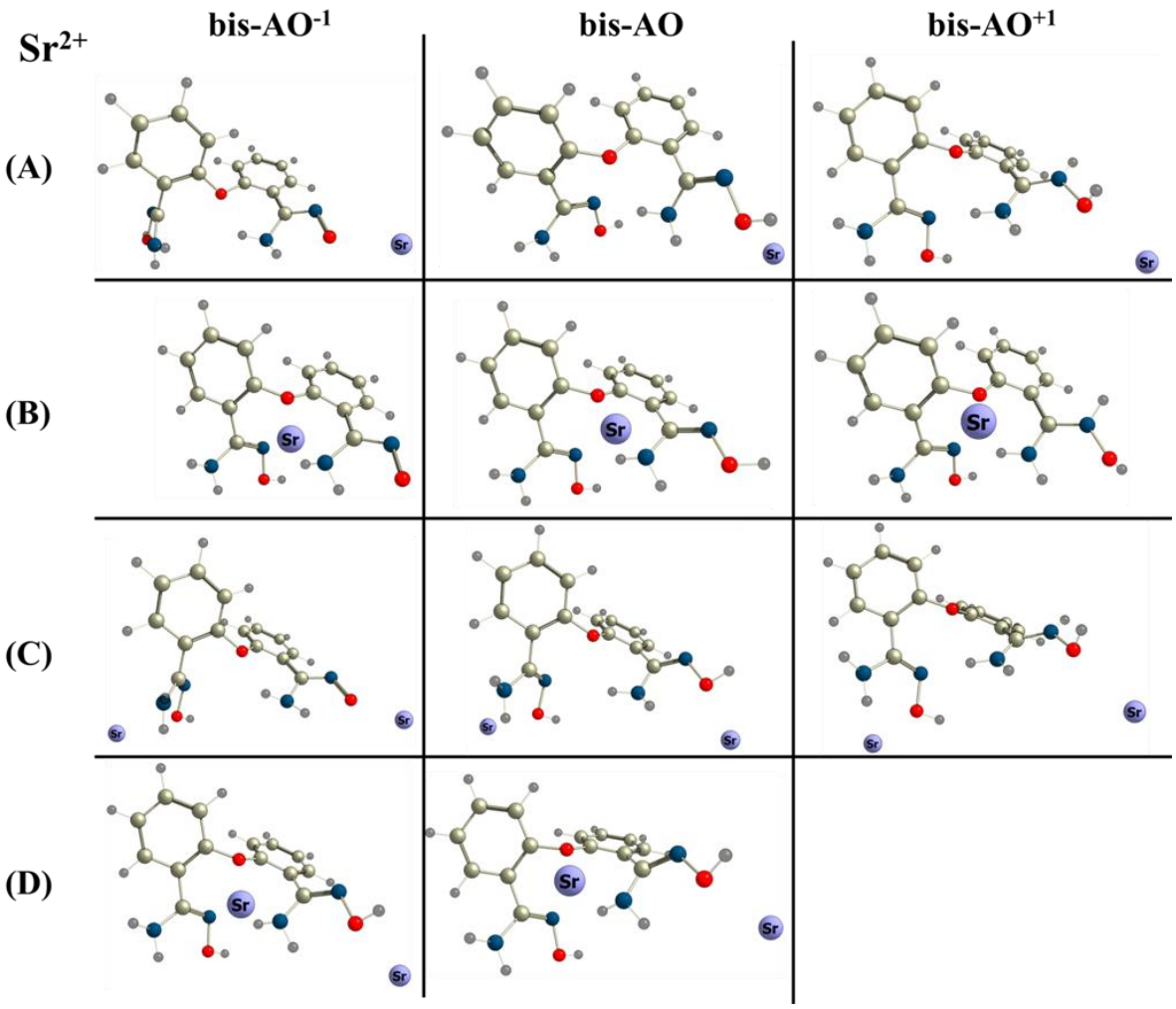

Figure 4.1 Geometrically optimized perspective structures of strontium complexes. The gray, dark gray, red, dark blue, and light blue spheres represent C, H, O, N, and Sr respectively. (A) series contains one strontium near one amidoxime as the starting geometry, (B) series contains one strontium in the binding pocket, (C) series contains one strontium near each amidoxime, and (D) series contains one strontium near amidoxime and one in the binding pocket as the starting geometry. In each case, the shortest Sr-ligand interaction is outside what is considered to be a binding interaction; consequently, lines signifying Sr-ligand bonds are not shown.

Table 4.2 Strontium Complex (A, B) Bond Distances, Bond Indices, Natural Population Analysis, and Selected Metrics

Species	Moiety	Bond	Distance (Å)	ρ	$\nabla^2\rho$	H	WBI	LBO	NPA
Sr (A)	bis-AO^{-1}	Sr-O(neg)	2.506	0.0322	0.1713	0.0045	3.29E-01	5.75E-02	1.99
		Sr-N	3.346	NA			6.98E-02	5.90E-05	
	bis-AO	Sr-O	2.793	0.0168	0.0773	0.0026	1.89E-01	1.38E-02	2.00
		Sr-N	3.669				3.15E-02	1.94E-06	
	bis-AO^{+1}	Sr-O (pos1)	2.982	0.0100	0.0469	0.0019	1.39E-01	6.49E-03	2.00
		Sr-N	3.946				1.47E-02	2.30E-07	
Sr (B)	bis-AO^{-1}	Sr-O	3.976	NA			1.32E-02	4.91E-06	1.99
		Sr-N(amine)	2.753	0.0234	0.1009	0.0026	2.57E-01	2.64E-02	
		Sr-C**O**C	3.281	NA			5.20E-02	8.35E-04	
	bis-AO	Sr-O	4.082				7.89E-03	1.13E-06	1.99
		Sr-N (amine)	2.913	0.0167	0.0684	0.0021	1.89E-01	1.13E-02	
		Sr-C**O**C	3.323				5.06E-02	6.05E-04	
	bis-AO^{+1}	Sr-O (pos1)	5.650				6.65E-04	0	2.00
		Sr-N (amine, pos1)	4.878				2.26E-03	1.00E-08	
		Sr-C**O**C	4.105	0.0007	0.0037	0.0002	6.38E-03	3.77E-06	

Placement of two strontium ions (one in binding pocket geometry and one amidoxime bound) yields optimized structures with one strontium associated with an amine in the binding pocket and one bound to the amidoxime in either monodentate or η^2 fashion in geometries consistent with the structures discussed above. The deprotonated complex yields a Sr-N and Sr-O binding geometry consistent with an η^2 interaction. The thermodynamic difference between monodentate and η^2 binding geometries is not expected to be significant based on literature precedent.[29,30] In both cases, the free energy change becomes more positive. When the bis-amidoxime ligand is neutral, the Sr-O and Sr-NH_2 interactions are approximately equivalent in strength according to WBI and LBO analysis. The positively charged bis-amidoxime with strontium in the binding pocket failed to converge, yielding the ligand internally hydrogen bonded.

Table 4.3 Strontium Complex (C,D) Bond Distances, Bond Indices, Natural Population Analysis, and Selected Metrics

Species	Moiety	Bond	Distance (Å)	ρ	$\nabla^2\rho$	H	WBI	LBO	NPA
Sr (C)	bis-AO^{-1}	Sr1-O (neutral AO)	2.782	0.0171	0.0796	0.0027	1.96E-01	1.41E-02	2.00
		Sr1-N	3.713				2.90E-02	1.07E-06	
		Sr2-O (neg1)	2.504	0.0319	0.1717	0.0046	3.30E-01	5.70E-02	1.99
		Sr2-N	3.404				6.05E-02	2.40E-05	
	bis-AO	Sr1-O	2.805	0.0164	0.0751	0.0025	1.88E-01	1.26E-02	2.00
		Sr1-N	3.695				3.06E-02	1.44E-06	
		Sr2-O	2.781	0.0173	0.0799	0.0027	1.92E-01	1.42E-02	2.00
		Sr2-N	3.631				3.44E-02	3.27E-06	
	bis-AO^{+1}	Sr1-O	2.950	0.0120	0.0524	0.0018	1.46E-01	6.03E-03	2.00
		Sr1-N	3.806				2.43E-02	6.50E-07	
		Sr2-O (pos1)	2.983	0.0100	0.0467	0.0019	1.38E-01	6.50E-03	2.00
		Sr2-N (pos1)	3.938				1.49E-02	2.40E-07	
Sr (D)	bis-AO^{-1}	Sr1-N (amine)	2.816				1.03E-01	9.45E-04	1.99
		Sr1-C**O**C	3.412				2.11E-02	7.15E-05	
		Sr2-O (neg1)	2.583	0.0106	0.0423	0.0012	1.42E-01	8.30E-03	1.99
		Sr2-N	2.684	0.0060	0.0234	0.0009	1.96E-01	1.24E-05	
	bis-AO	Sr1-N (amine)	2.996	0.0139	0.0557	0.0018	2.90E-02	6.08E-03	1.99
		Sr1-C**O**C	3.600	0.3011	-0.7083	-0.2935	3.30E-01	8.88E-05	
		Sr2-O	2.830	0.0157	0.0706	0.0023	6.05E-02	9.89E-03	2.00
		Sr2-N	3.619				1.88E-01	6.65E-06	

The DFT results for the Sr-ligand complexes confirm our hypothesis that Sr would not strongly interact with the bis-amidoxime ligand. Owing to the long amidoxime-Sr bond distances observed as well as metal NPA values > 1.99 in all cases suggestive of negligible ligand to metal charge transfer, we conclude that the amidoxime-Sr interactions can be considered non-bonding regardless of the ligand's protonation state. This is largely due to a mismatch in cavity size and metal ionic radius despite geometry optimization.

4.4.2 Calculations with Cs^+

The positively charged ligand with cesium in all four unique starting geometries failed to converge, despite efforts to ease convergence criteria by switching to a quadratically convergent SCF, increasing the number of cycles, or modifying the starting geometry. This lack of

convergence may result from the highly unfavorable electrostatics associated with multiple charged species as well as the large size of the cesium cation. Moreover, resulting structures yielded bis-amidoxime ligands with apparent hydrogen bonding between the amine of one amidoxime and the amine of another with cesium completely excluded from bonding. Rapid convergence was obtained for neutral and anionic species.

Cesium is η^2 bound in the anionic bis-amidoxime case with a Cs-O and Cs-N distance of 3.141 Å and 3.241 Å respectively. In contrast, cesium is bound monodentate to the oxime nitrogen with a Cs-N distance of 3.44 Å in the neutral ligand complex. The Gibbs free energy of complexation is slightly positive in both cases around 3 kcal mol^{-1} (**Table 4.4**).

Table 4.4 Thermodynamics of Cs-bis-AO Complexes

	Cs^+	
ΔG (kcal mol^{-1})	bis-AO^{-1}	bis-AO
(A) 1 Cs	2.841	2.918
(B) 1 Cs in binding pocket	3.970	4.126
(C) 2 Cs	7.290	8.398
(D) 2 Cs, only 1 in binding pocket	7.264	10.154

Interestingly, protonation of the amidoxime increases the free energy of complexation by only <0.1 kcal mol^{-1} suggesting that electrostatic interactions are not the dominant driving force in Cs complexation. Similar to the Sr cases, there is no appreciable difference between the Cs-N and Cs-O interactions in both deprotonated and neutral ligand cases. NPA values of 0.99 agree with the free ion ideal case of +1.0.

Optimized structures with cesium in binding-pocket geometry finds indistinguishable binding thermodynamics with energetics differing by about 1 kcal mol^{-1} (**Table 4.4**). Cesium as bound by the neutral ligand in binding pocket geometry situates itself 3.45 Å from the oxime

oxygen and 3.60 Å from the oxime nitrogen, with WBIs suggesting a stronger Cs-N bond **(Figure 4.2**). Upon deprotonation, the ligand distorts by rotation about the Ar-O-Ar bond in order to accommodate cesium by increasing the Cs-OAr_2 bond distance from 3.41 to 6.33 Å. The resulting structure shows a Cs-amine N distance of 4.10 Å and Cs-O distance of 3.07 Å. In this case, the Cs-O interaction is stronger than the Cs-N interaction as evidenced by higher WBI and LBO bond indices. No improvement is observed to the Gibbs free energy of this ligand distortion for cesium accommodation. To compare, the interaction between cesium cation and the well-known BoBCalixC6 yields a Gibbs free energy of -56.9 kcal mol^{-1} using the same computational parameters.[31]

The addition of another cesium cation to the neutral complex results in monodentate coordination in plane with the oxime nitrogen or above the plane of the oxime oxygen with average bond lengths on the order of ~3.5 Å (**Figure 4.2**). Thermodynamics of complexation become less favorable by 4.3 kcal mol^{-1}. Wiberg bond indices suggest approximately equivalent Cs-O and Cs-N bonds while LBO analysis indicates that the Cs-N interaction is slightly stronger. The anionic ligand complex shows similar cesium binding with the exception that one cesium is η^2 bound. No statistically significant increase in stability is found relative to the neutral ligand complex.

Finally, two complexes were optimized where one cesium was placed in binding pocket geometry and one was placed in close proximity to an amidoxime functional group. In the neutral ligand case, one cesium is bound in plane with an oxime nitrogen with a bond distance of 3.48 Å while the other is bound on the opposite face of the ligand in close proximity to the amine nitrogens of both amidoxime groups. The Gibbs free energy change of complexation becomes more positive by 1.76 kcal mol^{-1} suggesting that binding pocket geometry may be less favorable; specifically, indicating that binding two cesium cations on the same face of the ligand could be preferable.

Similarly, the deprotonated ligand complex with one cesium in the binding pocket and one η^2 bound to an amidoxime yields equivalent free energies.

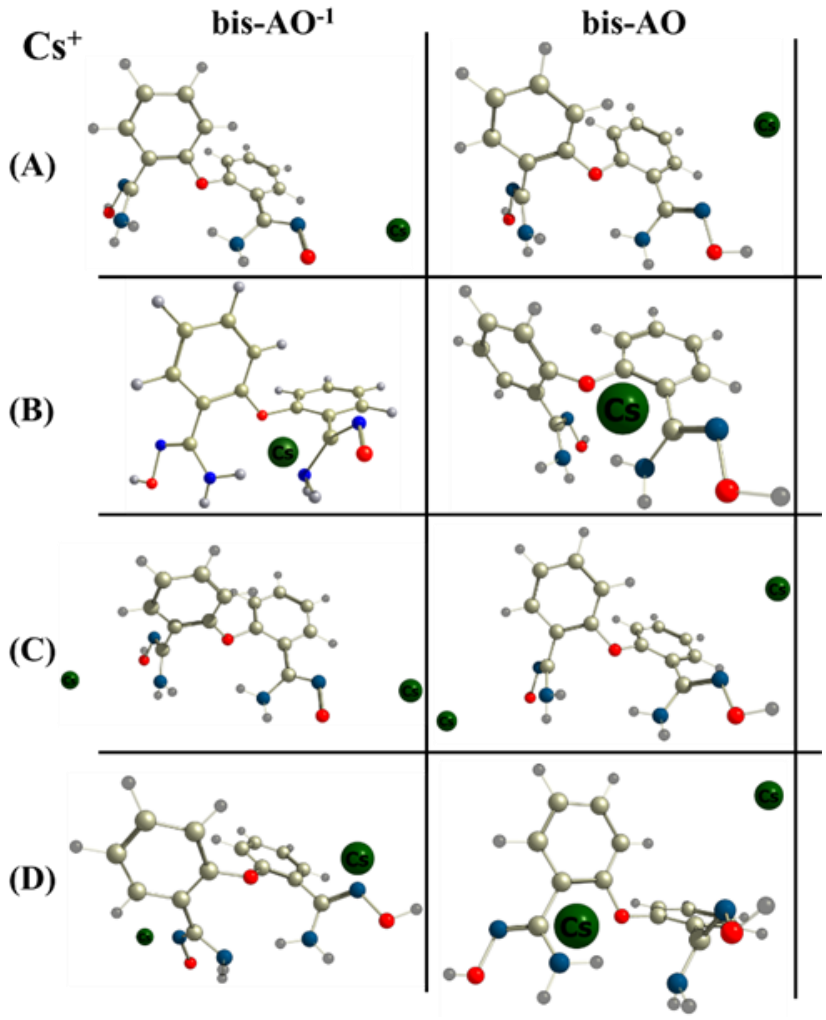

Figure 4.2 Geometrically optimized perspective structures of cesium complexes. The gray, dark gray, red, dark blue, and dark green spheres represent C, H, O, N, and Cs respectively. (A) series contains one Cs near one amidoxime as the starting geometry, (B) series contains one Cs in the binding pocket, (C) series contains one Cs near each amidoxime, and (D) series contains one Cs near amidoxime and one in the binding pocket as the starting geometry.

The positive ΔG values as well as the long Cs-amidoxime distances (~3-4 Å, **Table 4.5**), suggest non-bonding Cs-ligand interactions. Moreover, the small differences in the Gibbs free energy obtained upon addition of another Cs^+ demonstrate that the ligand provides no significant

stabilization through geometry optimization, resulting in poor expected affinity for Cs^+ in experimental studies.

Table 4.5 Cesium Complex Bond Distances, Bond Indices, Natural Population Analysis, and Selected Metrics

Species	Moiety	Bond	Distance (Å)	ρ	$\nabla^2\rho$	H	WBI	LBO	NPA
Cs (A)	bis-AO^{-1}	Cs-O(neg1)	3.141	0.0137	0.0477	0.0008	1.65E-01	5.88E-03	0.99
		Cs-N	3.241	0.0108	0.0443	0.0015	2.05E-01	3.89E-03	
	bis-AO	Cs-O	4.319				8.04E-03	2.20E-07	1.00
		Cs-N	3.442	0.0082	0.0279	0.0011	1.63E-01	4.42E-03	
Cs (B)	bis-AO^{-1}	Cs-N (neg)	4.101				3.52E-02	5.00E-07	1.00
		Cs-O (neg)	3.069	0.0152	0.0554	0.0012	2.35E-01	1.11E-02	
	bis-AO	Cs-O	3.450	0.0073	0.0258	0.0008	8.78E-02	6.39E-04	1.00
		Cs-N	3.604				1.03E-01	2.41E-04	
		Cs-C**O**C	4.576				5.54E-03	6.70E-07	
Cs (C)	bis-AO^{-1}	Cs1-O (neg1)	3.133	0.0140	0.0485	0.0008	1.69E-01	6.20E-03	0.99
		Cs1-N (neg1)	3.251				2.02E-01	3.61E-03	
		Cs2-O	3.364	0.0088	0.0301	0.0009	1.27E-01	1.76E-03	1.00
		Cs2-N	4.135				3.24E-02	1.20E-06	
	bis-AO	Cs1-O	3.356	0.0089	0.0306	0.0009	1.27E-01	1.82E-03	1.00
		Cs1-N	4.112				3.29E-02	1.31E-06	
		Cs2-O	4.326				7.96E-03	2.10E-07	1.00
		Cs2-N	3.442	0.0083	0.0280	0.0011	1.64E-01	4.59E-03	
Cs (D)	bis-AO^{-1}	Cs1-O	3.518	0.0063	0.0233	0.0008	7.14E-02	3.41E-04	1.00
		Cs1-N	3.570	0.0056	0.0214	0.0009	1.02E-01	2.58E-04	
		Cs1-C**O**C	3.895	0.0026	0.0106	0.0005	2.89E-02	5.42E-05	
		Cs2-O (neg1)	3.146	0.0136	0.0475	0.0008	1.65E-01	5.74E-03	0.99
		Cs2-N (neg1)	3.254				2.03E-01	3.64E-03	
	bis-AO	Cs1-COC	4.115				1.79E-02	3.05E-05	1.00
		Cs2-N	3.479	0.0076	0.0268	0.0011	1.58E-01	3.90E-03	
		Cs2-O	4.328	0.0015	0.0068	0.0004	8.23E-03	2.10E-07	1.00

4.4.3 Calculations with UO_2^{2+}

The uranyl dioxocation (UO_2^{2+}), by contrast, exhibits favorable thermodynamics when bound to the bis-amidoxime ligand regardless of the ligand's protonation state. Gibbs free energies decrease from -5.53 kcal mol^{-1} to -8.64 kcal mol^{-1} to -56.12 kcal mol^{-1} as the ligand undergoes successive deprotonations (**Table 4.6**). In the protonated ligand case, the uranyl cation lies parallel

to the plane of the amidoxime group (**Figure 4.3**). Despite long U-O and U-N bond distances, NPA suggests a large degree of ligand to metal charge transfer with values deviating from the +6.0 ideal case by 2.8 units. This trend holds for the neutral and deprotonated ligand cases with values decreasing from 3.20 to 2.67 respectively (**Table 4.7**). Both neutral and anionic ligand complexes exhibit hydrogen bonding between the amine N-H and the oxime N of the adjacent amidoxime moiety despite concomitant uranyl binding.

Comparing the uranyl case with that of cesium, we find the ligand is successful in accommodating the smaller uranyl cation and unsuccessful in accommodating the much larger cesium cation. Optimized structures with uranium show intramolecular hydrogen bonding as well as strong uranium binding. The same complexes with cesium reject the metal cation *in favor of* intra-molecular hydrogen bonding.

Importantly, the addition of another uranyl seems to increase the overall stability of the resulting complex. The free energy of complexation becomes more negative by an average of ~12 kcal mol^{-1}. In each of the three cases, there is pronounced ligand to metal charge transfer due to low natural charges on the metal center (< 3.24). Optimized geometries show similar U-O, U-N bonding motifs and the persistence of intra-molecular hydrogen bonding. Uranium-amidoxime N distances average 2.42 Å, in agreement with the 2.42 Å U-N distance observed in the similar uranium-benzamidoxime crystal structure.[30] Uranium-amidoxime O distances shows greater variability with average distances of 2.56 Å compared to the 2.35 Å U-O bond distance found in the uranium-benzamidoxime complex. Laplacian Bond Indices greater than 0.67 are found for the U-N and U-O interaction in the anionic ligand case, with similarly high LBOs for the U-N interaction in the neutral ligand case (0.64) and for the U-N interaction in the positively charged ligand case (0.52).

Table 4.6 Thermodynamics of U-bis-AO Complexes

		UO_2^{2+}	
ΔG (kcal mol^{-1})	bis-AO^{-1}	bis-AO	bis-AO^{+1}
(B) 1 U binding pocket	-56.124	-8.643	-5.532
(D) 2 U binding pocket	-70.400	-21.268	-13.860

Considering the mismatch in hardness between the soft, heavy alkali and alkaline earth metal ions and amidoxime as well as their much larger ionic radius relative to uranyl, it was hypothesized that uranyl would be sorbed preferentially to strontium and cesium. The results of the DFT study suggest that metal ion affinity by the bis-amidoxime functionalized polymer indeed goes as $Cs^+ \approx Sr^{2+} << UO_2^{2+}$. The deprotonated form of the bis-amidoxime ligand was the only case where complexation with Sr^{2+} was spontaneous at room temperature. Moreover, owing to low metal-ligand LBO values and NPA values close to +2.0 on the metal center, the metal-ligand interaction was expected to be weak and ionic. To compare, all optimized structures with cesium showed NPA values > 0.99 with very little variation in free energy of complexation upon deprotonation. It was also found that the ligand distorts via rotation around the central C-O-C linkage in order to accommodate the Cs^+ in binding pocket geometry. Since this rotation is sterically hindered in the polymeric material, it was thought that cesium binding would be even less favored. Finally, the calculations confirm amidoxime's remarkable affinity for the uranyl dioxocation. Free energies of complexation were exergonic at every geometric configuration and protonation state tested. More importantly, the Gibbs free energy becomes more favorable by ~8 kcal mol^{-1} upon binding another metal ion. In all cesium and strontium cases, multi-metal binding is disfavored at room temperature as evidenced by increasingly positive free energy values. Indeed,

in the computed complexes with uranyl, the ligand is able to orient itself in a way that favors strong binding of two metal ions, behavior not apparent in the optimization of Sr^{2+} and Cs^{+} complexes above. Bis-amidoxime's strong propensity for the formation of stabilizing interactions with uranyl as determined via DFT is one of the main reasons behind its empirically realized selectivity over strontium and cesium.

The computational results underscore several key ligand features that are necessary to exploit for sequestrations with tandem goals of elemental selectivity and high uptake. First, the amidoxime moiety possesses a strong affinity for uranyl owing to its unique geometry and mixture of N and O donors. Tailoring the energetics of the ligand to the metal of interest is a powerful method to instill high uptake characteristics.[24] Second, ligand pre-organization plays a significant role in metal selectivity. In this work, the diaryl ether was purposely chosen for its intermediate flexibility—less flexible than amidoxime functionalized aliphatic molecules but more flexible than the analogous functionalized fluorenes and dibenzofurans reported in the literature to possess high uranium affinity.[32,33] Moreover, the presence of several hydrogen bond acceptors allowed for the possibility of hydrogen bonding to preserve the orientation of the amidoxime moieties until a suitable metal could be exchanged. Intramolecular hydrogen bonding as a tool to preserve some of the ligand pre-organization without the need for a classic conformationally rigid aromatic backbone allows for stronger binding and correspondingly higher uptake. This characteristic of the ligand is expected to vary with pH, with the extent of intramolecular H-bonding more apparent in acidic solutions. Thus, it is the combined effects of favorable ligand electrostatics and high degree of pre-organization that should allow for selective separations.

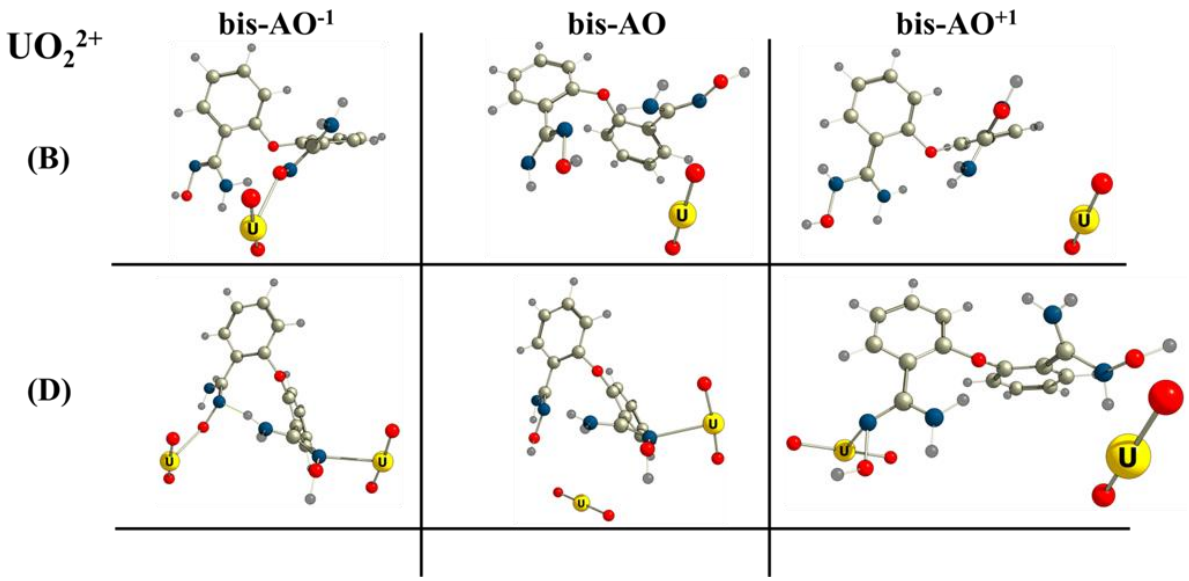

Figure 4.3 Geometrically optimized perspective structures of uranium complexes. The gray, dark gray, red, dark blue, and yellow spheres represent C, H, O, N , and U respectively. (B) and (D) series have the same definitions as before, *vide ante.*

Table 4.7 Uranium Complex Bond Distances, Bond Indices, Natural Population Analysis, and Selected Metrics

Species	Moiety	Bond	Distance (Å)	ρ	$\nabla^2\rho$	H	WBI	LBO	NPA
U (B)	bis-AO^{-1}	U-O(neg1)	2.135	0.0715	0.6498	0.0008	6.40E-01	7.36E-01	2.68
		U-N	3.232				7.15E-02	1.01E-04	
	bis-AO	U-O	4.033	0.0007	0.0057	0.0004	1.07E-02	6.62E-06	3.20
		U-N(amine)	3.856				2.91E-02	5.64E-04	
	bis-AO^{+1}	U-O	3.765	0.0027	0.0129	0.0004	2.10E-02	8.89E-04	3.21
		U-N (amine)	3.902	0.0014	0.0093	0.0006	2.26E-02	2.08E-04	
U (D)	bis-AO^{-1}	U1-O	3.001				1.11E-01	5.36E-03	2.85
		U1-N	2.425	0.0414	0.3240	0.0028	4.10E-01	6.70E-01	
		U2-O (neg)	2.147	0.0700	0.6282	0.0012	6.24E-01	7.25E-01	2.69
		U2-N	3.214				7.23E-02	1.44E-04	
	bis-AO	U1-O	2.902				1.89E-02	2.16E-04	2.82
		U1-N	2.412	0.0422	0.3305	0.0024	1.74E-03	1.00E-08	
		U1-C**O**C	5.370				1.23E-03	0.00E+00	
		U2-O	3.814	0.0011	0.0094	0.0006	1.36E-01	1.22E-02	3.23
		U2-N	4.803				4.11E-01	6.36E-01	
	bis-AO^{+1}	U1-O	2.637				2.25E-01	7.08E-02	2.75
		U1-N	2.413	0.0406	0.3137	0.0018	3.86E-01	5.17E-01	
		U2-O(pos)	3.873	0.0009	0.0078	0.0005	1.57E-02	1.15E-03	3.24
		U2-N	4.747				2.74E-03	4.00E-08	

4.5 Separation Studies

The *in silico* predictions of the relative stabilities of bis-amidoxime coordination complexes have been tested experimentally via pH-dependent studies of Sr^{2+}, Cs^{+}, and UO_2^{2+} uptake (see **Appendix 4.2)**. Depicted in **Figure 4.4**, the amidoximated sorbent shows the highest uranium uptake under near-neutral conditions, sorbing upwards of 99% of U from solution in 30 minutes. This is in line with the computation results, which showed uranium uptake is thermodynamically favorable across the pH range probed in the experiments. Strontium uptake is negligible throughout the same pH range and Cs uptake is small (<15%) under acidic conditions and higher (<30%) under basic conditions.

We observe negligible strontium uptake throughout the pH range (**Table 4.8**). The low affinity for strontium by the bis-amidoxime ligand is best explained by the positive values obtained for the free energy of complexation as well as small deviations from the NPA on the metal center (indicative of a low degree of ligand to metal charge transfer) as determined via DFT calculations.

Table 4.8 Uptake of Sr^{2+}, Cs^{+}, and UO_2^{2+} as a Function of pH

% Sorbed	**Sr^{2+}**	**Cs^{+}**	**UO_2^{2+}**
pH = 10	0	23	45
pH = 9	0	27	43
pH = 8	0	27	30
pH = 6	0	11	99
pH = 5	1.0	10.	99
pH = 4	0	11	72
pH = 3	1.2	18	38
pH = 2	2.0	10	35

Cesium uptake is slightly higher at both pH extremes studied, as expected by the similar free energies obtained from computation. Cs^{+} uptake averages 25.6% between pH = 8 and pH = 10 and

diminishes to an average of 14% between pH = 2 and pH = 3. Distribution ratios of $3.73 \cdot 10^2$ mL g^{-1} at pH = 8 and $2.26 \cdot 10^2$ mL g^{-1} at pH = 3 represent the highest values within

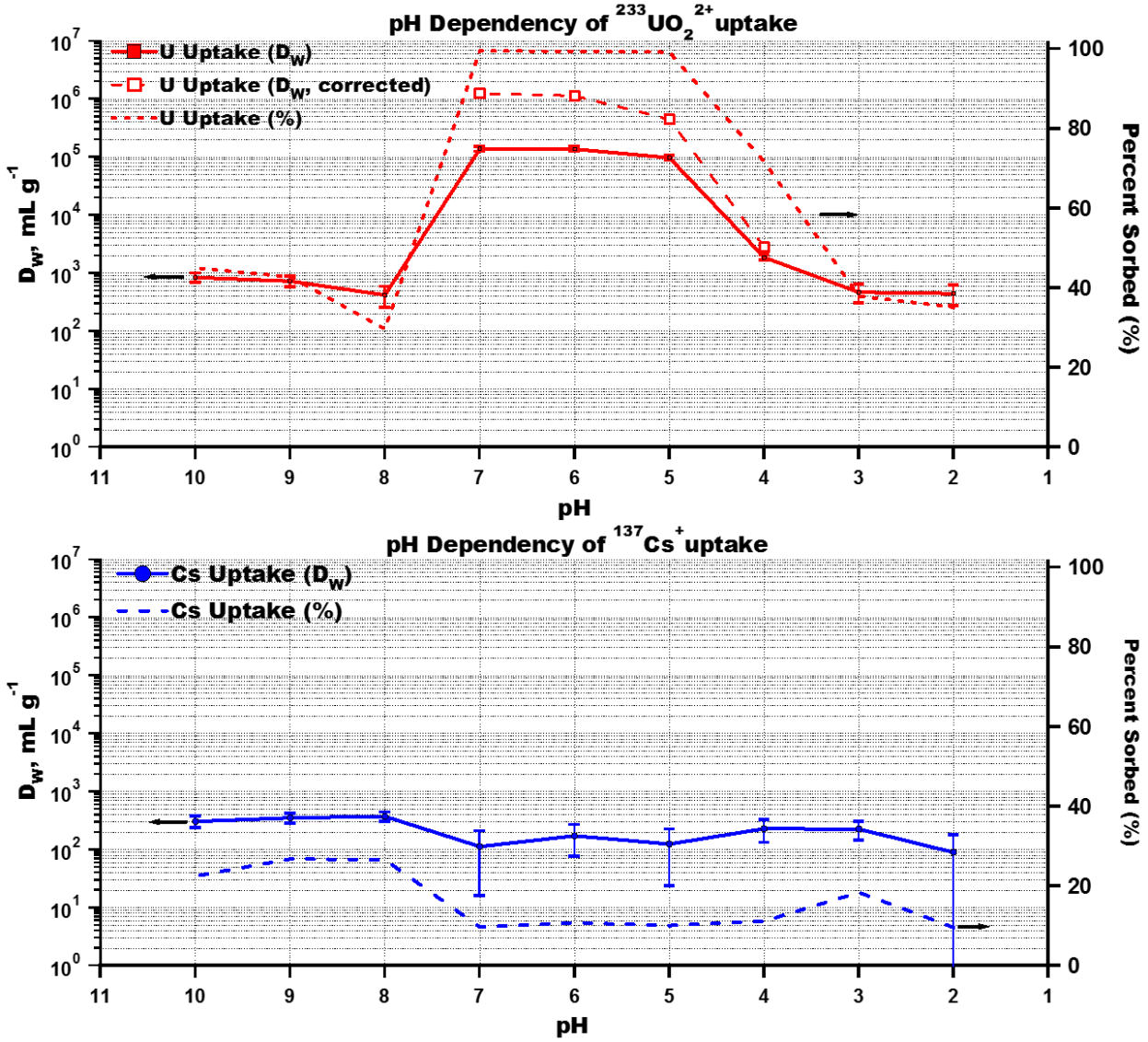

Figure 4.4 Acid dependency studies on $^{90}Sr^{2+}$, $^{137}Cs^+$, and $^{233}UO_2^{2+}$ uptake. Experiments conducted at room temperature at a phase ratio of 1 mg sorbent to 1 mL solution with a mixing time of 30 min. Uptake experiments were repeated to determine the error interval. Error bars are depicted for each point as shown.

the high and low pH ranges, respectively. This small amount of cesium that is sorbed by the polymer may be attributed to binding by the methylenebisacrylamide crosslinker used in the

preparation of the polymeric material. Several examples of amide-Cs^+ complexes exist in the literature[34–37] and some Cs^+ binding contribution from the C=O of the crosslinker would be expected.

Uranium uptake is moderate to high throughout the pH range studied. Under more basic conditions, we see a leveling off of uranyl uptake with a maximum uptake of 45% ($D_W = \mathbf{8.44 \cdot 10^2}$ mL g^{-1} at pH = 10). The drop in uranium uptake under basic conditions could be attributable to buffer effects, since there is an appreciable time dependence in metal uptake (**Figure 4.5**) and/or to the formation of uranyl hydroxo complexes since the formation of monomeric $UO_2(OH)_2$ and dimeric $(UO_2)_2(OH)_2^{2+}$ species directly compete with bis-amidoxime complexation at higher pH.[38]

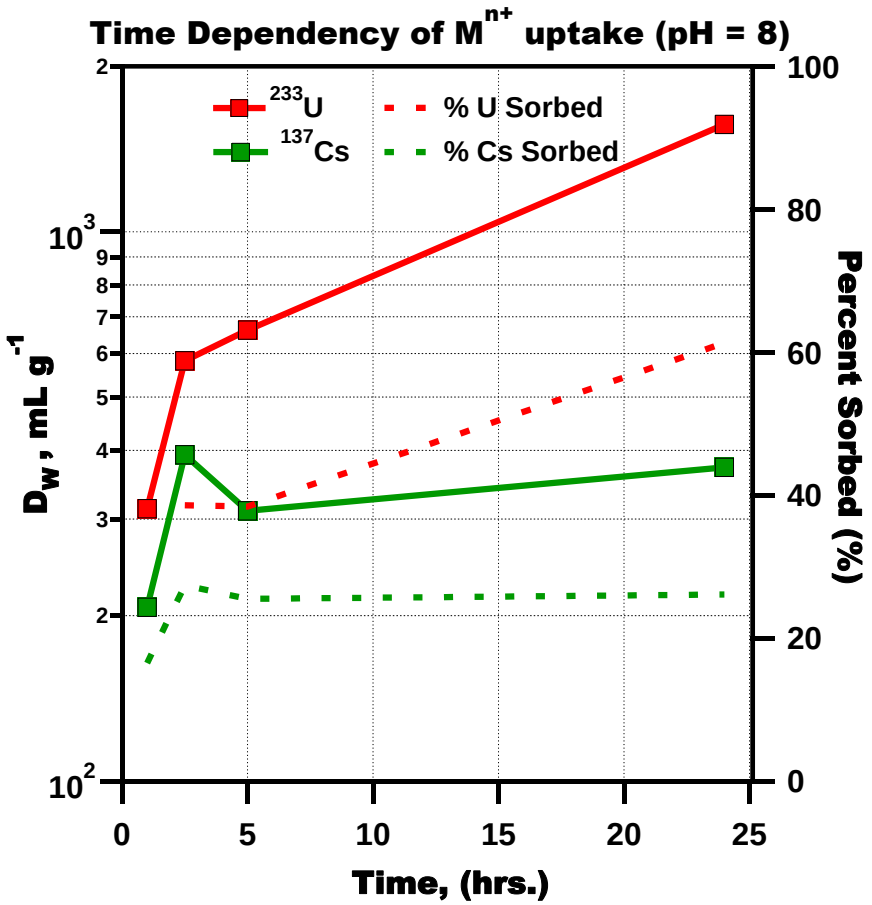

Figure 4.5 Uptake of Cs^+ and UO_2^{2+} at pH = 8 as a function of time.

Similar behavior is seen under acidic conditions with an average U uptake of 37% between pH = 2 and pH = 3 and a maximum D_W of $\mathbf{4.69 \cdot 10^2}$mL g^{-1}at pH = 3.

At near neutral pH, the bis-amidoximated material sorbs upwards of 99% of uranium from solution. Calculated distribution ratios are equal to about 10^5 in the pH 5 to 7 range. Correcting for acetate ion complexation by using **Equation 4.6** found in **Appendix 4.2** gives distribution ratios of about 10^6 in that pH range. These results compare very well to amidoxime functionalized porous aromatic framework materials used for uranium from seawater applications. Ma and co-workers[39] calculated a distribution coefficient (functional form equivalent to the distribution ratio discussed herein) of $1.05 \cdot 10^6$mL g^{-1} for uranium uptake from water at pH = 6 (**Table 4.9**).

Table 4.9 Comparison of Advanced Sorbent Materials for U Uptake

Adsorbent	Type	U uptake	M^+ Uptake	M^{2+} Uptake	Conditions	Uptake Time
Bis-amidoxime functionalized polymer (this work)	Polymer	$D_W^{UO_2^{2+}} = 1.38 \cdot 10^5 mL\ g^{-1}$	$D_W^{Cs^+} = 1.8 \cdot 10^1 mL\ g^{-1}$	$D_W^{Sr^{2+}} = 0$	pH = 6, aqueous solution	30 min
Amidoxime Functionalized Porous Aromatic Framework[40]	Polymer	$K_D^{UO_2^{2+}} = 1.05 \cdot 10^6\ mL\ g^{-1}$	U uptake affected by presence of NaCl, and $NaHCO_3$		pH = 6, aqueous solution	30 min
Polysulfide/Layered Double Hydroxide[41]	Inorganic	$K_D^{UO_2^{2+}} = 8.4 \cdot 10^5\ mL\ g^{-1} - 3.4 \cdot 10^6\ mL\ g^{-1}$	U uptake not affected by presence of $CaCl_2$, NaCl, and $NaNO_3$		pH = 6, aqueous solution	24 hrs. – 3 days
Layered metal sulfide[42]	Inorganic	$K_D^{UO_2^{2+}} = 2.7 \cdot 10^4\ mL\ g^{-1}$	$K_D^{Cs^+} = 5.5 \cdot 10^4\ mL\ g^{-1}$	$K_D^{Sr^{2+}} = 2.7 \cdot 10^4 mL\ g^{-1}$	pH = 7, aqueous solution	15 hrs.
Fe_3O_4@MOF composite material[43]	Inorganic	$K_D^{UO_2^{2+}} \sim 2.1 \cdot 10^3\ mL\ g^{-1}$	Not investigated		pH = 5.5, aqueous solution	24 hrs.
Amidoxime functionalized hydrogel particles[44]	Polymer	$K_D^{UO_2^{2+}} \sim 6 \cdot 10^4\ mL\ g^{-1}$	U uptake affected by Na^+ and Mg^+,		Artificial groundwater, pH = 5.9	5 min

The selectivity of uranium over cesium and strontium stands in direct juxtaposition to certain conventional ion-exchange resins such as Dowex 50-X8 whose affinity for Sr^{2+} over UO_2^{2+}

under similar conditions is twice as high.[1] A more direct comparison with other amidoximated polymeric sorbents[39,43] shows that the bis-amidoximated material discussed herein holds a distinct advantage in its selectivity for uranyl over alkali or alkaline earth metals at near neutral conditions. Amidoxime functionalized hydrogel particles developed by Blake and co-workers[43] realize nearly 100% uranium uptake from groundwater solutions spiked with 30 ppb or 1 ppm U in under 5 minutes. However, significant amounts of Na^+ (~100%) and Mg^{2+} (~25%) are also sorbed suggesting poor selectivity of their hydrogel material for uranium in the presence of mono- and divalent cations (**Table 4.9**).

The bis-amidoxime functionalized polymer also outperforms layered metal sulfide materials both in terms of uptake and selectivity. Using one such material, Sarma *et al*.[41] found distribution coefficients of $5.5 \cdot 10^4$mL g^{-1} for Cs^+, $3.9 \cdot 10^5$ mL $g^{-1}$for Sr^{2+}, and $2.7 \cdot 10^4$mL g^{-1} for UO_2^{2+} from uptake studies conducted in water at pH ~ 7. Distribution ratios obtained using the bis-amidoxime polymer at pH = 6 are $1.8 \cdot 10^1$mL g^{-1} for Cs^+, 0 mL g^{-1} for Sr^{2+}, and $1.4 \cdot 10^5$mL g^{-1} for UO_2^{2+} demonstrating this material's high U affinity and selectivity (**Table 4.9**).

4.6 Conclusion and Outlook

We provide evidence for the selective nature of uranium uptake by bis-amidoxime functionalized polymer materials and compare the computational and experimental results to other state of the art materials.

DFT calculations determined that the bis-amidoxime ligand has poor affinity for both cesium and strontium as evidenced by: (i) Large, positive Gibbs free energies on the order of 3-6 kcal mol^{-1}; (ii) low WBI and LBO ligand-metal bond indices; and (iii) a small deviation from the NPA on each metal center. Uranyl bound ligands, on the other hand, showed favorable binding

thermodynamics and significant reductions in the NPA on each metal center. The bis-amidoxime ligand was found to exhibit stabilizing interactions with uranium with little to no affinity for strontium and cesium despite undergoing the same geometry optimization. Multiple uranium ions can be favorably bound to the bis-amidoxime ligand regardless of the ligand's protonation state. The notion that a singular uranyl binding event enhances bis-amidoxime's affinity for a second uranyl ion[44,45] holds important implications for the design of more effective radionuclide chelators and merits further study.

The amidoximated polymer was found to sorb nearly 100% of ^{233}U from a 0.01 M acetate buffered solution at near neutral pH in 30 minutes.[46] Importantly, ^{90}Sr uptake was insignificant and ^{137}Cs uptake was low under the same conditions corroborating the computational calculations. Moreover, at near neutral pH, the amidoximated polymer is able to decontaminate water to significantly below the 30 ppb U target set by the US Environmental Protection Agency[46] with a starting U concentration of 330 ppb and a final U concentration of 2.6 ppb.

The judicious combination of hydrophilic crosslinker and highly uranophilic ligand as predicted via computational calculations resulted in fast kinetics and uranium selectivity in the <400 ppb regime; both features highly desirable for time-sensitive decontamination applications.

4.7 Funding and Acknowledgements

This work is supported by the U.S. Department of Energy, Office of Science, Office of Basic Energy Sciences, Division of Chemical Sciences, Biosciences and Geosciences, the Heavy Element Chemistry program, under Contract DE-AC02-06CH11357. We acknowledge the University of Chicago Research Computing Center for support of this work. We acknowledge Professor Wenbin Lin at the University of Chicago for support of this work.

4.8 References

(1) Bonner, O. D. A Selectivity Scale for Some Monovalent Cations on Dowex 50. *J. Phys. Chem.* **1954**, *58* (4), 318–320.

(2) Lashley, M. A.; Mehio, N.; Nugent, J. W.; Holguin, E.; Do-Thanh, C.-L.; Bryantsev, V. S.; Dai, S.; Hancock, R. D. Amidoximes as Ligand Functionalities for Braided Polymeric Materials for the Recovery of Uranium from Seawater. *Polyhedron* **2016**, *109*, 81–91.

(3) Chiariza, R.; Horwitz, E. P.; Alexandrators, S. D.; Gula, M. J. Diphonix® Resin: A Review of Its Properties and Applications. *Sep. Sci. Technol.* **1997**, *32* (1–4), 1–35.

(4) Abney, C. W.; Mayes, R. T.; Saito, T.; Dai, S. Materials for the Recovery of Uranium from Seawater. *Chem. Rev.* **2017**, *117* (23), 13935–14013.

(5) Hirotsu, T.; Katoh, S.; Sugasaka, K.; Seno, M.; Itagaki, T. Binding Properties of a Polymer Having Amidoxime Groups with Proton and Metal Ions. *Sep. Sci. Technol.* **1986**, *21* (10), 1101–1110.

(6) Schenk, H. J.; Astheimer, L.; Witte, E. G. G.; Schwochau, K. Development of Sorbers for the Recovery of Uranium from Seawater. 1. Assessment of Key Parameters and Screening Studies of Sorber Materials. *Sep. Sci. Technol.* **1982**, *17* (11), 1293–1308.

(7) Sun, X.; Xu, C.; Tian, G.; Rao, L. Complexation of Glutarimidedioxime with Fe(III), Cu(II), Pb(II), and Ni(II), the Competing Ions for the Sequestration of U(vi) from Seawater. *Dalt. Trans.* **2013**, *42* (40), 14621.

(8) Kelley, S. P.; Barber, P. S.; Mullins, P. H. K.; Rogers, R. D. Structural Clues to UO_2^{2+} /VO_2^{+} Competition in Seawater Extraction Using Amidoxime-Based Extractants. *Chem. Commun.* **2014**, *50* (83), 12504–12507.

(9) Piechowicz, M.; Abney, C. W.; Thacker, N. C.; Gilhula, J. C.; Wang, Y.; Veroneau, S. S.; Hu, A.; Lin, W. Successful Coupling of a Bis-Amidoxime Uranophile with a Hydrophilic Backbone for Selective Uranium Sequestration. *ACS Appl. Mater. Interfaces* **2017**, *9* (33), 27894–27904.

(10) Frisch, M. J.; Trucks, G. W.; Schlegel, H. B.; Scuseria, G. E.; Robb, M. A.; Cheeseman, J. R.; Scalmani, G.; Barone, V.; Mennucci, B.; Petersson, G. A.; Nakatsuji, H.; Caricato, M.; Li, X.; Hratchian, H. P.; Izmaylov, A. F.; Bloino, J.; Zheng, G.; Sonnenberg, J. L.; Hada, M.; Ehara, M.; Toyota, K.; Fukuda, R.; Hasegawa, J.; Ishida, M.; Nakajima, T.; Honda, Y.; Kitao, O.; Nakai, H.; Vreven, T.; Montgomery, J. A., Jr.; Peralta, J. E.; Ogliaro, F.; Bearpark, M.; Heyd, J. J.; Brothers, E.; Kudin, K. N.; Staroverov, V. N.; Kobayashi, R.; Normand, J.; Raghavachari, K.; Rendell, A.; Burant, J. C.; Iyengar, S. S.; Tomasi, J.; Cossi, M.; Rega, N.; Millam, J. M.; Klene, M.; Knox, J. E.; Cross, J. B.; Bakken, V.; Adamo, C.; Jaramillo, J.; Gomperts, R.; Stratmann, R. E.; Yazyev, O.; Austin, A. J.; Cammi, R.; Pomelli, C.; Ochterski, J. W.; Martin, R. L.; Morokuma, K.; Zakrzewski, V. G.; Voth, G.

A.; Salvador, P.; Dannenberg, J. J.; Dapprich, S.; Daniels, A. D.; Farkas, O.; Foresman, J. B.; Ortiz, J. V.; Cioslowski, J.; Fox, D. J.Gaussian 09, revision A.02; Gaussian, Inc.: Wallingford, CT, **2009**.

(11) Lee, C.; Yang, W.; Parr, R. G. Development of the Colle-Salvetti Correlation-Energy Formula into a Functional of the Electron Density. *Phys. Rev. B* **1988**, *37* (2), 785–789.

(12) Becke, A. D. Density-functional Thermochemistry. III. The Role of Exact Exchange. *J. Chem. Phys.* **1993**, *98* (7), 5648–5652.

(13) Boda, A.; De, S.; Ali, S. M.; Tulishetti, S.; Khan, S.; Singh, J. K. From Microhydration to Bulk Hydration of Sr^{2+} Metal Ion: DFT, MP2 and Molecular Dynamics Study. *J. Mol. Liq.* **2012**, *172*, 110–118.

(14) Ali, S. M. Design and Screening of Suitable Ligand/Diluents Systems for Removal of Sr2+ Ion from Nuclear Waste: Density Functional Theoretical Modelling. *Comput. Theor. Chem.* **2014**, *1034*, 38–52.

(15) Yang, Y.; Weaver, M. N.; Merz, K. M. Assessment of the "6-31+G** + LANL2DZ" Mixed Basis Set Coupled with Density Functional Theory Methods and the Effective Core Potential: Prediction of Heats of Formation and Ionization Potentials for First-Row-Transition-Metal Complexes. *J. Phys. Chem. A* **2009**, *113* (36), 9843–9851.

(16) Sonnenberg, J. L.; Hay, P. J.; Martin, R. L.; Bursten, B. E. Theoretical Investigations of Uranyl-Ligand Bonding: Four- and Five-Coordinate Uranyl Cyanide, Isocyanide, Carbonyl, and Hydroxide Complexes. *Inorg. Chem.* **2005**, *44* (7), 2255–2262.

(17) Iché-Tarrat, N.; Marsden, C. J. Examining the Performance of DFT Methods in Uranium Chemistry: Does Core Size Matter for a Pseudopotential? *J. Phys. Chem. A* **2008**, *112* (33), 7632–7642.

(18) Vukovic, S.; Watson, L. A.; Kang, S. O.; Custelcean, R.; Hay, B. P. How Amidoximate Binds the Uranyl Cation. *Inorg. Chem.* **2012**, *51* (6), 3855–3859.

(19) Cossi, M.; Rega, N.; Scalmani, G.; Barone, V. Energies, Structures, and Electronic Properties of Molecules in Solution with the C-PCM Solvation Model. *J. Comput. Chem.* **2003**, *24* (6), 669–681.

(20) Lu, T.; Chen, F. Multiwfn: A Multifunctional Wavefunction Analyzer. *J. Comput. Chem.* **2012**, *33* (5), 580–592.

(21) Vallet, V.; Wahlgren, U.; Grenthe, I. Probing the Nature of Chemical Bonding in Uranyl(VI) Complexes with Quantum Chemical Methods. *J. Phys. Chem. A.* **2012**, *116* (50), 12373–12380.

(22) Mehio, N.; Williamson, B.; Oyola, Y.; Mayes, R. T.; Janke, C.; Brown, S.; Dai, S. Acidity of the Poly(Acrylamidoxime) Adsorbent in Aqueous Solution: Determination of the Proton Affinity Distribution via Potentiometric Titrations. *Ind. Eng. Chem. Res.* **2015**, *55* (15), 4217–4223.

(23) Mehio, N.; Lashely, M. a.; Nugent, J. W.; Tucker, L.; Correia, B.; Do-Thanh, C.-L.; Dai, S.; Hancock, R. D.; Bryantsev, V. S. Acidity of the Amidoxime Functional Group in Aqueous Solution: A Combined Experimental and Computational Study. *J. Phys. Chem. B.* **2015**, *119* (8), 3567–3576.

(24) Abney, C. W.; Liu, S.; Lin, W. Tuning Amidoximate to Enhance Uranyl Binding: A Density Functional Theory Study. *J. Phys. Chem. A.* **2013**, *117* (45), 11558–11565.

(25) Klapötke, T. M.; Müller, T. G.; Rusan, M.; Stierstorfer, J. Metal Salts of 4,5-Dinitro-1,3-Imidazole as Colorants in Pyrotechnic Compositions. *Zeitschrift für Anorg. und Allg. Chemie* **2014**, *640* (7), 1347–1354.

(26) Xiao, C.-L.; Wu, Q.-Y.; Wang, C.-Z.; Zhao, Y.-L.; Chai, Z.-F.; Shi, W.-Q. Quantum Chemistry Study of Uranium(VI), Neptunium(V), and Plutonium(IV,VI) Complexes with Preorganized Tetradentate Phenanthrolineamide Ligands. *Inorg. Chem.* **2014**, *53* (20), 10846–10853.

(27) Philip Horwitz, E.; Chiarizia, R.; Dietz, M. L. A Novel Strontium-Selective Extraction Chromatographic Resin. *Solvent Extr. Ion Exch.* **1992**, *10* (2), 313–336.

(28) Boda, A.; Ali, S. M.; Shenoi, M. R. K.; Rao, H.; Ghosh, S. K. DFT Modeling on the Suitable Crown Ether Architecture for Complexation with Cs^{+} and Sr^{2+} Metal Ions. *J. Mol. Model.* **2011**, *17* (5), 1091–1108.

(29) Vukovic, S.; Watson, L. A.; Kang, S. O.; Custelcean, R.; Hay, B. P. How Amidoximate Binds the Uranyl Cation. *Inorg. Chem.* **2012**, *51* (6), 3855–3859.

(30) Abney, C. W.; Mayes, R. T.; Piechowicz, M.; Lin, Z.; Bryantsev, V. S.; Veith, G. M.; Dai, S.; Lin, W. XAFS Investigation of Polyamidoxime-Bound Uranyl Contests the Paradigm from Small Molecule Studies. *Energy Environ. Sci.* **2016**, *9* (2), 448–453.

(31) Kříž, J.; Dybal, J.; Makrlík, E.; Vaňura, P.; Moyer, B. A. Interaction of Cesium Ions with Calix[4]Arene-Bis(t-Octylbenzo-18-Crown-6): NMR and Theoretical Study. *J. Phys. Chem. B* **2011**, *115* (23), 7578–7587.

(32) Vukovic, S.; Hay, B. P. De Novo Structure-Based Design of Bis-Amidoxime Uranophiles. *Inorg. Chem.* **2013**, *52* (13), 7805–7810.

(33) Vukovic, S.; Hay, B. P.; Bryantsev, V. S. Predicting Stability Constants for Uranyl Complexes Using Density Functional Theory. *Inorg. Chem.* **2015**, *54* (8), 3995–4001.

(34) Burgard, M.; Yaftian, M. R.; Jeunesse, C.; Bagatin, I.; Matt, D. Mixed ``Amide-Phosphoryl'' Calix[4]Arenes. On the Selectivity of Two Conformers Towards Alkali Ion Complexation. *J. Incl. Phenom. Macrocycl. Chem.* **2000**, *38* (1/4), 413–421.

(35) Qin, B.; Ren, C.; Ye, R.; Sun, C.; Chiad, K.; Chen, X.; Li, Z.; Xue, F.; Su, H.; Chass, G. A.; et al. Persistently Folded Circular Aromatic Amide Pentamers Containing Modularly Tunable Cation-Binding Cavities with High Ion Selectivity. *J. Am. Chem. Soc.* **2010**, *132* (28), 9564–9566.

(36) He, Q.; Peters, G. M.; Lynch, V. M.; Sessler, J. L. Recognition and Extraction of Cesium Hydroxide and Carbonate by Using a Neutral Multitopic Ion-Pair Receptor. *Angew. Chemie Int. Ed.* **2017**, *56* (43), 13396–13400.

(37) Horvat, G.; Frkanec, L.; Cindro, N.; Tomišić, V. A Comprehensive Study of the Complexation of Alkali Metal Cations by Lower Rim Calix[4]Arene Amide Derivatives. *Phys. Chem. Chem. Phys.* **2017**, *19* (35), 24316–24329.

(38) Tsushima, S.; Reich, T. A Theoretical Study of Uranyl Hydroxide Monomeric and Dimeric Complexes. *Chem. Phys. Lett.* **2001**, *347* (1–3), 127–132.

(39) Li, B.; Sun, Q.; Zhang, Y.; Abney, C. W.; Aguila, B.; Lin, W.; Ma, S. Functionalized Porous Aromatic Framework for Efficient Uranium Adsorption from Aqueous Solutions. *ACS Appl. Mater. Interfaces* **2017**, *9* (14), 12511–12517.

(40) Ma, S.; Huang, L.; Ma, L.; Shim, Y.; Islam, S. M.; Wang, P.; Zhao, L. D.; Wang, S.; Sun, G.; Yang, X.; et al. Efficient Uranium Capture by Polysulfide/Layered Double Hydroxide Composites. *J. Am. Chem. Soc.* **2015**, *137* (10), 3670–3677.

(41) Sarma, D.; Malliakas, C. D.; Subrahmanyam, K. S.; Islam, S. M.; Kanatzidis, M. G. K 2x Sn 4−x S 8−x (x = 0.65–1): A New Metal Sulfide for Rapid and Selective Removal of Cs + , Sr^{2+} and UO_2^{2+} Ions. *Chem. Sci.* **2016**, *7* (2), 1121–1132.

(42) Alqadami, A. A.; Naushad, M.; Alothman, Z. A.; Ghfar, A. A. Novel Metal–Organic Framework (MOF) Based Composite Material for the Sequestration of U(VI) and Th(IV) Metal Ions from Aqueous Environment. *ACS Appl. Mater. Interfaces* **2017**, *9* (41), 36026–36037.

(43) Sahiner, N.; Yu, H.; Tan, G.; He, J.; John, V. T.; Blake, D. A. Highly Porous Acrylonitrile-Based Submicron Particles for UO_2^{2+} Absorption in an Immunosensor Assay. *ACS Appl. Mater. Interfaces* **2012**, *4* (1), 163–170.

(44) Stemmler, A. A Planar [15]Metallacrown-5 That Selectively Binds the Uranyl Cation. *Angew. Chemie (International ed. English) Commun.* **1996**, *35* (23/24), 2841–2843.

(45) Parac-Vogt, T. N.; Pacco, A.; Nockemann, P.; Yuan, Y. F.; Görller-Walrand, C.; Binnemans, K. Mandelohydroxamic Acid as Ligand for Copper(II) 15-Metallacrown-5 Lanthanide(III) and Copper(II) 15-Metallacrown-5 Uranyl Complexes. *Eur. J. Inorg. Chem.* **2006**, *7*, 1466–1474.

(46) US Environmental Protection Agency. US Environmental Protection Agency. Radionuclides Rule: A Quick Reference Guide. *Office of Water* **2001**, No. 4606, EPA 816-F-01-003.

4.9 Appendix 4.1 Cartesian Coordinates for Optimized Sr, Cs, and U Complexes

Metal	Starting Geometry	Ligand Protonation State		
		bis-AO^{-1}	**bis-AO**	**bis-AO^{+1}**
Sr	(A)	SrA1	SrA2	SrA3
	(B)	SrB1	SrB2	SrB3
	(C)	SrC1	SrC2	SrC3
	(D)	SrD1	SrD2	NA
Cs	(A)	CsA1	CsA2	
	(B)	CsB1	CsB2	
	(C)	CsC1	CsC2	
	(D)	CsD1	CsD2	
U	(B)	UB1	UB2	UB3
	(D)	UD1	UD2	UD3

SrA1

C	5.012073000000	5.548133000000	-2.398450000000
C	4.464289000000	4.314425000000	-2.741354000000
C	3.296158000000	4.266692000000	-3.502673000000
C	2.668579000000	5.447769000000	-3.922207000000
C	3.230688000000	6.675794000000	-3.560752000000
C	4.399208000000	6.733148000000	-2.804994000000
H	5.920086000000	5.579084000000	-1.805654000000
H	4.939155000000	3.394415000000	-2.422280000000
H	2.746909000000	7.590349000000	-3.886917000000
H	4.827375000000	7.692719000000	-2.537850000000
O	2.674189000000	3.077264000000	-3.827379000000
C	3.441687000000	1.932598000000	-4.055887000000
C	4.426335000000	1.968324000000	-5.042521000000
C	3.162246000000	0.764029000000	-3.326218000000
C	5.181762000000	0.833244000000	-5.314347000000
H	4.597382000000	2.890972000000	-5.586151000000
C	3.935647000000	-0.371933000000	-3.636553000000
C	4.934821000000	-0.342164000000	-4.601081000000
H	5.945940000000	0.864095000000	-6.083478000000
H	3.727943000000	-1.287923000000	-3.097579000000
H	5.508384000000	-1.238958000000	-4.810701000000
C	2.123408000000	0.676034000000	-2.273304000000
N	0.918847000000	1.370224000000	-2.409013000000
H	0.999189000000	2.281969000000	-2.835623000000
H	0.433838000000	1.374599000000	-1.516562000000
N	2.326179000000	-0.133405000000	-1.276321000000
C	1.420739000000	5.403449000000	-4.741320000000
N	0.222399000000	5.402047000000	-4.086730000000
N	1.563101000000	5.433757000000	-6.023170000000
H	0.203977000000	5.163814000000	-3.108347000000
H	-0.605809000000	5.177210000000	-4.617727000000
O	1.302093000000	-0.162437000000	-0.365024000000
O	0.270402000000	5.400913000000	-6.645509000000
H	0.476130000000	5.383463000000	-7.587404000000
Sr	1.320781000000	-2.069404000000	1.260373000000

SrA2

C	5.292005000000	6.155048000000	-2.776284000000
C	4.893466000000	4.830479000000	-2.624403000000
C	3.658669000000	4.409720000000	-3.111686000000
C	2.777055000000	5.310985000000	-3.731411000000

C	3.200821000000	6.643694000000	-3.868721000000
C	4.443653000000	7.063281000000	-3.407307000000
H	6.257267000000	6.473643000000	-2.398620000000
H	5.532141000000	4.112196000000	-2.122924000000
H	2.548480000000	7.355318000000	-4.360989000000
H	4.744776000000	8.096707000000	-3.537138000000
O	3.255742000000	3.105574000000	-2.871776000000
C	3.791590000000	2.052305000000	-3.577790000000
C	4.813284000000	2.188043000000	-4.516281000000
C	3.252571000000	0.785007000000	-3.291151000000
C	5.321250000000	1.056522000000	-5.153183000000
H	5.217224000000	3.165239000000	-4.746815000000
C	3.784925000000	-0.335188000000	-3.936444000000
C	4.818767000000	-0.209307000000	-4.861012000000
H	6.115907000000	1.174224000000	-5.882210000000
H	3.364525000000	-1.309230000000	-3.715104000000
H	5.215949000000	-1.087950000000	-5.356452000000
C	2.111069000000	0.623927000000	-2.349162000000
N	0.975886000000	1.339102000000	-2.580882000000
H	1.062590000000	2.161781000000	-3.165102000000
H	0.318122000000	1.408866000000	-1.817248000000
N	2.262153000000	-0.266584000000	-1.418937000000
C	1.418431000000	4.939619000000	-4.212170000000
N	0.442256000000	5.897252000000	-4.125636000000
N	1.240432000000	3.779978000000	-4.761555000000
H	0.522049000000	6.588196000000	-3.395695000000
H	-0.499782000000	5.592950000000	-4.321598000000
O	1.020327000000	-0.387411000000	-0.671932000000
H	1.311756000000	-0.702066000000	0.192980000000
O	-0.123470000000	3.651708000000	-5.168819000000
H	-0.149292000000	2.793001000000	-5.607651000000
Sr	-0.884708000000	-2.124389000000	-1.746616000000

SrA3

C	5.308126000000	6.170840000000	-2.744252000000
C	4.907728000000	4.848379000000	-2.579370000000
C	3.680014000000	4.423416000000	-3.075609000000
C	2.794695000000	5.311774000000	-3.709767000000
C	3.229813000000	6.639094000000	-3.870713000000
C	4.468017000000	7.065321000000	-3.403281000000
H	6.268356000000	6.495576000000	-2.359714000000
H	5.540332000000	4.135322000000	-2.063177000000
H	2.594718000000	7.346157000000	-4.390049000000
H	4.770908000000	8.095590000000	-3.551450000000

O	3.290889000000	3.110881000000	-2.835809000000
C	3.803579000000	2.074750000000	-3.565925000000
C	4.850019000000	2.197879000000	-4.477090000000
C	3.222311000000	0.810514000000	-3.336994000000
C	5.325922000000	1.069317000000	-5.140540000000
H	5.295560000000	3.165329000000	-4.666343000000
C	3.721711000000	-0.313738000000	-4.008861000000
C	4.772571000000	-0.188940000000	-4.908349000000
H	6.139440000000	1.181532000000	-5.848670000000
H	3.255353000000	-1.281120000000	-3.860719000000
H	5.143712000000	-1.060834000000	-5.433071000000
C	2.060167000000	0.672369000000	-2.441713000000
N	1.041123000000	1.494481000000	-2.508058000000
H	1.079573000000	2.287701000000	-3.151073000000
H	0.250163000000	1.395590000000	-1.886498000000
C	1.433885000000	4.942932000000	-4.190346000000
N	0.511802000000	5.945849000000	-4.286480000000
N	1.194793000000	3.723838000000	-4.573507000000
H	0.596512000000	6.740241000000	-3.672418000000
H	-0.434327000000	5.666636000000	-4.497569000000
O	0.917185000000	-0.626872000000	-0.867913000000
H	1.062107000000	-0.353431000000	0.053564000000
O	-0.159069000000	3.625786000000	-5.020326000000
H	-0.204556000000	2.752842000000	-5.429240000000
Sr	-0.748845000000	-3.069391000000	-1.254334000000
N	2.073306000000	-0.329198000000	-1.565356000000
H	2.797475000000	-1.034624000000	-1.535757000000

SrB1

C	5.218071000000	6.273431000000	-2.730712000000
C	4.862372000000	4.937049000000	-2.572712000000
C	3.673996000000	4.458765000000	-3.120618000000
C	2.804231000000	5.315161000000	-3.814649000000
C	3.177439000000	6.661595000000	-3.952169000000
C	4.373858000000	7.137877000000	-3.426629000000
H	6.146259000000	6.637354000000	-2.303984000000
H	5.496133000000	4.254768000000	-2.017490000000
H	2.519419000000	7.336301000000	-4.487868000000
H	4.641756000000	8.180661000000	-3.555132000000
O	3.292856000000	3.151496000000	-2.853751000000
C	3.824526000000	2.092025000000	-3.580267000000
C	4.890310000000	2.261617000000	-4.461930000000
C	3.250491000000	0.822276000000	-3.355957000000
C	5.435753000000	1.161167000000	-5.120976000000
H	5.303460000000	3.248013000000	-4.630256000000

C	3.826609000000	-0.264415000000	-4.039329000000
C	4.909317000000	-0.110232000000	-4.898706000000
H	6.264562000000	1.306137000000	-5.805863000000
H	3.387183000000	-1.243243000000	-3.890528000000
H	5.321920000000	-0.973518000000	-5.410243000000
C	2.092765000000	0.592184000000	-2.473852000000
N	1.079968000000	1.587134000000	-2.317915000000
H	0.952581000000	2.150893000000	-3.151971000000
H	0.226642000000	1.079453000000	-2.075929000000
N	1.979137000000	-0.534992000000	-1.831194000000
C	1.491195000000	4.874378000000	-4.359669000000
N	0.423175000000	5.713009000000	-4.167895000000
N	1.442984000000	3.780596000000	-5.046362000000
H	0.440842000000	6.321569000000	-3.364082000000
H	-0.485959000000	5.343912000000	-4.404555000000
O	0.853806000000	-0.671505000000	-1.104549000000
O	0.098987000000	3.546406000000	-5.475962000000
H	0.164158000000	2.728601000000	-5.983245000000
Sr	1.557324000000	3.102850000000	-0.070174000000

SrB2

C	5.202436000000	6.256394000000	-2.682993000000
C	4.837591000000	4.924837000000	-2.506900000000
C	3.658844000000	4.441270000000	-3.066520000000
C	2.791582000000	5.284050000000	-3.782679000000
C	3.184105000000	6.623493000000	-3.947208000000
C	4.374745000000	7.105599000000	-3.414579000000
H	6.125336000000	6.624704000000	-2.249154000000
H	5.460836000000	4.247545000000	-1.934053000000
H	2.548809000000	7.291922000000	-4.516039000000
H	4.650204000000	8.142987000000	-3.567464000000
O	3.299299000000	3.123283000000	-2.800027000000
C	3.830515000000	2.092372000000	-3.555366000000
C	4.889676000000	2.284125000000	-4.441829000000
C	3.271053000000	0.812951000000	-3.375979000000
C	5.417217000000	1.202876000000	-5.142731000000
H	5.307015000000	3.272232000000	-4.583695000000
C	3.825434000000	-0.257618000000	-4.092998000000
C	4.892299000000	-0.075409000000	-4.964920000000
H	6.239636000000	1.368514000000	-5.830305000000
H	3.388037000000	-1.240163000000	-3.966369000000
H	5.297037000000	-0.919380000000	-5.511873000000
C	2.106023000000	0.555382000000	-2.493626000000
N	1.117843000000	1.530995000000	-2.343898000000
H	1.088204000000	2.199945000000	-3.108662000000

H	0.208052000000	1.124639000000	-2.151024000000
N	2.064010000000	-0.579377000000	-1.883798000000
C	1.477281000000	4.854127000000	-4.333334000000
N	0.483762000000	5.796112000000	-4.387675000000
N	1.353266000000	3.653950000000	-4.805642000000
H	0.495864000000	6.537805000000	-3.704783000000
H	-0.435768000000	5.458800000000	-4.630997000000
O	0.859794000000	-0.690096000000	-1.141490000000
H	0.895397000000	-1.583598000000	-0.779166000000
O	0.024581000000	3.470494000000	-5.295878000000
H	0.042331000000	2.583487000000	-5.675055000000
Sr	1.561176000000	3.155927000000	0.032418000000

SrB3

C	5.131446000000	6.175956000000	-2.625626000000
C	4.777430000000	4.834224000000	-2.521140000000
C	3.591618000000	4.377716000000	-3.087218000000
C	2.699604000000	5.252253000000	-3.731907000000
C	3.088337000000	6.600017000000	-3.830740000000
C	4.286397000000	7.058415000000	-3.294367000000
H	6.060358000000	6.524435000000	-2.188532000000
H	5.415989000000	4.129247000000	-2.001177000000
H	2.450160000000	7.299060000000	-4.357075000000
H	4.554338000000	8.103737000000	-3.397463000000
O	3.247203000000	3.043089000000	-2.910856000000
C	3.850971000000	2.052874000000	-3.637130000000
C	4.942673000000	2.256271000000	-4.478590000000
C	3.321731000000	0.754293000000	-3.480926000000
C	5.518229000000	1.174914000000	-5.141382000000
H	5.346861000000	3.250380000000	-4.614574000000
C	3.922896000000	-0.321195000000	-4.151563000000
C	5.020493000000	-0.116779000000	-4.976832000000
H	6.365292000000	1.351090000000	-5.795138000000
H	3.498831000000	-1.313796000000	-4.054547000000
H	5.469517000000	-0.952506000000	-5.499663000000
C	2.112994000000	0.516595000000	-2.674792000000
N	1.079465000000	1.320800000000	-2.722233000000
H	1.110979000000	2.150232000000	-3.317618000000
H	0.275620000000	1.153492000000	-2.132094000000
C	1.377344000000	4.847184000000	-4.285141000000
N	0.426715000000	5.820226000000	-4.412691000000
N	1.197831000000	3.627385000000	-4.696701000000
H	0.452811000000	6.606357000000	-3.783068000000
H	-0.498013000000	5.510848000000	-4.671488000000
O	0.970616000000	-0.780374000000	-1.114014000000

H	0.502652000000	-1.562692000000	-1.449067000000
O	-0.127083000000	3.492175000000	-5.211603000000
H	-0.129996000000	2.615751000000	-5.615565000000
Sr	2.408897000000	4.296259000000	0.907184000000
N	2.066980000000	-0.598845000000	-1.940304000000
H	2.914836000000	-1.045818000000	-1.614728000000

SrC1

C	5.087781000000	5.905398000000	-2.665286000000
C	4.606131000000	4.600621000000	-2.700355000000
C	3.375046000000	4.332525000000	-3.298333000000
C	2.613459000000	5.364898000000	-3.860011000000
C	3.105147000000	6.675489000000	-3.798388000000
C	4.337493000000	6.947282000000	-3.213028000000
H	6.045163000000	6.109002000000	-2.198024000000
H	5.172168000000	3.788459000000	-2.258765000000
H	2.518036000000	7.480541000000	-4.226780000000
H	4.709714000000	7.965062000000	-3.182492000000
O	2.827740000000	3.064776000000	-3.244075000000
C	3.494833000000	1.969958000000	-3.778698000000
C	4.439338000000	2.123068000000	-4.793375000000
C	3.149769000000	0.698227000000	-3.278148000000
C	5.085739000000	1.007642000000	-5.318985000000
H	4.672246000000	3.113034000000	-5.166339000000
C	3.813250000000	-0.405879000000	-3.842015000000
C	4.774768000000	-0.263398000000	-4.836543000000
H	5.818816000000	1.136177000000	-6.108226000000
H	3.550011000000	-1.391474000000	-3.478458000000
H	5.264600000000	-1.140834000000	-5.245340000000
C	2.143380000000	0.476957000000	-2.211323000000
N	0.985150000000	1.258533000000	-2.156265000000
H	1.120746000000	2.234602000000	-2.377702000000
H	0.525927000000	1.102548000000	-1.263369000000
N	2.316099000000	-0.527112000000	-1.403673000000
C	1.288978000000	5.096429000000	-4.491351000000
N	0.196876000000	5.692705000000	-3.937949000000
N	1.290769000000	4.367775000000	-5.559161000000
H	0.261544000000	6.018382000000	-2.986248000000
H	-0.714187000000	5.374952000000	-4.235075000000
O	1.317421000000	-0.676326000000	-0.475740000000
O	-0.071310000000	4.223946000000	-6.042455000000
H	-0.059792000000	3.366737000000	-6.486939000000
Sr	0.853423000000	-2.928499000000	0.515430000000
Sr	-1.108613000000	6.145192000000	-7.766506000000

SrC2

C	5.157400000000	6.038178000000	-2.750497000000
C	4.727321000000	4.716726000000	-2.682140000000
C	3.480653000000	4.363608000000	-3.194008000000
C	2.636613000000	5.326388000000	-3.764379000000
C	3.082952000000	6.655859000000	-3.809893000000
C	4.333912000000	7.011092000000	-3.316960000000
H	6.129334000000	6.306890000000	-2.351659000000
H	5.347290000000	3.954111000000	-2.224650000000
H	2.443355000000	7.411847000000	-4.251232000000
H	4.662427000000	8.042775000000	-3.371478000000
O	3.017578000000	3.068159000000	-3.027311000000
C	3.614679000000	2.011172000000	-3.677683000000
C	4.536381000000	2.169588000000	-4.711125000000
C	3.231652000000	0.726283000000	-3.253375000000
C	5.094658000000	1.045742000000	-5.317385000000
H	4.820612000000	3.161350000000	-5.039060000000
C	3.807560000000	-0.385804000000	-3.876624000000
C	4.737459000000	-0.235205000000	-4.901790000000
H	5.809689000000	1.180117000000	-6.121953000000
H	3.508708000000	-1.375041000000	-3.550608000000
H	5.170563000000	-1.108753000000	-5.375583000000
C	2.234165000000	0.527757000000	-2.166200000000
N	1.008093000000	1.113953000000	-2.277643000000
H	0.941689000000	1.922707000000	-2.877559000000
H	0.453567000000	1.159423000000	-1.433958000000
N	2.591461000000	-0.277263000000	-1.215316000000
C	1.281718000000	4.995198000000	-4.287421000000
N	0.255505000000	5.820213000000	-3.929823000000
N	1.184216000000	3.997721000000	-5.106285000000
H	0.356340000000	6.361120000000	-3.084807000000
H	-0.681160000000	5.500538000000	-4.129494000000
O	1.477198000000	-0.454470000000	-0.298838000000
H	1.909860000000	-0.628286000000	0.546923000000
O	-0.194907000000	3.864722000000	-5.532732000000
H	-0.273011000000	2.925510000000	-5.744163000000
Sr	-0.202539000000	-2.578967000000	-0.931678000000
Sr	-0.975472000000	5.344153000000	-7.784681000000

SrC3

C	5.234780000000	6.174890000000	-2.922144000000
C	4.877167000000	4.841168000000	-2.749990000000
C	3.614894000000	4.403112000000	-3.136417000000

C	2.659508000000	5.289428000000	-3.658982000000
C	3.048325000000	6.629457000000	-3.826764000000
C	4.319078000000	7.068727000000	-3.472736000000
H	6.221830000000	6.510041000000	-2.624318000000
H	5.569789000000	4.132362000000	-2.311127000000
H	2.350181000000	7.334945000000	-4.260848000000
H	4.588358000000	8.107912000000	-3.622687000000
O	3.257281000000	3.084204000000	-2.890722000000
C	3.783796000000	2.048395000000	-3.612221000000
C	4.774040000000	2.187285000000	-4.581665000000
C	3.269317000000	0.768542000000	-3.315944000000
C	5.263039000000	1.059572000000	-5.236955000000
H	5.165845000000	3.165958000000	-4.824006000000
C	3.780705000000	-0.353594000000	-3.983160000000
C	4.777175000000	-0.212763000000	-4.939900000000
H	6.032230000000	1.183906000000	-5.991021000000
H	3.364466000000	-1.334824000000	-3.785455000000
H	5.157481000000	-1.084128000000	-5.458813000000
C	2.164336000000	0.608349000000	-2.355497000000
N	1.122324000000	1.406152000000	-2.364410000000
H	1.105370000000	2.200491000000	-3.001878000000
H	0.371425000000	1.291686000000	-1.697479000000
C	1.265255000000	4.902247000000	-4.017328000000
N	0.308230000000	5.865903000000	-3.910754000000
N	1.037015000000	3.711774000000	-4.490908000000
H	0.467378000000	6.630339000000	-3.273511000000
H	-0.652091000000	5.564376000000	-3.985973000000
O	1.135274000000	-0.708827000000	-0.720923000000
H	1.325571000000	-0.438837000000	0.193218000000
O	-0.350798000000	3.618433000000	-4.874268000000
H	-0.497572000000	2.669719000000	-4.981028000000
Sr	-0.530309000000	-3.154891000000	-1.097389000000
Sr	-1.032506000000	4.758134000000	-7.508691000000
N	2.246611000000	-0.388522000000	-1.478125000000
H	2.987818000000	-1.076773000000	-1.482543000000

SrD1

C	5.023446000000	6.348345000000	-2.152401000000
C	4.601607000000	5.022228000000	-2.156496000000
C	3.523020000000	4.631062000000	-2.946174000000
C	2.819632000000	5.564309000000	-3.725708000000
C	3.261208000000	6.897927000000	-3.701381000000
C	4.353418000000	7.288241000000	-2.934057000000
H	5.867111000000	6.643622000000	-1.538410000000
H	5.100621000000	4.277775000000	-1.546295000000

H	2.744437000000	7.633529000000	-4.306707000000
H	4.675713000000	8.323433000000	-2.943769000000
O	3.078239000000	3.320356000000	-2.856440000000
C	3.727519000000	2.303543000000	-3.537232000000
C	4.908057000000	2.522609000000	-4.247073000000
C	3.147775000000	1.019394000000	-3.468292000000
C	5.551127000000	1.463522000000	-4.882485000000
H	5.330423000000	3.517738000000	-4.300031000000
C	3.821255000000	-0.024874000000	-4.126551000000
C	5.010283000000	0.180527000000	-4.815765000000
H	6.468223000000	1.649185000000	-5.431346000000
H	3.377225000000	-1.012188000000	-4.096658000000
H	5.498588000000	-0.650286000000	-5.313489000000
C	1.879921000000	0.724540000000	-2.768367000000
N	0.887917000000	1.717935000000	-2.588551000000
H	0.884545000000	2.417375000000	-3.323390000000
H	-0.008415000000	1.237011000000	-2.510260000000
N	1.664793000000	-0.470813000000	-2.318441000000
C	1.616000000000	5.221260000000	-4.530096000000
N	0.624219000000	6.167651000000	-4.606040000000
N	1.596273000000	4.101669000000	-5.177220000000
H	0.518635000000	6.798986000000	-3.826692000000
H	-0.243363000000	5.866564000000	-5.024991000000
O	0.436446000000	-0.687316000000	-1.755434000000
O	0.363411000000	3.982741000000	-5.887937000000
H	0.441371000000	3.130889000000	-6.333554000000
Sr	1.456259000000	-3.056994000000	-1.631134000000
Sr	1.093740000000	3.014595000000	-0.097755000000

SrD2

C	5.357169000000	6.210281000000	-2.836253000000
C	4.957816000000	4.889882000000	-2.651754000000
C	3.723659000000	4.460153000000	-3.131312000000
C	2.845808000000	5.344451000000	-3.778104000000
C	3.268669000000	6.673383000000	-3.946466000000
C	4.510506000000	7.103205000000	-3.491119000000
H	6.321505000000	6.537983000000	-2.464177000000
H	5.593854000000	4.183805000000	-2.129969000000
H	2.615618000000	7.372786000000	-4.455272000000
H	4.812313000000	8.133282000000	-3.643739000000
O	3.315072000000	3.163285000000	-2.850343000000
C	3.797026000000	2.094869000000	-3.569202000000
C	4.811876000000	2.203302000000	-4.518496000000
C	3.220675000000	0.844293000000	-3.281869000000
C	5.274695000000	1.062696000000	-5.171266000000

H	5.244352000000	3.169077000000	-4.745102000000
C	3.710398000000	-0.287937000000	-3.945112000000
C	4.733594000000	-0.188131000000	-4.882626000000
H	6.063023000000	1.160757000000	-5.909858000000
H	3.260400000000	-1.249152000000	-3.728749000000
H	5.092688000000	-1.075269000000	-5.391549000000
C	2.088561000000	0.688313000000	-2.330935000000
N	1.027082000000	1.578641000000	-2.377991000000
H	0.981508000000	2.141175000000	-3.221361000000
H	0.136934000000	1.169724000000	-2.120852000000
N	2.171843000000	-0.301601000000	-1.506321000000
C	1.488172000000	4.958126000000	-4.250623000000
N	0.495932000000	5.891833000000	-4.121802000000
N	1.329419000000	3.809481000000	-4.827681000000
H	0.578856000000	6.580311000000	-3.390291000000
H	-0.444122000000	5.586144000000	-4.323319000000
O	0.935665000000	-0.420594000000	-0.759695000000
H	1.231027000000	-0.648807000000	0.132259000000
O	-0.042015000000	3.655518000000	-5.207141000000
H	-0.044510000000	2.841090000000	-5.724309000000
Sr	-0.555392000000	-2.678486000000	-1.588569000000
Sr	0.967309000000	3.585683000000	-0.154499000000

CsA1

C	4.969773000000	5.454945000000	-2.353278000000
C	4.428106000000	4.239510000000	-2.765967000000
C	3.273135000000	4.229108000000	-3.548965000000
C	2.653363000000	5.432233000000	-3.919102000000
C	3.211059000000	6.639876000000	-3.490628000000
C	4.366358000000	6.659457000000	-2.712341000000
H	5.867422000000	5.454927000000	-1.743988000000
H	4.899473000000	3.305714000000	-2.484928000000
H	2.733002000000	7.569613000000	-3.780373000000
H	4.790507000000	7.604280000000	-2.391597000000
O	2.658819000000	3.063968000000	-3.958016000000
C	3.416680000000	1.894730000000	-4.096890000000
C	4.418505000000	1.868027000000	-5.065483000000
C	3.117107000000	0.776754000000	-3.297513000000
C	5.180696000000	0.719597000000	-5.249205000000
H	4.598698000000	2.755920000000	-5.662024000000
C	3.901615000000	-0.375049000000	-3.518333000000
C	4.920291000000	-0.405339000000	-4.461737000000
H	5.959401000000	0.700305000000	-6.003990000000
H	3.683844000000	-1.255394000000	-2.926157000000
H	5.498728000000	-1.313114000000	-4.599555000000

C	2.055198000000	0.757034000000	-2.271236000000
N	0.849885000000	1.445559000000	-2.480027000000
H	0.951705000000	2.334547000000	-2.949052000000
H	0.359634000000	1.512784000000	-1.591615000000
N	2.223117000000	0.011374000000	-1.214520000000
C	1.417435000000	5.430011000000	-4.756785000000
N	0.211762000000	5.345230000000	-4.122559000000
N	1.574105000000	5.570731000000	-6.029858000000
H	0.185176000000	5.047229000000	-3.161133000000
H	-0.605995000000	5.146370000000	-4.679205000000
O	1.199954000000	0.029564000000	-0.325472000000
O	0.289153000000	5.565723000000	-6.669722000000
H	0.506310000000	5.623310000000	-7.607429000000
Cs	3.006239000000	-2.093058000000	1.122967000000

CsA2

C	5.135494000000	5.706771000000	-2.393471000000
C	4.533547000000	4.457631000000	-2.519663000000
C	3.366498000000	4.330957000000	-3.270024000000
C	2.780369000000	5.441966000000	-3.887522000000
C	3.399021000000	6.689203000000	-3.746139000000
C	4.571910000000	6.825086000000	-3.008381000000
H	6.043573000000	5.804221000000	-1.808459000000
H	4.965902000000	3.584385000000	-2.044977000000
H	2.950054000000	7.553344000000	-4.222928000000
H	5.040043000000	7.798010000000	-2.909578000000
O	2.710275000000	3.112919000000	-3.375255000000
C	3.398707000000	1.976374000000	-3.762526000000
C	4.461203000000	2.030456000000	-4.663125000000
C	2.947631000000	0.747543000000	-3.252490000000
C	5.096389000000	0.855023000000	-5.054877000000
H	4.789615000000	2.986555000000	-5.052406000000
C	3.597993000000	-0.421339000000	-3.669660000000
C	4.668341000000	-0.375157000000	-4.557691000000
H	5.920651000000	0.905376000000	-5.758075000000
H	3.245698000000	-1.372778000000	-3.289006000000
H	5.155971000000	-1.292625000000	-4.867302000000
C	1.812062000000	0.653386000000	-2.294807000000
N	0.626412000000	1.263607000000	-2.601088000000
H	0.664068000000	2.046436000000	-3.235360000000
H	-0.032408000000	1.363717000000	-1.841934000000
N	1.998658000000	-0.092670000000	-1.253305000000
C	1.521999000000	5.309754000000	-4.677295000000
N	0.351407000000	5.118719000000	-4.002015000000
N	1.621798000000	5.452874000000	-5.956441000000

H	0.385393000000	4.838151000000	-3.035714000000
H	-0.457698000000	4.824625000000	-4.528315000000
O	0.322574000000	5.335875000000	-6.549039000000
H	0.501394000000	5.390964000000	-7.495047000000
Cs	4.992963000000	-0.823324000000	0.279386000000
O	0.797486000000	-0.135830000000	-0.479356000000
H	1.040234000000	-0.655276000000	0.296061000000

CsB1

C	4.975307000000	5.529986000000	-2.580119000000
C	4.624121000000	4.325880000000	-3.188519000000
C	3.420749000000	4.227598000000	-3.890798000000
C	2.556902000000	5.333625000000	-3.979619000000
C	2.937028000000	6.532091000000	-3.367438000000
C	4.138341000000	6.640478000000	-2.671210000000
H	5.912993000000	5.594859000000	-2.038257000000
H	5.287814000000	3.473089000000	-3.127965000000
H	2.267660000000	7.382078000000	-3.436212000000
H	4.412083000000	7.577647000000	-2.199377000000
O	3.040541000000	3.090683000000	-4.568377000000
C	3.750373000000	1.904542000000	-4.365566000000
C	4.755396000000	1.591260000000	-5.274329000000
C	3.427496000000	1.059008000000	-3.290924000000
C	5.498104000000	0.423397000000	-5.114248000000
H	4.958443000000	2.277311000000	-6.089711000000
C	4.199545000000	-0.107335000000	-3.148485000000
C	5.226436000000	-0.419505000000	-4.036216000000
H	6.281555000000	0.178783000000	-5.823510000000
H	3.963809000000	-0.780884000000	-2.332817000000
H	5.797792000000	-1.331782000000	-3.899718000000
C	2.320795000000	1.338503000000	-2.353176000000
N	1.058739000000	1.719701000000	-2.862643000000
H	0.780333000000	1.200995000000	-3.688419000000
H	0.387393000000	1.594752000000	-2.104791000000
N	2.517833000000	1.226667000000	-1.072157000000
C	1.254925000000	5.254842000000	-4.699025000000
N	0.341360000000	4.330865000000	-4.290127000000
N	1.054776000000	6.142853000000	-5.621144000000
H	0.665830000000	3.521088000000	-3.758307000000
H	-0.436398000000	4.165620000000	-4.912679000000
O	1.424561000000	1.451023000000	-0.300830000000
O	-0.264105000000	5.973432000000	-6.164186000000
H	-0.291182000000	6.612576000000	-6.885529000000
Cs	2.357062000000	4.138635000000	0.988286000000

CsB2

C	5.133188000000	5.464023000000	-2.718726000000
C	4.737646000000	4.246157000000	-3.269658000000
C	3.487127000000	4.135629000000	-3.876033000000
C	2.618081000000	5.239428000000	-3.932238000000
C	3.041917000000	6.451445000000	-3.377824000000
C	4.290727000000	6.571961000000	-2.773146000000
H	6.107590000000	5.539613000000	-2.247992000000
H	5.402703000000	3.392526000000	-3.234218000000
H	2.370436000000	7.301175000000	-3.417505000000
H	4.597572000000	7.518844000000	-2.343451000000
O	3.042497000000	2.976053000000	-4.479906000000
C	3.763437000000	1.796587000000	-4.331793000000
C	4.699108000000	1.456558000000	-5.302730000000
C	3.501533000000	0.949240000000	-3.246400000000
C	5.404132000000	0.259531000000	-5.192107000000
H	4.872123000000	2.135237000000	-6.130316000000
C	4.226785000000	-0.244213000000	-3.147327000000
C	5.173208000000	-0.588105000000	-4.109522000000
H	6.132794000000	-0.006126000000	-5.950085000000
H	4.030617000000	-0.907661000000	-2.312893000000
H	5.720387000000	-1.519763000000	-4.018524000000
C	2.470108000000	1.279055000000	-2.223919000000
N	1.167642000000	1.473237000000	-2.643303000000
H	0.897082000000	0.950830000000	-3.465643000000
H	0.479785000000	1.427330000000	-1.901946000000
N	2.869727000000	1.388317000000	-1.004436000000
C	1.269092000000	5.148252000000	-4.558541000000
N	0.394981000000	4.207399000000	-4.109287000000
N	0.997646000000	6.046021000000	-5.454534000000
H	0.749131000000	3.401729000000	-3.605315000000
H	-0.442493000000	4.057795000000	-4.651819000000
O	-0.343288000000	5.842892000000	-5.938470000000
H	-0.530271000000	6.652930000000	-6.428009000000
Cs	1.208975000000	4.142180000000	-8.507266000000
O	1.759462000000	1.654123000000	-0.152388000000
H	2.150057000000	1.684330000000	0.729078000000

CsC1

C	4.900700000000	5.370258000000	-2.462272000000
C	4.367954000000	4.139163000000	-2.838640000000
C	3.193380000000	4.096112000000	-3.590555000000

C	2.545785000000	5.283029000000	-3.965723000000
C	3.095823000000	6.507137000000	-3.575966000000
C	4.269884000000	6.558594000000	-2.827919000000
H	5.813654000000	5.395248000000	-1.876752000000
H	4.861767000000	3.218075000000	-2.554217000000
H	2.596582000000	7.423784000000	-3.871319000000
H	4.687518000000	7.515489000000	-2.535792000000
O	2.591367000000	2.913973000000	-3.967730000000
C	3.374824000000	1.761416000000	-4.112118000000
C	4.321013000000	1.732119000000	-5.134589000000
C	3.157077000000	0.663840000000	-3.260610000000
C	5.108104000000	0.601101000000	-5.323237000000
H	4.439252000000	2.604196000000	-5.768802000000
C	3.965064000000	-0.470259000000	-3.485589000000
C	4.929395000000	-0.502558000000	-4.484886000000
H	5.843448000000	0.578828000000	-6.120236000000
H	3.809054000000	-1.335935000000	-2.853543000000
H	5.528473000000	-1.396417000000	-4.625346000000
C	2.153737000000	0.649760000000	-2.177096000000
N	0.902892000000	1.260489000000	-2.360274000000
H	0.933432000000	2.127006000000	-2.879028000000
H	0.454376000000	1.351368000000	-1.451817000000
N	2.415930000000	-0.022688000000	-1.091371000000
C	1.291334000000	5.245607000000	-4.773899000000
N	0.104607000000	5.099701000000	-4.117057000000
N	1.416162000000	5.417917000000	-6.047302000000
H	0.115546000000	4.793951000000	-3.157578000000
H	-0.708561000000	4.845980000000	-4.658830000000
O	1.437742000000	-0.007074000000	-0.152884000000
O	0.112352000000	5.399442000000	-6.659360000000
H	0.310592000000	5.317138000000	-7.599928000000
Cs	3.505946000000	-1.728414000000	1.452110000000
Cs	-1.460911000000	8.363958000000	-6.424210000000

CsC2

C	5.018035000000	5.570387000000	-2.474645000000
C	4.441667000000	4.309475000000	-2.602570000000
C	3.260656000000	4.163243000000	-3.327323000000
C	2.635869000000	5.268842000000	-3.918099000000
C	3.230471000000	6.527990000000	-3.776117000000
C	4.416056000000	6.682662000000	-3.063254000000
H	5.936780000000	5.681252000000	-1.908997000000
H	4.905740000000	3.441237000000	-2.149306000000
H	2.751205000000	7.386458000000	-4.232850000000
H	4.864068000000	7.664866000000	-2.963343000000

O	2.633993000000	2.930919000000	-3.438750000000
C	3.364794000000	1.811106000000	-3.801084000000
C	4.383144000000	1.879222000000	-4.750289000000
C	3.003979000000	0.586475000000	-3.217603000000
C	5.063091000000	0.721469000000	-5.118572000000
H	4.642653000000	2.832940000000	-5.194174000000
C	3.697013000000	-0.565807000000	-3.610989000000
C	4.723377000000	-0.504997000000	-4.548760000000
H	5.852742000000	0.781426000000	-5.859678000000
H	3.414332000000	-1.515505000000	-3.172004000000
H	5.246313000000	-1.409097000000	-4.839485000000
C	1.918409000000	0.482078000000	-2.204304000000
N	0.671264000000	0.948740000000	-2.514902000000
H	0.605710000000	1.648381000000	-3.237342000000
H	0.030033000000	1.068473000000	-1.743746000000
N	2.213104000000	-0.136848000000	-1.106661000000
C	1.367182000000	5.122779000000	-4.686751000000
N	0.223792000000	4.809760000000	-4.007791000000
N	1.426828000000	5.381953000000	-5.950879000000
H	0.310945000000	4.433856000000	-3.077234000000
H	-0.557398000000	4.465576000000	-4.547594000000
O	0.113241000000	5.265170000000	-6.521614000000
H	0.281230000000	5.271175000000	-7.471667000000
Cs	5.311512000000	-0.704707000000	0.281119000000
Cs	-1.751173000000	7.991445000000	-5.926167000000
O	1.050409000000	-0.210898000000	-0.277580000000
H	1.370352000000	-0.622986000000	0.533521000000

CsD1

C	4.914701000000	5.271139000000	-2.383539000000
C	4.545373000000	4.126404000000	-3.088323000000
C	3.377093000000	4.129391000000	-3.851423000000
C	2.568037000000	5.277614000000	-3.906093000000
C	2.964012000000	6.416295000000	-3.199188000000
C	4.131309000000	6.422013000000	-2.438679000000
H	5.824945000000	5.257567000000	-1.793256000000
H	5.167527000000	3.241100000000	-3.052815000000
H	2.336674000000	7.299454000000	-3.243922000000
H	4.420248000000	7.312275000000	-1.891398000000
O	2.976653000000	3.061074000000	-4.623219000000
C	3.603761000000	1.825375000000	-4.451271000000
C	4.606972000000	1.483119000000	-5.352332000000
C	3.206531000000	0.962017000000	-3.414360000000
C	5.270780000000	0.264442000000	-5.225815000000
H	4.871357000000	2.185891000000	-6.135111000000

C	3.900881000000	-0.256808000000	-3.307206000000
C	4.922272000000	-0.600607000000	-4.188116000000
H	6.052672000000	-0.001895000000	-5.928785000000
H	3.606555000000	-0.944854000000	-2.523257000000
H	5.430689000000	-1.552775000000	-4.077501000000
C	2.114153000000	1.270798000000	-2.469470000000
N	0.887955000000	1.787415000000	-2.955669000000
H	0.549893000000	1.281718000000	-3.768728000000
H	0.224393000000	1.703711000000	-2.183515000000
N	2.290081000000	1.053312000000	-1.199306000000
C	1.301931000000	5.290539000000	-4.691828000000
N	0.318026000000	4.421480000000	-4.342160000000
N	1.218056000000	6.187148000000	-5.625663000000
H	0.566048000000	3.588156000000	-3.802572000000
H	-0.463419000000	4.331235000000	-4.974872000000
O	1.221384000000	1.302231000000	-0.409573000000
O	-0.063143000000	6.071867000000	-6.275806000000
H	-0.085776000000	6.838153000000	-6.861303000000
Cs	1.807300000000	3.845523000000	-8.255309000000
Cs	3.205608000000	0.374373000000	1.848533000000

CsD2

C	5.174243000000	5.260874000000	-2.453470000000
C	4.706635000000	4.100519000000	-3.068107000000
C	3.486443000000	4.117501000000	-3.741728000000
C	2.711919000000	5.290477000000	-3.798166000000
C	3.208115000000	6.441643000000	-3.174936000000
C	4.430886000000	6.437239000000	-2.509116000000
H	6.124863000000	5.236760000000	-1.931493000000
H	5.294211000000	3.192295000000	-3.029064000000
H	2.610243000000	7.344427000000	-3.211058000000
H	4.791772000000	7.340409000000	-2.030034000000
O	2.976220000000	3.016204000000	-4.403848000000
C	3.611595000000	1.783612000000	-4.306919000000
C	4.673224000000	1.484977000000	-5.154115000000
C	3.124024000000	0.840087000000	-3.394379000000
C	5.276830000000	0.230871000000	-5.081488000000
H	5.021320000000	2.234244000000	-5.856097000000
C	3.743965000000	-0.412532000000	-3.331898000000
C	4.817491000000	-0.715727000000	-4.166260000000
H	6.104854000000	-0.004012000000	-5.741161000000
H	3.370258000000	-1.151192000000	-2.631714000000
H	5.286112000000	-1.691737000000	-4.108791000000
C	1.943072000000	1.144239000000	-2.536854000000
N	0.733760000000	1.342759000000	-3.160774000000

H	0.617248000000	0.894542000000	-4.058597000000
H	-0.079783000000	1.277122000000	-2.563000000000
N	2.139276000000	1.243550000000	-1.266552000000
C	1.390155000000	5.343698000000	-4.482286000000
N	0.435342000000	4.402302000000	-4.183910000000
N	1.188505000000	6.364278000000	-5.251010000000
H	0.753922000000	3.482066000000	-3.900627000000
H	-0.350780000000	4.380594000000	-4.819649000000
O	-0.144412000000	6.323206000000	-5.765280000000
H	-0.168155000000	7.059393000000	-6.387793000000
Cs	-0.564461000000	4.753993000000	-0.681750000000
Cs	5.066743000000	1.252916000000	0.595634000000
O	0.899605000000	1.528248000000	-0.611139000000
H	1.103062000000	1.418458000000	0.325746000000

UB1

C	3.909698000000	3.290433000000	1.588155000000
C	3.696969000000	1.917383000000	1.683938000000
C	2.635756000000	1.324482000000	1.007016000000
C	1.758886000000	2.092395000000	0.222316000000
C	2.000532000000	3.471928000000	0.129823000000
C	3.060355000000	4.069396000000	0.804969000000
H	4.736926000000	3.745457000000	2.121591000000
H	4.349291000000	1.289371000000	2.279939000000
H	1.328495000000	4.084401000000	-0.460333000000
H	3.214726000000	5.139535000000	0.724826000000
O	2.444342000000	-0.034519000000	1.197282000000
C	2.753430000000	-0.934937000000	0.199737000000
C	3.549512000000	-0.607901000000	-0.896740000000
C	2.271025000000	-2.243738000000	0.373963000000
C	3.873097000000	-1.590225000000	-1.831902000000
H	3.926411000000	0.400853000000	-1.013728000000
C	2.616398000000	-3.211616000000	-0.574271000000
C	3.412163000000	-2.895175000000	-1.673439000000
H	4.493322000000	-1.327858000000	-2.682397000000
H	2.241733000000	-4.220257000000	-0.443935000000
H	3.663223000000	-3.659446000000	-2.400381000000
C	1.411279000000	-2.608870000000	1.534494000000
N	0.262528000000	-1.905822000000	1.747890000000
H	0.177262000000	-0.981745000000	1.332709000000
H	-0.181745000000	-2.030562000000	2.645743000000
N	1.788666000000	-3.639108000000	2.223112000000
C	0.595861000000	1.522667000000	-0.508481000000
N	0.349407000000	1.999431000000	-1.758241000000
N	-0.179721000000	0.677290000000	0.112130000000

H	1.106585000000	2.401567000000	-2.287570000000
H	-0.373592000000	1.534536000000	-2.287209000000
O	-1.227948000000	0.271677000000	-0.713128000000
O	0.828666000000	-3.894948000000	3.257780000000
H	1.231238000000	-4.610621000000	3.763264000000
U	-3.189232000000	-0.440082000000	-0.260737000000
O	-3.537412000000	-0.500952000000	-2.005285000000
O	-2.804881000000	-0.289265000000	1.465097000000

UB2

C	4.054330000000	3.284680000000	1.532233000000
C	3.766390000000	1.926934000000	1.648727000000
C	2.659147000000	1.390606000000	0.999202000000
C	1.810086000000	2.199127000000	0.227194000000
C	2.127327000000	3.560637000000	0.110981000000
C	3.234944000000	4.102481000000	0.756365000000
H	4.916552000000	3.697801000000	2.043918000000
H	4.394372000000	1.269168000000	2.238797000000
H	1.479424000000	4.202541000000	-0.475046000000
H	3.449773000000	5.160808000000	0.659875000000
O	2.390065000000	0.044238000000	1.198537000000
C	2.680228000000	-0.877972000000	0.215207000000
C	3.510729000000	-0.594042000000	-0.867799000000
C	2.136139000000	-2.163620000000	0.386542000000
C	3.809841000000	-1.595515000000	-1.790269000000
H	3.933243000000	0.396491000000	-0.983372000000
C	2.457114000000	-3.151526000000	-0.550650000000
C	3.288375000000	-2.877878000000	-1.634217000000
H	4.457941000000	-1.365947000000	-2.629331000000
H	2.035259000000	-4.141507000000	-0.422874000000
H	3.519816000000	-3.657105000000	-2.351662000000
C	1.241009000000	-2.488635000000	1.530282000000
N	0.157477000000	-1.694168000000	1.774066000000
H	0.156162000000	-0.750658000000	1.396691000000
H	-0.287271000000	-1.809261000000	2.673578000000
N	1.515705000000	-3.573461000000	2.184086000000
C	0.594172000000	1.686980000000	-0.462380000000
N	0.378670000000	2.105131000000	-1.744581000000
N	-0.236614000000	0.964226000000	0.218252000000
H	1.174423000000	2.381305000000	-2.298059000000
H	-0.376603000000	1.668908000000	-2.251404000000
O	0.528934000000	-3.781654000000	3.196686000000
H	0.866830000000	-4.539367000000	3.688484000000
U	-2.633455000000	-3.215390000000	-0.409104000000
O	-2.012018000000	-3.521696000000	-2.013900000000

O	-3.251964000000	-2.906036000000	1.195135000000
O	-1.343534000000	0.600766000000	-0.610489000000
H	-1.969785000000	0.205460000000	0.007672000000

UB3

C	3.814879000000	2.083005000000	1.846158000000
C	3.410741000000	1.055634000000	0.999066000000
C	2.235752000000	1.183276000000	0.262754000000
C	1.445107000000	2.347838000000	0.386540000000
C	1.883656000000	3.374302000000	1.241529000000
C	3.057757000000	3.247417000000	1.968193000000
H	4.735745000000	1.970951000000	2.407422000000
H	4.010199000000	0.159464000000	0.907447000000
H	1.315369000000	4.294297000000	1.306936000000
H	3.384993000000	4.053716000000	2.613117000000
O	1.780377000000	0.208540000000	-0.589313000000
C	2.539275000000	-0.948490000000	-0.811559000000
C	3.484879000000	-0.926651000000	-1.829019000000
C	2.289557000000	-2.101514000000	-0.056484000000
C	4.218957000000	-2.076979000000	-2.107060000000
H	3.640631000000	-0.011959000000	-2.389584000000
C	3.041552000000	-3.246890000000	-0.354862000000
C	3.998030000000	-3.236902000000	-1.365339000000
H	4.955750000000	-2.064779000000	-2.902328000000
H	2.856730000000	-4.150571000000	0.212911000000
H	4.562387000000	-4.137361000000	-1.580274000000
C	1.277826000000	-2.148172000000	1.034215000000
N	0.009170000000	-1.692287000000	0.799077000000
H	-0.131457000000	-1.061427000000	0.026209000000
H	-0.562849000000	-1.511169000000	1.611411000000
N	1.655507000000	-2.706759000000	2.138738000000
C	0.188426000000	2.526379000000	-0.354641000000
N	-0.026391000000	2.024464000000	-1.549374000000
H	0.675723000000	1.462016000000	-2.004613000000
H	-0.926011000000	2.144374000000	-1.995372000000
O	0.565790000000	-2.729468000000	3.055037000000
H	0.948867000000	-3.102844000000	3.857909000000
U	-1.800773000000	-5.105633000000	1.342911000000
O	-1.788327000000	-5.088359000000	-0.402698000000
O	-1.829322000000	-5.135816000000	3.087002000000
O	-1.980401000000	3.361628000000	-0.443280000000
H	-2.093960000000	4.288464000000	-0.709988000000
N	-0.758651000000	3.291052000000	0.205697000000
H	-0.824086000000	3.378853000000	1.211802000000

UD1

C	3.867265000000	3.456574000000	1.545524000000
C	3.729686000000	2.079927000000	1.706638000000
C	2.710744000000	1.399394000000	1.049761000000
C	1.800068000000	2.077091000000	0.220990000000
C	1.968146000000	3.461412000000	0.062953000000
C	2.986058000000	4.148152000000	0.717248000000
H	4.661863000000	3.981875000000	2.063489000000
H	4.408214000000	1.518115000000	2.338108000000
H	1.269386000000	4.007449000000	-0.560336000000
H	3.082279000000	5.219939000000	0.586043000000
O	2.593577000000	0.040014000000	1.311712000000
C	2.847444000000	-0.885930000000	0.330808000000
C	3.651140000000	-0.611487000000	-0.773753000000
C	2.306828000000	-2.173541000000	0.512876000000
C	3.907969000000	-1.610551000000	-1.709605000000
H	4.079242000000	0.375730000000	-0.896773000000
C	2.578341000000	-3.161898000000	-0.442897000000
C	3.371917000000	-2.887193000000	-1.550917000000
H	4.533727000000	-1.384053000000	-2.565928000000
H	2.140344000000	-4.144823000000	-0.321525000000
H	3.563616000000	-3.660639000000	-2.285237000000
C	1.425539000000	-2.492065000000	1.662926000000
N	0.459235000000	-1.665720000000	2.016140000000
H	0.305651000000	-0.787698000000	1.507948000000
H	-0.113156000000	-1.888296000000	2.818049000000
N	1.627621000000	-3.656683000000	2.271233000000
C	0.672084000000	1.412155000000	-0.483931000000
N	0.394045000000	1.818546000000	-1.749166000000
N	-0.050295000000	0.546282000000	0.171713000000
H	1.118230000000	2.252461000000	-2.298954000000
H	-0.306322000000	1.295645000000	-2.253920000000
O	-1.070011000000	0.028632000000	-0.626313000000
O	0.736637000000	-3.868201000000	3.365137000000
H	0.110903000000	-4.551871000000	3.074878000000
U	-3.036394000000	-0.620377000000	-0.058925000000
O	-3.313844000000	-1.061267000000	-1.757500000000
O	-2.661937000000	-0.169787000000	1.615178000000
U	3.439732000000	-5.109066000000	2.968030000000
O	3.254238000000	-5.979889000000	1.453050000000
O	3.514821000000	-4.165988000000	4.446203000000

UD2

C	4.197249000000	3.390869000000	1.330168000000
C	3.961394000000	2.036402000000	1.552552000000
C	2.814937000000	1.437129000000	1.043417000000
C	1.872420000000	2.173788000000	0.307687000000
C	2.138865000000	3.533311000000	0.084827000000
C	3.284884000000	4.139821000000	0.590060000000
H	5.091628000000	3.854013000000	1.731686000000
H	4.659722000000	1.429754000000	2.117455000000
H	1.420987000000	4.125057000000	-0.471368000000
H	3.457796000000	5.195054000000	0.411755000000
O	2.610696000000	0.100250000000	1.361773000000
C	2.654412000000	-0.865519000000	0.389578000000
C	3.325247000000	-0.695180000000	-0.819786000000
C	2.040149000000	-2.095229000000	0.691470000000
C	3.377977000000	-1.743397000000	-1.735573000000
H	3.812683000000	0.246882000000	-1.038680000000
C	2.111487000000	-3.138648000000	-0.242432000000
C	2.771626000000	-2.966761000000	-1.453809000000
H	3.903140000000	-1.599100000000	-2.673398000000
H	1.625466000000	-4.079851000000	-0.017398000000
H	2.810514000000	-3.778822000000	-2.170184000000
C	1.316416000000	-2.310655000000	1.966699000000
N	0.475159000000	-1.408376000000	2.436377000000
H	0.317177000000	-0.534383000000	1.928922000000
H	0.023322000000	-1.559847000000	3.327246000000
N	1.538571000000	-3.477132000000	2.556713000000
C	0.620087000000	1.591580000000	-0.246653000000
N	0.247409000000	1.990798000000	-1.495369000000
N	-0.093545000000	0.811771000000	0.504622000000
H	0.954115000000	2.332205000000	-2.127246000000
H	-0.536252000000	1.520154000000	-1.921353000000
O	0.847995000000	-3.648341000000	3.792850000000
H	0.142591000000	-4.294748000000	3.623364000000
U	-1.877290000000	-3.095120000000	-1.645641000000
O	-2.282628000000	-1.844933000000	-2.797349000000
O	-1.477487000000	-4.349495000000	-0.495453000000
U	3.389965000000	-4.898556000000	3.163180000000
O	2.917264000000	-6.027603000000	1.899973000000
O	3.783764000000	-3.672686000000	4.357734000000
O	-1.247988000000	0.385038000000	-0.218028000000
H	-1.771694000000	-0.095305000000	0.434736000000

UD3

C	3.554772000000	2.532245000000	1.687431000000
C	3.348817000000	1.241869000000	1.207055000000
C	2.205210000000	0.955818000000	0.470122000000
C	1.247055000000	1.956137000000	0.222636000000
C	1.470814000000	3.248612000000	0.724336000000
C	2.620566000000	3.538582000000	1.446304000000
H	4.450226000000	2.746256000000	2.259707000000
H	4.068330000000	0.459177000000	1.412827000000
H	0.752770000000	4.033101000000	0.516758000000
H	2.787079000000	4.543327000000	1.815054000000
O	1.914389000000	-0.322713000000	0.032719000000
C	2.924992000000	-1.205870000000	-0.322642000000
C	3.882445000000	-0.826875000000	-1.257870000000
C	2.910164000000	-2.507993000000	0.212498000000
C	4.831257000000	-1.746462000000	-1.691075000000
H	3.876873000000	0.182699000000	-1.651088000000
C	3.866874000000	-3.424971000000	-0.262256000000
C	4.817800000000	-3.051709000000	-1.200183000000
H	5.567678000000	-1.444864000000	-2.427095000000
H	3.846828000000	-4.444200000000	0.101067000000
H	5.540123000000	-3.778033000000	-1.552992000000
C	1.977103000000	-2.938752000000	1.276710000000
N	0.806307000000	-2.360443000000	1.478163000000
H	0.514301000000	-1.577724000000	0.914216000000
H	0.228140000000	-2.648312000000	2.254811000000
N	2.386567000000	-3.974781000000	2.008447000000
C	0.012063000000	1.691789000000	-0.539447000000
N	-0.013440000000	1.015385000000	-1.664747000000
H	0.833124000000	0.677890000000	-2.093734000000
H	-0.892227000000	0.835081000000	-2.132148000000
O	1.521883000000	-4.250240000000	3.117387000000
H	1.104623000000	-5.112284000000	2.948131000000
U	-4.630688000000	-0.914542000000	0.489841000000
O	-5.494051000000	-1.509636000000	-0.904743000000
O	-3.765650000000	-0.321173000000	1.884507000000
U	4.098491000000	-4.445248000000	3.643278000000
O	4.033893000000	-6.111491000000	3.080617000000
O	3.957497000000	-2.764035000000	4.138643000000
O	-2.295813000000	1.926865000000	-0.724370000000
H	-2.622870000000	2.761493000000	-1.099517000000
N	-1.115161000000	2.225687000000	-0.070034000000
H	-1.218874000000	2.469175000000	0.907229000000

4.10 Appendix 4.2 Calculations for Uptake Studies:

Consider the uptake of a metal ion, M^{n+} by a solid sorbent. The process can be described by a chemical equilibrium of the type:

$$M^{n+} \rightleftharpoons \overline{M} \qquad \textbf{Equation 4.2}$$

where the bar denotes the solid phase species and M^{n+} is the equilibrium concentration of the metal ion in the aqueous phase. The weight distribution ratio of the metal ion, D_W, (proportional to the equilibrium constant of reaction 1) can be written as:

$$D_W = \frac{[\overline{M}]}{[M^{n+}]} \quad \textbf{Equation 4.3}$$

In the presence of complexing agents in the aqueous phase, we can determine the total concentration of M^{n+}, given by the sum of all chemical species containing M. The experimentally determined $D_{W,exp}$ is given by:

$$D_{W,exp} = \frac{[\overline{M}]}{[M^{n+}]_{tot}} \qquad \textbf{Equation 4.4}$$

In eq. 3, the total equilibrium metal concentration in the aqueous phase can be written as:

$$[M^{n+}]_{tot} = [M^{n+}](1 + \beta_1[L^-]^1 + \cdots + \beta_p[L^-]^p) \qquad \textbf{Equation 4.5}$$

where L^- represents the aqueous complexing agent (e.g. the anion of a weak acid) and β_1 through β_p are the total formation constants for the aqueous phase metal complexes from ML to ML_p (charges omitted for simplicity). By substituting **Equation 4.5** into **Equation 4.4**, we obtain:

$$D_W = D_{W,exp}(1 + \beta_1[L^-]^1 + \cdots + \beta_p[L^-]^p) \qquad \textbf{Equation 4.6}$$

From **Equation 4.6**, the actual value of D_W for M^{n+} can be calculated if the β values are known and the concentration of L^- can be estimated. L^- in all instances is the anion of the ionic medium used in the experiments (e.g. NO_3^-) or another anion introduced in solution for a particular reason (e.g. using a buffer). In the former case, because of the very low complexing power of nitrate ions, the formation of nitrato-complexes can be neglected, unless the NO_3^- concentration is very high. In the case of a buffer (for example, an acetate/acetic acid buffer), the concentration of the anion, $[L^-]$, at each pH value can be calculated knowing the pK_a of the acid and the buffer concentration.

For an HL/L^- buffer the following relation holds:

$$K_a = \frac{[H^+][L^-]}{[HL]} \qquad \textbf{Equation 4.7}$$

where K_a is the acid dissociation constant, $[H^+]$ is the concentration of protons in solution, $[L^-]$ is the concentration of conjugate base, and [HL] is the initial concentration of acid. Rearranging gives (7),

$$[H^+] = K_a \frac{[HL]}{[L^-]} \qquad \textbf{Equation 4.8}$$

The total concentration, C, of the buffer is known.

Therefore,

$$\frac{[H^+]}{K_a} = \frac{[HL]}{[L^-]} = \frac{C-[L^-]}{[L]} \qquad \textbf{Equation 4.9}$$

Equation 4.9 can be rearranged as

$$\frac{[H^+]}{K_a}[L^-] + [L^-] = C \qquad \textbf{Equation 4.10}$$

$$\left(\frac{[H^+]}{K_a} + 1\right)[L^-] = C \qquad \textbf{Equation 4.11}$$

and finally

$$[L^-] = \frac{C}{\frac{[H^+]}{K_a}+1} \qquad \textbf{Equation 4.12}$$

Chapter 5: An Introduction to the poly(HIPE): A New Actinide Adsorbent Platform Technology

Marek Piechowicz, R. Chiarizia, S. Skanthakumar, Stuart J. Rowan, and L. Soderholm. *Submitted*

5.1 Introduction

Lack of clean water access due to contamination from mining activities remains a source of anxiety and a critical health concern for people worldwide. Heavy element separation via solid adsorbents is often chosen to address this crisis without the generation of large volumes of hazardous organic waste as would be the case with solvent extraction methods.[1] As such, there is an acute need for the structure-by-design synthesis of advanced adsorbent materials with high selectivity, large capacity, and fast adsorption kinetics necessary for efficient contaminant removal from water.[2]

Presented herein is the development of an understudied class of actinide adsorbent material with the potential to meet these challenges. Polymerized high internal phase emulsions (poly(HIPE)s) are monolithic, porous polymer materials synthesized through the careful addition of an aqueous solution (internal phase) into a well-stirred organic phase (external phase) containing monomers (**Scheme 5.1**).[3–11] Owing to their high degree of porosity and open-cell structure, poly(HIPE)s have found use in water uptake,[12] oil remediation,[13] and heavy-metal adsorption.[14–18] Poly(HIPE) materials represent robust systems with which to interrogate fundamental separations chemistry owning to great synthetic control over polymer macro-characteristics such as porosity, hydrophilicity, and surface area. Moreover, as industrial scale synthesis of poly(HIPE)s is already

a well-established process,[19] these functionalized materials can be produced on a large-scale providing significant cost savings over other advanced materials.

While there have been several reports of functionalized poly(HIPE) materials for metal-ion separations,[16,20] only a handful report the use of these materials for actinide uptake.[21–23] Recent work by Benicewicz and co-workers[21–23] successfully demonstrated the incorporation of vinylpyridine monomers into styrenic poly(HIPE)s resulting in Pu uptake via an anion-exchange mechanism.

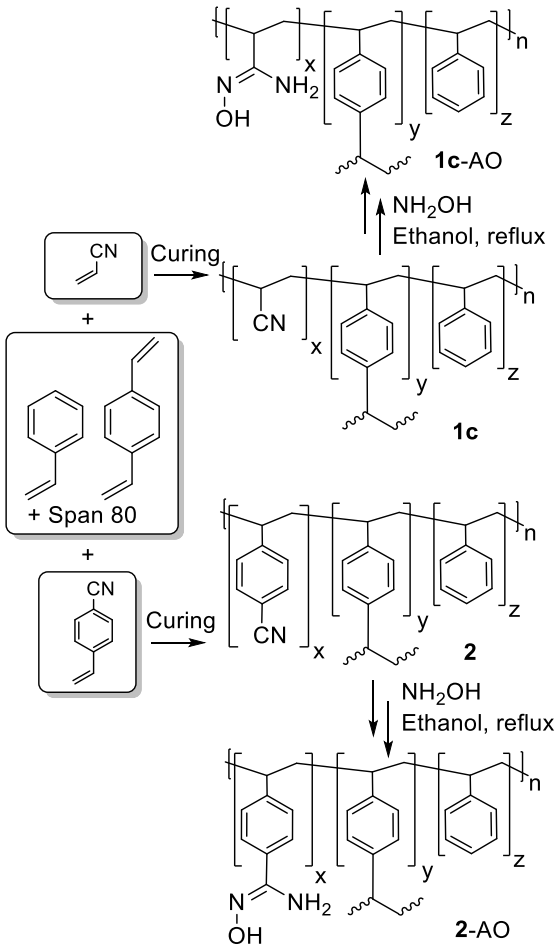

Scheme 5.1 General synthetic scheme for poly(HIPE) materials discussed in this work.

It was found that uptake kinetics and capacity were dramatically improved over conventional ion exchange materials on account of the porous structure of the poly(HIPE)s highlighting that judicious choice of functional groups and a readily amenable synthetic preparation makes poly(HIPE)s attractive materials for actinide separations.

Reported herein is the synthesis of nitrile-containing poly(HIPE)s, post-synthetic amidoximation, and demonstration of such materials for Th, U, and Pu uptake. The amidoxime functional group (CNH_2NOH) was chosen on account of its extensive use in uranium from seawater applications[24] and its expected high affinity for uranium in these poly(HIPE) systems. While there are literature reports of amidoxime (**AO**) functionalized materials for thorium[25] and uranium[26] separations, there is a paucity of reports describing porous **AO** functionalized materials for selective uptake with fast kinetics. Th, U, and Pu were chosen as the metals of interest on account of their significance as environmental contaminants[27] and, in the case of U from seawater, a potential source of nuclear fuel.[24] The use of radiotracers in this work allows for easy access to dilute metal concentrations characteristic of environmental remediation applications as well as facile uptake efficiency determination.

5.2 Experimental Methods

5.2.1 General Experimental

Caution! Materials used herein are radioactive and are considered health risks. Their use requires proper facilities, correct PPE, and appropriate training.

5.2.2 Materials

Nitric acid was ACS reagent grade and used as received. Divinylbenzene (DVB) was technical grade and used as received. Styrene (St) was purchased from Sigma Aldrich and acrylonitrile (AN) was 99% pure purchased from ACROS organics. All monomers were stored in the refrigerator and allowed to warm to room temperature before use. All other reagents including Optima Gold liquid scintillation counting (LSC) cocktail, sodium acetate, ammonium hydroxide, calcium chloride, potassium persulfate, and Span ® 80 were used as received. All water used for uptake experiments was obtained from a Milli-Q2 system with a measured resistivity of at least 18 MΩ. Radiotracer uptake experiments were performed using stock solutions of the alpha emitters ^{230}Th, ^{233}U, and ^{239}Pu. The ^{230}Th stock was 12.0 mM in 1 M HNO_3 solution. The solution was diluted 10x with desired aqueous media before use. The ^{233}U stock was 11.6 mM in 1 M HNO_3 solution. The ^{239}Pu stock was 0.26 mM in 1 M HNO_3 solution. Aliquots for uptake studies were treated with $NaNO_2$ overnight to ensure conversion of Pu(III & VI) to Pu(IV).

5.2.3 Instrumentation

IR spectra were collected on a Nicolet Nexus 870 FTIR system. Samples were dried in a vacuum oven, diluted with dried KBr, and pressed into a pellet. Spectra were collected between 400–4000 cm^{-1} with 64 scans and 2 cm^{-1} resolution. Surface area measurements were obtained via N_2 uptake with a Micromeritics 3Flex instrument using an appropriate pressure table. Samples were dried in vacuo prior to analysis. Approximately 100 mg of sample was used for each analysis. Brunauer–Emmett–Teller (BET) surface areas were calculated from the N_2 adsorption isotherms. The morphology of the poly(HIPE) materials was discerned using a Karl Zeiss Merlin scanning electron microscope (SEM) with an accelerating voltage of 5.00 kV. Small pieces of dried samples

were carefully mounted atop double-sided carbon tape affixed on aluminum SEM stages. Prior to imaging, the samples were coated with 8nm of Pt/Pd using a Ted Pella sputter coater. Multiple images were taken at various sample locations to ensure faithful representation of the material. Alpha counting was performed via liquid scintillation on a Packard Model 2000 CA counter using an LSC cocktail volume of 5 mL. Regions of interest (ROIs) were individually selected for each isotope so as to include energy ranges with highest counts.

High energy X-ray scattering (HEXS) data were obtained on beamline 11-ID-B at the Advanced Photon Source (APS), Argonne National Laboratory. Using an incident-beam energy of 86.7 keV, corresponding to a wavelength of 0.143 Å, experiments were performed in transmission geometry. The scattered intensity was measured using an amorphous silicon flat panel X-ray detector mounted in a static position ($2\theta = 0°$) at two different distances, providing detection in momentum transfer space across a Q range from 0.26 to 31 $Å^{-1}$. After data reduction, $S(Q)$ patterns were Fourier transformed to yield pair distribution functions (PDF)s, presented as $G(r)$ vs r, which include all atom-atom correlations, weighted by their atomic numbers. As such, all the peaks in the plots are quantitatively related to the relative concentrations of the correlated pairs. Polymer samples were first contacted with aqueous solutions containing 100 ppm metal of interest. Alpha/beta counting before and after 2-hour contact was used to determine percent uptake. The metal loaded polymers were allowed to dry completely before pressed into disks for HEXS analysis.

5.2.4 Uptake Studies

In general, uptake studies were conducted in 10 mL glass vials with ~1 mg polymer at a phase ratio of 1 mg polymer per 1 mL spiked solution. Radionuclides were spiked in such a way

to yield A_0 < 10 000 cpm 100 μL^{-1},where A_0 represents the initial counts via LSC. This corresponds to an initial concentration of ~ 10.2 μM for Th, ~27.1 μM for U, and ~ 3.6 μM for Pu. Since the amount of polymer (i.e. 10^{-6} moles AO) used is in vast excess to the amount of radioactive isotope in solution (i.e. 10^{-8} moles metal), observed differences in uptake characteristics are not due to differences in metal ion diffusion rate into the poly(HIPE) sample or metal precipitation onto the surface of the polymer.

Separations samples were shaken for 60 minutes on a plate shaker at 500 rpm prior to syringe filtration (Whatman, PVDF, 0.2 μm pore size). Empirically, weight distribution ratios were calculated according to the following equation:

$$D_{W,exp} = \frac{A_{0,corr} - A_{F,corr}}{A_{F,corr}} \cdot \frac{V}{m} \quad \textbf{Equation 5.1}$$

where $A_{0,corr}$ is the background corrected initial counts as determined by alpha counting, $A_{F,corr}$ is the background corrected final counts post-uptake, V is the volume of the solution in μL, and m is the mass of the polymer in mg. This distribution ratio metric scales the percent metal ion adsorbed by the volume of solution and mass of polymer used. It is the radiotracer analogue to the uptake capacity metric (Q_e) used for bulk metal studies commonly encountered in the literature.[28]

Kinetics studies were performed using a combination of radiotracer and less-radioactive bulk metal aqueous starting solutions. An advantage of radiotracer studies is the ability to easily probe dilute metal solutions but more concentrated solutions prove challenging as the level of associated radioactivity is usually unacceptable. Therefore, under "bulk metal" conditions, the starting metal concentration is established via less-radioactive ^{232}Th and ^{238}U stock solutions spiked with a minimal amount of radiotracer. LSC counting of the solutions before and after uptake quantifies separation efficacy.

Selective uptake between metal ions was determined via an analysis of the separation factors (α) obtained for each pair where the separation factor is calculated according to **Equation 5.2**:

$$\alpha_{M_B}^{M_A} = \frac{D_{W,M_A}}{D_{W,M_B}} \quad \textbf{Equation 5.2}$$

where $\alpha_{M_B}^{M_A}$ is the separation factor between metal ion A (M_A) and metal ion B (M_B) and D_{W,M_A} and D_{W,M_B} are the distribution ratios obtained for metal ions A and B respectively.

Error analysis considers measurement (i.e. LSC counting) error as well as mass error (i.e. balance error). Counting error (2σ) can be made arbitrarily small with extended counting time. Error bars are included throughout the figures may not be visible due to this fact.

Buffers were prepared according to standard procedures found in the literature. The alkaline pH region (pH 8–10) was attained with an ammonium buffer ($[NH_3] + [NH_4^+] = 0.01$ M). The near neutral pH region (pH 4–7) was attained with a sodium acetate buffer ($[CH_3COO^-] + [CH_3COOH] = 0.01$ M). Acidic conditions (pH ≤ 3) were attained with HNO_3 at the proper concentration. Complexing ion concentration was calculated for the acetate and hydroxide ligands used as part of the buffer media. Significant deviations in D_W values obtained with the equation above have been corrected using methods discussed elsewhere.[29]

5.3 Poly(HIPE) Synthesis

Table 5.1 Feed Organic Phase Conditions

Organic Phase						mole fraction –CN in the poly(HIPE)[a]	mole fraction –AO in the poly(HIPE)
Sample	AN, g	DVB, g	St, g	4CS, g	% AN/St		
1a	0.08	0.16	1.64	0	4.8	0	0
1b	0.46	0.16	1.21		38		
1c	1.62	0.16	1.36		119	93	38[c]
2[b]	0	0.32	2.78	0.39	14[b]	77	32[c]

[a]as determined by FTIR
[b]4-cyanostyrene (4CS) was used
[c]upon treatment with NH_2OH (**1c-AO** and **2-AO** materials)

Table 5.2 Feed Aqueous Phase Conditions

Sample	H_2O (mL)	Span 80 (μL)	$CaCl_2$ (mg)	$K_2S_2O_8$ (mg)
1a	30	350	217	70
1b	30	350	217	70
1c	25	350	217	70
2*	50	700	435	140

In order to maximize –CN group loading, trials were attempted using only acrylonitrile (AN) as the organic phase. However, none of these resulted in a stable emulsion. It was only when styrene (St) and the crosslinker divinylbenzene (DVB) were used in addition to AN in the organic phase that a stable emulsion could be obtained and converted into a porous monolith upon curing (**1a**). However, there was no evidence of –CN incorporation in this trial. Increasing the feed AN/St ratio yielded a similar result (**1b**). Increasing the feed AN while decreasing the amount of aqueous phase resulted in a stable HIPE and evidence of –CN incorporation via IR spectroscopy. Efforts to maximize the AN feed ratio without compromising HIPE stability were successful (**1c**).

5.3.1 Synthesis of 1c

In a typical synthesis, styrene (1.5 mL, 1.36 g), divinylbenzene (175 µL, 160 mg), acrylonitrile (AN, 2 mL, 1.62 g), and Span ® 80 (350 µL, 345 mg) were added to a 150 mL glass beaker and stirred at 200 rpm with an overhead stirrer for 2 minutes. The aqueous phase was prepared in a 100 mL beaker by addition of calcium chloride (217 mg) into distilled water (25 mL) and sonication for 2 minutes. Potassium persulfate (100 mg) was used as the radical initiator and dissolved in the aqueous phase. A 50mL syringe was used to dispense the aqueous solution dropwise using a syringe pump set at ~2.25 mL min-1. During dropwise addition of the aqueous phase, the mixture was continuously stirred at 900 rpm at room temperature. After addition, the resulting white emulsion was allowed to stir for another 5 minutes before being placed into a sealed glass vial for curing.

The emulsion was cured in a vacuum oven under ambient pressure at 75 °C for 24 hours before being placed under vacuum to dry at 85 °C for an additional 48 hours.

5.3.2 Synthesis of 1c-AO

Dried poly(HIPE) (250 mg) was added to a 100 mL round bottom flask with ethanol (25 mL). The mixture was heated to 80 °C before NH_2OH (aq., 30% w/w, 15 eq. with respect to nitrile) was added and the reaction mixture was allowed to stir for 24 hours. The reaction was monitored via FTIR and 15 equivalents of NH_2OH were added until the –CN peak disappeared or greatly diminished in intensity. The material was washed with ethanol and dried in vacuo prior to use in uptake studies.

5.3.3 Synthesis of 2

In a typical synthesis, styrene (3.07 mL, 2.78 g), divinylbenzene (347 µL, 320 mg), 4-cyanostryrene (4CS, 390 mg), and Span ® 80 (700 µL) were added to a 150 mL glass beaker and

stirred at 200 rpm with an overhead stirrer for 2 minutes. The aqueous phase was prepared in a 100 mL beaker by addition of calcium chloride (435 mg) into distilled water (50 mL) and sonication for 2 minutes. Potassium persulfate (140 mg) was used as the radical initiator and dissolved in the aqueous phase. A 50mL syringe was used to dispense the aqueous solution dropwise using a syringe pump set at ~2.25 mL min^{-1}. During dropwise addition of the aqueous phase, the mixture was continuously stirred at 900 rpm at room temperature. After addition, the resulting white emulsion was allowed to stir for another 5 minutes before being placed into a sealed glass vial for curing.

The emulsion was cured in a vacuum oven under ambient pressure at 75 °C for 24 hours before being placed under vacuum to dry at 85 °C for an additional 48 hours.

5.3.4 Synthesis of 2-AO

Dried poly(HIPE) (250 mg) was added to a 100 mL round bottom flask with ethanol (25 mL). The mixture was heated to 80 °C. Afterwards NH_2OH (aq., 30% w/w, 15 eq. with respect to nitrile) was added and the mixture was allowed to stir for 24 hours. The reaction was monitored via FTIR and 15 equivalents of NH_2OH were added until the –CN peak disappeared or greatly diminished in intensity. The material was washed with ethanol and dried in vacuo prior to use in uptake studies.

5.4 Poly(HIPE) Characterization Methods

5.4.1 Nitrile Group Loading

Twelve poly(styrene-co-acrylonitrile) disks were synthesized in the bulk with varying amounts of acrylonitrile monomer (**Table 5.2**). The molar amounts of styrene and divinylbenzene were kept constant throughout. The mol fraction of acrylonitrile was varied from 0 to 0.85.

Standard curves were constructed with the absorbance ratios of –CN to –CH stretches as a function of acrylonitrile mole fraction (**Figures 5.4-5.5**). Comparison of the FTIR spectra obtained for the as-synthesized poly(HIPE) materials with standard curves obtained from measurements of bulk polymer discs provides quantitative nitrile loading information. The same protocol was used to determine the nitrile content in the 4-cyanostyrene functionalized poly(HIPE) materials (**Table 5.4, Figures 5.6-5.7**).

5.4.2 Amidoxime Conversion

Comparing the absorbance ratio of the normalized-CN peak around ~2230 cm^{-1} and –CH stretches at ~2850 cm^{-1} or ~2919 cm^{-1} between the as-synthesized and amidoximated poly(HIPE)s provides a quantitative degree of amidoximation. Under the conditions employed, 63% of the nitrile groups were converted in **1c** while 41% were converted in **2**, resulting in a calculated AO-loading of 38 and 32 mmol/mol poly(HIPE), respectively. The appearance of strong bands around 1650 cm^{-1} (-C=N stretch) and 1580 cm^{-1} (-NH_2 deformation) provide further evidence of successful amidoxime formation. Not all of the nitrile groups are converted to amidoxime groups likely due to their surface inaccessibility.

In order to access **AO** functionalized poly(HIPE)s the strategy was to first synthesize nitrile-containing poly(HIPE)s and then convert the nitrile moiety to an **AO** functional group to enhance actinide sequestration (**Scheme 5.1**). In general, the procedure involves dropwise addition of an aqueous phase into an organic phase to form the HIPE, curing of the HIPE to obtain nitrile-functionalized poly(HIPE), Soxhlet extraction with water then methanol, and finally, treatment with NH_2OH to afford amidoximated material.

5.5 Poly(HIPE) Characterization

Despite the abundance of reports on poly(HIPE) syntheses published in the last two decades, only a few describe materials with acrylonitrile incorporation.[30,31] Successful copolymerization of acrylonitrile (AN) is challenging in poly(HIPE) syntheses as the monomer has pronounced solubility in the aqueous phase—ca. 7.5 wt.% at room temperature (**Figure 5.1**).[32]

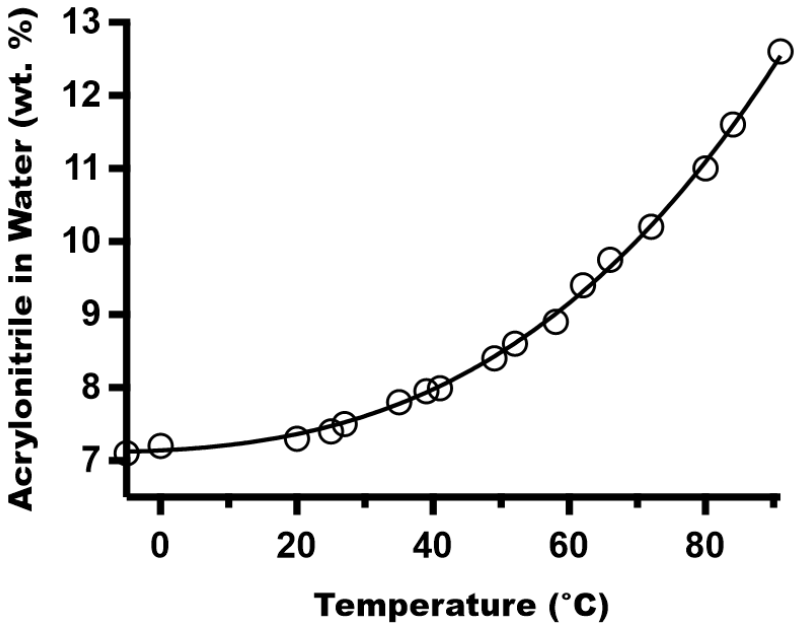

Figure 5.1 Acrylonitrile solubility in water (wt. %) as a function of temperature. Data adapted from Davis, H. S.; Wiedeman, O. F. *Ind. Eng. Chem.* **1945**, *37,* 5, 482–485.

Several trials, based on modifications from literature protocols,[30,31] were attempted to address this difficulty as detailed in **Table 5.1**. Trials using only AN resulted in poor emulsion stability and were not pursued further. Stable emulsions were only obtained though the addition of styrene (St) and the crosslinker divinylbenzene (DVB) (**1a** – **1b**). However, in both cases there was no evidence of –CN incorporation as determined by IR spectroscopy (**Figure 5.2**).

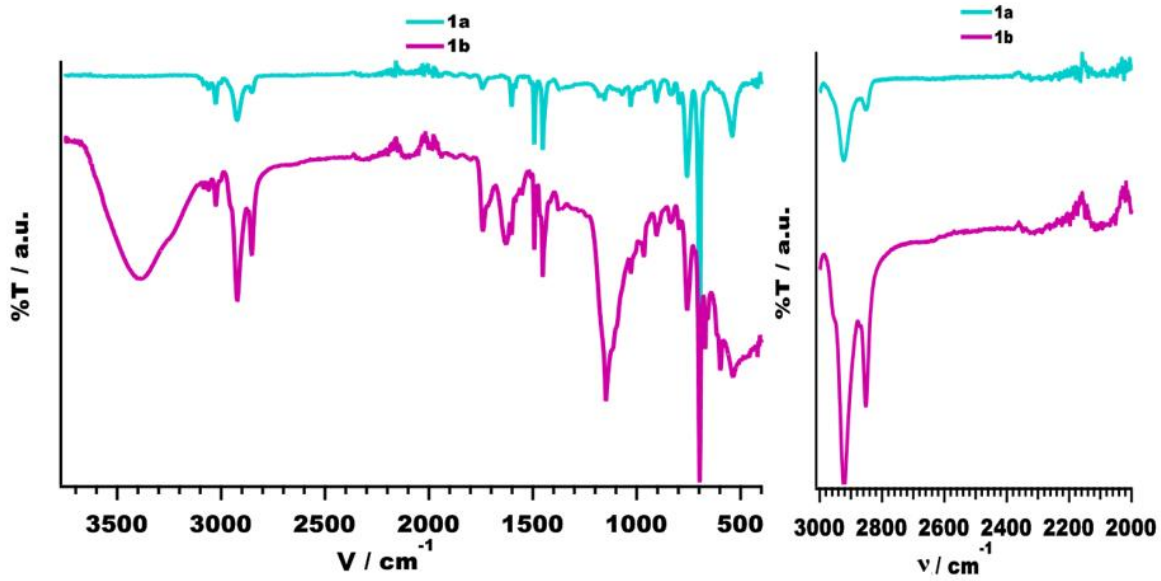

Figure 5.2 FTIR spectra of samples **1a** and **1b**. (Right side shows a zoomin of the region of interest).

Increasing the feed AN and decreasing the amount of aqueous phase resulted in a stable HIPE and poly(HIPE), **1c**, after polymerization. Gratifyingly, after purification by Soxhlet extraction, FTIR analysis of **1c** confirmed successful incorporation of the nitrile moiety as evidenced by the characteristic –CN stretching frequency around 2230 cm^{-1} (**Figure 5.3A**).

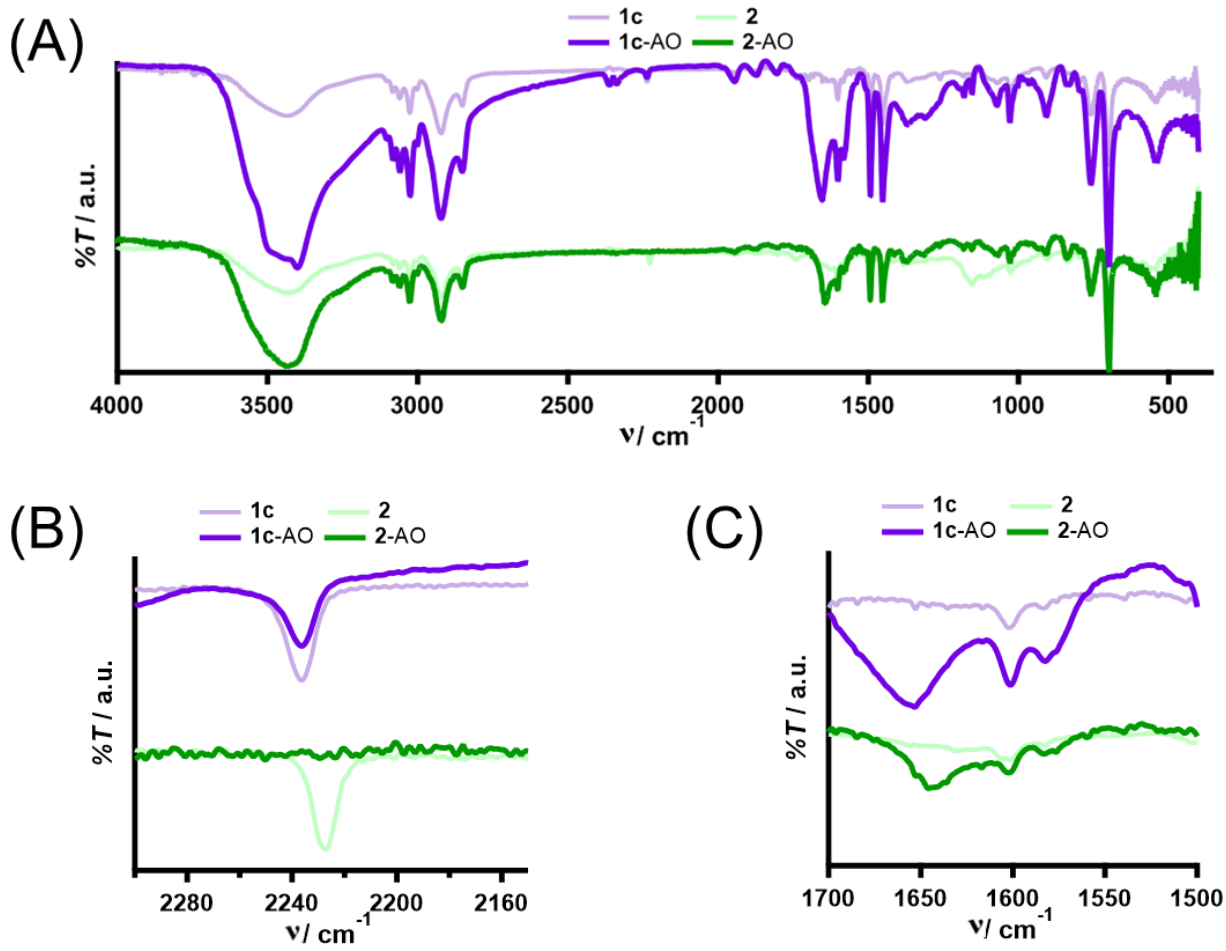

Figure 5.3 FTIR data of nitrile (**1c** and **2**) and amidoxime (**1c-AO** and **2-AO**) functionalized poly(HIPE)s (A) Full IR spectra comparing acrylonitrile-based poly(HIPE)s (purple traces) with 4-cyanostyrene poly(HIPE)s (green traces) (B) Magnified portion of the IR spectra between 2160 and 2280 cm^{-1} (C) Magnified portion of the IR spectra between 1500 and 1700 cm^{-1}.

Strong bands occurring around 2919, 2850, 1450 and 700 cm^{-1} correspond to CH_2 and CH stretching, CH_2 bending, and CH out of plane deformations respectively. The theoretical maximum nitrile loading (expressed in mol fraction –CN), based on feed monomer, was calculated to be 680 mmol/mol for **1c**. The actual degree of nitrile group loading was experimentally determined according to established protocols in the literature using standard curves produced via FTIR of copolymer standards (**Table 5.3, Figures 5.4-5.6**).[28,33] It was found that **1c** has a loading of 93 mmol –CN/mol, corresponding to a 14% incorporation of the feed AN into the polymer (**Table**

5.4). It is evident that despite the modified protocol, much of the AN partitions into the aqueous phase and is subsequently removed upon washing and drying.

Table 5.3 Synthetic Details for Synthesis of Poly(styrene-co-acrylonitrile-co-divinyl benzene) FTIR Standards

Mol Frac CN	Styrene (µL)	Styrene (mmol)	DVB (µL)	DVB (mmol)	AN (µL)	AN (mmol)	AIBN (mg)
0	787.5	**6.9**	86.75	**0.61**	0	**0**	3.96
0.05	787.5	**6.9**	86.75	**0.61**	25.72	**0.39**	4.07
0.1	787.5	**6.9**	86.75	**0.61**	54.29	**0.83**	4.18
0.15	787.5	**6.9**	86.75	**0.61**	86.23	**1.32**	4.31
0.2	787.5	**6.9**	86.75	**0.61**	122.16	**1.86**	4.46
0.25	787.5	**6.9**	86.75	**0.61**	162.88	**2.49**	4.62
0.3	787.5	**6.9**	86.75	**0.61**	209.42	**3.20**	4.81
0.4	787.5	**6.9**	86.75	**0.61**	325.76	**4.97**	5.28
0.5	787.5	**6.9**	86.75	**0.61**	488.64	**7.46**	5.94
0.6	787.5	**6.9**	86.75	**0.61**	732.96	**11.19**	6.93
0.7	787.5	**6.9**	86.75	**0.61**	1140.17	**17.41**	8.58
0.8	787.5	**6.9**	86.75	**0.61**	1954.57	**29.84**	11.88
Abbreviations Used: AIBN = Azobisisobutyronitrile, AN = Acrylonitrile, DVB = Divinylbenzene, Frac = Fraction							

Table 5.4 Functional Group Loading of Cyano- and Amidoximated Poly(HIPE) Samples

Name	CN Loading (mmol/mol frac.)		% CN incorporation	AO-Loading mmol/mol frac.
	Theoretical	Actual		
1c	680	93	14%	38
1c-AO				
2	93	77	82%	32
2-AO				

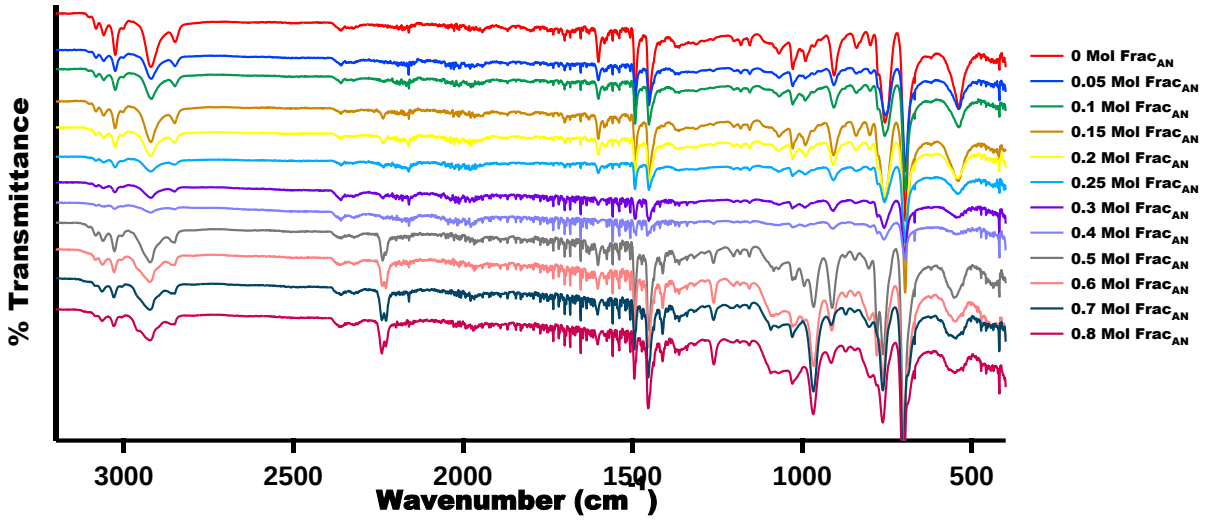

Figure 5.4 FTIR spectra of bulk poly(styrene-co-acrylonitrile-co-divinyl benzene) standards.

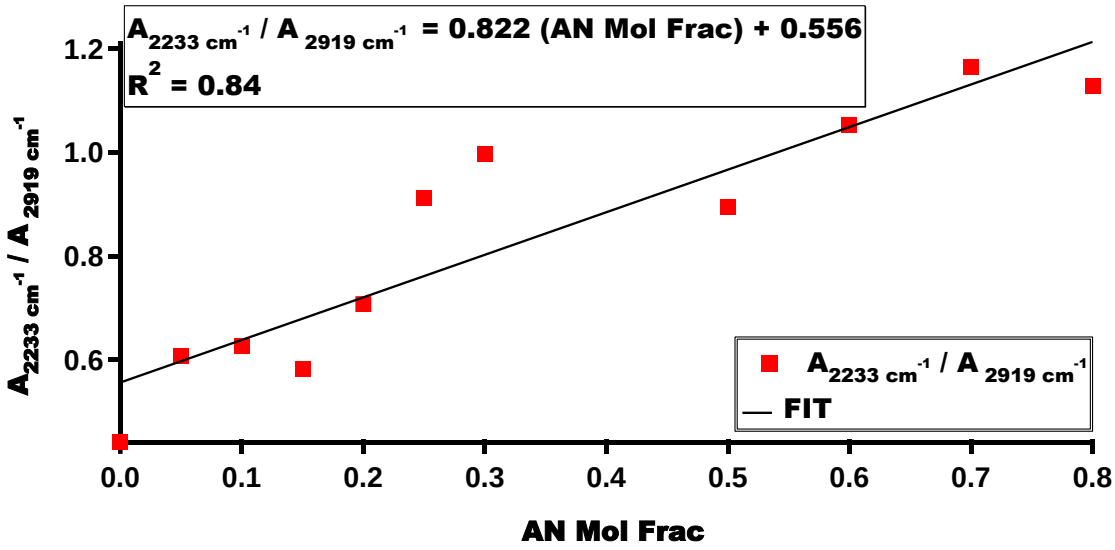

Figure 5.5 poly(styrene-co-acrylonitrile-co-divinyl benzene) standard curve depicting the 2233 cm^{-1}/2919 cm^{-1} absorbance ratio as a function of acrylonitrile (AN) mol fraction.

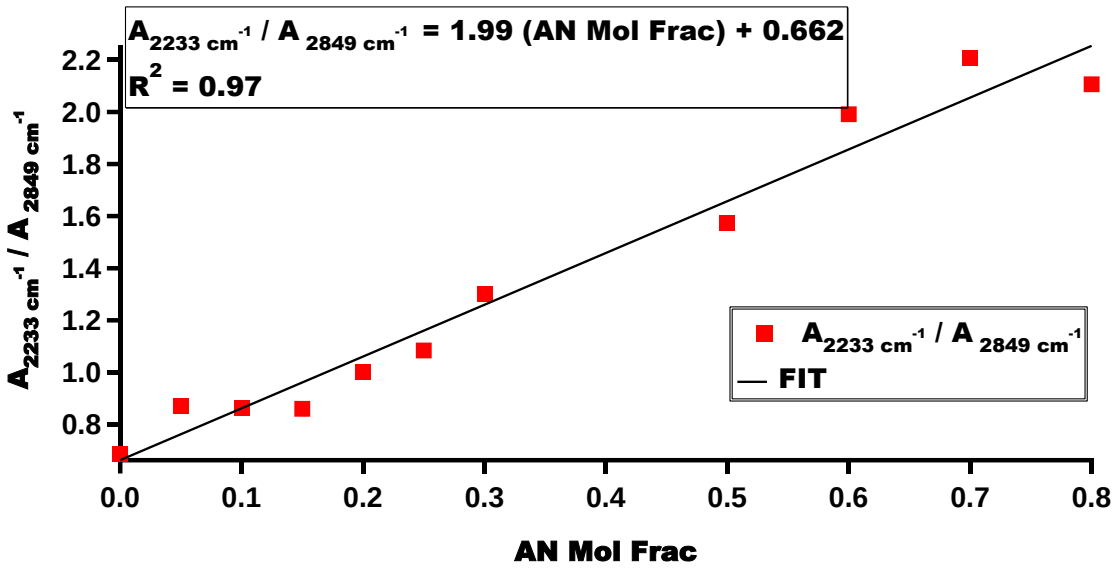

Figure 5.6 poly(styrene-co-acrylonitrile-co-divinyl benzene) standard curve depicting the 2233 cm^{-1}/2849 cm^{-1} absorbance ratio as a function of acrylonitrile (AN) mol fraction.

The relatively low incorporation of AN into the poly(HIPE) prompted the use of the less water soluble 4-cyanostyrene (4CS) as the nitrile-containing monomer (**sample 2**). Indeed, it was found that the incorporation of the arylnitrile into the poly(HIPE) was much more efficient than AN. Based on FTIR, (**Table 5.5, Figures 5.7-5.9**) 77 mmol –CN/mol was found in **2** which corresponds to an 82% incorporation. Use of the arylnitrile comonomer allows for enhanced synthetic control over final –CN group loading within the polymer and is discussed in detail in Chapter 6 although poly(HIPE)s with 100% 4CS loading are still inaccessible under the current set of conditions.

Table 5.5 Synthetic Details for Synthesis of Poly(styrene-co-4-cyanostyrene-co-divinyl benzene) FTIR Standards

Mol Frac CN	Styrene (µL)	Styrene (mmol)	DVB (µL)	DVB (mmol)	4CS (µL)	4CS (mmol)	AIBN (mg)
0	261	2.3	30	0.21	0	0	1.32
0.05	261	2.3	30	0.21	16.87	0.13	1.40
0.1	261	2.3	30	0.21	35.61	0.28	1.50
0.15	261	2.3	30	0.21	56.55	0.44	1.60
0.2	261	2.3	30	0.21	80.11	0.62	1.72
0.25	261	2.3	30	0.21	106.82	0.83	1.85
0.3	261	2.3	30	0.21	137.34	1.06	2.01
0.4	261	2.3	30	0.21	172.55	1.34	2.18
0.45	261	2.3	30	0.21	213.64	1.65	2.39

Abbreviations Used: AIBN = Azobisisobutyronitrile, 4CS= 4-cyanostryrene, DVB = Divinylbenzene, Frac = Fraction

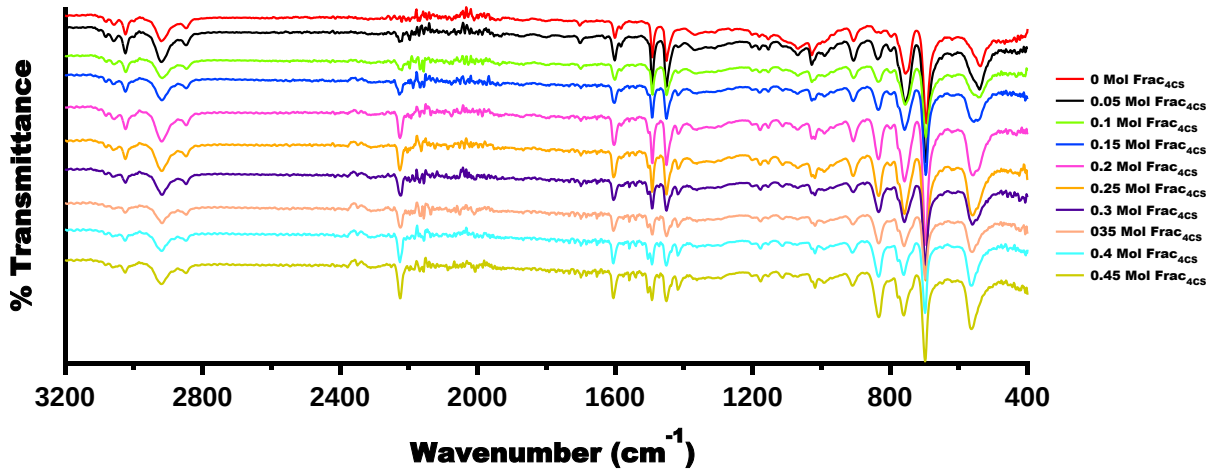

Figure 5.7 FTIR spectra of bulk poly(styrene-co-4-cyanostyrene-co-divinyl benzene) standards.

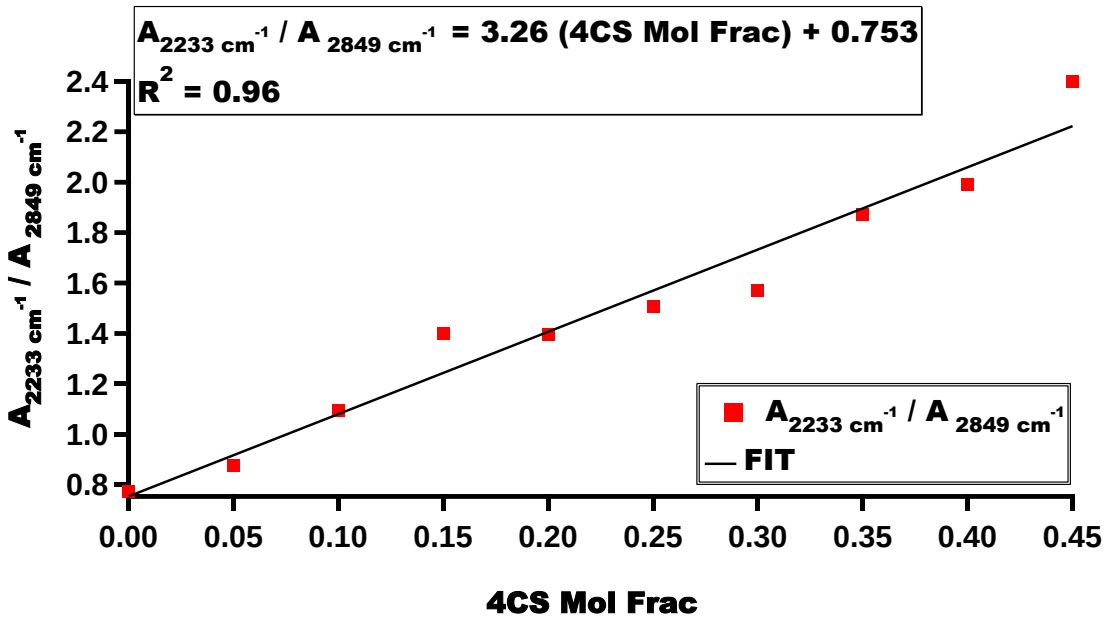

Figure 5.8 poly(styrene-co-4-cyanostyrene-co-divinyl benzene) standard curve depicting the 2233 cm^{-1}/2849 cm^{-1} absorbance ratio as a function of 4-cyanostyrene (4CS) mol fraction.

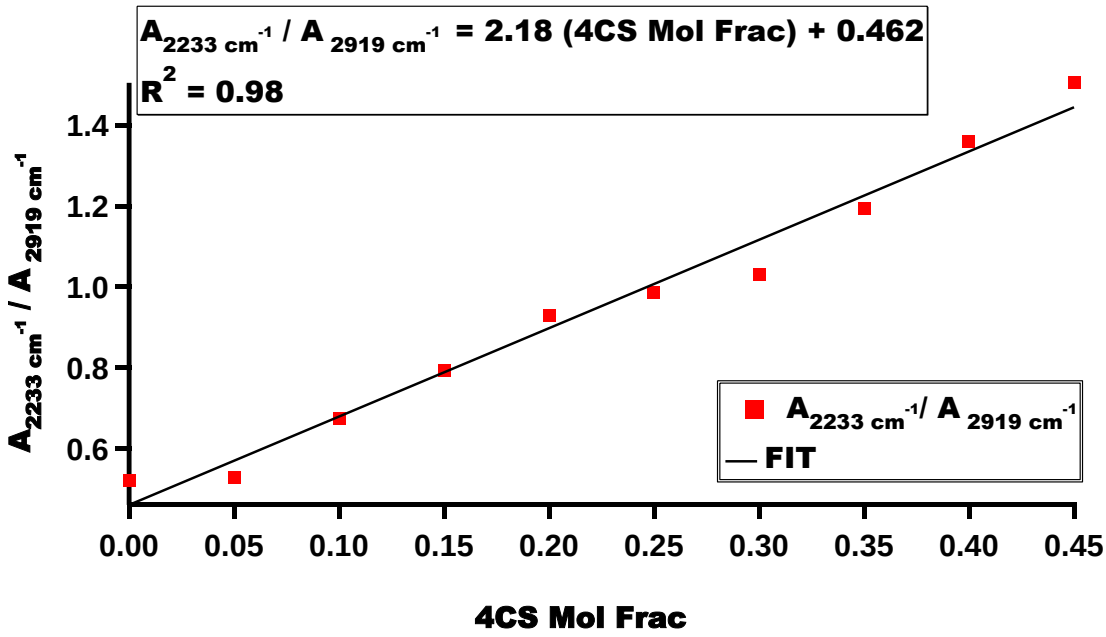

Figure 5.9 poly(styrene-co-4-cyanostyrene-co-divinyl benzene) standard curve depicting the 2233 cm^{-1}/2919 cm^{-1} absorbance ratio as a function of 4-cyanostyrene (4CS) mol fraction.

The nitrile-containing poly(HIPE)s **1c** and **2** were then treated with NH_2OH in order to form amidoxime functionalized poly(HIPE)s, **1c-AO** and **2-AO**, respectively. The decrease in intensity of the –CN peak around 2230 cm^{-1} in both materials upon treatment with NH_2OH suggests conversion of the nitrile group to the target amidoxime (**Figure 5.3B**). The appearance of strong bands around 1650 cm^{-1} (-C=N stretch) and 1580 cm^{-1} (-NH_2 deformation) provide further evidence of successful amidoxime formation (**Figure 5.3C**). The amount of **AO** in these poly(HIPE)s was determined by comparing the absorbance of the normalized –CN IR stretch before and after amidoximation and shown to be 38 and 32 mmol/mol poly(HIPE) corresponding to ~0.9 and ~0.3 mmol AO g^{-1} polymer for **1c-AO** and **2-AO** respectively. Some nitrile groups remain unreacted presumably due to their inaccessibility within the polymer as evidenced by the persistence of the –CN peak upon amidoximation.

SEM confirmed typical open-cell, interconnected void structures were evident in the poly(HIPE) samples (**Figure 5.10**).[6]

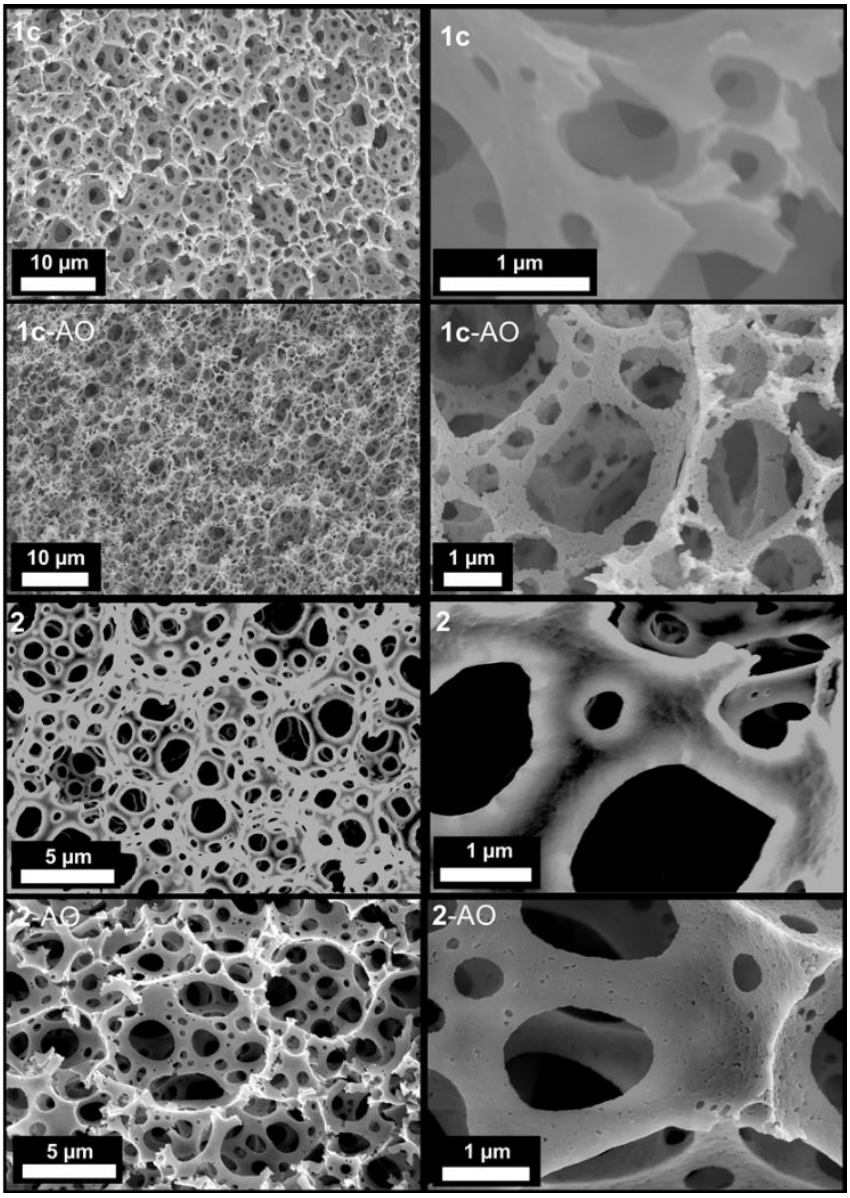

Figure 5.10 SEM images of as-synthesized (1c and 2) and post-amidoximation (**1c-AO** and **2-AO**) poly(HIPE) materials at variable magnification levels (2,000 – 25,000 X).

Interestingly, small pores within the cell walls are increasingly evident upon NH_2OH treatment illustrating that amidoximation has some effect on poly(HIPE) morphology. Surface area measurements were obtained via N_2 uptake and for both samples, Brunauer–Emmett–Teller (BET) surface areas increase upon amidoximation consistent with the SEM images (**Table 5.6**)

Table 5.6 BET Surface Areas for Poly(HIPE) Materials

Name	BET Surface Area (m^2 g^{-1})
1c	2.07
1c-AO	23.29
2	4.95
2-AO	22.70

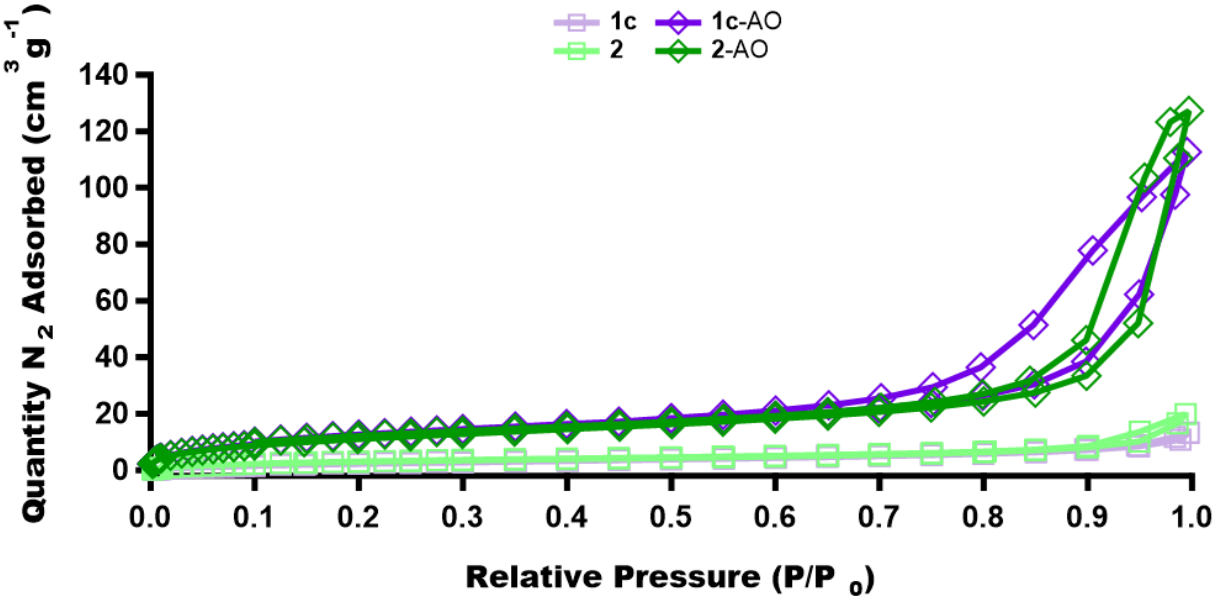

Figure 5.11 Nitrogen Uptake Isotherm of as synthesized (**1c, 2**) and amidoxime functionalized (**1c-AO**, and **2-AO**) poly(HIPE) materials.

In general, the surface areas of the as-synthesized polymers are similar to values reported for other polystyrene-based poly(HIPE)s.[34] Although no particular surface area was targeted with these samples, poly(HIPE) surface areas, in general, can be tuned from ~2 m^2g^{-1} to ~800 m^2g^{-1}.[10] This range allows for facile access to surface areas characteristic of more conventional materials such as the state-of-the-art braided AO-functionalized polymer fibers discussed in **Chapter 1** (~1 m^2g^{-1}) to functionalized metal-organic-framework (MOF) materials (>1000 m^2g^{-1}).[35] Nitrogen uptake isotherms show some hysteresis between the adsorption and desorption branches

suggesting a degree of mesoporosity which is accentuated in the amidoximated poly(HIPE) materials (**Figure 5.11**).

5.6 Separations Experiments with AO-functionalized poly(HIPE)s

To test their heavy-metal uptake from aqueous solution, studies were first conducted with tracer levels of ^{230}Th (10 μM), ^{233}U (27 μM), and ^{239}Pu (4 μM) between pH -1 and 10 to ascertain the materials' selectivity over a broad pH range. Uptake data were collected for U and Th, present as the hexavalent uranyl cation (UO_2^{2+}) and tetravalent thorium cation (Th^{4+}) over the entire pH range. Data for tetravalent Pu were collected over a more limited pH range, from -1 to 4, on account of complications with hydrolysis at near-neutral conditions[36,37].

U uptake averages 30% between pH 4-10 with the highest uptake for both **1c** and **2** materials at the near neutral conditions (pH = 6-7) typical of groundwater decontamination (**Figures 5.12-5.13**). Under most conditions studied, Th uptake exceeds U uptake. Th uptake approaches 90% between pH 5-6 while U uptake is lower in the same region but varies between 33% - 60%. (**Figures 5.12-5.13**). Data show that Pu uptake is lower than Th uptake and only slightly higher than U in this region. None-the-less some selectivity between U and Pu is observed at pH < 4.

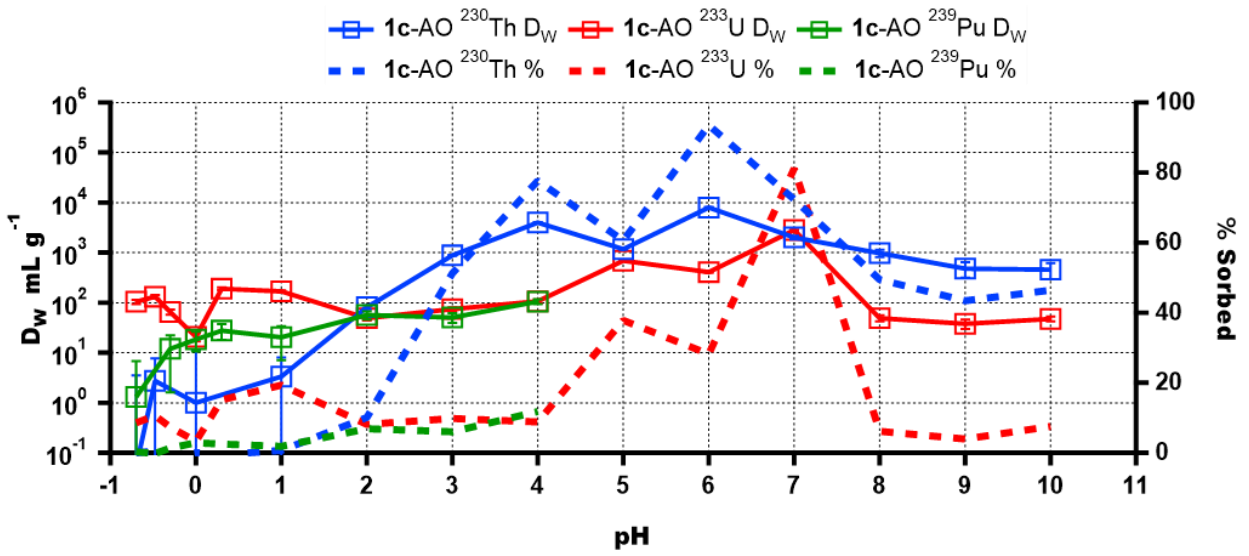

Figure 5.12 Uncorrected D_W values for **1c-AO** materials with ^{230}Th, ^{233}U, and ^{239}Pu.

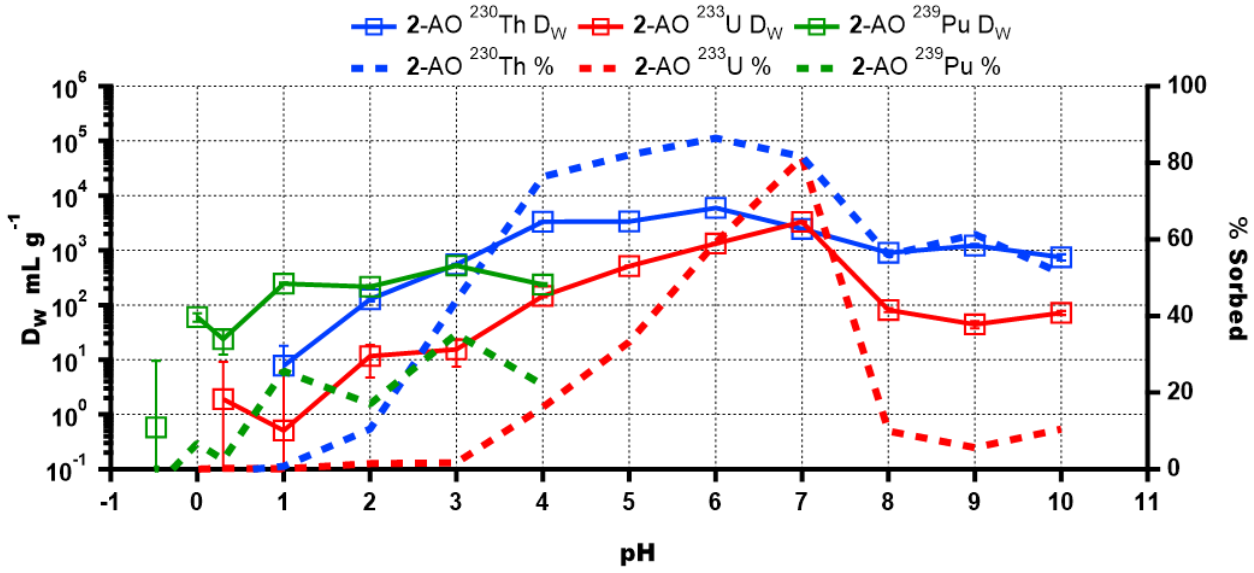

Figure 5.13 Uncorrected D_W values for **2-AO** materials with ^{230}Th, ^{233}U, and ^{239}Pu.

Distribution ratios (D_W, mL g^{-1}, **Equation 4.1**) corrected for buffer effects,[29] are plotted in **Figure 5.14A** below. Selectivity was ascertained via the separation factor (α), the quotient of relative distribution coefficients (**Equation 5.1**).

Th uptake exceeds $D_W = 10^{11}$ around pH = 6 and is much higher than U in the circumneutral region when evaluated using this metric. Fully corrected distribution values for ^{239}Pu uptake suggest both adsorbents possess some affinity for Pu especially in acidic conditions.

The time dependency of metal uptake was then investigated, using 1 ppm natural ^{232}Th and ^{238}U solutions spiked with tracer levels of ^{230}Th and ^{233}U. Time dependent studies show that sorption maxima are achieved after about 2 hours, remaining constant up to 5 hours of contact (**Figure 5.14B**). As expected from the distribution coefficients presented above, Th uptake is greater than U for both **1c-AO** and **2-AO** systems. It is noteworthy that nearly 100% of Th is adsorbed from solution with **2-AO** after only 30 minutes.

Interestingly, both polymer materials exhibited poor radionuclide uptake below pH = 1, suggesting that acid elution could be a potentially effective means of recycling the adsorbent by stripping all loaded metal ions. In fact, two rounds of contact of the metal-loaded poly(HIPE)s with 1 M HNO_3 resulted in a cumulative 94% Th and 37% U eluted from the aromatic amidoxime functionalized samples (i.e. **2-AO**). The aliphatic AO functionalized poly(HIPE) exhibited slightly worse elution with 78% Th and 32% U removed after HNO_3 contact. This result suggests a difference in binding affinity between the amidoxime functional groups and metal ions or differences between functional group accessibility within the polymer.

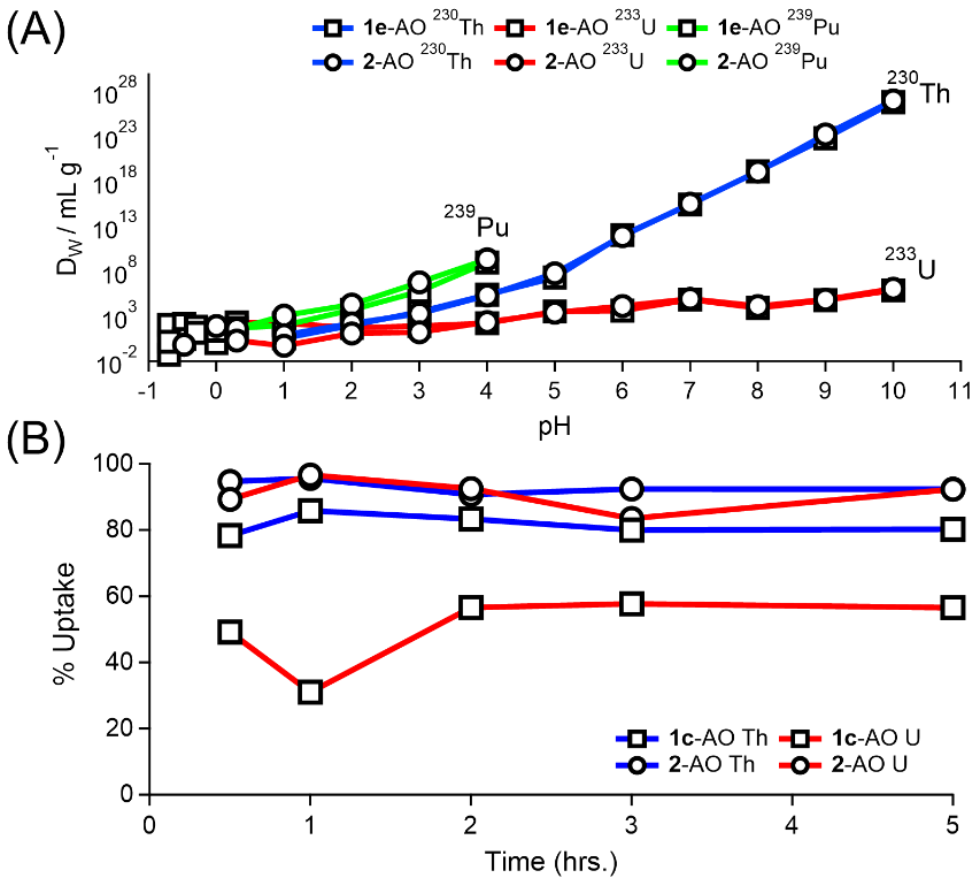

Figure 5.14 A) D_W values fully corrected for buffer effects for **1c-AO** and **2-AO** materials with radiotracers ^{230}Th, ^{233}U, and ^{239}Pu as a function of pH B) Bulk metal uptake as a function of time.

5.7 Metal Hydrolysis Chemistry Informs Separations Efficacy

Thus, the overall radionuclide uptake trend for these amidoximated poly(HIPE)s is $D_W^{Pu} > D_W^{Th} > D_W^{U}$ under acidic conditions and $D_W^{Th} >> D_W^{U}$ under circumneutral to basic conditions. Without correcting for buffer effects (**Figures 5.13-5.14**), Pu uptake is lower than Th despite both ions existing in the (IV) state; consistent with significant hydrolysis and condensation into Pu polynuclear species, even under acidic conditions. These multinuclear species can present as differently charged species dependent on solution conditions and may be difficult to extract.[38]

The actinides have a strong tendency to hydrolyze in solution.[39] This tendency along with their propensity to form extended structures including dimers, trimers, other-higher-order species,

and hydroxo/oxo bridged species is key to rationalizing separations results.[37] The hydrolysis reaction is depicted in **Equation 5.3** below:

$$[M\text{-}(OH_2)_x]^{z+} \xrightarrow{\text{hydrolysis}} [M\text{-}(OH)(OH_2)_{x-1}]^{z-1+} + H^+ \quad \textbf{Equation 5.3}$$

Generally, the extent to which a metal ion hydrolyzes in solution can be quantified by the β coefficient:

$$\beta_1 \approx \frac{[M\text{-}(OH)(OH_2)_{x-1}]\ [H^+]}{[M\text{-}(OH_2)_x]} \quad \textbf{Equation 5.4}$$

Higher β coefficients indicate a greater proportion of the hydrolysis product under a certain set of conditions. The β coefficients for the formation of mono-hydroxo species (i.e. $[M\text{-}(OH)(OH_2)_{x-1}]^{(z-1)+}$ are shown for selected +4 and +6 actinides below (**Table 5.7**).

Table 5.7: Formation Constants for Selected An(IV/VI)$(OH)^{n+}$ Species

	Th(IV)$(OH)^{3+}$	**U(IV)$(OH)^{3+}$**	**U(VI)$O_2(OH)^+$**	**Np(IV)$(OH)^{3+}$**	**Pu(IV)$(OH)^{3+}$**
log(β_1)	11.8	13.6	8.19	14.5	14.6

Although the least likely to hydrolyze among the +4 actinides, Th^{4+} nevertheless exhibits a higher hydrolysis tendency (log β_{11} = 11.8, $Th(OH)^{+3}$) than UO_2^{2+} (log β_{11} = 8.19, $UO_2(OH)^+$).[40] This tendency towards hydrolysis ensures a high degree of mono-hydroxo Th products which can undergo olation (**Equation 5.5**) (i.e. the process by which metal ions form polymeric hydroxide-bridged species in aqueous solution).

$$M\text{-}OH + M\text{-}OH_2 \xrightarrow{\text{olation}} M\text{-}OH\text{-}M + H_2O \quad \textbf{Equation 5.5}$$

Owing to their variable tendency to hydrolyze, multinuclear Th-“ol” (condensation) products are expected to be present in solution to a much greater extent than analogous U products. Several

reports[41,42] in the literature of thorium dimers, tetramers, hexamers, and OH^- bridged oligomers underscores the importance of the olation reaction in understanding Th's aqueous chemistry.

The U/Th separations trend found experimentally is unexpected based on amidoxime's well-known affinity for U and precedence set by other **AO**-based polymers for U/Th separations.[25,43,44] The apparent reversal in affinity for Th and U can be explained partially by electroselectivity wherein the more positively charged cation is preferentially adsorbed—a behaviour typical of conventional cation exchange materials.[45] In this case, $Th^{4+} > [U(VI)O_2]^{2+}$. However, when the acetate concentration in the aqueous solution of a separations experiment increases from 0.01 M to 6 M, U uptake drops to near 0% while Th uptake remains above 90% (**Figure 5.15**). Therefore, electrostatic interactions between functionalized polymer and metal alone cannot fully explain the difference in observed selectivity. From another perspective, changing the aqueous acetate concentration may serve as a benign way to selectively elute U from the polymer.

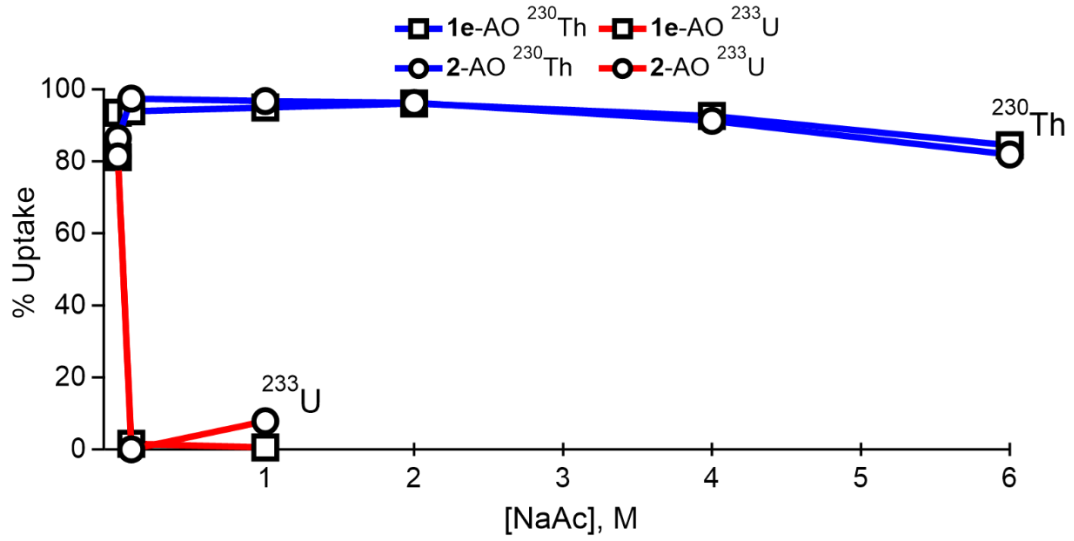

Figure 5.15 Radiotracer uptake as a function of starting sodium acetate concentration in the aqueous phase.

Work done by others[25,44] using amidoximated polymers for U/Th separations consistently found higher U uptake capacity and different binding mechanisms between the two metals. Precipitation of $Th(OH)_4$ and blockage of functionalized pores was indicated as the explanation for lower Th uptake capacity. Further, investigation of the U binding environment in these systems produced models consistent with at least two amidoxime groups in the inner sphere. It is possible that the relatively low amidoxime loading in these poly(HIPE) materials compared with amidoxime-functionalized polymer fibers used for uranium from seawater purposes[46] limits the ability of multiple amidoxime groups to bind U, thus preventing the formation of stable $(\mathbf{AO})_x$-U-$(\mathbf{AO})_y$ environments and explaining, at least in part, the Th selectively. On the other hand, recent work by Li and co-workers[47] found a direct relationship between UO_2^{2+} uptake and AO functional group loading on polymer fibers up to a point where higher levels of AO loading actually resulted in worse U uptake performance. The sum of these studies suggests that there is an unexpected, non-linear correspondence between separations efficacy and adsorbent functional group loading, Maximizing the functional group parameter may not be the optimal strategy, therefore, for every separations application.

High-Energy X-ray scattering was used to interrogate the metal-loaded poly(HIPE) materials in order to bolster understanding of the Th/U separations behavior in these systems.

5.8 A Brief Introduction to High-Energy X-ray Scattering

In general, X-ray scattering involves the elastic interaction of X-ray photons with the electrons in a sample.[48] X-ray diffraction is considered a specific case that can be used to simplify the quantification of these interactions only when the sample is comprised of atoms arranged in a three-dimensional ordered array.[49] In the absence of such order (e.g. amorphous solids, liquids,

gases, and solutions) it is necessary to treat the scattering pattern as the sum of *all* atom-atom correlations in the sample.[50] The scattering response is a function of the reciprocal-space (Q) range over which it is obtained. Analysis of low-Q data (~0.001 to 1 $Å^{-1}$), referred to as small-angle X-ray scattering (SAXS), provides information on the size and shape of large-sized clusters, on the order of 10 to ~1000 Å and is commonly used to extract information on nanoparticle or polymer morphology. Data collected over an intermediate-Q range (~ 0.5 to 20 $Å^{-1}$), known as wide-angle X-ray scattering (WAXS), provide interatomic information on all atom-atom pair correlations in a sample. With the availability of high-flux, high-energy X-rays from synchrotrons such as the Advanced Photon Source (APS), the Q-range can be extended to >50 $Å^{-1}$ in a technique known as high-energy X-ray scattering (HEXS).

There are several advantages of using high-energy X-rays to investigate amorphous materials. First, absorption by the sample is low, thus providing information from the sample bulk, even for high-Z materials. As a result, corrections applied in data-reduction and analysis can be significantly reduced providing more accuracy. Second, the extended Q-range permits the subtraction of scattering from an empty sample holder and, in some cases, from matrix contributions. This feature of HEXS is important because X-ray scattering is not a single-ion probe, instead including all atom-atomic correlations within a sample. However, as scattering intensity is proportional to the square of electron density, the technique is particularly well suited to the study of actinides. Third, typical analysis of HEXS data involves the conversion of the scattering pattern into a pair-distribution function (PDF) via a Fourier transform (FT). The peak resolution of the resulting PDF depends on $2\pi/Q$ so that an increase in Q by a factor of two improves the resolution by the same amount. It should be noted that even with the improved resolution afforded by HEXS,

EXAFS (discussed in **Chapter 1**) provides better peak resolution and is often used as a complementary technique for ascertaining nearest coordinating-neighbor distances.[51]

Combining the improved resolution of PDF over SAXS and WAXS with the overall accuracy of scattering over spectroscopy (e.g. standard deviations of ± 1% and 10% for HEXS vs EXAFS in coordination number assignment[52]) provides for a powerful tool to investigate metal-loaded adsorbents to capture understanding of separations chemistry.

The PDF pattern obtained from HEXS data can be understood as a histogram of all the atomic-scale correlations present in the sample, weighted by their electron count (atomic number). What follows is a simplified account of data genesis within a HEXS experiment.

Considering **Figure 5.16,** assume that the blue sphere is a functionalized polymer while the smaller, grey spheres are metal ions adsorbed onto the polymer.

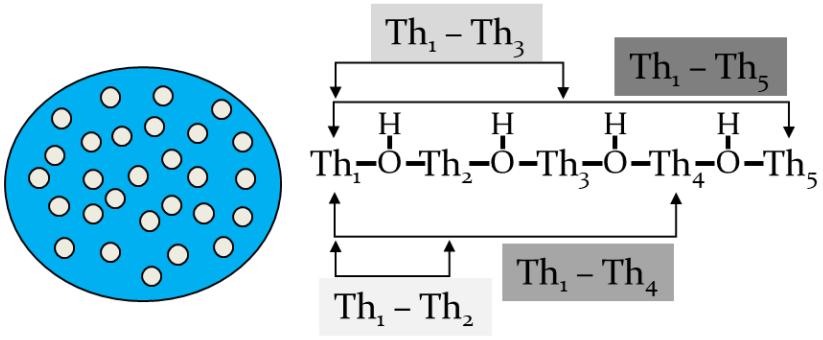

Figure 5.16 Cartoon of a metal loaded polymer (left) and an example of a hydroxo-bridged thorium oligomer (right).

Further, assume that the thorium atoms, in this case labelled Th_1, …, Th_5, are associated via hydroxo linkages of an arbitrary distance of 4 Å (**Figure 5.16**). An analysis of a PDF pattern generated from HEXS data provides correlation peaks, with intensities directly proportional to the electron count of the two correlating species as a function of distance between two scatterers.

In the figure, the first major atomic correlation, $Th_1 – Th_2$, occurs at a distance of 4 Å and is represented by a blue block in **Figure 5.17**. Note that Th-O, Th-polymer, or polymer-polymer correlations are not considered in this example as their correlation intensities (Z_1*Z_2, i.e. 6*6 = 36 for C-C backbone, 90*16 = 1440 for Th=O, and 90*90=8100 for Th-Th). This attribute allows the detection of Th correlations above polymer background peaks even for dilute samples.

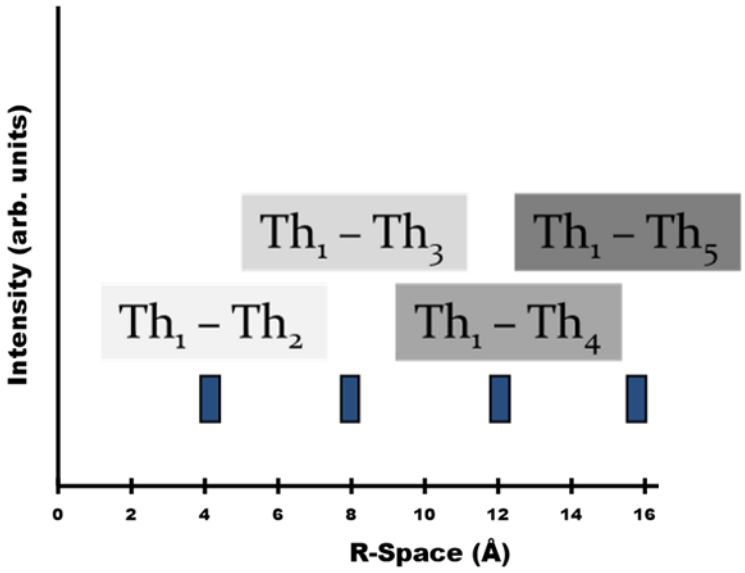

Figure 5.17 Building up of scattering intensity as a function of scatterer distance.

The $Th_1 – Th_3$ correlation occurs at twice the distance of the $Th_1 – Th_2$ correlation and is represented by a blue block at 8 Å. This same exercise is repeated for the $Th_1 – Th_4$ and $Th_1 – Th_5$ correlations resulting in a single "block" of intensity at 4, 8, 12, and 16 Å (**Figure 5.17**). Repeating this for each unique pair of Th correlations in **Figure 5.16** results in the pattern of intensity blocks shown on the left in **Figure 5.18**.

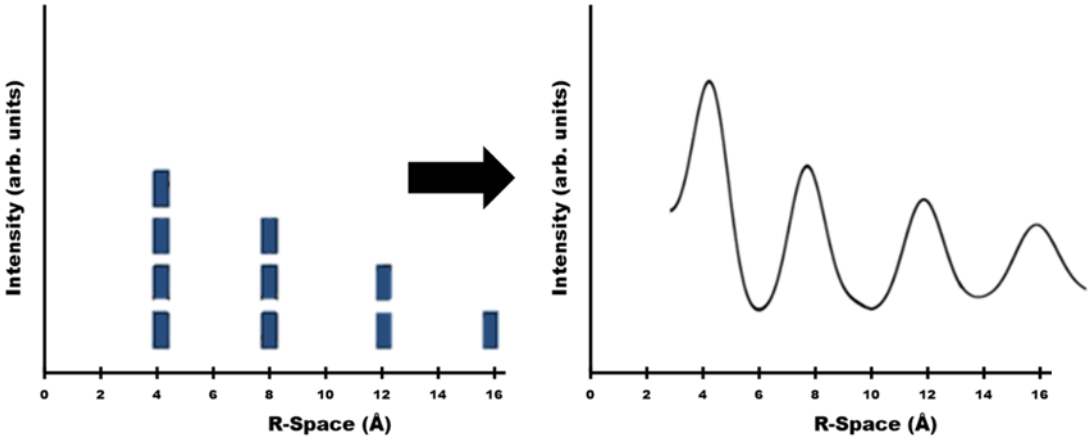

Figure 5.18 Schematic representation of intensity blocks obtained from experiment (left) to smooth, averaged data (right).

A depiction of the smooth, weighted data corresponding to the intensity blocks for Th-Th correlations is shown on the right in **Figure 5.18**. This form of the data allows for the extraction of chemically useful information including coordination numbers.

5.9 HEXS Data of Metal-Contacted Polymers

Background subtracted HEXS data collected for uranium and thorium loaded poly(HIPE) samples are shown in **Figure 5.19**.

The patterns shown in **Figure 5.18** represent average electron density profiles (G(r)) as a function of distance for all scatterers present in the metal-loaded poly(HIPE) sample.[53]The scattering intensities are adjusted with the relevant form factors and incident photon flux. Unlike HEXS analysis of solution phases, the absolute calibration in this case is not accurate due to uncertainties in the bulk-packing density and, to a lesser extent, the sample unit-densities. For these reasons, the G(r) is reported in arbitrary units. In the uranium loaded **1c-AO** case, the scattering pattern is not significantly different from the unloaded polymer, particularly in the longer *r* (>5 Å).

This suggests that the polymer structure itself is not significantly influenced by the aqueous conditions used to contact with uranium. Furthermore, the lack of additional scattering intensity at

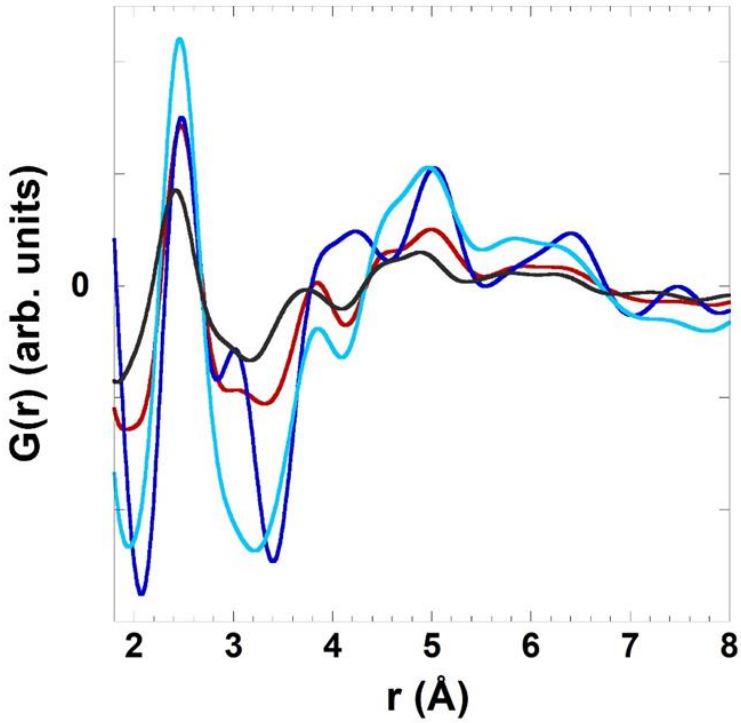

Figure 5.19 Pair-distribution function (PDF) obtained from HEXS data of Th and U loaded poly(HIPE) materials. Correlations from the empty sample holder have been subtracted from the scattering data before Fourier transform. Uranium loaded **1c-AO** (red), thorium loaded **1c-AO** (light blue), thorium loaded **2-AO** (dark blue) poly(HIPE). Representative PDF from the poly(HIPE) after soaking in metal-free buffer solution is included for reference (black). Note: the uranium loading of **2-AO** was too low to extract meaningful U correlations.

larger r indicates no observable U-U correlations, consistent with the separations results that show less U than Th uptake under these conditions. In the case of the thorium-loaded samples, much higher absolute intensity is evident and high intensity is maintained to high *Q*-space. Consideration of the form factor of the heavy (i.e. Th) and light (i.e. C, H, O, N) scatterers involved, it is expected that higher-*Q* intensity has substantial contribution from Th correlations.

Of particular interest in the Th PDF patterns shown in **Figure 5.19** is the general increase in the magnitude of G(r) at distances longer than ~ 4 Å. This behaviour is consistent with the presence of heavy-ion interactions; in this case, Th-Th correlations. Previous work[41] on the crystal growth and analysis of hydroxo-bridged thorium dimers in solution attributed features present in HEXS data around 4.05 Å to Th-Th correlations while peaks found around 5 Å were attributed to correlations between Th and interstitial Cl^- ions. These attributions were enabled by the availability of single-crystal x-ray diffraction data for comparison and by the relative monodispersity of the solution phases under study. Since the poly(HIPE) samples discussed herein provide neither scenario, the options for *direct* peak assignments are limited. As the separation studies in this work were conducted in acetate media, it is possible that Th oligomers in solution present as acetate-bridged species or as Th clusters. What is clear from the PDF analysis is the presence of Th-Th correlations which would be absent if Th were to be adsorbed in a totally mononuclear fashion (i.e. Th-AO), that is homogeneously dispersed throughout the polymer. While an absolute determination of Th speciation cannot be made with HEXS alone, the presence of Th-Th correlations is consistent with their presentation as oligomers or clusters, in line with the expected Th hydrolysis chemistry in solution.

Small angle x-ray scattering (SAXS) data obtained from the same Th and U loaded poly(HIPE)s are also consistent with significant clustering in the Th loaded materials that is not present in the U samples (**Figure 5.20**). The overall higher intensity of the Th scattering compared to the U scattering in this low Q region along with the increased scattering with decreasing Q are indicative of particle or aggregate species in the Th sample and further support the conclusion of Th clustering determined from the HEXS data.

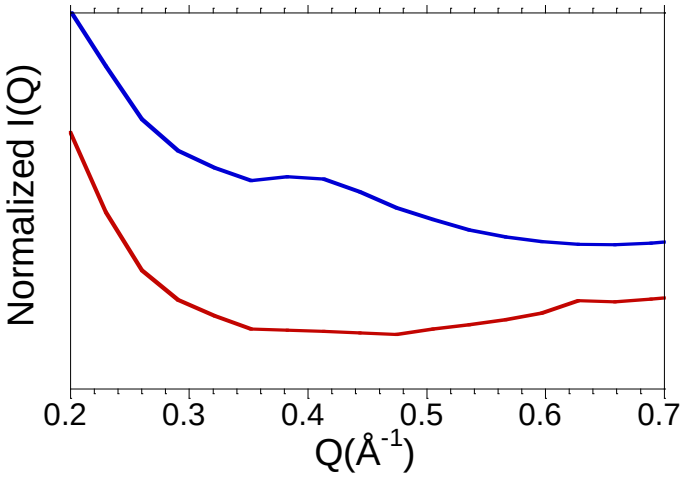

Figure 5.20 Small angle X-ray scattering (SAXS) response of Th (blue) and U(red) loaded **1c-AO** samples at low *Q*.

Coupled with the separations results, the X-ray scattering analyses provide several key takeaways. First, the presence of high intensity at high *Q* in the Th-loaded polymer case can be attributed to high Z correlations and is suggestive of Th oligomers or Th clusters present within the polymer sample. It is not yet known the extent to which these Th condensation products are present in solution before uptake or form within a poly(HIPE) pore during the separation experiment. Unambiguous identity assignment of the major Th-species present on the polymer can only be achieved by careful synthesis of several series of samples in which pH, concentration, and specific choice of counterions are systematically varied. These series could then be quantified using a multimodal approach with separations experiments combined with IR, Raman, SAXS, EXAFS, HEXS, and SXRD studies of metal-loaded polymer, solution, and crystalline Th samples— an effort beyond the scope of the current work. Second, scattering intensity in the U loaded **1c-AO** sample is indistinguishable from unloaded **1c-AO** polymer, providing no evidence of U-U correlations consistent with relatively homogenous, mononuclear U-AO binding events. This supports the separations results wherein U was bound to a lesser extent than Th. Third, SAXS

analysis corroborates the hypothesis that Th presents as clusters or oligomers on the metal-loaded polymer due to high intensity in the low *Q* region. These results are consistent with the higher Th uptake capacity found in the radiotracer separations experiments as well as the poor binding of U under high aqueous NaOAc concentrations (i.e. OAc^- outcompetes amidoxime's weak, mononuclear U binding).

5.10 Conclusions

Poly(HIPE)s have been prepared at a similar functional group loading (< 1 mmol AO/gram polymer), surface area, and morphology but with different substitution. Challenges with nitrile incorporation were addressed by using the less water-soluble 4-cyanostyrene monomer affording porous monoliths amenable to synthetic modification. Even though there is a relatively low loading of amidoxime moeities in these poly(HIPE)s, tracer level uptake studies found that both samples performed nearly the same, each exhibiting a higher affinity for Th than U—a trend not often encountered with amidoxime-based sorbents for U/Th separations. Nearly 90% of Th was adsorbed from an aqueous solution at pH 5-6 with the **2-AO** sorbent. Ease of Th elution suggested the presence of weakly bound Th species while salt screen experiments highlighted stark differences in the role of electrostatics between AO & U/Th. Pair distribution functions obtained from high energy X-ray scattering data suggest a more complex metal uptake mechanism than simple monomeric Th-ion adsorption, providing an opportunity to investigate actinide-uptake separation mechanisms in future studies.

As the actinide(IV) hydrolysis products have conventionally been characterized as intractable and challenging to extract,[38] the poly(HIPE) adsorbents discussed herein represent a potentially new approach to the selective separation of actinides providing a platform to investigate

actinide separation mechanisms in future studies. Tailoring the separations selectivity of an adsorbent via exploitation of a metal's hydrolysis chemistry represents one interesting perspective in separations science and adds another avenue for consideration when designing materials for specific metal separations. Further, the results of this study suggest that maximizing functional group loading in porous adsorbents may not always be the ideal strategy to achieve selective uptake in every application. Amidoxime functionalized polymers in which ultrahigh functional group loading was a necessity for cooperative binding have long been used for uranium uptake.[24] This work suggests that simply by decreasing the effective functional group loading in polymer materials, heavy metal selectivity can be altered. This insight helps us in our exploration of the relationship between functional group loading, polymer mechanical properties, metal speciation, and separations performance required to deconvolve the myriad interactions and their impact on selective actinide uptake.

5.11 Acknowledgements

This work is supported by the U.S. DOE, OBES, Division of Chemical Sciences, Biosciences and Geosciences, the Heavy Element Chemistry program, under Contract DE-AC02-06CH11357, and the U.S. Department of Energy, Office of Science, Office of Workforce Development for Teachers and Scientists, Office of Science Graduate Student Research (SCGSR) program. The SCGSR program is administered by the Oak Ridge Institute for Science and Education for the DOE under contract number DE-SC0014664. Parts of this work were carried out at the Soft Matter Characterization Facility of the University of Chicago.

5.12 References

(1) Chavan, A. A.; Li, H.; Scarpellini, A.; Marras, S.; Manna, L.; Athanassiou, A.; Fragouli, D. Elastomeric Nanocomposite Foams for the Removal of Heavy Metal Ions from Water. *ACS Appl. Mater. Interfaces* **2015**, *7* (27), 14778–14784.

(2) Archer, W. R.; Hall, B. A.; Thompson, T. N.; Wadsworth, O. J.; Schulz, M. D. Polymer Sequestrants for Biological and Environmental Applications. *Polym. Int.* **2019**.

(3) Foudazi, R.; Gokun, P.; Feke, D. L.; Rowan, S. J.; Manas-Zloczower, I. Chemorheology of Poly(High Internal Phase Emulsions). *Macromolecules* **2013**, *46* (13), 5393–5396.

(4) Silverstein, M. S. PolyHIPEs: Recent Advances in Emulsion-Templated Porous Polymers. *Prog. Polym. Sci.* **2014**, *39* (1), 199–234.

(5) Silverstein, M. S. Emulsion-Templated Porous Polymers: A Retrospective Perspective. *Polymer.* **2014**, *55* (1), 304–320.

(6) Cameron, N. R. High Internal Phase Emulsion Templating as a Route to Well-Defined Porous Polymers. *Polymer.* **2005**, *46* (5), 1439–1449.

(7) Barbetta, A.; Cameron, N. R.; Cooper, S. J. High Internal Phase Emulsions (HIPEs) Containing Divinylbenzene and 4-Vinylbenzyl Chloride and the Morphology of the Resulting PolyHIPE Materials. *Chem. Commun.* **2000**, No. 3, 221–222.

(8) Kimmins, S. D.; Cameron, N. R. Functional Porous Polymers by Emulsion Templating: Recent Advances. *Adv. Funct. Mater.* **2011**, *21* (2), 211–225.

(9) Carnachan, R. J.; Bokhari, M.; Przyborski, S. A.; Cameron, N. R. Tailoring the Morphology of Emulsion-Templated Porous Polymers. *Soft Matter* **2006**, *2* (7), 608–616.

(10) Cameron, N. R.; Barbetta, A. The Influence of Porogen Type on the Porosity, Surface Area and Morphology of Poly(Divinylbenzene) PolyHIPE Foams. *J. Mater. Chem.* **2000**, *10* (11), 2466–2471.

(11) Cameron, N. R.; Sherrington, D. C. Preparation and Glass Transition Temperatures of Elastomeric PolyHIPE Materials. *J. Mater. Chem.* **1997**, *7* (11), 2209–2212.

(12) Wickenheisser, M.; Paul, T.; Janiak, C. Prospects of Monolithic MIL-MOF@poly(NIPAM)HIPE Composites as Water Sorption Materials. *Microporous Mesoporous Mater.* **2016**, *220*, 258–269.

(13) Zhang, N.; Jiang, W.; Wang, T.; Gu, J.; Zhong, S.; Zhou, S.; Xie, T.; Fu, J. Facile Preparation of Magnetic Poly(Styrene-Divinylbenzene) Foam and Its Application as an Oil Absorbent. *Ind. Eng. Chem. Res.* **2015**, *54* (44), 11033–11039.

(14) Katsoyiannis, I. A.; Zouboulis, A. I. Removal of Arsenic from Contaminated Water Sources by Sorption onto Iron-Oxide-Coated Polymeric Materials. *Water Res.* **2002**, *36* (20), 5141–5155.

(15) Mert, E. H.; Kaya, M. A.; Yildirim, H. Preparation and Characterization of Polyester-Glycidyl Methacrylate PolyHIPE Monoliths to Use in Heavy Metal Removal. *Des. Monomers Polym.* **2012**, *15* (2), 113–126.

(16) Huš, S.; Kolar, M.; Krajnc, P. Separation of Heavy Metals from Water by Functionalized Glycidyl Methacrylate Poly (High Internal Phase Emulsions). *J. Chromatogr. A* **2016**, *1437*, 168–175.

(17) Zhu, Y.; Zheng, Y.; Wang, F.; Wang, A. Monolithic Supermacroporous Hydrogel Prepared from High Internal Phase Emulsions (HIPEs) for Fast Removal of $Cu^{2+}$and Pb^{2+}. *Chem. Eng. J.* **2016**, *284*, 422–430.

(18) Moghbeli, M. R.; Khajeh, A.; Alikhani, M. Nanosilica Reinforced Ion-Exchange PolyHIPE Type Membrane for Removal of Nickel Ions: Preparation, Characterization and Adsorption Studies. *Chem. Eng. J.* **2017**, *309*, 552–562.

(19) Edwards, C.; Gregory, D.; Sharples, M. Low Density Porous Elastic Cross-Linked Polymeric Materials and Their Preparation. 4,788,225, **1988**.

(20) Taylor-Pashow, K. M. L.; Pribyl, J. G. PolyHIPEs for Separations and Chemical Transformations: A Review. *Solvent Extr. Ion Exch.* **2019**, *0* (0), 1–26.

(21) Benicewicz, B. C.; Jarvinen, G. D.; Kathios, D. J.; Jorgensen, B. S. Open-Celled Polymeric Foam Monoliths for Heavy Metal Separations Study. *J. Radioanal. Nucl. Chem.* **1998**, *235* (1–2), 31–35.

(22) Pribyl, J.; Fletcher, B.; Steckle, W.; Taylor-Pashow, K.; Shehee, T.; Benicewicz, B. Photoinitiated Polymerization of 4-Vinylpyridine on PolyHIPE Foam Surface toward Improved Pu Separations. *Anal. Chem.* **2017**, *89* (10), 5174–5178.

(23) Pribyl, J. G.; Taylor-Pashow, K. M. L.; Shehee, T. C.; Benicewicz, B. C. High-Capacity Poly(4-Vinylpyridine) Grafted PolyHIPE Foams for Efficient Plutonium Separation and Purification. *ACS Omega* **2018**, *3* (7), 8181–8189.

(24) Abney, C. W.; Mayes, R. T.; Saito, T.; Dai, S. Materials for the Recovery of Uranium from Seawater. *Chem. Rev.* **2017**, *117* (23), 13935–14013.

(25) Xiong, J.; Hu, S.; Liu, Y.; Yu, J.; Yu, H.; Xie, L.; Wen, J.; Wang, X. Polypropylene Modified with Amidoxime/Carboxyl Groups in Separating Uranium(VI) from Thorium(IV) in Aqueous Solutions. *ACS Sustain. Chem. Eng.* **2017**, *5* (2), 1924–1930.

(26) Yue, Y. F.; Mayes, R. T.; Gill, G.; Kuo, L. J.; Wood, J.; Binder, A.; Brown, S.; Dai, S. Macroporous Monoliths for Trace Metal Extraction from Seawater. *Rsc Adv.* **2015**, *5* (62), 50005–50010.

(27) Steinhauser, G. Fukushima's Forgotten Radionuclides: A Review of the Understudied Radioactive Emissions. *Environ. Sci. Technol.* **2014**, *48* (9), 4649–4663.

(28) Piechowicz, M.; Abney, C. W.; Thacker, N. C.; Gilhula, J. C.; Wang, Y.; Veroneau, S. S.; Hu, A.; Lin, W. Successful Coupling of a Bis-Amidoxime Uranophile with a Hydrophilic Backbone for Selective Uranium Sequestration. *ACS Appl. Mater. Interfaces* **2017**, *9* (33), 27894–27904.

(29) Piechowicz, M.; Chiarizia, R.; Soderholm, L. Insight into Selectivity: Uptake Studies of Radionuclides $^{90}Sr^{2+}$, $^{137}Cs^{+}$, and $^{233}UO_2^{2+}$ with Bis-Amidoxime Polymers. *Dalt. Trans.* **2018**, *47* (15), 5348–5358.

(30) Abbasian, Z.; Moghbeli, M. R. Preparation of Highly Open Porous Styrene/Acrylonitrile and Styrene/Acrylonitrile/Organoclay Polymerized High Internal Phase Emulsion (PolyHIPE) Foams via Emulsion Templating. *J. Appl. Polym. Sci.* **2011**, *119* (6), 3728–3738.

(31) Cohen, N.; Silverstein, M. S. Synthesis of Emulsion-Templated Porous Polyacrylonitrile and Its Pyrolysis to Porous Carbon Monoliths. *Polymer.* **2011**, *52* (2), 282–287.

(32) Davis, H. S.; Wiedeman, O. F. Physical Properties of Acrylonitrile. *Ind. Eng. Chem.* **1945**, *37* (5), 482–485.

(33) Mao, R.; Huglin, M. B.; Davis, T. P. Quantitative Analysis of Copolymers by FTIR. *Eur. Polym. J.* **1993**, *29* (4), 475–481.

(34) Huš, S.; Krajnc, P. PolyHIPEs from Methyl Methacrylate: Hierarchically Structured Microcellular Polymers with Exceptional Mechanical Properties. *Polymer.* **2014**, *55* (17), 4420–4424.

(35) Katz, M. J.; Brown, Z. J.; Colón, Y. J.; Siu, P. W.; Scheidt, K. A.; Snurr, R. Q.; Hupp, J. T.; Farha, O. K. A Facile Synthesis of UiO-66, UiO-67 and Their Derivatives. *Chem. Commun.* **2013**, *49* (82), 9449.

(36) Baes, C. E.; Mesmer, R. F. *The Hydrolysis of Cations*; Wiley: New York, **1976**.

(37) Knope, K. E.; Soderholm, L. Solution and Solid-State Structural Chemistry of Actinide Hydrates and Their Hydrolysis and Condensation Products. *Chem. Rev.* **2013**, *113* (2), 944–994.

(38) Wilson, R. E.; Skanthakumar, S.; Soderholm, L. Separation of Plutonium Oxide Nanoparticles and Colloids. *Angew. Chemie - Int. Ed.* **2011**, *50* (47), 11234–11237.

(39) Neck, V.; Kim, J. I. Solubility and Hydrolysis of Tetravalent Actinides. *Radiochim. Acta* **2001**, *89* (1), 1–16.

(40) Kotrly, S. *Handbook of Chemical Equilibria in Analytical Chemistry*; Ellis Horwood Limited: Chichester, UK.

(41) Wilson, R. E.; Skanthakumar, S.; Sigmon, G.; Burns, P. C.; Soderholm, L. Structures of Dimeric Hydrolysis Products of Thorium. *Inorg. Chem.* **2007**, *46* (7), 2368–2372.

(42) Knope, K. E.; Wilson, R. E.; Vasiliu, M.; Dixon, D. A.; Soderholm, L. Thorium(IV) Molecular Clusters with a Hexanuclear Th Core. *Inorg. Chem.* **2011**, *50* (19), 9696–9704.

(43) Egawa, H.; Nonaka, T.; Nakayama, M. Recovery of Uranium from Seawater. 7. Concentration and Separation of Uranium in Acidic Eluate. *Ind. Eng. Chem. Res.* **1990**, *29* (11), 2273–2277.

(44) Jin, C.; Hu, J.; Wang, J.; Xie, C.; Tong, Y.; Zhang, L.; Zhou, J.; Guo, X.; Wu, G. An Amidoximated-UHMEPE Fiber for Selective and High Efficient Removal of Uranyl and Thorium from Acid Aqueous Solution. *Adv. Chem. Eng. Sci.* **2017**, *07* (01), 45–59.

(45) Helfferich, F. G.; Dranoff, J. S. *Ion Exchange*; McGraw-Hill: New York, **1962**.

(46) Das, S.; Oyola, Y.; Mayes, R. T.; Janke, C. J.; Kuo, L.-J.; Gill, G.; Wood, J. R.; Dai, S. Extracting Uranium from Seawater: Promising AF Series Adsorbents. *Ind. Eng. Chem. Res.* **2016**, *55* (15), 4110–4117.

(47) Zhao, H.; Liu, X.; Yu, M.; Wang, Z.; Zhang, B.; Ma, H.; Wang, M.; Li, J. A Study on the Degree of Amidoximation of Polyacrylonitrile Fibers and Its Effect on Their Capacity to Adsorb Uranyl Ions. *Ind. Eng. Chem. Res.* **2015**, *54* (12), 3101–3106.

(48) Correspondence with Dr. Soderholm, October 2019.

(49) Als-Nielsen, J.; McMorrow, D. *Elements of Modern X-Ray Physics*; John Wiley & Sons, Ltd: New York, **2001**.

(50) Egami, T.; Billinge, S. J. . *Underneath the Bragg Peaks: Structural Analysis of Complex Materials*; Pergammon: Amsterdam, **2003**.

(51) Skanthakumar, S.; Antonio, M. R.; Wilson, R. E.; Soderholm, L. The Curium Aqua Ion. *Inorg. Chem.* **2007**, *46* (9), 3485–3491.

(52) Wilson, R. E.; Skanthakumar, S.; Burns, P. C.; Soderholm, L. Structure of the Homoleptic Thorium(IV) Aqua Ion $[Th(H_2O)_{10}]Br_4$. *Angew. Chemie - Int. Ed.* **2007**, *46* (42), 8043–8045.

(53) Takeshi, E.; Billinge, S. J. L. The Method of Total Scattering and Atomic Pair Distribution Function Analysis. In *Pergamon Materials Series*; 2012; Vol. 16, pp 55–111.

Chapter 6: Benzamidoxime Functionalized poly(HIPE)s for Actinide Separations: A Multidisciplinary Approach

6.1 Introduction

Underlying the five criteria of an ideal adsorbent outlined in the introduction (**Ch. 1**) are *primary* and *secondary* material characteristics. *Primary* material characteristics encompass the traditional metrics reported by the separations community for adsorbents including but not limited to functional group loading, surface area, and porosity. Explanations of separations efficacy are usually reported as a combination of these qualities and in terms of data obtained on the used, metal-loaded adsorbent. However, subtle changes in often overlooked *secondary* characteristics can have profound effects on resulting metal capacity, selectivity, and kinetics. Such *secondary* material characteristics include polymer morphology, accessible functional groups, functional group cooperativity, hierarchical structure, confinement effects, the role of interfaces, and hydrophilicity. While causation with any *one* of these metrics cannot be ascertained with certainty owing to their high level of interconnectedness, meaningful correlations can be drawn which help inform the design of next generation materials.

Presented herein is the development of a series of 4-cyanostyrene (4CS)-containing polystyrene-based poly(HIPE) materials, their conversion to amidoxime (**Scheme 6.1**), and separations studies with Th, U, and Pu. Ostensibly, the materials differ only in their feed ratio of 4-cyanostyrene: styrene and, as such, their nitrile group loading. However, key characteristics including surface area, pore structure, and morphology change across the series providing useful handles to interrogate separations efficacy.

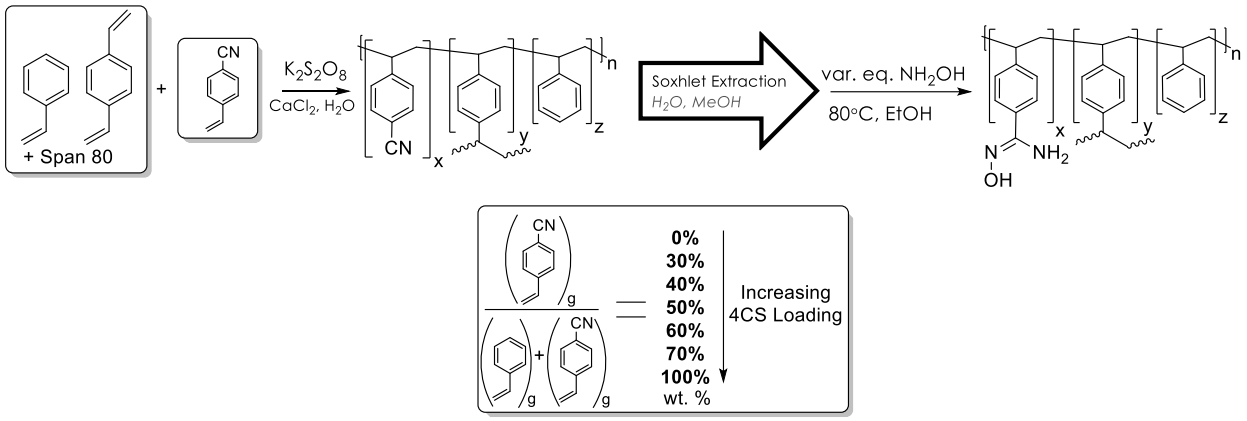

Scheme 6.1 General synthetic scheme for nitrile functionalized poly(HIPE) materials discussed in this work and description of the 4-cyanostyrene:styrene wt% feed ratios used.

6.2 Experimental Methods

6.2.1 General Experimental

Caution! The materials used in these experiments are radioactive and require proper facilities, correct PPE, and appropriate training.

6.2.2 Materials

Nitric acid was ACS reagent grade and used as received. Divinylbenzene was technical grade and used as received. Styrene was purchased from Sigma Aldrich and acrylonitrile was 99% pure purchased from ACROS organics. All monomers were stored in the refrigerator and allowed to warm to room temperature before use. All other reagents including Optima Gold liquid scintillation counting (LSC) cocktail, sodium acetate, ammonium hydroxide, calcium chloride, potassium persulfate, and Span ® 80 were used as received. All water used for uptake experiments was obtained from a Milli-Q2 system with a measured resistivity of at least 18 MΩ. Radiotracer uptake experiments were performed using stock solutions of the alpha emitters ^{230}Th, ^{233}U, and ^{239}Pu. The ^{230}Th stock was 9.68 mM in 1 M HNO_3 solution. The solution was

diluted 10x with desired aqueous media before use. The ^{233}U stock was 30.6 mM in 1 M HNO_3 solution. The ^{239}Pu stock was 0.17 mM in 1 M HNO_3 solution. Aliquots for uptake studies were treated with $NaNO_2$ overnight to ensure conversion of Pu(III & VI) to Pu(IV).

6.2.3 Instrumentation

IR spectra were collected on a Nicolet Nexus 870 FTIR system. Samples were dried in a vacuum oven, diluted with dried KBr, and pressed into a pellet. Spectra were collected between 400–4000 cm^{-1} with 64 scans and 2 cm^{-1} resolution. Surface area measurements were obtained via N_2 uptake with a Micromeritics 3Flex instrument using an appropriate pressure table. Samples were dried in vacuo prior to analysis. Approximately 100 mg of sample was used for each analysis. Brunauer–Emmett–Teller (BET) surface areas were calculated from the N_2 adsorption isotherms. The morphology of the poly(HIPE) materials was discerned using a Karl Zeiss Merlin scanning electron microscope (SEM) with an accelerating voltage of 5.00 kV. Small pieces of dried samples were carefully mounted atop double-sided carbon tape affixed on aluminum SEM stages. Prior to imaging, the samples were coated with 8nm of Pt/Pd using a Ted Pella sputter coater. Multiple images were taken at various sample locations to ensure faithful representation of the material. Alpha counting was performed via liquid scintillation on a Packard Model 2000 CA counter using an LSC cocktail volume of 5 mL. Regions of interest (ROIs) were individually selected for each isotope so as to include energy ranges with highest counts. X-ray crystallography was performed using full spheres of diffraction data collected using a Bruker SMART diffractometer equipped with an APEXII detector. All data were collected at 100 K using an Oxford Cryosystems cryostat. The structures were solved using the SHELXTL module within OLEX 2[1] with direct methods and subsequent full matrix least-squares

refinement. Positional disorder was addressed conventionally with partial occupancy assigned to disordered atoms.

6.2.4 Uptake Studies

In general, uptake studies were conducted in 10 mL glass vials with ~1 mg polymer at a phase ratio of 1 mg polymer per 1 mL spiked solution. Radionuclides were spiked in such a way to yield A_0 < 10 000 cpm 100 μL^{-1}, where A_0 represents the initial counts via LSC. Expressed in a different way, this corresponds to an initial stock concentration of ~ 99 µM for Th, ~298 µM for U, and ~ 20 µM for Pu.

Separations samples were shaken for 60 minutes on a plate shaker at 500 rpm prior to syringe filtration (Whatman, PVDF, 0.2 µm pore size). Buffers were prepared according to standard procedures found in the literature. The alkaline pH region (pH 8–10) was attained with an ammonium buffer ($[NH_3]$ + $[NH_4^+]$ = 0.01 M). The near neutral pH region (pH 4–7) was attained with a sodium acetate buffer ($[CH_3COO^-]$ + $[CH_3COOH]$ = 0.01 M). Acidic conditions (pH ≤ 3) were attained with HNO_3 at the proper concentration.

6.2.5 Theoretical Methods

All calculations utilized the Gaussian 16RevA.03 quantum chemistry program[2] with DFT at the B3LYP[3,4] level of theory. All light atoms were modeled by the 6-311+G* basis set. Th was modeled with the Stuttgart RSC 1997 relativistic effective core potential. All calculations were done in the gas phase. All coordination complexes were geometrically optimized before being subjected to frequency calculations in order to obtain thermodynamic values.

6.3 Poly(HIPE) Synthesis

Nitrile functionalized polystyrene-based poly(HIPE)s were accessed using varying ratios of styrene and 4-cyanostyrene as comonomers and divinyl benzene as the crosslinker as outlined in **Scheme 6.1**. Six samples were synthesized according to the conditions found in **Table 6.1**. In general, the amount of feed 4-cyanostyrene was varied from 0 grams to 1.6 grams (12.4 mmol) while keeping the total organic phase mass constant (i.e. 1.76 grams). In this way, the only difference between samples is the degree of nitrile functionalization. Yields were as expected with conversion ratios calculated on as-synthesized materials above 100%. Ratios of 100% denote complete conversions. Ratios above 100% are observed here due to salt contamination. Sample codes follow 1_x where *1* signifies use of 4-cyanostyrene, and *x* is the weight % of 4CS relative to the sum of styrene and 4-cyanostyrene used. Sample codes in wt. % and mol % are included in **Table 6.2**. Sample codes described with wt. % will be used throughout this chapter.

It is worthwhile to note that no poly(HIPE) was obtained when no styrene was included in the reaction (**1_{100}**) possibly due to the mismatch in reactivity ratios between the 4CS and DVB crosslinker used. A detailed discussion of reactivity ratios is included in the following section. Samples were made using the same apparatus outlined in the previous chapter.

Table 6.1 Feed Conditions for Arylnitrile Functionalized Poly(HIPE)s

	Organic Phase				Aqueous Phase			Results	
Sample	ST (g)	DVB (g)	4CS (g)	Span 80 (μL)	DI H_2O (mL)	$CaCl_2$ (mg)	$K_2S_2O_8$ (mg)	Yield (g)	% conversion
$\mathbf{1_0}$	1.6	0.16	0	350	25	218	70	1.24	70
$\mathbf{1_{30}}$	1.12		0.48					1.94	110
$\mathbf{1_{40}}$	0.96		0.64					1.67	95
$\mathbf{1_{50}}$	0.8		0.80					1.92	109
$\mathbf{1_{60}}$	0.64		0.96					2.02	115
$\mathbf{1_{70}}$	0.48		1.12					2.04	116
$\mathbf{1_{100}}$	0		1.6					N/A	N/A

Table 6.2 Sample Codes in Wt. % and Mol % 4CS Monomer

Sample* wt. %	Sample† mol %
$\mathbf{1_0}$	$\mathbf{1_0}$
$\mathbf{1_{30}}$	$\mathbf{1_{26}}$
$\mathbf{1_{40}}$	$\mathbf{1_{35}}$
$\mathbf{1_{50}}$	$\mathbf{1_{45}}$
$\mathbf{1_{60}}$	$\mathbf{1_{55}}$
$\mathbf{1_{70}}$	$\mathbf{1_{65}}$
$\mathbf{1_{100}}$	$\mathbf{1_{100}}$
* $\mathbf{1_x}$ where x is the wt. %4CS relative to ∑(ST & 4CS) by mass †$\mathbf{1_x}$ where x is the mol %4CS relative to ∑(ST & 4CS) in moles	

6.4 Poly(HIPE) Characterization

After purification of the poly(HIPE)s $\mathbf{1_0}$ … $\mathbf{1_{70}}$ by water then methanol soxhlet extraction, FTIR confirmed the successful incorporation of the nitrile containing comonomer, 4CS, via the appearance of the -CN stretching frequency at 2227 cm^{-1} (**Figure 6.1**).

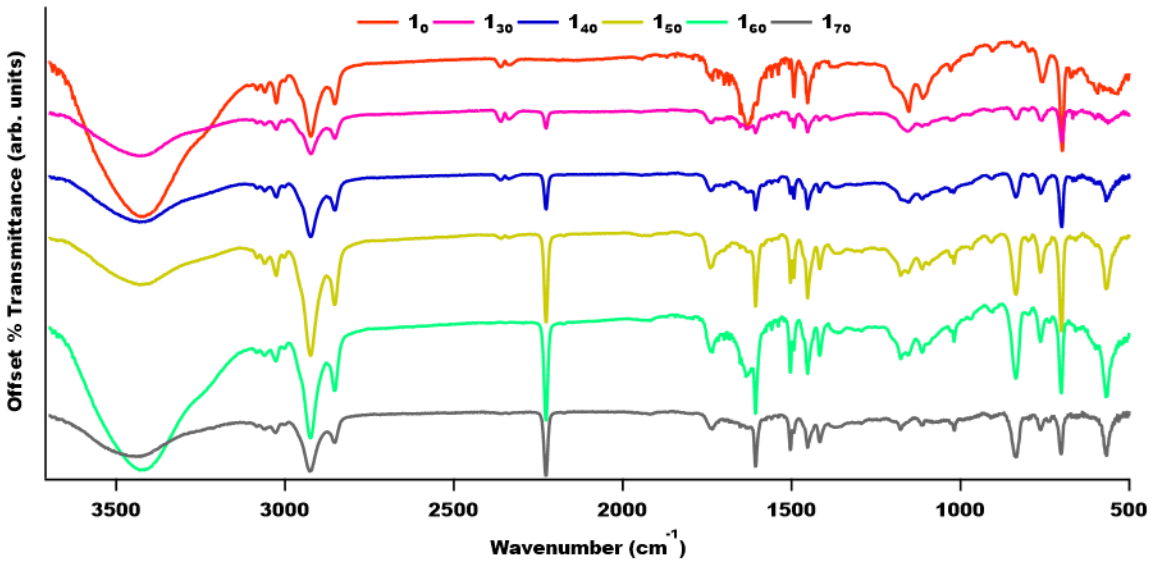

Figure 6.1 FTIR spectra of as-synthesized poly(HIPE) materials. The diagnostic -CN stretching frequency is located at 2227 cm^{-1}.

Using an approach similar to that described in the previous chapter, -CN loading in mmol fraction was obtained (**Table 6.3**). In brief, several poly(styrene-co-cyanostyrene) disks were synthesized in the bulk with varying amounts of 4CS monomer, the only variable to change among the samples. The molar amounts of styrene and divinylbenzene crosslinker were kept constant throughout. FTIR was taken of each disk and standard curves were constructed with the absorbance ratios of -CN to -CH stretches plotted as a function of 4CS mol fraction. Comparison of the FTIR spectra obtained for the as-synthesized **1** series of poly(HIPE) materials with the standard curves provides quantitative nitrile group loading information.

Table 6.3 Functional Group Loading Information of Nitrile-Functionalized Poly(HIPE) Materials

Sample	CN Loading (mmol/mol frac.)
1_0	0
1_{30}	44.85
1_{40}	76.89
1_{50}	118.09
1_{60}	155.56
1_{70}	211.08
1_{100}	NA

Scanning electron microscopy (SEM) was used to ascertain polymer morphology and provide an estimate of typical pore size. SEM images of dried samples after soxhlet extraction with water are shown in **Figure 6.2.** Typical poly(HIPE) morphology consisting of open-celled, interconnected pore structure is apparent in samples $\mathbf{1_0}$ to $\mathbf{1_{40}}$ However, deviations from this morphology become evident at higher loading of 4CS, $\mathbf{1_{50}}$ SEM images of post-methanol washed poly(HIPE) materials reveal agglomeration and a shift from an open-celled structure to one with thick pore walls characteristic of more close-celled materials (**Figure 6.3**). This dramatic shift in morphology as a function of 4CS loading can possibly be explained by the mismatch in reactivity ratios between 4-cyanostyrene and styrene/divinylbenzene. Reactivity ratios are defined as the ratios of rate constants between two comonomer components of a polymerization reaction. For the case of 4CS and St, the reactivity ratios can be defined in terms of the following reactions:

$$\begin{aligned}
\text{St} + \text{St} &\xrightarrow{k_{\text{St-St}}} \text{St-St} \\
\text{St} + \text{4CS} &\xrightarrow{k_{\text{St-4CS}}} \text{St-4CS} \\
\text{4CS} + \text{4CS} &\xrightarrow{k_{\text{4CS-4CS}}} \text{4CS-4CS} \\
\text{4CS} + \text{St} &\xrightarrow{k_{\text{4CS-St}}} \text{4CS-St}
\end{aligned}$$

where k_{St-St}, k_{St-4CS}, $k_{4CS-4CS}$, and k_{4CS-St} are the reaction rate constants for each addition reaction.

The reactivity ratios for each monomer is defined as the ratio of rate constants describing addition of that monomer to the rate constant describing addition of the other monomer. The reactivity ratios corresponding to the previous reactions, therefore, can be noted as:

$$r_{St} = \frac{k_{St-St}}{k_{St-4CS}} \qquad \textbf{Equation 6.1}$$

$$r_{4CS} = \frac{k_{4CS-4CS}}{k_{4CS-ST}} \qquad \textbf{Equation 6.2}$$

It follows that values >1 imply that monomers of the same identity have greater affinity for themselves than for comonomers in the reaction. Values <1 imply that a certain monomer has higher affinity for comonomers in a reaction than with monomers of the same identity. In the specific case of styrene and 4-cyanostyrene, $r_{St} = 0.28$ and $r_{4CS} = 1.16$.[5] This mismatch in reactivity ratios suggests the likely formation of areas rich in cyanostyrene adjacent to areas rich in styrene. Such "blocky" behavior helps explain the morphological differences observed via SEM.

As the feed 4CS fraction increases in the prepared samples, the relative concentration of the crosslinker divinylbenzene (DVB) to 4CS decreases. While data on the kinetics of copolymerization between 4-cyanostyrene and divinylbenzene are not available in the literature, the semi-empirical Q (general reactivity factor) and e (polar factor) values first developed by Alfrey and Price[6] could be used to derive an estimate of reactivity ratios between the two monomers. In this case, Q and e for 4CS and meta- and -para-substituted DVB are 1.67 and 0.325, 3.35 and -1.77, and 26.4 and -2.43 respectively. These values yield the following reactivity ratios for the copolymerization of 4CS and DVB:

$$r_{4CS-mDVB} = 0.25$$

$$r_{mDVB-4CS} = 0.05$$

$$r_{4CS-pDVB} = 0.026$$

$$r_{pDVB-4CS} = 0.02$$

As $r_{4CS-pDVB} \approx r_{pDVB-4CS} \approx 0$, 4CS is expected to form pure alternating polymer with the crosslinker with little homopolymer. Thus, the lack of DVB in $\mathbf{1_{100}}$ suggest an inability to form a network and concomitant phase separation as evidenced in the SEM images.

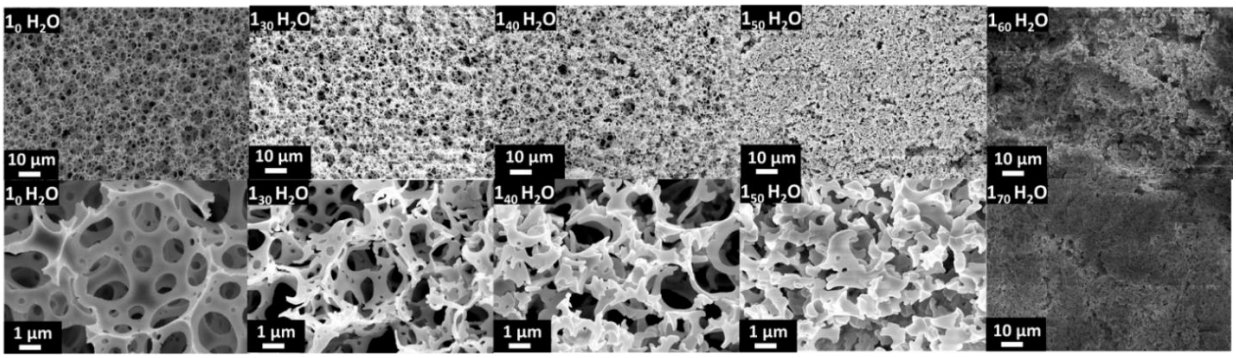

Figure 6.2 SEM images of water washed poly(HIPE) materials.

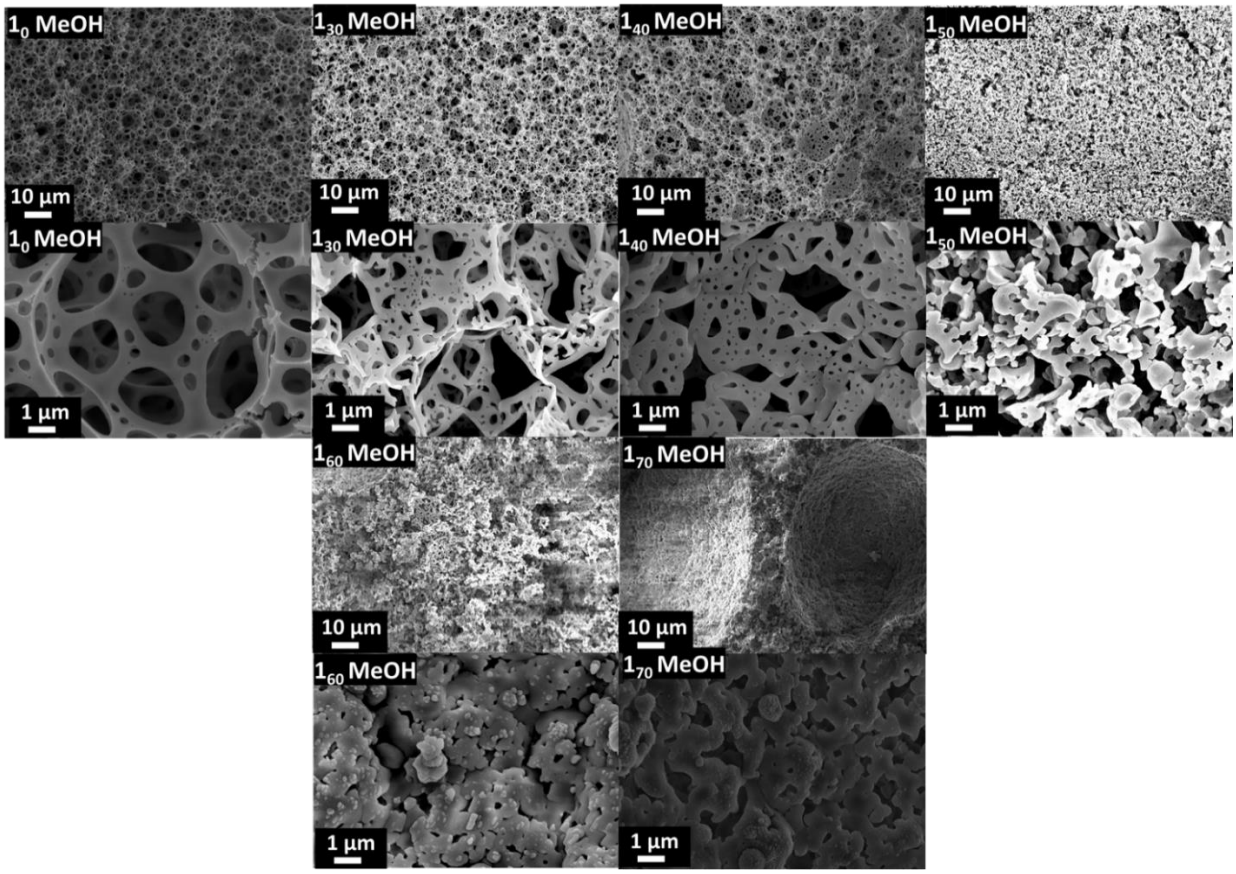

Figure 6.3 SEM images of methanol washed poly(HIPE) materials.

Amidoximation of the 4CS materials to obtain the AO group of interest proceeded as discussed in the previous chapter. In brief, multiple equivalents of NH_2OH (50% wt/wt, aqueous) with respect to the 4CS loading were added to the poly(HIPE) under reflux in ethanol over

multiple days. FTIR Spectra of 2_{30}, 2_{50}, and 2_{70} materials representing low, mid, and high AO loading, respectively are shown in **Figure 6.4**. Reaction progress was followed via FTIR as the disappearance of the -CN peak is diagnostic of a successful reaction (**Figure 6.4A**).) The appearance of a strong band around 1650 cm^{-1} (-C=N stretch) and broad feature around 1580 cm^{-1} (-NH_2 deformation) provide further evidence of successful amidoxime formation (**Figure 6.4C**). SEM of amidoximated materials (**Figure 6.5**) show no discernable differences in morphology before and after conversion.

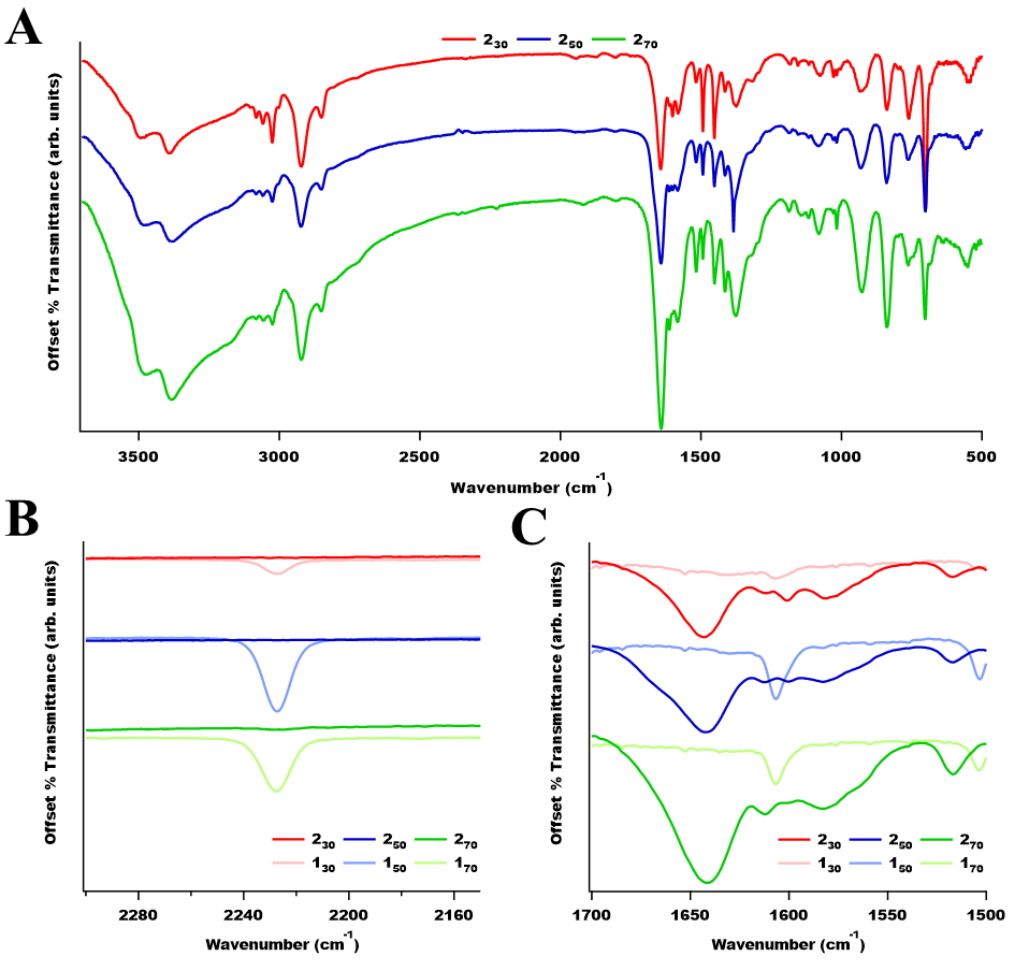

Figure 6.4 FTIR spectra of **2_{30}**, **2_{50}**, and **2_{70}** poly(HIPE) materials. **A**. Full spectra of amidoximated poly(HIPE) materials **B**. Zoom-in of region between 2300 and 2150 cm^{-1} **C**. Zoom-in of region between 1700 and 1500 cm^{-1}.

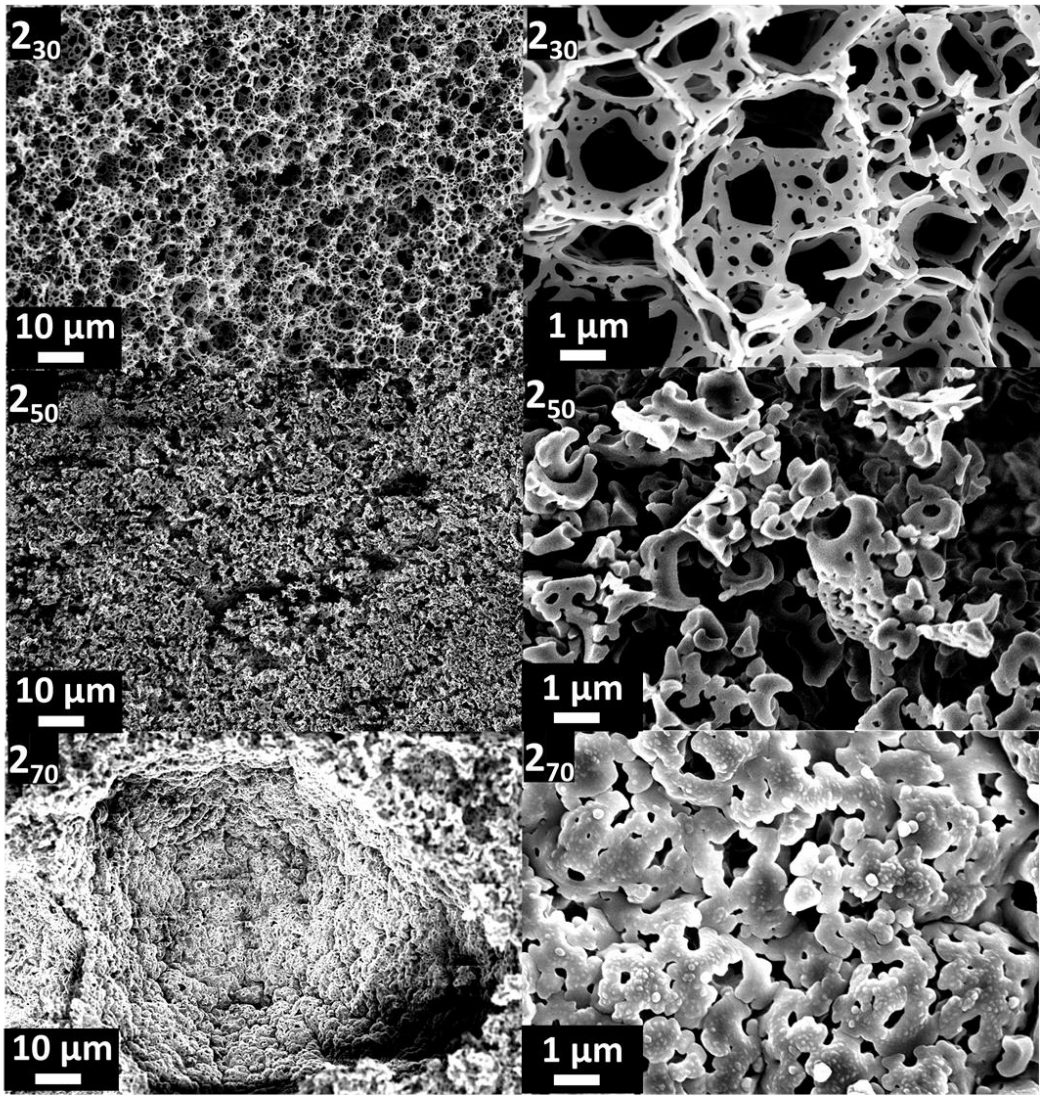

Figure 6.5 SEM images of amidoximated poly(HIPE) materials.

In every case, the diagnostic -CN peak ~2227 cm^{-1} disappears indicative of successful conversion to -NNH_2OH. The appearance of strong bands around 1650 cm^{-1} and 1580 cm^{-1} corresponding to -C=N stretching and -NH_2 deformation, respectively, provide further evidence for conversion of -CN to -AO. One advantage of 4CS materials over their AN functionalized analogues is more complete conversion to AO. This is likely a result of the greater accessibility of the arylnitrile relative to the aliphatic nitrile to hydroxylamine.

Thermograms of pristine, nitrile functionalized poly(HIPE)s show a smooth weight loss around 400 ºC ending with near 0% weight remaining around 475 ºC (**Figure 6.6**). Amidoximated materials show more variability in their thermograms exhibiting three distinct regimes of weight loss (**Figure 6.7**). The first prominent weight loss is taken as the region between 25-150 ºC and likely corresponds to residual ethanol remaining in the poly(HIPE) pores after amidoximation. This weight loss is less than 10% for each polymer sample and follows the degree of amidoximation. It is expected that materials with a greater degree of hydrophilic functional groups will contain more ethanol. The second weight loss regime is taken to be from 150-300 ºC. This region likely corresponds to H_2O and N_2O loss from partial decomposition of the amidoxime groups scaling with degree of AO loading as before. The final weight loss regime is taken from 300-500 ºC and corresponds to bulk decomposition of the crosslinked polystyrene backbone. Contrary to the pristine, CN-functionalized polymers, the AO-functionalized polymers show a much greater % wt. remaining at the end of pyrolosis. In fact, 4CS-30% shows ~8% wt. remaining after 750 ºC. This can be explained by the formation of thermally stable 5 and 6 membered heteronuclear rings within the polymer. Weight loss values are shown in **Table 6.2**.

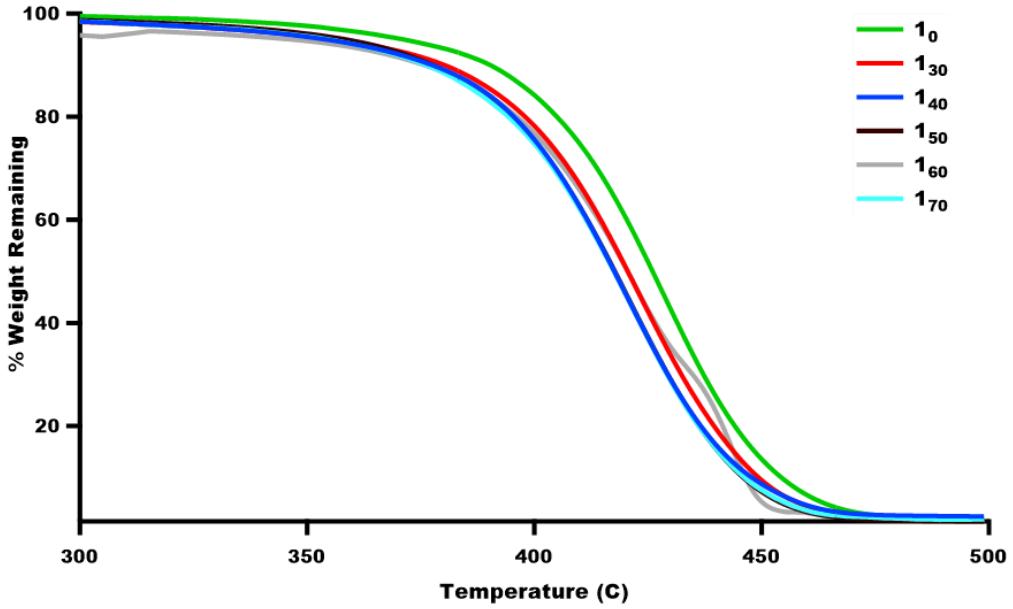

Figure 6.6 Thermograms of pristine, 4CS functionalized poly(HIPE) materials.

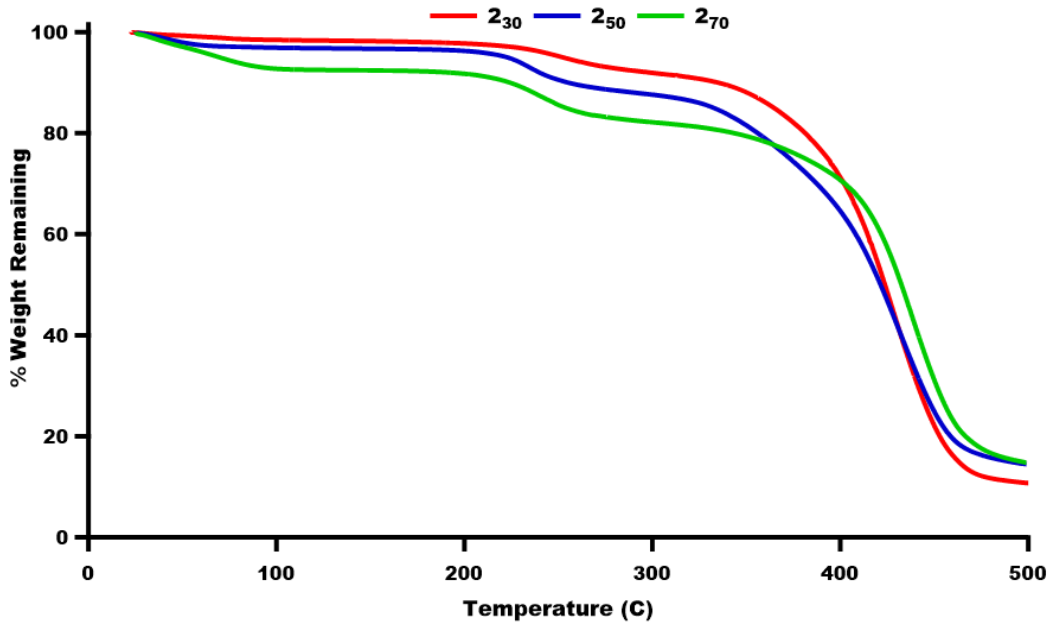

Figure 6.7 Thermograms of **2**$_{30}$, **2**$_{50}$, and **2**$_{70}$ poly(HIPE) materials.

Table 6.4 Weight Loss percentages for **2_{30}**, **2_{50}**, and **2_{70}** Poly(HIPE) Materials

	Temperature Range (°C)			
Sample	**25 – 150**	**150 – 300**	**300 – 500**	Residual wt. remaining
2_{30}	1.67	6.29	81.20	10.84
2_{50}	3.26	9.10	73.14	14.50
2_{70}	7.54	10.26	67.36	14.83

Differential Scanning Calorimetry (DSC) data is presented in **Figure 6.8**. Subtle dips in the traces reveal long glass transition temperatures (T_g) around 115 °C with the broadest feature evident in the most crosslinked polymer (i.e. **2_{30}**).

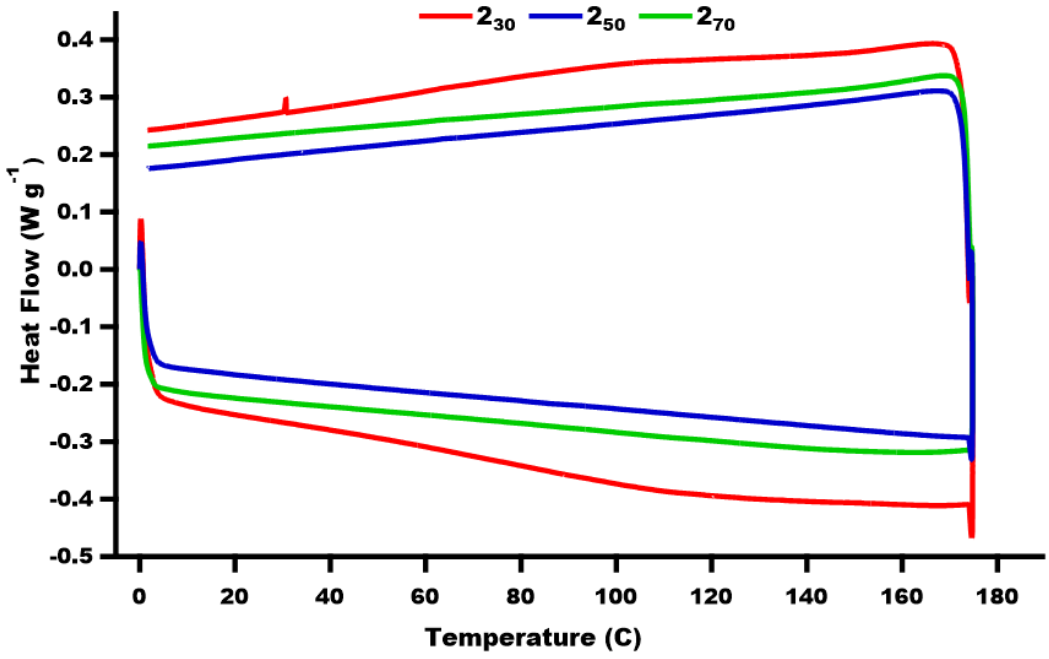

Figure 6.8 DSC curves of **2_{30}**, **2_{50}**, and **2_{70}** poly(HIPE) materials. The second of two cycles are shown.

Nitrogen uptake measurements, used to ascertain the degree of porosity in the poly(HIPE) materials, are shown in **Figure 6.9**. The poly(HIPE)s show typical type II isotherms characteristic of macroporous adsorbents. Hysteresis between the adsorption and desorption

branches of the uptake curves, especially evident in the unfunctionalized 4CS-0% poly(HIPE), is indicative of capillary N_2 condensation suggestive of hierarchical porosity. Surface area measurements described in **Table 6.3** are in good agreement with the morphology described by SEM. Poly(HIPE) surface areas decrease from 20 m^2g^{-1} to 4 m^2g^{-1} as the 4CS loading increases.

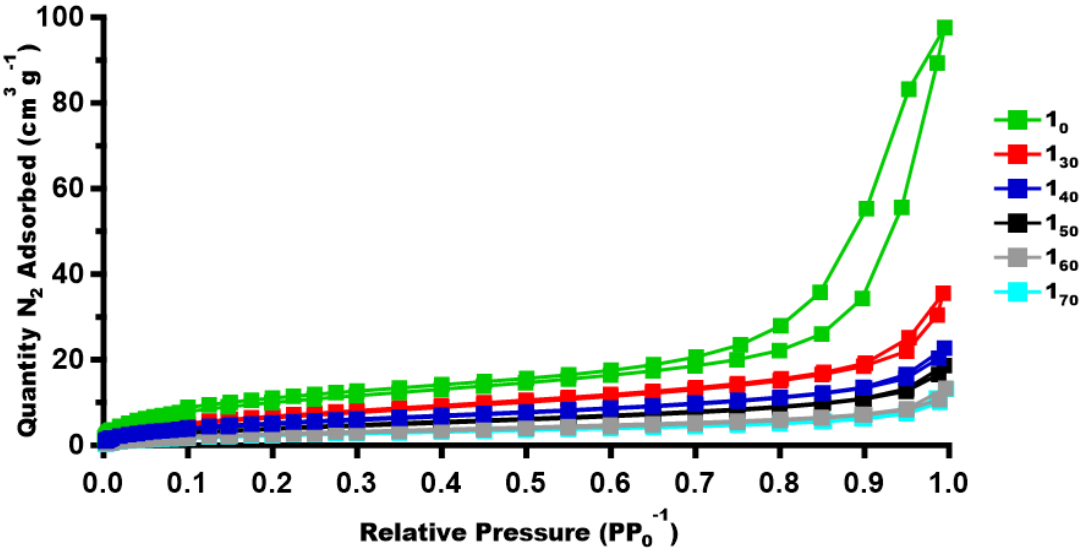

Figure 6.9 Nitrogen uptake isotherms of post-methanol washed nitrile-functionalized poly(HIPE) materials.

Surface areas increase slightly upon amidoximation in agreement with the appearance of small voids within the poly(HIPE) pore walls evident in the SEM images (**Table 6.4**). Nitrogen uptake isotherms of selected amidoxime-functionalized poly(HIPE)s are shown in **Figure 6.10**.

Table 6.5 Brunauer-Emmett-Teller (BET) Surface Areas for Nitrile- and Selected Amidoxime-Functionalized Poly(HIPE) Materials

Sample	BET Surface Area (m^2 g^{-1}) post MeOH	Sample	BET Surface Area (m^2 g^{-1}) post Amidoximation
1_0	19.78	**2_{30}**	14.24
1_{30}	12.06		
1_{40}	10.02	**2_{50}**	7.94
1_{50}	7.19		
1_{60}	4.88	**2_{70}**	4.59
1_{70}	3.57		

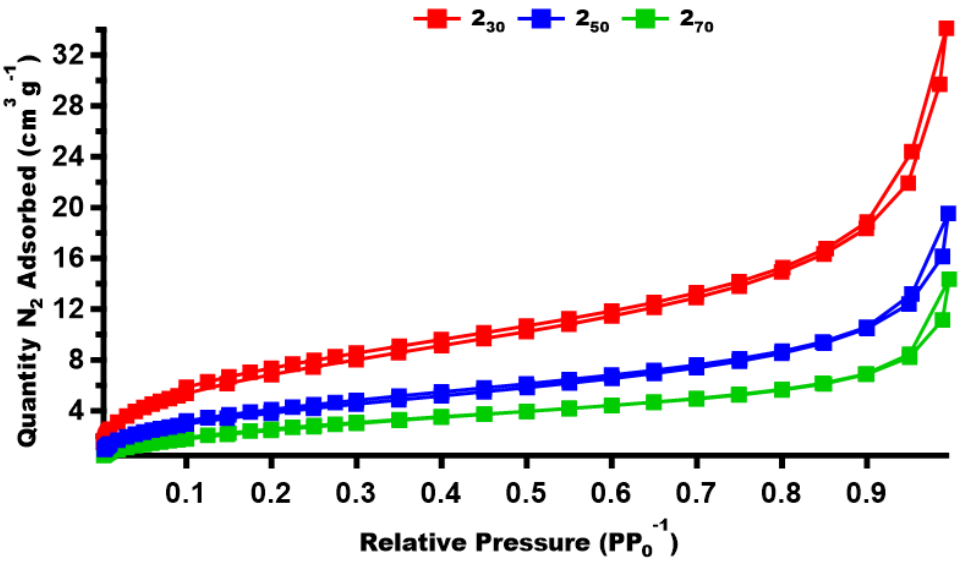

Figure 6.10 Nitrogen uptake isotherms of selected amidoxime-functionalized poly(HIPE) materials.

6.5 Uptake Studies

Three poly(HIPE) materials were chosen with high (2_{70}), mid (2_{50}), and low (2_{30}) amidoxime loading to study for their actinide uptake efficacy. Separation studies were conducted according to the protocols outlined in Chapter 4. In brief, polymer was added to a 5 mL glass vial before aqueous solution of a certain pH spiked with radiotracer was added to maintain a phase ratio of 1 mg polymer : 1 mL solution. This mixture was shaken for 2 hours (unless otherwise

specified) before being filtered and counted via LSC. The radioactivity counts before and after uptake were used to ascertain %metal adsorbed. This value, corrected for the amount of polymer and volume of solution, is the distribution ratio (D_W).

The amidoxime functionalized poly(HIPE)s showed high Th uptake and low U uptake, corroborating the trend evidenced in Chapter 4. Data for Th show high uptake between pH 3 – 10 although the data are variable presumably due to the inhomogeneous nature of the polymer (**Figure 6.11**).

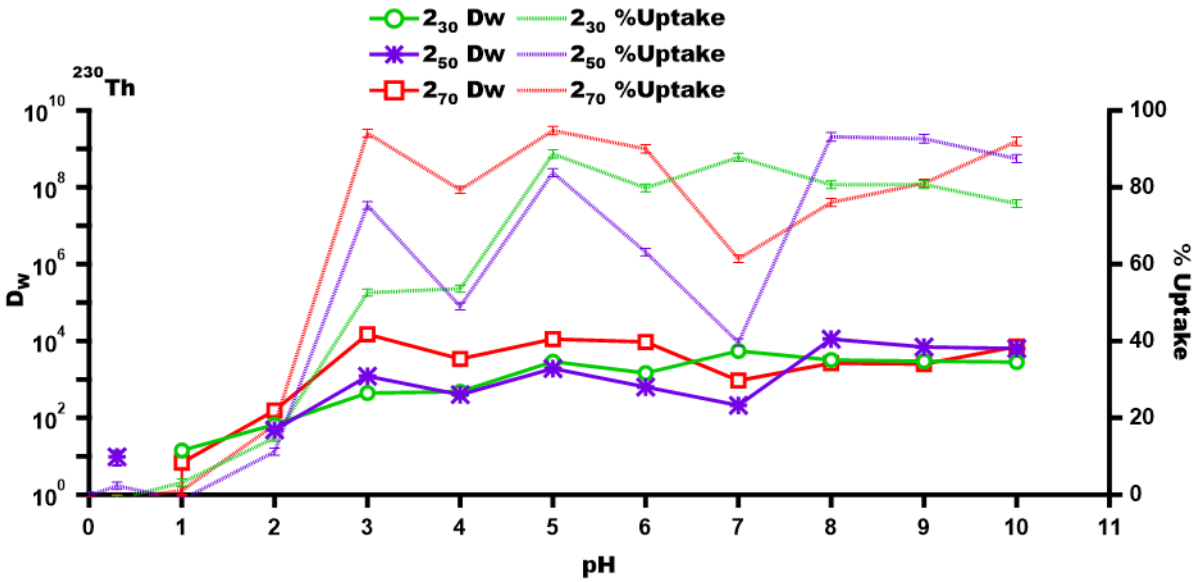

Figure 6.11 ^{230}Th uptake as a function of pH for **2_{30}**, **2_{50}**, and **2_{70}** poly(HIPE) materials.

It is interesting to note that uranium uptake is much lower averaging <10% across the entire pH range studied (**Figure 6.12)**, while thorium is consistently above > 60% and averages around 80% above a pH 3. Regardless of degree of AO functional group loading, each AO-functionalized poly(HIPE) material exhibits similar Th and U uptake trends.

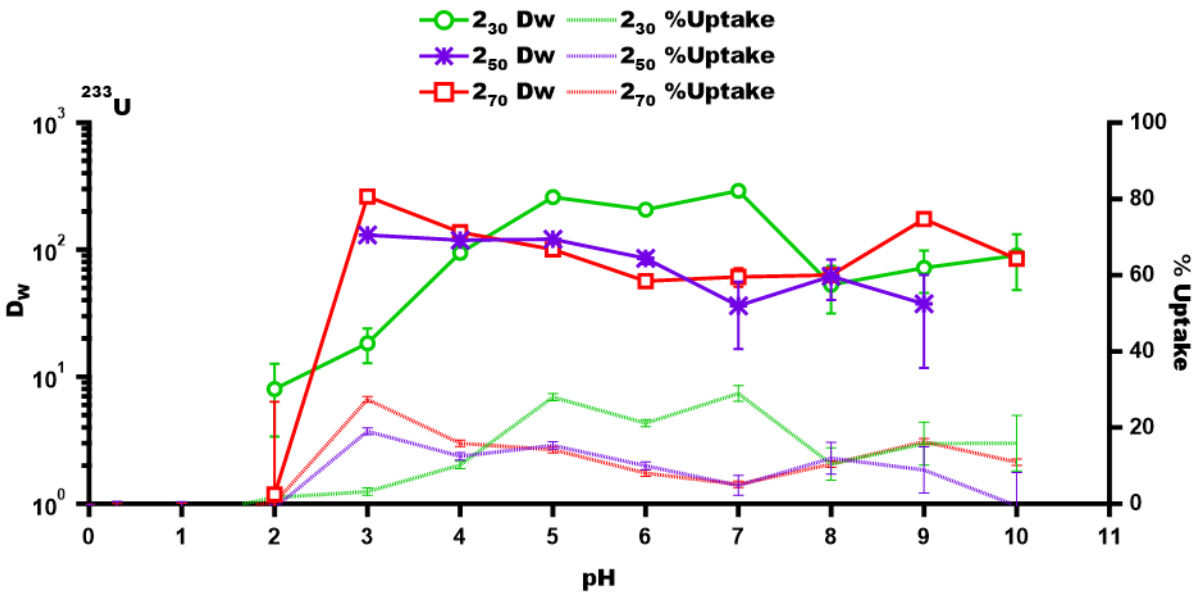

Figure 6.12 ^{233}U uptake as a function of pH for **2_{30}**, **2_{50}**, and **2_{70}** poly(HIPE) materials.

This seems to suggest, at least for radiotracer studies, that functional group loading, bulk polymer morphology, and surface area are not major drivers of separations efficacy.

Kinetics experiments were conducted using Th and U radiotracer spiked solutions as a function of time from 5 to 180 minutes (**Figure 6.13**). In general, Th uptake was much higher than U uptake over the entire timescale of the experiment. U uptake averages <10% over the course of the kinetics experiment while Th uptake is more variable. Sample 2_{70} shows constant Th uptake while samples 2_{50} and 2_{30} show more variability. This could possibly be due to initial slow diffusion of Th into the pore of the poly(HIPE), a feature not present in the phase-separated, globular structure of 2_{70}.

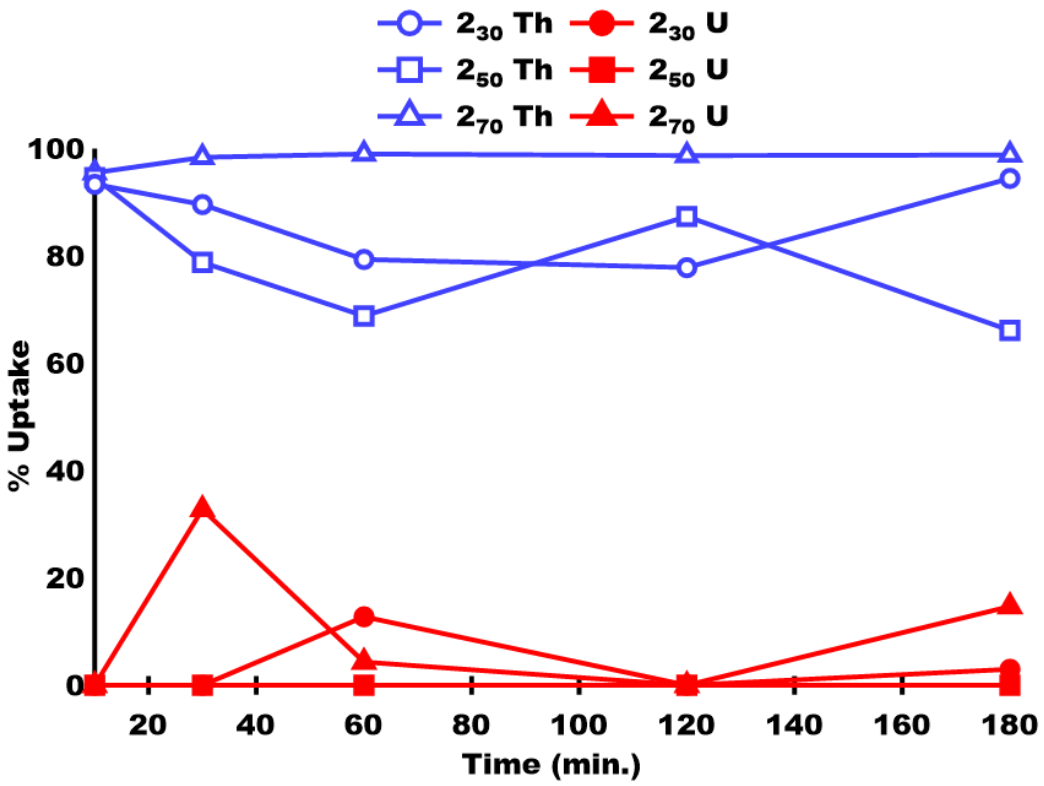

Figure 6.13 ^{230}Th and ^{233}U uptake as a function of time for **2_{30}**, **2_{50}**, and **2_{70}** materials.

6.6 *in silico* Optimization of Th-Amidoxime Complexes

Density functional theory was used to probe the molecular level interactions likely occurring in the AO-functionalized poly(HIPE)s. The following reactions were studied:

$$Th^{4+}(H_2O)_9 + C_6H_5CNNH_2O^- \longrightarrow [Th(H_2O)_8(C_6H_5CNNH_2O)]^{3+} + H_2O$$

$$Th^{4+}(H_2O)_9 + C_6H_5CNNH_2OH \longrightarrow [Th(H_2O)_8(C_6H_5CNNH_2OH)]^{4+} + H_2O$$

Both are single-displacement reactions wherein a benzamidoxime ligand in the deprotonated or neutral state displaces a water molecule to form the corresponding mixed ligand Th complex. In either case, commonly encountered starting geometries including monodentate, chelate, and η^2 metal-ligand interactions were investigated (**Scheme 6.2**)

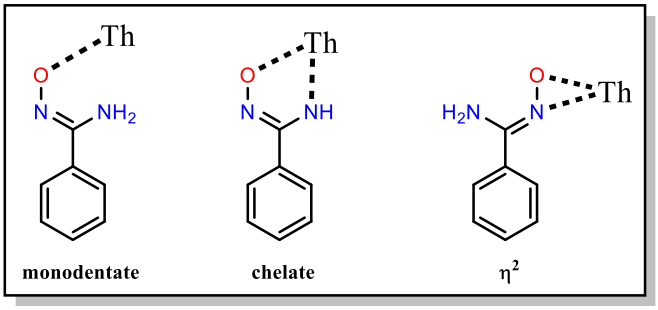

Scheme 6.2 Starting geometries used for DFT calculations of Th-amidoxime complexes. Optimized structures with Th and neutral ligands are shown in **Figure 6.14** for each starting geometry.

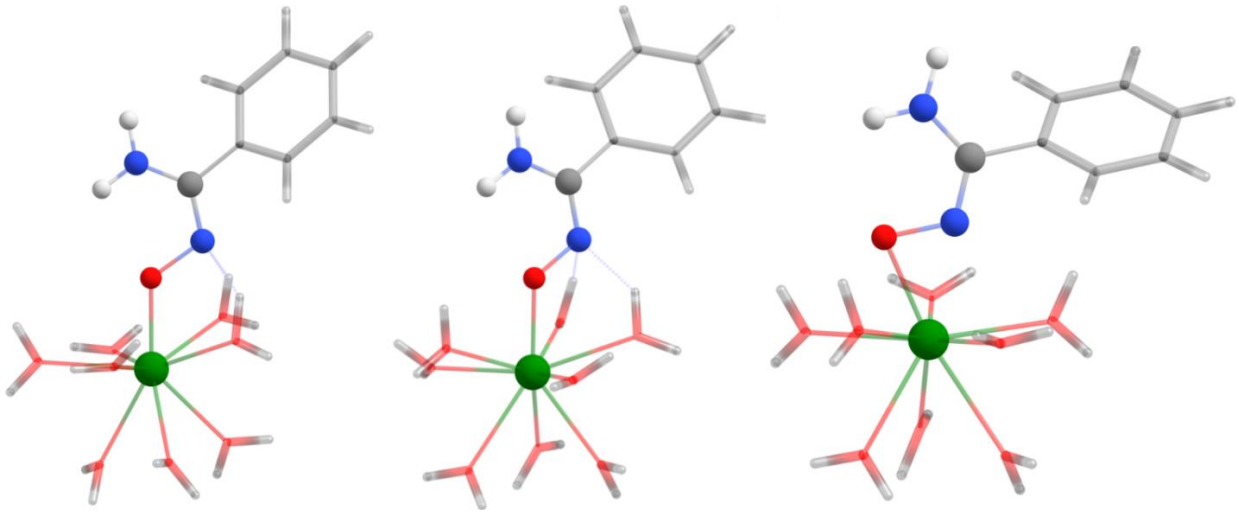

Figure 6.14 Optimized geometries for Th-benzamidoxime coordination complexes. Starting ligand geometries were monodentate (left), chelate (middle), and η^2 (right). Thorium, oxygen, nitrogen, carbon, and hydrogen are green, red, blue, grey, and white spheres respectively. Water molecules and carbon and hydrogen atoms on the phenyl ring are represented as sticks for clarity.

Despite starting with three distinct ligand-metal binding geometries (**Scheme 6.2**), only monodentate and η^2 geometries were apparent in optimized structures. These results indicate that the chelate motif, identified as the primary driver behind uranyl binding in AO-functionalized RIGP polymer fibers used for the UFS effort,[7] is not a main contributor to Th binding under the conditions studied. Frequency calculations on optimized structures were used to obtain the free

energy of complexation between Th and deprotonated benzamidoxime. The η^2 configuration was found to be ~5 kcal mol^{-1} more favorable than the monodentate motif (-417.25 kcal mol^{-1} vs. 412.48 kcal mol^{-1}) suggesting a slight preference for the η^2 interaction. These interactions are ~130 kcal mol^{-1} more favorable than bis-amidoxime/uranyl complexation discussed in Chapter 2, providing some rationale for the selectivity trends encountered in radiotracer studies. Notably, the same computational treatment applied to the neutral ligand failed to yield stable structures for monodentate and chelate starting ligand geometries. The η^2 motif was the only starting geometry to converge, suggesting that thorium is bound in this fashion when $pH < pKa^{benzamidoxime}$ (i.e. pH < 12)[8].

Finally, Th hydrolysis products which may explain the identity of the metal bound to the poly(HIPE)s after separations experiments, have been probed computationally. Of particular interest are acetate bridged Th-Th dimer or trimer complexes which may occur in solution or within a poly(HIPE) pore upon uptake. An example of an acetato-bridged dimer is show in **Figure 6.15**.

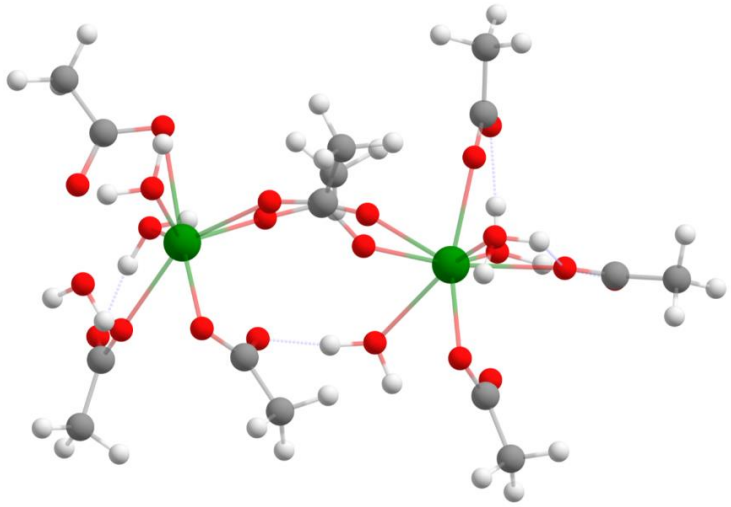

$Th^{IV}(OAc)_3(H_2O)_3(\mu\text{-}OAc)_2Th^{IV}(OAc)_3(H_2O)_3$

Figure 6.15: Optimized structure of a Th-Th acetato bridged dimer. Atom coloring is as stated above.

The optimized cluster includes two thorium atoms 5.72 Å apart bridged by two acetate ligands. Each Th center has a coordination number of 8 or 9 with either one or two coordinating water molecules. Acetate ions bind in a monodentate fashion with pronounced hydrogen bonding between coordinating waters and acetate carbonyl groups. This cluster will be used as one model fit for EXAFS data to be collected 2019-3. All cartesian coordinates of optimized structures are included in **Appendix 6.1**.

6.7 Outlook and Future Work

The future is bright and the author remains motivated by investigating the fundamental chemistry underlying new and emerging separation systems. A general outlook on the future of separation science can be found in the most recent report concerning a research agenda for transforming separation science by The National Academies of Sciences, Engineering, and Medicine.[9] Here will be provided some specific comments on proposed future work.

One shortcoming of the separation studies conducted with the poly(HIPE) materials is their use in batch mode, precluding serious industrial application. Although batch mode uptake experiments (i.e. a piece of adsorbent is shaken with metal containing aqueous solution then subsequently filtered) is used in the laboratory setting to ascertain the efficacy of an adsorbent, most industrial scale separations using solid adsorbents (e.g. ion-exchange resins) use columns. Column-based separations can be achieved with poly(HIPE) materials simply by increasing the synthesis scale and finding a suitable curing vessel. This method would greatly showcase the benefits of using poly(HIPE) materials, namely faster kinetics and sharper elution profiles due to convective mass transport through the polymer. Poly(HIPE)s would overcome the diffusion limited uptake behavior exhibited in conventional ion exchange resins. Challenges associated

with this switch to poly(HIPE)s would include the hydrophobicity of the polymer and uncontrolled swelling within the column. Both issues could be remedied with judicious choice of crosslinker and appropriate surface coatings.

Another opportunity to study separation systems lies in *operando* studies. As has been discussed, analysis of materials after a separation event yields information which may not fully describe a system during a separation. Recent advances at the Advanced Photon Source allow for the study of separation systems under operating conditions, providing a more accurate idea of uptake mechanisms and adsorbent changes. These data coupled with computational chemistry simulations of metal speciation, solvation, and affinity for active sites are expected to yield valuable fundamental information on metal-adsorbent interactions.

The synthesis of new materials, especially those with controlled *secondary* characteristics is an exciting approach to study the drivers of separation systems. In particular, membranes and porous imprinted polymers are ideal candidates to interrogate the role of hierarchical porosity and confinement in determining separations efficacy. Metal behavior in the bulk and interfacial regions is expected to be highly variable and critical information for the continued development of advanced sorbent materials.

6.8 References

(1) Dolomanov, O. V.; Bourhis, L. J.; Gildea, R. J.; Howard, J. A. K.; Puschmann, H. OLEX2 : A Complete Structure Solution, Refinement and Analysis Program. *J. Appl. Crystallogr.* **2009**, *42* (2), 339–341.

(2) Frisch, M. J.; Trucks, G. W.; Schlegel, H. B.; Scuseria, G. E.; Robb, M. A.; Cheeseman, J. R.; Scalmani, G.; Barone, V.; Mennucci, B.; Petersson, G. A.; Nakatsuji, H.; Caricato, M.; Li, X.; Hratchian, H. P.; Izmaylov, A. F.; Bloino, J.; Zheng, G.; Sonnenberg, J. L.; Hada, M.; Ehara, M.; Toyota, K.; Fukuda, R.; Hasegawa, J.; Ishida, M.; Nakajima, T.; Honda, Y.; Kitao, O.; Nakai, H.; Vreven, T.; Montgomery, J. A., Jr.; Peralta, J. E.; Ogliaro, F.; Bearpark, M.; Heyd, J. J.; Brothers, E.; Kudin, K. N.; Staroverov, V. N.; Kobayashi, R.;

Normand, J.; Raghavachari, K.; Rendell, A.; Burant, J. C.; Iyengar, S. S.; Tomasi, J.; Cossi, M.; Rega, N.; Millam, J. M.; Klene, M.; Knox, J. E.; Cross, J. B.; Bakken, V.; Adamo, C.; Jaramillo, J.; Gomperts, R.; Stratmann, R. E.; Yazyev, O.; Austin, A. J.; Cammi, R.; Pomelli, C.; Ochterski, J. W.; Martin, R. L.; Morokuma, K.; Zakrzewski, V. G.; Voth, G. A.; Salvador, P.; Dannenberg, J. J.; Dapprich, S.; Daniels, A. D.; Farkas, O.; Foresman, J. B.; Ortiz, J. V.; Cioslowski, J.; Fox, D. J.Gaussian 09, revision A.02; Gaussian, Inc.: Wallingford, CT, **2009**.

(3) Lee, C.; Yang, W.; Parr, R. G. Development of the Colle-Salvetti Correlation-Energy Formula into a Functional of the Electron Density. *Phys. Rev. B* **1988**, *37* (2), 785–789.

(4) Becke, A. D. Density-functional Thermochemistry. III. The Role of Exact Exchange. *J. Chem. Phys.* **1993**, *98* (7), 5648–5652.

(5) Walling, C.; Briggs, E. R.; Wolfstirn, K. B.; Mayo, F. R.; Wolfstirn, K. B. Copolymerization. X. The Effect of Meta- and Para-Substitution on the Reactivity of the Styrene Double Bond. *J. Am. Chem. Soc.* **1948**, *70* (4), 1537–1542.

(6) Alfey, T.; Price, C. Relative Reactivities in Vinyl Copolymerization. *J. Polym. Sci.* **1947**, *2* (1), 101–106.

(7) Abney, C. W.; Mayes, R. T.; Piechowicz, M.; Lin, Z.; Bryantsev, V. S.; Veith, G. M.; Dai, S.; Lin, W. XAFS Investigation of Polyamidoxime-Bound Uranyl Contests the Paradigm from Small Molecule Studies. *Energy Environ. Sci.* **2016**, *9* (2), 448–453.

(8) Mehio, N.; Lashely, M. a.; Nugent, J. W.; Tucker, L.; Correia, B.; Do-Thanh, C.-L.; Dai, S.; Hancock, R. D.; Bryantsev, V. S. Acidity of the Amidoxime Functional Group in Aqueous Solution: A Combined Experimental and Computational Study. *J. Phys. Chem. B* **2015**, *119* (8), 3567–3576.

(9) Science, S.; Sciences, C.; Earth, D.; Studies, L.; Academies, N. *A Research Agenda for Transforming Separation Science*; National Academies Press, **2019**.

(10) Xian, L.; Tian, G.; Beavers, C. M.; Teat, S. J.; Shuh, D. K. Glutarimidedioxime: A Complexing and Reducing Reagent for Plutonium Recovery from Spent Nuclear Fuel Reprocessing. *Angew. Chemie Int. Ed.* **2016**, *55* (15), 4671–4673.

(11) Kaltsoyannis, N. Does Covalency Increase or Decrease across the Actinide Series? Implications for Minor Actinide Partitioning. *Inorg. Chem.* **2013**, *52* (7), 3407–3413.

6.9 Appendix 6.1 Cartesian Coordinates for DFT Calculations

$Th(H_2O)_8$(Benzamidoxime)
Monodentate starting geometry
Neutral ligand

Th	-11.044281000000	0.496709000000	3.376248000000
O	-12.563475000000	-1.618969000000	2.909674000000
H	-12.751577000000	-2.260455000000	3.611315000000
H	-12.530738000000	-2.125971000000	2.084149000000
O	-13.627852000000	0.837553000000	3.242922000000
H	-14.240438000000	1.587713000000	3.274248000000
H	-14.163722000000	0.032826000000	3.165469000000
O	-11.426095000000	2.966736000000	2.537520000000
H	-11.779644000000	3.204106000000	1.666652000000
H	-11.274192000000	3.801128000000	3.007095000000
O	-9.108999000000	1.376123000000	4.840156000000
H	-8.831148000000	2.255655000000	5.136813000000
H	-8.355215000000	0.785041000000	4.989816000000
O	-11.766995000000	0.396738000000	0.912777000000
H	-11.119843000000	0.364193000000	0.191430000000
H	-12.647824000000	0.331133000000	0.513999000000
O	-11.755981000000	2.115963000000	5.340458000000
H	-11.271648000000	2.155195000000	6.178884000000
H	-12.529498000000	2.689830000000	5.446202000000
O	-11.577339000000	-0.794111000000	5.536744000000
H	-11.036555000000	-1.539522000000	5.840250000000
H	-12.202888000000	-0.590511000000	6.248398000000
O	-9.210887000000	1.223145000000	1.710433000000
H	-9.017513000000	2.091154000000	1.326832000000
H	-8.422739000000	0.673502000000	1.584608000000
C	57.541055000000	-17.832629000000	-13.401480000000
C	56.496511000000	-18.648729000000	-13.864260000000
C	55.237033000000	-18.518687000000	-13.317566000000
C	55.016796000000	-17.530899000000	-12.313146000000
C	56.093830000000	-16.730753000000	-11.827954000000
C	57.344138000000	-16.878206000000	-12.390442000000
H	58.532603000000	-17.954574000000	-13.825030000000
H	56.686085000000	-19.391382000000	-14.630036000000
H	54.414624000000	-19.154326000000	-13.626696000000
H	55.911311000000	-16.028479000000	-11.022147000000
H	58.176233000000	-16.279172000000	-12.040144000000
C	53.582853000000	-16.928839000000	-12.204503000000
N	52.862764000000	-16.036687000000	-12.852522000000
H	51.916107000000	-15.838938000000	-12.553559000000
H	53.221703000000	-15.555962000000	-13.662826000000

N	53.757625000000	-17.761495000000	-11.312064000000
O	-9.652203000000	-1.035849000000	3.340047000000
H	-9.088982000000	-1.819158000000	3.276701000000

$Th(H_2O)_8$(Benzamidoxime)
η^2 starting geometry
Neutral ligand

Th	11.941063000000	-5.170790000000	-1.606742000000
O	11.775562000000	-2.730687000000	-2.520951000000
H	11.807044000000	-1.926496000000	-1.978177000000
H	11.660755000000	-2.436676000000	-3.438974000000
O	9.534487000000	-4.308196000000	-1.890069000000
H	8.732004000000	-4.661282000000	-1.474390000000
H	9.265628000000	-3.514886000000	-2.380292000000
O	10.194283000000	-6.341860000000	-0.028041000000
H	9.939848000000	-6.105967000000	0.878450000000
H	9.698852000000	-7.144033000000	-0.256947000000
O	13.247969000000	-7.232907000000	-2.314865000000
H	13.673725000000	-7.848658000000	-1.697313000000
H	13.575067000000	-7.454917000000	-3.201691000000
O	11.533512000000	-3.648419000000	0.360615000000
H	12.251407000000	-3.451918000000	0.995185000000
H	10.741453000000	-3.173487000000	0.659714000000
O	10.411795000000	-7.046229000000	-2.704978000000
H	10.739617000000	-7.928270000000	-2.943662000000
H	9.494730000000	-7.004638000000	-3.021312000000
O	11.980249000000	-5.165512000000	-4.172339000000
H	12.697585000000	-4.875394000000	-4.758631000000
H	11.299149000000	-5.551158000000	-4.746762000000
O	12.926100000000	-6.414431000000	0.381511000000
H	12.462623000000	-7.041432000000	0.957813000000
H	13.746081000000	-6.148489000000	0.842511000000
C	15.251428000000	-3.970711000000	3.783627000000
C	15.928765000000	-5.038081000000	3.190774000000
C	15.946425000000	-5.174591000000	1.801694000000
C	15.250784000000	-4.245800000000	1.001163000000
C	14.563728000000	-3.166419000000	1.605215000000
C	14.581646000000	-3.029251000000	2.990482000000
H	15.273483000000	-3.849451000000	4.861488000000
H	16.469676000000	-5.748666000000	3.806445000000
H	16.511233000000	-5.987043000000	1.352539000000
H	14.170330000000	-2.360848000000	0.989636000000
H	14.120177000000	-2.165169000000	3.456836000000
C	15.319681000000	-4.345059000000	-0.467283000000
N	16.471964000000	-4.480849000000	-1.085658000000

H	16.551247000000	-4.625011000000	-2.085778000000
H	17.343067000000	-4.389429000000	-0.572155000000
N	14.129300000000	-4.304213000000	-1.109713000000
O	14.229684000000	-4.358500000000	-2.567214000000
H	14.333905000000	-3.442563000000	-2.885265000000

$Th(H_2O)_8$(Benzamidoxime)
Chelate starting geometry
Neutral ligand

Th	9.911639000000	-6.035772000000	-2.322693000000
O	8.811991000000	-3.747081000000	-2.537948000000
H	9.228771000000	-3.135798000000	-1.914754000000
H	8.258242000000	-3.232283000000	-3.145403000000
O	7.991709000000	-5.982368000000	-4.194752000000
H	7.187709000000	-6.488193000000	-4.002595000000
H	7.813793000000	-5.494059000000	-5.014462000000
O	8.348604000000	-8.169936000000	-2.035763000000
H	7.536190000000	-8.175991000000	-1.506392000000
H	8.419437000000	-9.051794000000	-2.435640000000
O	12.219925000000	-7.223755000000	-2.322572000000
H	12.462844000000	-7.799229000000	-1.581996000000
H	13.041269000000	-6.993464000000	-2.780305000000
O	7.964626000000	-5.660070000000	-0.667997000000
H	7.869450000000	-6.017881000000	0.228001000000
H	7.356014000000	-4.908070000000	-0.733985000000
O	10.301011000000	-7.713233000000	-4.291330000000
H	11.063534000000	-8.306951000000	-4.374215000000
H	9.638898000000	-7.979874000000	-4.948340000000
O	11.238105000000	-5.039189000000	-4.310448000000
H	11.671277000000	-4.213763000000	-4.585739000000
H	11.205838000000	-5.596278000000	-5.104382000000
O	10.418834000000	-7.339251000000	-0.140579000000
H	10.154188000000	-8.189860000000	0.243696000000
H	10.889668000000	-6.844156000000	0.547401000000
C	17.918816000000	-1.589134000000	5.707921000000
C	18.573063000000	-1.420225000000	4.477398000000
C	17.906817000000	-0.821537000000	3.423629000000
C	16.574723000000	-0.369564000000	3.626723000000
C	15.906025000000	-0.562432000000	4.863626000000
C	16.593985000000	-1.164988000000	5.901643000000
H	18.450183000000	-2.057789000000	6.530863000000
H	19.595694000000	-1.758679000000	4.355072000000
H	18.381299000000	-0.678155000000	2.458943000000
H	14.885181000000	-0.216976000000	4.986987000000
H	16.114310000000	-1.306866000000	6.863035000000

C	16.175191000000	0.973542000000	2.833956000000
N	16.478926000000	2.237319000000	3.034774000000
H	16.241577000000	2.962227000000	2.368249000000
H	17.087318000000	2.499184000000	3.799529000000
N	15.668764000000	-0.024821000000	2.322626000000
O	10.976612000000	-4.701976000000	-1.108169000000
H	11.584096000000	-4.096433000000	-0.663990000000

$Th^{IV}(OAc)_3(H_2O)_3(\mu\text{-}OAc)_2Th^{IV}(OAc)_3(H_2O)_3$

Th	12.386193000000	-1.600413000000	1.835320000000
C	15.793031000000	-3.202274000000	-0.835349000000
H	16.114518000000	-3.486322000000	-1.838590000000
H	16.334027000000	-3.829318000000	-0.118674000000
H	16.045146000000	-2.162373000000	-0.633790000000
C	14.310739000000	-3.442864000000	-0.657607000000
O	13.653331000000	-2.640700000000	0.045839000000
O	13.809659000000	-4.469268000000	-1.219893000000
Th	11.891519000000	-5.708936000000	-2.109738000000
C	10.196650000000	-1.255303000000	-1.818985000000
H	10.307125000000	-0.344780000000	-1.231976000000
H	9.128256000000	-1.425593000000	-1.989452000000
H	10.677406000000	-1.147308000000	-2.791743000000
C	10.754142000000	-2.448266000000	-1.076809000000
O	11.113369000000	-3.451512000000	-1.749849000000
O	10.808075000000	-2.401214000000	0.188138000000
C	14.036639000000	1.596450000000	-1.186190000000
H	13.554064000000	1.121064000000	-2.044698000000
H	15.007033000000	1.988869000000	-1.485917000000
H	13.387022000000	2.415190000000	-0.867365000000
C	14.185183000000	0.590075000000	-0.064922000000
O	15.302811000000	0.260824000000	0.348764000000
O	13.069986000000	0.115306000000	0.407431000000
C	12.484216000000	1.990479000000	5.040095000000
H	13.176424000000	2.349436000000	5.799845000000
H	11.552006000000	1.670408000000	5.512633000000
H	12.237814000000	2.811998000000	4.361167000000
C	13.095454000000	0.846375000000	4.254857000000
O	12.315566000000	0.295811000000	3.371189000000
O	14.261912000000	0.498415000000	4.464123000000
C	10.286688000000	-2.737272000000	5.625421000000
H	10.063478000000	-1.774361000000	6.095541000000
H	10.908039000000	-3.310859000000	6.312611000000
H	9.338221000000	-3.245109000000	5.446318000000
C	11.012375000000	-2.481847000000	4.328260000000
O	12.275351000000	-2.507644000000	4.289169000000

O	10.343940000000	-2.215250000000	3.275197000000
C	13.370454000000	-5.820282000000	-6.250110000000
H	14.369322000000	-6.244099000000	-6.106661000000
H	13.481787000000	-4.833643000000	-6.699623000000
H	12.817486000000	-6.488064000000	-6.911246000000
C	12.706099000000	-5.728517000000	-4.903711000000
O	12.804565000000	-4.663794000000	-4.212852000000
O	12.071937000000	-6.722204000000	-4.434591000000
C	12.120547000000	-10.097553000000	-0.305409000000
H	11.690455000000	-9.698616000000	0.616907000000
H	12.845052000000	-10.874074000000	-0.066285000000
H	11.298645000000	-10.532528000000	-0.880768000000
C	12.771526000000	-8.979221000000	-1.092778000000
O	13.971385000000	-9.034627000000	-1.386915000000
O	11.989121000000	-7.995652000000	-1.424351000000
C	9.569638000000	-5.780552000000	1.733081000000
H	8.546668000000	-6.119728000000	1.577796000000
H	9.550118000000	-4.744693000000	2.085930000000
H	10.052038000000	-6.386125000000	2.503324000000
C	10.352910000000	-5.838876000000	0.450553000000
O	11.622995000000	-5.699094000000	0.469979000000
O	9.770383000000	-5.997245000000	-0.657915000000
O	14.716759000000	-1.233682000000	2.518919000000
H	15.158578000000	-0.737457000000	1.781779000000
H	14.738418000000	-0.647770000000	3.326371000000
O	10.318027000000	0.058901000000	1.679997000000
H	10.634434000000	0.661472000000	2.375224000000
H	9.586694000000	-0.446114000000	2.060588000000
O	12.799819000000	-4.084961000000	2.215680000000
H	12.431222000000	-4.786845000000	1.623789000000
H	12.799784000000	-4.368166000000	3.136349000000
O	9.900326000000	-4.920406000000	-3.642209000000
H	10.102015000000	-4.180244000000	-4.224544000000
H	9.603420000000	-5.680723000000	-4.160077000000
O	14.222650000000	-6.686109000000	-2.519022000000
H	14.316955000000	-7.615092000000	-2.167689000000
H	14.855037000000	-6.105469000000	-2.079607000000
O	9.786480000000	-7.390230000000	-2.951292000000
H	9.319167000000	-7.424137000000	-2.103977000000
H	10.247730000000	-8.229717000000	-3.061477000000

$Th(H_2O)_8$(Benzamidoxime)
Monodentate starting geometry
Deprotonated ligand

Th	11.297077000000	-5.496961000000	-1.954397000000
O	11.408037000000	-3.376190000000	-3.522820000000
H	11.213726000000	-3.315812000000	-4.468881000000
H	12.076987000000	-2.702518000000	-3.330472000000
O	9.429436000000	-3.690142000000	-1.685010000000
H	8.803202000000	-3.547776000000	-0.961386000000
H	9.440566000000	-2.890564000000	-2.231033000000
O	9.894166000000	-5.759191000000	0.262775000000
H	10.144776000000	-5.495905000000	1.160379000000
H	9.071971000000	-6.264388000000	0.340263000000
O	11.324099000000	-8.065076000000	-2.137931000000
H	11.877640000000	-8.522268000000	-1.487028000000
H	11.202155000000	-8.666365000000	-2.886103000000
O	12.425931000000	-3.694554000000	-0.688313000000
H	13.404214000000	-3.932481000000	-0.711861000000
H	12.266473000000	-2.956376000000	-0.085919000000
O	8.833980000000	-6.488377000000	-2.421151000000
H	8.566834000000	-7.419289000000	-2.436370000000
H	8.035316000000	-5.965048000000	-2.583946000000
O	10.967032000000	-6.143237000000	-4.451579000000
H	11.679498000000	-6.211210000000	-5.104842000000
H	10.145585000000	-6.390459000000	-4.900749000000
O	12.643503000000	-6.645663000000	-0.141005000000
H	12.543528000000	-6.953691000000	0.769154000000
H	13.580877000000	-6.331093000000	-0.282829000000
C	18.949571000000	-4.295466000000	0.528616000000
C	18.999619000000	-5.441603000000	-0.265941000000
C	17.920300000000	-5.777216000000	-1.074932000000
C	16.772156000000	-4.965247000000	-1.083963000000
C	16.725285000000	-3.817325000000	-0.276103000000
C	17.814150000000	-3.483505000000	0.520066000000
H	19.798044000000	-4.031393000000	1.149762000000
H	19.879562000000	-6.074347000000	-0.253767000000
H	17.961782000000	-6.686077000000	-1.666531000000
H	15.865372000000	-3.157293000000	-0.310395000000
H	17.787779000000	-2.582942000000	1.122843000000
C	15.639546000000	-5.321737000000	-1.954344000000
N	15.873503000000	-5.780905000000	-3.180923000000
H	15.121718000000	-6.085661000000	-3.777365000000
H	16.809330000000	-5.773813000000	-3.559355000000
N	14.416687000000	-5.193506000000	-1.440760000000
O	13.356919000000	-5.489629000000	-2.392825000000

$Th(H_2O)_8$(Benzamidoxime)
η^2 starting geometry
Deprotonated ligand

Th	11.501069000000	-4.984663000000	-1.510916000000
O	11.240815000000	-2.657739000000	-2.708676000000
H	12.097491000000	-2.226375000000	-2.849645000000
H	10.580553000000	-2.207760000000	-3.253816000000
O	9.378262000000	-4.795858000000	-3.117690000000
H	8.476145000000	-4.793281000000	-2.768358000000
H	9.320555000000	-4.611847000000	-4.065892000000
O	9.023328000000	-5.371353000000	-0.404048000000
H	8.571536000000	-4.682929000000	0.104337000000
H	8.528457000000	-6.192236000000	-0.271782000000
O	13.000006000000	-7.158754000000	-1.418681000000
H	13.432404000000	-7.444781000000	-0.601808000000
H	13.576378000000	-7.422766000000	-2.149849000000
O	10.598676000000	-3.045039000000	-0.048781000000
H	10.635034000000	-2.942722000000	0.912385000000
H	10.576764000000	-2.157459000000	-0.435126000000
O	10.407301000000	-7.303637000000	-2.076618000000
H	10.914020000000	-8.113115000000	-1.917856000000
H	9.621653000000	-7.538279000000	-2.589117000000
O	12.265704000000	-5.613316000000	-3.897380000000
H	13.067695000000	-5.175897000000	-4.220437000000
H	11.924479000000	-6.168720000000	-4.612487000000
O	11.677230000000	-5.820790000000	0.897689000000
H	11.061069000000	-6.311445000000	1.458865000000
H	12.435703000000	-5.542369000000	1.451339000000
C	15.242371000000	-5.289712000000	4.006639000000
C	16.152633000000	-5.741614000000	3.051579000000
C	16.004135000000	-5.384476000000	1.712261000000
C	14.932091000000	-4.569888000000	1.319582000000
C	14.019251000000	-4.107932000000	2.287245000000
C	14.180701000000	-4.466183000000	3.625468000000
H	15.373806000000	-5.556256000000	5.049261000000
H	16.985724000000	-6.368224000000	3.349454000000
H	16.717153000000	-5.750830000000	0.980703000000
H	13.265208000000	-3.377244000000	2.010755000000
H	13.507621000000	-4.069760000000	4.377880000000
C	14.763893000000	-4.203827000000	-0.104772000000
N	15.814610000000	-3.842961000000	-0.838043000000
H	15.700227000000	-3.593091000000	-1.809885000000
H	16.704747000000	-3.645686000000	-0.403403000000
N	13.549336000000	-4.291799000000	-0.609820000000
O	13.412263000000	-4.003325000000	-2.005651000000

$Th(H_2O)_8$(Benzamidoxime)
Chelate starting geometry
Deprotonated ligand

Th	11.020041000000	-5.243290000000	-1.357462000000
O	11.767579000000	-2.873398000000	-1.553878000000
H	12.710691000000	-2.891037000000	-1.205044000000
H	11.503012000000	-1.958877000000	-1.716391000000
O	9.316423000000	-3.783646000000	-2.758763000000
H	8.373671000000	-3.977518000000	-2.864399000000
H	9.489225000000	-2.967314000000	-3.250164000000
O	8.595224000000	-6.363351000000	-1.372047000000
H	7.870456000000	-6.188469000000	-0.753998000000
H	8.275679000000	-7.027727000000	-2.000233000000
O	11.990120000000	-7.624925000000	-1.800543000000
H	11.804664000000	-8.488551000000	-1.405208000000
H	12.907201000000	-7.641212000000	-2.113796000000
O	9.458712000000	-4.073346000000	0.344756000000
H	9.503276000000	-4.245096000000	1.296720000000
H	9.032670000000	-3.210473000000	0.237653000000
O	10.456344000000	-6.273183000000	-3.700887000000
H	10.833758000000	-7.115852000000	-3.992017000000
H	10.004572000000	-5.877084000000	-4.459397000000
O	13.095533000000	-5.214878000000	-2.746953000000
H	13.780385000000	-4.759958000000	-2.168246000000
H	13.316835000000	-5.090336000000	-3.679316000000
O	10.657655000000	-6.707351000000	0.755579000000
H	9.947122000000	-7.307720000000	1.023599000000
H	11.395851000000	-6.841392000000	1.367942000000
C	18.274387000000	-1.710367000000	-0.579330000000
C	17.616023000000	-1.462553000000	0.625994000000
C	16.467023000000	-2.173498000000	0.952179000000
C	15.962192000000	-3.136152000000	0.059913000000
C	16.625642000000	-3.376099000000	-1.154591000000
C	17.780541000000	-2.668760000000	-1.465964000000
H	19.176627000000	-1.161475000000	-0.824607000000
H	17.998018000000	-0.714445000000	1.311009000000
H	15.950003000000	-1.952390000000	1.880397000000
H	16.275326000000	-4.151573000000	-1.827047000000
H	18.307526000000	-2.873669000000	-2.390812000000
C	14.752388000000	-3.894033000000	0.419775000000
N	14.596409000000	-4.324285000000	1.668734000000
H	13.752072000000	-4.787296000000	1.961272000000
H	15.350379000000	-4.243121000000	2.335167000000
N	13.848735000000	-4.080371000000	-0.540892000000
O	12.723395000000	-4.909751000000	-0.136293000000

6.10 Appendix 6.2 Crystallographic Studies with Amidoxime-Based Ligands

In an effort to develop synthetic protocols to probe the AO-Th, U, Pu ,Np molecular interaction, small molecule coordination complexes were synthesized with the tridentate amidoxime analogue glutarimidedioxime (H_2A) according to literature precedent[10] as proposed in **Scheme 6.3**. H_2A was used on account of its denticity and was expected to afford the greatest degree of crystal growth success.

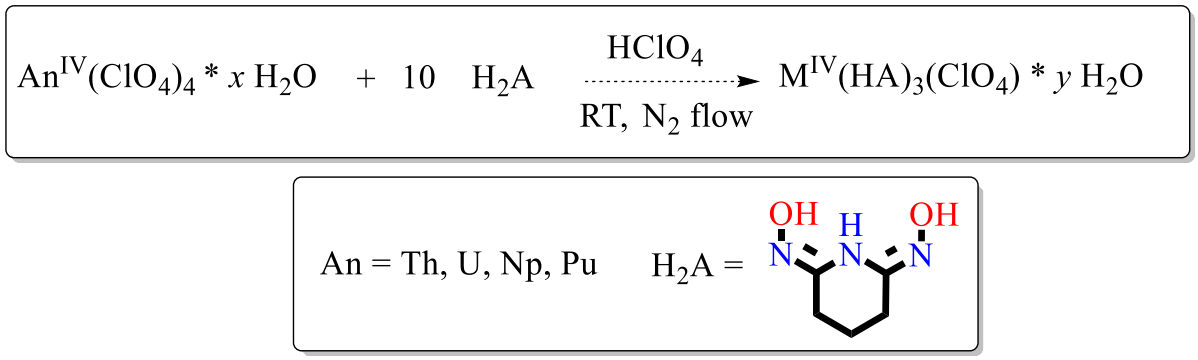

Scheme 6.3: Proposed scheme for the synthesis of early actinide-amidoxime complexes

In each case, the metal stock solution is first counted with LSC in order to assay concentration before being diluted in 1-2 M $HClO_4$. Ten equivalents of H_2A in 1-2M $HClO_4$ are then added dropwise to afford a final volume no greater than 1 mL. The solutions are placed under gentle nitrogen flow and diffraction quality crystals are obtained within 24-72 hours.

Products obtained for each synthesis conform to the following reaction:

$$An^{IV}(ClO_4)_4 * x\ H_2O + 10\ H_2A \xrightarrow[RT,\ N_2\ flow]{1\text{-}2\ M\ HClO_4} An^{IV}(HA)_3(ClO_4) * 1\ H_2O$$

In every case, the resulting complex exhibits 3:1 ligand:metal stoichiometry. Each H_2A ligand bears a negative charge (deprotonated via the coordinating nitrogen) resulting in a positively charged metal complex crystallized with one perchlorate ion for charge balance. Structures for each actinide are show in **Figure 6.16** below. In each case, disorder was apparent

in refining the ClO_4^- and the anion has been omitted for clarity. Crystal structure parameters are included in **Tables 6.5-6.6.**

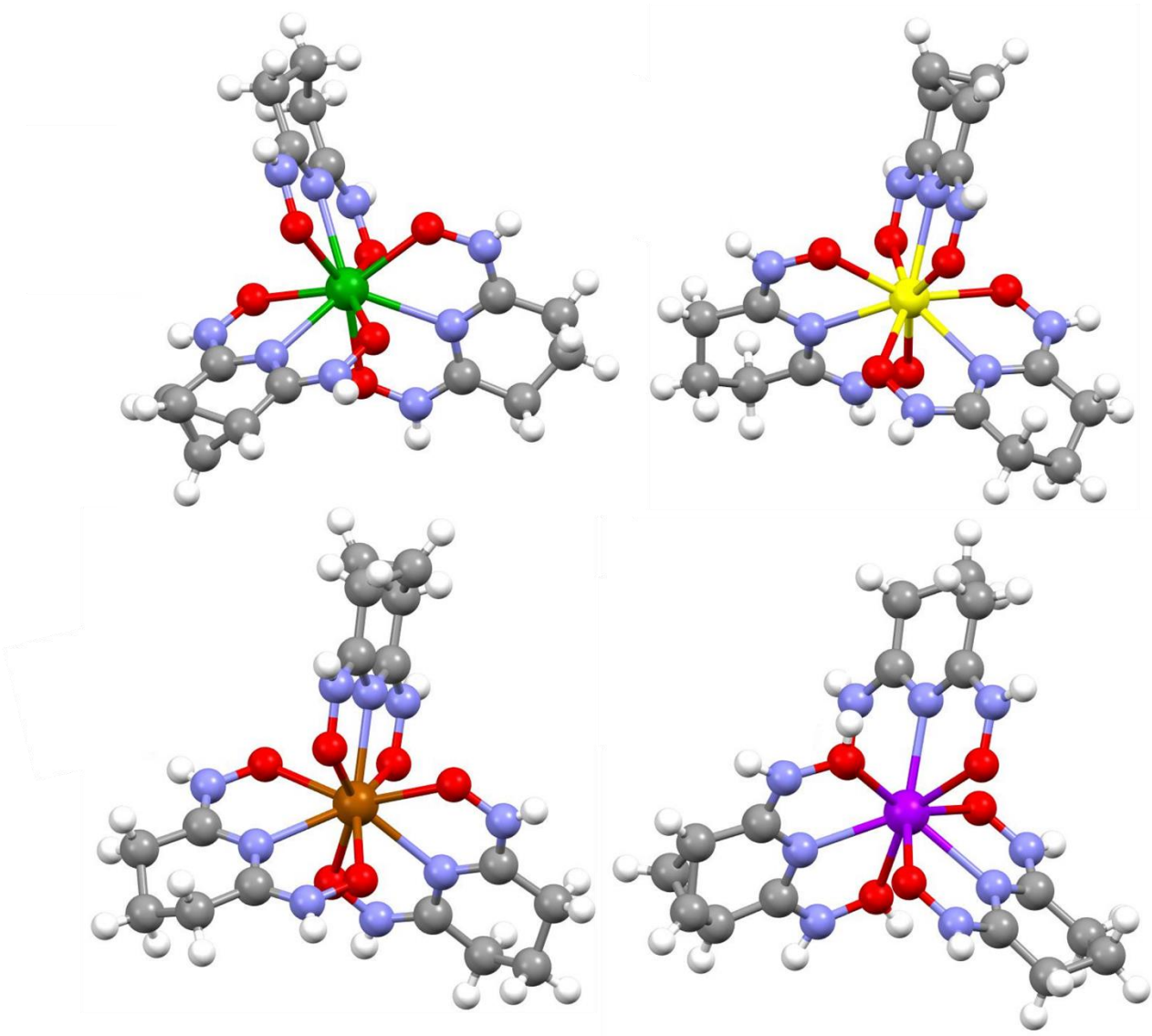

Figure 6.16 Crystal structure of isostructural $An^{IV}(HA)$ complexes. Clockwise from top left are $Th(HA)_3(ClO_4)*H_2O$, $U(HA)_3(ClO_4)*H_2O$, $Np(HA)_3(ClO_4)*H_2O$, and $Pu(HA)_3(ClO_4)*H_2O$. Note that non coordinating ClO_4^- and H_2O have been omitted for clarity. Thorium, uranium, neptunium, plutonium, oxygen, nitrogen, carbon, and hydrogen are green, yellow, purple, bronze, red, blue, grey, and white sphere respectively.

Table 6.6 Selected Crystal Structure Parameters and Reflection Statistics for Th and U Complexes

Sample	**$Th(HA)_3(ClO_4) \bullet H_2O$**	**$U(HA)_3(ClO_4) \bullet H_2O$**
Formula	$C_{2.7}H_{4.5}Cl_{0.3}N_{1.5}O_{2.7}Th_{0.2}$	$C_{2.1}H_3Cl_{0.1}N_{1.2}O_{1.8}U_{0.1}$
Temperature (K)	100	100
Wavelength (Å)	0.71073	0.71073
Crystal system	monoclinic	monoclinic
Space group	*C2/c*	*C2/c*
a, Å	25.6326(13)	25.520(4)
b, Å	10.2139(5)	10.2158(15)
c, Å	11.1996(6)	11.1588(17)
α, °	90	90
β, °	109.0570(10)°	107.843(2)°
γ, °	90	90
V, $Å^3$	2771.5(3)	2769.2(7)
Z	24	30
Density (calcd. g/cm^3)	2.178	1.980
F(000)	1761	1288
θ range data collection	2.164 - 30.529	1.677 – 33.075
Limiting indices	$-36 \le h \le 36$ $-14 \le k \le 14$ $-15 \le l \le 15$	$-39 \le h \le 38$ $-15 \le k \le 15$ $-16 \le l \le 16$
Reflection collected	20194	24495
R(int)	0.0346	0.0573
Data/restraints/parameters	4032/0/247	5002/0/242
Goodness-of-fit on F^2	1.119	1.028
R indices (all data)	0.0322	0.0449
Final R indices [I>4σ(I)]	R1 = 0.0277, wR2 = 0.0729	R1 = 0.0345, wR2 = 0.0796

Table 6.7 Selected Crystal Structure Parameters and Reflection Statistics for Np and Pu Complexes

Sample	**$Np(HA)_3(ClO_4) \bullet H_2O$**	**$Pu(HA)_3(ClO_4) \bullet H_2O$**
Formula	$C_{2.1}H_{3.6}Cl_{0.3}N_{1.2}Np_{0.1}O_{2.2}$	$C_{2.2}H_4Cl_{0.3}N_{1.3}O_{2.2}Pu_{0.1}$
Temperature (K)	100	100
Wavelength (Å)	0.71073	0.71073
Crystal system	monoclinic	monoclinic
Space group	*C2/c*	*C2/c*
a, Å	25.2271(15)	24.782(3)
b, Å	10.1359(6)	10.0339(10)
c, Å	11.1521(7)	11.2030(11)
α, °	90	90
β, °	107.4670(10)	107.189(2)°
γ, °	90	90
V, $Å^3$	2720.1(3)	2661.3(5)
Z	30	28
Density (calcd. g/cm^3)	5.132	5.002
F(000)	3438	3265
θ range data collection	1.692 – 33.066	1.720 – 30.557
Limiting indices	$-37 \leq h \leq 37$ $-14 \leq k \leq 14$ $-16 \leq l \leq 16$	$-34 \leq h \leq 35$ $-14 \leq k \leq 14$ $-15 \leq l \leq 15$
Reflection collected	23640	18038
R(int)	0.1374	0.0804
Data/restraints/parameters	4894/3/229	3859/0/223
Goodness-of-fit on F^2	1.048	1.116
R indices (all data)	0.0579	0.0457
Final R indices [I>4σ(I)]	R1 = 0.0468, wR2 = 0.1207	R1 = 0.0414, wR2 = 0.1241

All complexes crystalized in the monoclinic C2/c space group in a 3:1 ligand:metal stoichiometry. Perchloric acid solution was chosen as non-complexing media and 10 equivalents of ligand were used to accommodate the 8-10 coordination numbers characteristic of early actinide complexes. Selected metal-ligand bond lengths are shown in **Table 6.7**. Metal nitrogen (middle) interactions decrease from 2.56 to 2.45 Å across the series. The same trend is evident in metal-oxygen and metal-nitrogen (outer) bonds with lengths ranging from 2.45 – 2.37 and 3.37 – 3.28 Å respectively. This decrease in average bond length maybe explained by the increase in

covalency across the f block as suggested by others[11] as well as the increased contribution of the less diffuse 5f orbitals compared with the 6d orbitals.

Table 6.8 Selected Metal-Ligand Bond Lengths for Th, U, Np, and Pu Crystal Structures. Averages of 3, 6, and 6 bond lengths are taken for the metal-middle HA nitrogen, metal-HA oxygen, and metal-HA outer nitrogen interactions respectively

Sample	Bond	Distance (Å)
$Th(HA)_3(ClO_4) \bullet H_2O$	$Th\text{-}O_{outer}$	2.45 ± 0.01
	$Th\text{-}N_{middle}$	2.56 ± 0.02
	$Th\text{-}N_{outer}$	3.37 ± 0.01
$U(HA)_3(ClO_4) \bullet H_2O$	$U\text{-}O_{outer}$	2.40 ± 0.01
	$U\text{-}N_{middle}$	2.51 ± 0.02
	$U\text{-}N_{outer}$	3.32 ± 0.01
$Np(HA)_3(ClO_4) \bullet H_2O$	$Np\text{-}O_{outer}$	2.39 ± 0.01
	$Np\text{-}N_{middle}$	2.47 ± 0.02
	$Np\text{-}N_{outer}$	3.31 ± 0.01
$Pu(HA)_3(ClO_4) \bullet H_2O$	$Pu\text{-}O_{outer}$	2.37 ± 0.01
	$Pu\text{-}N_{middle}$	2.45 ± 0.01
	$Pu\text{-}N_{outer}$	3.28 ± 0.01